Assessing toxicity of Carbon based nanoparticles in cells and zebrafish by using biospectroscopy

An alternative format thesis submitted for the degree of Doctor of Philosophy in the Faculty of Science and Technology

Lancaster University

September 2015

Junyi Li BSc

Lancaster environment centre

Declaration

I declare that this thesis is my work and has not been submitted for the award of a higher degree or qualification at this university or elsewhere.

Abstract

Raman and infrared (IR) spectroscopies provide detailed information about biological constituents such as lipids, proteins, carbohydrates and DNA/RNA, *etc*. Based on this, these techniques can be used to differentiate cells and tissues, as well as employed as a diagnostic tool for detecting post-exposure biochemical alterations in toxicity assessment due to the induced changes of chemical composition and structure reflected by their spectral properties. Over the past few decades, Raman and IR spectroscopies with the development of more sophisticated instruments can provide high-resolution spectral data from heterogeneous biological samples, which consisting of large amount of biochemical information, is complex. Therefore, computational analysis is employed to process and analyse the data for obtaining meaningful information and getting deeper insight into the wavenumbers-related biochemical alterations. Carbon-based nanoparticles (CNPs) are most widely used novel nanomaterials. With their widespread application, concerns emerge on their potential risk to the health of organism and human, and investigation on their possible toxicity is urgently required. This thesis is contributing to the toxicity assessment of CNPs by using spectroscopic techniques coupled with computational analysis. Findings from our projects indicated that this approach has the capability of detecting the CNPs-induced biochemical alterations both *in vitro* and *in vivo*, which implies that techniques involved in IR and Raman spectroscopy can provide a rapid and highly sensitive tool to detect minimal changes at the subcellular level.

Acknowledgements

I am extremely grateful to my supervisors Frank Martin and Kevin Jones. During the whole course, Frank not only gave me academic guides, but also offered me lots of valuable suggestions on many parts. Also, I need to give my special thanks to Dr Hong Li, who firstly introduce me to Lancaster University and offered me lots of help during my study.

I would like to give thanks to my friends and colleagues in Lancaster: Becky, Blessing, Kelly, Holly, Julio, Weiyi, Imran, Valon, Adil, Matt, Simon, Lara, Ketan, Georgios, Alana, Changer, Chun, Ying W, Ying Z, Xiaoqin, Shizhen, Wei, Naifu, and Yan. Additionally, I also need to deserve my thanks to the friends or collaborators in CAS: Prof. Guangguo Ying and his colleagues in GIG, Guangzhou, China; Prof. Heqing Shen, Dr. Li Cui and their colleagues in IUE, Xiamen, China, for their great help during my research there.

Finally, I would like to give my deep thanks to my parents, who funded my study and always stand a strong support for me. As well, great thanks to my uncle, Dr. Jianming Wu, for his patient guide in life.

Table of contents

List of abbreviations

AFM: Atomic Force Microscopy

B[*a*]P: Benzo[*a*]pyrene

BBB: Blood-Brain Barrier

BGB: Blood-Gonad Barrier

BSA: Bovine Serum Albumin

CNPs: Carbon Nanoparticles

CNTs: Carbon Nanotubes

DLS: Dynamic Light Scattering

DMSO: Dimethylsulfoxide

DPPC: 1,2-dipalmitoyl-sn-glycero-3-phosphocholine

EE2: 17α-ethinylestradiol

FPA: Focal Plane Array

FTIR: Fourier-Transform Infrared

HOCs: Hydrophobic organic compounds

IR: Infrared

IRE: Internal Reflection Element

LDA: Linear Discriminant Analysis

LDH: Lactate Dehydrogenase

Low-E: Low-emissivity

MIR: Mid-Infrared

MWCNTs: Multi-Walled Carbon Nanotubes

NIR: Near-Infrared

NOM: Natural Organic Matter

OS: Oxidative Stress

PC: Principal component

PCA: Principal Component Analysis

PEI: Polyethyleneimine

PLS: Partial least squares

PVP: Polyvinylpyrrolidone

ROS: Reactive Oxygen Species

S-G: Savizky-Golay

SEM: Scanning Electron Microscopy

SDS: Sodium Dodecyl Sulphate

SNT: Signal-to-Noise Ratio

STP: Sewage Treatment Plants

SWCNTs: Single-Walled Carbon Nanotubes

TEM: Transmission Electron Microscopy

THF: Tetrahydrofuran

UV: Ultraviolet

WDN: Wavelet De-noising

WIP: Wastewater Incineration Plants

Chapter 1 General introduction

1. Introduction

With the rapid development, nanotechnology is no longer mysterious for the public and is no longer the privilege on scientist's bench; it is more common that the nanomaterials present in the commercial or industrial products. They are now increasingly found in plastic wares, clothing, cosmetics, electrical appliances, and even food products (Becheri et al. 2008; Serpone et al. 2007). Their applications also extend into the biomedical field and healthcare, particularly in medical imaging and diagnosis, pharmaceuticals, drug delivery, and clinical therapy (Bakry et al. 2007; Bianco et al. 2005; Gooding 2005; Katz and Willner 2004; Liu et al. 2009). Due to the increasing production of synthetic nanoparticles, the potential release of nanoparticles in the environment is supposed to dramatically increase, as well as occupational and public exposure to nanoparticles in the coming years. However, many researchers have commented that in actuality, there is still much more to be understood about nanomaterials, especially that knowledge regarding to the health risks and hazards is still limited.

Traditional Toxicology addresses adverse poisoning effects of chemicals to humans, animals and the environment, and it is often associated with the concept of dose and dose response. In conventional toxicology, concentration and timeare the two key parameters. For single chemicals, it is easy to measure these factors; or for certain chemicals of established dose response, threshold levels can be determined whether safe or dangerous. However, nanotoxicology as a new branch in toxicology has only recently emerged years after the development of nanotechnology. While the properties of bulk materials or chemicals have already been largely understood, new propertiesare being discovered with the nanomaterials introduced at nanoscale. Their

physicochemical properties changes when bulk materials are made into nanomaterials (Nel et al. 2006). Additionally, interaction mechanisms between nanoparticles and living systems are not yet fully understood. The complexity comes with the particles' ability to bind and interact with biological matter and change their surface characteristics, depending on the environment they are in. For example, nanoparticles of the same material can show different behaviour intracellularly due to their slight difference in shape, size and surface charging or coating. The complexity increases when moving from *in-vitro* to *in-vivo* models. Furthermore, conventional bioassays show limitations involving nanotoxicity assessment and new paradigms are required to be introduced (Monteiro-Riviere et al. 2009), because there are many more variables to be considered in nanotoxoclogy, including the material, size, shape, surface, charge, coating, dispersion, agglomeration, aggregation, and concentration (Savolainen et al. 2010). In order to better understand nanotoxicology, reliable and reproducible screening protocols are required to test basic materials as well as consumer products made from them (Meng et al. 2009).

Biospectroscopy is a powerful technique widely applied in biological research, providing us with information about the structure, functional groups and environment of the biomolecules in the biological samples (Martin et al. 2010). Moreover, spectroscopic methods are optimised with the rapid development of the instrumentation, and coupled with spectral data-analysis techniques it provides a sensitive and costless method as alternative for conventional bioassays in the toxicological research (Ellis and Goodacre 2006; Trevisan et al. 2010).

In this thesis, biospectroscopic techniques have been used to explore the toxic effects in cells and fishes induced by carbon-based nanoparticles.

2. Carbon-based nanoparticles

Carbon-based nanoparticles (CNPs) are man-made materials mainly consisting of carbon with a tiny size scale of 100 nm or even less. Among CNPs, Fullerene, single-walled carbon nanotubes (SWCNTs) and multi-walled carbon nanotubes (MWCNTs) are the most widely used and well developed three types of the CNPs in terms of research investigations and current applications consumer products. Fullerene is known as the carbon molecules arranged into a spherical shape resembling a geodesic dome (McHedlov-Petrossyan 2013). And it is commonly identified as molecules of C*N*, N is the number of carbon atoms in the fullerene, such as C60, C70 and C84, all well-known. By far, the fullerenes C60 are the most studied and widely used compound, and especially they are employed to serve as platforms for producing advanced materials. The fullerenes exhibit enormous electron affinity (*e.g.*, the high electron-acceptor ability and polarizability), and they are used in versatile applications (*e.g.*, electronics, optics, fuel cells, etc.) (Jensen et al. 1996). Single-walled carbon nanotubes (SWNTs) are one-layered graphitic cylinders with diameters of a few nanometers, whereas multi-walled carbon nanotubes (MWNTs) have between two and more concentric cylinders with outer diameters commonly between 30 and 50 nm. They are consisting of extensive sp^2 carbon atoms arranged in fused benzene rings. Their extraordinary structures give them exceptional material properties, which contribute to the applications in composite materials, sensors, hydrogen-storage fuel cells, and various environmental utilizations (Mauter and Elimelech 2008). Thus, it is expected that there will be a high production of these CNPs in the following years (Gottschalk et al. 2009).

2.1 The release of Carbon-based nanoparticles into environment

Incorporating CNPs into products means that these nanomaterials will ultimately be released into the environment. Carbon nanoparticles enter the environment through various routes. It is determined that potential release of nanoparticles to the environment possibly occurs during the production of CNPs and the manufacturing of CNPs-incorporated products (Bello et al. 2009). Direct release is possible from accident causes or spill from equipment during manufacture. It also could lead to indirect release via exhaust emission and wastewater discharge. Normal mechanical use of the carbon-based consumer products has a lifetime of years. During use and disposal, CNPs nanocomposites will be exposed to a wide range of harsh environmental conditions, and it is likely to cause the release of CNPs from the composites. For example, during use of a CNTs composite framed tennis racket, some CNTs may be released whenever the racket frame is scratched by abrasion on the court, or after disposal in a landfill or by incineration. In a landfill, the matrix may undergo hydrolytic degradation and, to a lesser extent, photodegradation, release to the environment (Petersen et al. 2011b). Furthermore, fire or ultraviolet UV radiation exposure during the long-term also can accelerate the release of the CNPs from the products (Wohlleben et al. 2011). However, there is a knowledge gap regarding the fate and transport of any CNPs within engineered systems, including wastewater treatment facilities. Nanoparticles synthesized from silver, copper, fullerenes, and titanium, cerium, and silicon oxides have already been detected in the sludge at the site of wastewater treatment plants (Benn and Westerhoff 2008; Ganesh et al. 2010; Kiser et al. 2010). Unfortunately, the removal of the CNPs in wastewater treatment plants is not clearly understood. In addition, it is similar to many other pollutants that some of the CNPs release occurs from non-point source (*e.g.*, using cosmetics or

sunscreen containing nanoparticles; textiles with nanomaterials), which is difficult to control.

Generally, the possible release routes includes discharge during material production, incorporation of CNPs into products, the lifecycle of CNPs containing products, as well as disposal processes at sewage treatment plants (STP), wastewater incineration plants (WIP), landfills and recycling (Gottschalk and Nowack 2011) (Figure 1). Thus, it is possible that humans would be exposed to nanoparticles via inhalation, ingestion and dermal absorption in occupational, environmental and consumer settings (Johnston et al. 2013). All these potential release pathways pose a serious concern from material performance and environmental health and safety for organism and human.

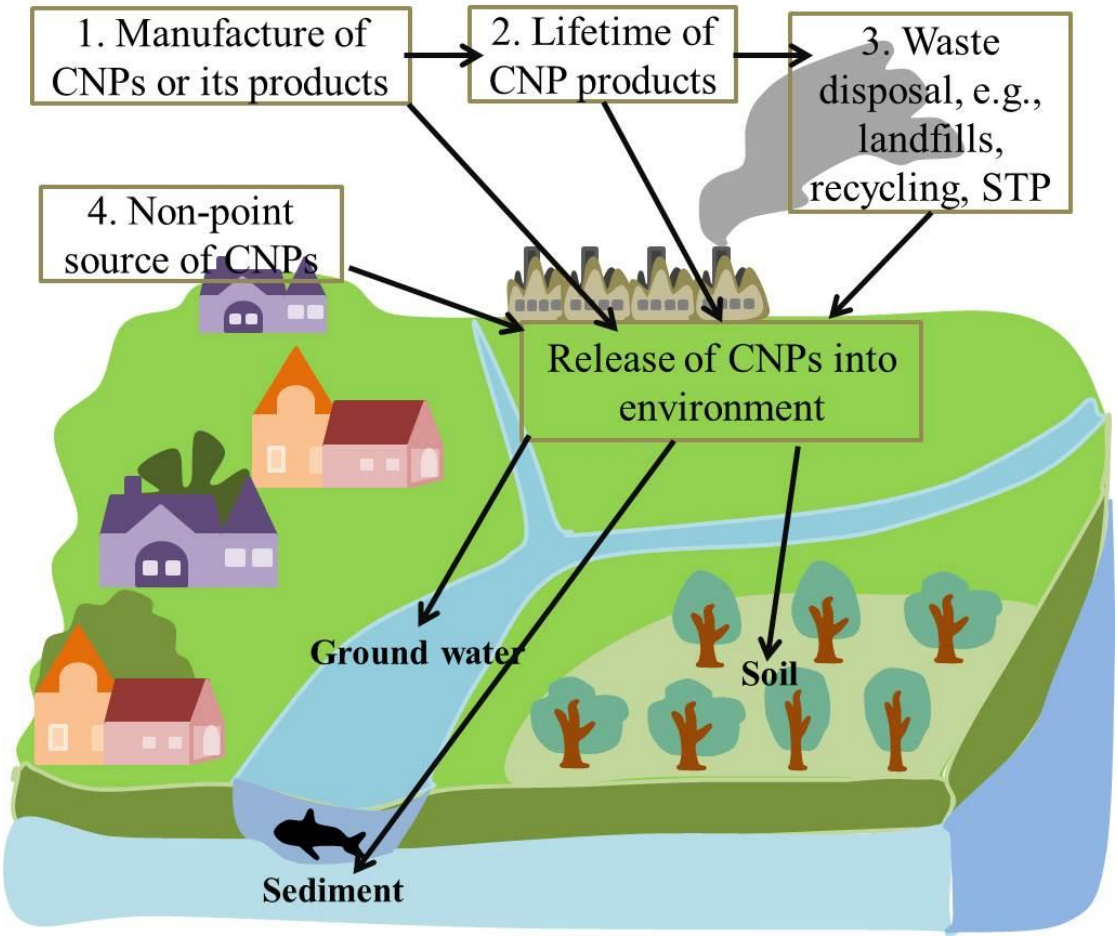

Figure 1 The potential pathway for carbon based nanoparticles (CNPs) releasing to the environment.

2.2 Toxicity of Carbon-based nanoparticles

Although they are consisting of only one element, the carbon nanoparticle types are complex, and they are varying in size, shape, surface charge, production method and physicochemical property. These factors may affect their potential toxicity both *in vitro* and *in vivo* (Figure 2).

Among these CNPs, C60 is considered to be the least toxic CNP (Jia et al. 2005). Toxic test on the alveolar macrophage, after six hours of exposure to C60, no significant toxicity was observed. However, C60 was found to aggregate along the plasma membrane. Furthermore, it is evidenced that C60 is likely to pass into the cells and accumulates in lysosomes, cytoplasm, and even presents at the nuclear membrane and insides the nucleus. Further studies showed that C60 exerts genotoxicity in bacteria and leads to DNA damage (Matsuda et al. 2011). However in a previous study, it is reported that C60 did not show genotoxicity either *in vitro* or *in vivo* (Shinohara et al. 2009). Additionally, it showed that in aquatic environment C60 could induce oxidative stress in the fish brain and result in lipid peroxidation (Oberdörster 2004a).

In contrast to the complicated toxic results for C60, SWCNTs have consistent reports on its toxic effects both *in vitro* and in *vivo*. In the toxic assessment, SWCNTs ranked as the most toxic one among the three types CNPs (Jia et al. 2005). When cells were exposed to SWCNTs, toxic effects were found both dose-dependent and time-dependent (Nel et al. 2009). It is also determined that SWCNTs are able to induce oxidative stress in biological systems (Ren and Zhong 2010). In aquatic environment, it is reported that the SWCNTs are a respiratory toxicant in fish, involving gill irritation and brain injury by SWCNTs (Smith et al. 2007). Studies on MWCNTs have

yielded results similar to those of SWCNTs. Studies indicated that CNTs have the ability to induce pulmonary toxicity (Kayat et al. 2011), and test on mice showed that CNTs could induce inflammation (Crouzier et al. 2010). However, for MWCNTs, the one with larger size (especially in length) seems to be more toxic (Lowry et al. 2012).

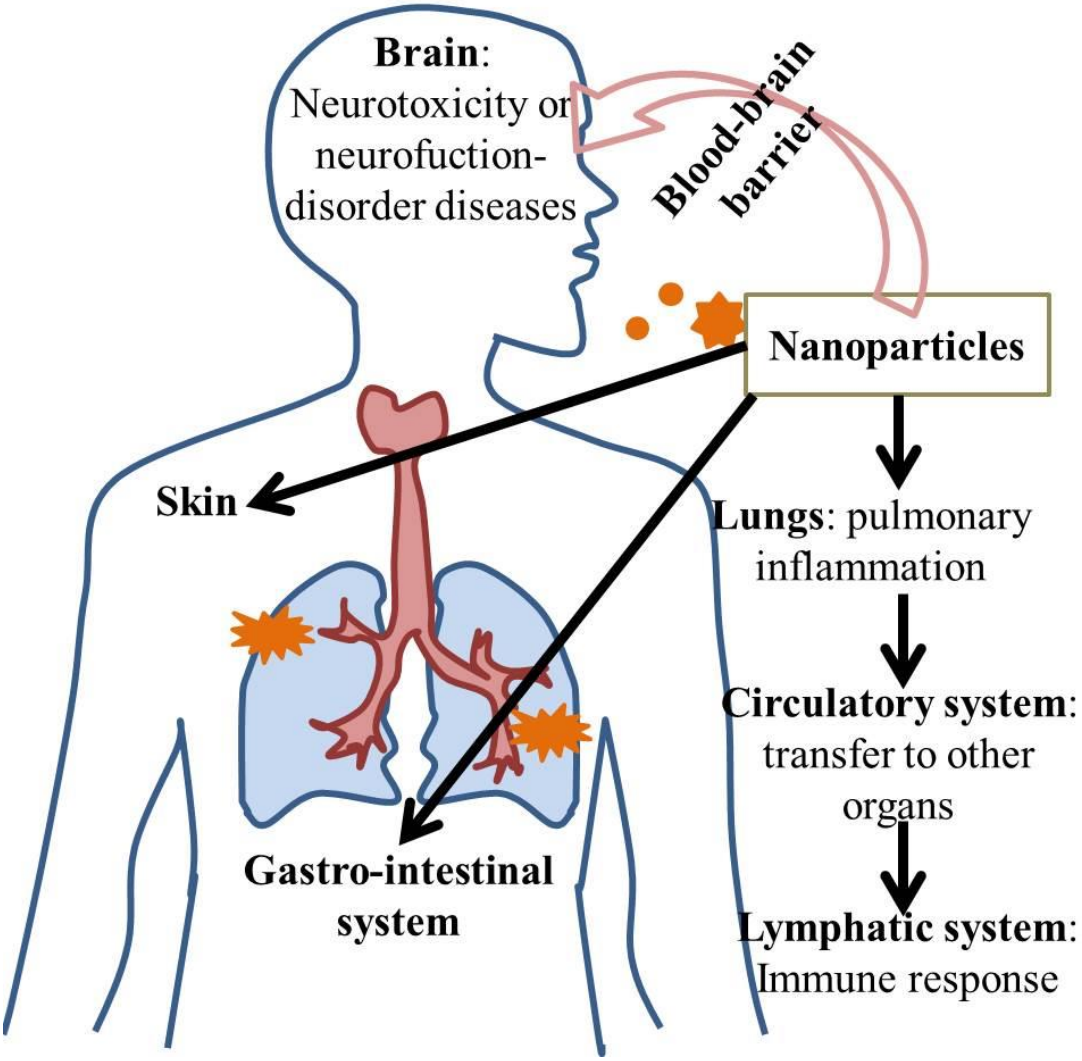

Figure 2 The possible toxicity of carbon based nanoparticles (CNPs) *in vivo*.

2.3 Mechanism of nanotoxicity

The mechanisms underlying the toxicity of nanoparticles have been studied intensively, and the generation of reactive oxygen species (ROS) is considered to be a predominant mechanism in nanotoxicity, which may lead to subsequent formation of oxidative stress (OS) in cells or tissues (Gonzalez et al. 2008) (Figure 3). During the metabolism inside the cells, a small amount of the oxygen escaping from the process of the ATP synthesis, where a sequence of coupled proton and electron transfer reactions involved in, has not been reduced completely and further cause the production of the superoxide anion radicals or forming other oxygen-containing radicals. Consequently, ROS, biologically including superoxide anion radicals, hydroxyl radicals, singlet oxygen, and hydrogen peroxide (H_2O_2), are then produced as the by-products of the cellular oxidative metabolism, and this usually occurs in the mitochondria (Halliwell 1991; Turrens 2003). In some cases, overproduction of ROS occurs in cells and induces oxidative stress, resulting in cells failing to maintain normal physiological redox-regulated functions (Simon et al. 2000). The dysfunction in cells will then cause oxidative modification of proteins to generate protein radicals, lipid peroxidation, DNA-strand breaks, and even modification to nucleic acids (Bagchi et al. 1995; Cabiscol et al. 2010; Griveau et al. 1995). Furthermore, it will impact on the modulation of gene expression through activation of redox-sensitive transcription factors, and modulation of inflammatory responses through signal transduction, finally leading to cell death and genotoxic effects (Shi et al. 2004; Xia et al. 2006). The level of ROS generated by nanoparticles is dependent on the physicochemical property of the nanoparticles, including that their small size, large surface area and high reactivity.

Additionally, the direct interaction between nanoparticles and cells at this nano-bio interface is regarded as a physical mechanism (non-oxidative stress effects) in the nanotoxicity resulting from the size and surface property of the nanoparticles (Elsaesser and Howard 2012). It could lead to membrane disruption, and disturb the transport processed on membrane, and even pass the nanoparticle itself into the cell and interfere directly with cell function (Shvedova et al. 2012). These effects would finally lead to a number of follow-up biological responses in the cell. These cellular responses can occur before or after internalisation of particles.

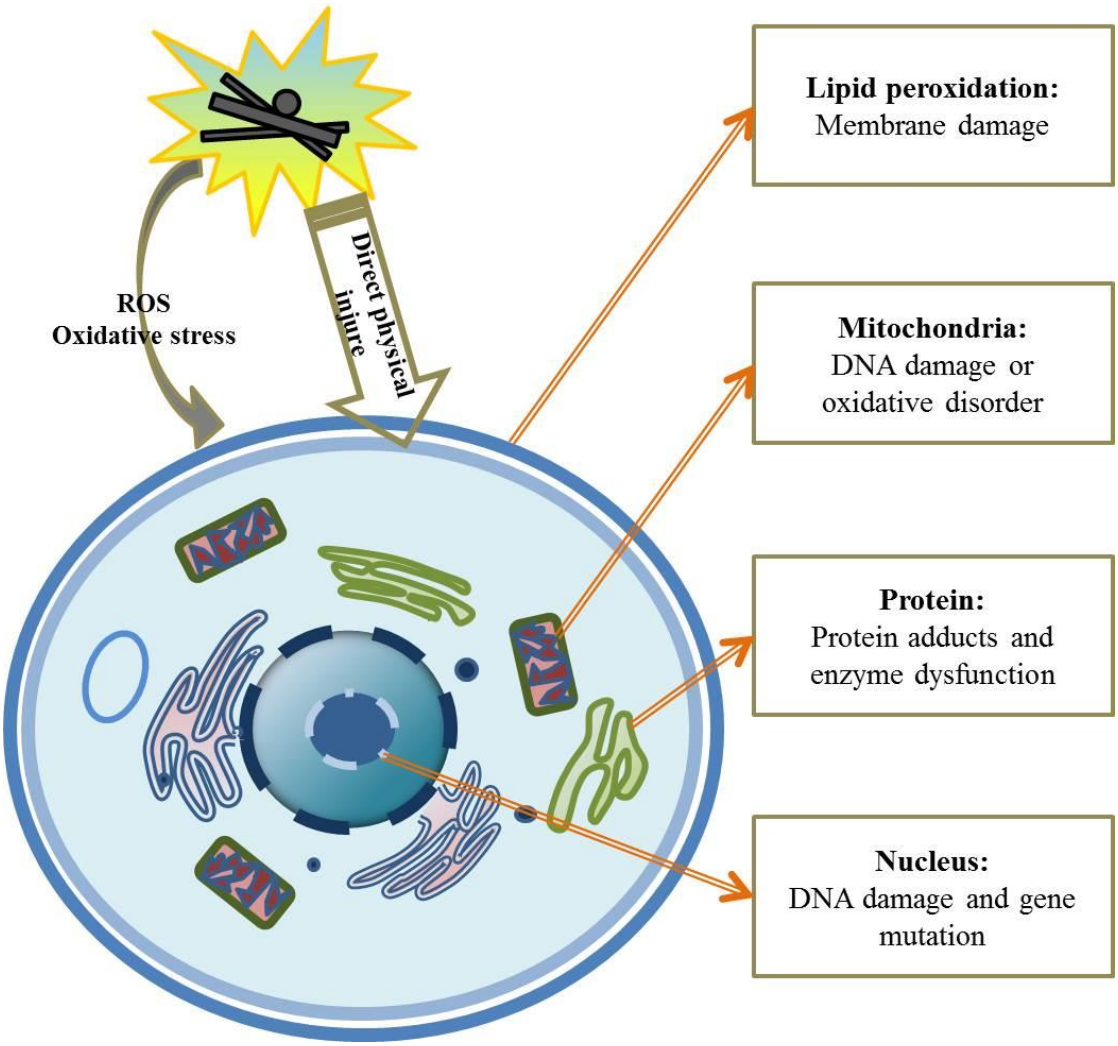

Figure 3 The potential toxicity mechanism for carbon based nanoparticles (CNPs) in cells.

2.4 Interaction of nanoparticles with environmental contamination

Due to their high adsorption capacity, nanoparticles can be utilized for biomedical applications (Bakry et al. 2007; Bianco et al. 2005) or environmental remediation (Mauter and Elimelech 2008). However, when nanoparticles are released to environment, this inherent property can represent a double-edged sword. Especially in aquatic environments, NPs will interact with other components, including not only dissolved organic matter, but also hydrophobic organic contaminants and inorganic ions, including heavy metals (Aiken et al. 2011; Nowack and Bucheli 2007; Zhang et al. 2009). The interaction of nanoparticles with toxic compounds can amplify or as well as alleviate the toxicity of both the nanoparticles or/and the compounds, which is still largely unknown. Investigations on such binary effects of nanoparticles with other compounds were started from the "Trojan horse" effect first postulated by Limbach et al, which reported that nanoparticles could facilitate the cellular intake of the absorbed toxic molecules (Limbach et al. 2007). However, when this concept is extended to the environmental context, the biological effects of the mixtures are difficult to predict. It is more challenging to deal with mixture of nanoparticles with other chemical compounds rather than that mixtures of common pollution compounds, as the interaction of contaminates with nanoparticles is dependent on the characteristics of nanoparticles, including the size, composition, morphology, structure, and the status of agglomeration/aggregation (Christian et al. 2008).

Carbon-based nanoparticles have been widely applied in many areas, and they exhibit a strong affinity for organic contaminants due to their excellent absorption capacity. Adsorption of hydrophobic organic compounds (HOCs) by CNPs may impact on their toxicity and affect the fate, transformation, and transport of HOCs in the environment

(Yang et al. 2006). Investigations on the absorption of chemical compounds showed that it is a complicated process (Pan and Xing 2008), which would turn to be more complex in real environmental conditions. Although there are already quite a lot of studies being carried out on the toxicity of CNPs, few studies investigated their interactive effects with other pollutions or biological organism. The reports on such interactive toxicity are sometimes quite controversial. A few investigations determined that CNPs could enhance the toxicity of pollution with co-exposure. Investigation on the exposure of phenanthrene with the presence of SWCNTs showed that the SWCNTs acting as a contaminants carrier could enhance the bioavailability of phenanthrene (Su et al. 2013). Other studies also highlighted the same fact underlying on C60 (Baun et al. 2008; Lehto et al. 2014). It was determined by *in vitro* evidence that co-exposure of arsenium and C60 could facilitate the uptake of arsenium in zebrafish hepatocytes (Azevedo Costa et al. 2012). Another similar study showed that C60 could enhance the toxicity in when interacted with B[*a*]P (Ferreira et al. 2014). However, it is not always the case. It was found that when the 17α-ethinylestradiol (EE2) was delivered to cultured cells together with carboxyl-functionalized SWCNTs, the bioactivity of adsorbed EE2 on cf-SWCNTs was significantly inhibited (Song et al. 2014). C60 was also found of the capability to reduce the bioavailability of EE2 in zebrafish during co-exposure (Park et al. 2011; Park et al. 2010). Additionally, it was reported that MWCNTs could reduce the bioavailability and the toxicity of the biocide triclocarban in cells (Simon et al. 2014). In general, the toxicity data reported is quite complicated and further work is required to explore the mechanism underlying this issue. Moreover, most of the investigations were conducted at a quite high dose of CNPs, which requires further studies should be carried out at a realistic environmental level, or closer to that level.

3. Nanotoxicity assessment: challenges and methods

Despite the fact that there are already quite a lot of investigations carried out on nanotoxicity, the knowledge of the health and safety aspects on nanotechnology still lag far behind its development. This is possibly due to that there are still many experimental challenges in the toxic assessment of nanoparticles. Recently, most methods used are from conventional toxic assessment, which is initially designed for chemical toxicity. However, the unique physicochemical properties of nanoparticles may interfere with the classical toxicity assays. Their high adsorption capacities, different optical properties, and increased catalytic activities can influence the results of many *in vitro* toxicity assays, leading to the misinterpretation of results (Dhawan and Sharma 2010). Thus, much more extensive characterization is initially required to be carried out on the nanoparticles (such as size, shape, solubility, agglomeration, elemental purity, surface area, etc.) than other chemical compounds (Bouwmeester et al. 2011; Powers et al. 2007). Incomplete characterization and incorrect preparation of nanoparticle dispersion for experiments will hinder attempts to find a correlation between various biological effects and particle properties. Moreover, it also requires a standard methodology and guideline for different research groups, making it possible to compare the toxicity assessment.

3.1 Limitations in recent toxicity tests for nanotoxicology

Currently, *in vitro* assays are commonly applied to screen adverse biological effects prior to *in vivo* testing, allowing for a simpler, faster and more cost efficient assessment of defined toxicity endpoints. A number of classical *in vitro* toxicity assays have been utilized to determine cytotoxicity of nanoparticles in cultured cells. These relatively simple assays use colorimetric or fluorescent dyes as markers to

determine cell viability assessing membrane integrity (*e.g.*, neutral red, calcein AM) or cell metabolism (*e.g.*, MTT, alamar Blue). Although these assays have been found to provide accurate toxic data for classic pure chemical cytotoxicity studies, they it displayed less reliable when assessing nanoparticles. For example, the colorimetric MTT assay is a widely used cell viability assay based on the reduction of the yellow tetrazolium dye 3-(4,5-dimethylthiazol-2-yl)-2,5-diphenyltet-razolium bromide (MTT) to a purple water insoluble formazan in cells bearing intact mitochondria. When it was applied in the experiment to assess the impact of SWCNTs on the cell viability, false negative results were reported (Casey et al. 2007b). This is because nanoparticles present in the reaction mixture may influence the reaction by increasing the light absorption due to their optical property (Wörle-Knirsch et al. 2006). Additionally, the same problem appears in other colorimetric methods, including lactate dehydrogenase (LDH) assays for cell necrosis (Holder et al. 2012), detection of intact lysosomes via neutral red uptaking (Casey et al. 2007a; Monteiro-Riviere and Inman 2006), and caspase-3 activity assays for cell apoptosis (Kroll et al. 2009). Furthermore, it is also evidenced that NPs could exert influence on the substrates or enzymes in immunological experiments (Kroll et al. 2012; Kroll et al. 2009). Absorption of cytokines by carbon nanoparticles was observed (Monteiro-Riviere and Inman 2006). Generally, it is concluded that the obstacles in these bioassays results from the unique properties of nanoparticles including their high adsorption capacity, optical property, and potential catalytic activity (Kroll et al. 2009).

It is generally accepted that *in vitro* toxicity test on nanoparticles have been the first choice for most researchers due to its advantages of faster, convenient, cost less, and devoid of ethical issues by contrast to *in vivo* tests. However, the cell type for *in vitro* testing system is dependent on the route of exposure condition and the investigation

aim, but the cell type can influence the results greatly, because different cell type would possibly increase or reduce the cellar response as the measurable endpoint of the experiments. It is also a trouble that using cultured cells for *in vitro* tests have lost all the information about the complexity of cell-matrix interactions, the diversity of cell types, and hormonal effects present *in vivo*. Especially, it is impossible to explore the long term chronic toxicity without *in vivo* experiments. It is also reported that toxicity monitoring by *in vitro* screening studies cannot reflect the actual effects of nanoparticles observed by *in vivo* experiments (Sayes et al. 2007; Warheit et al. 2009). While an in vitro system can be used to detect the potential pass across the cell membrane of nanoparticles, it cannot explain the realistic pharmacokinetics or toxicokinetics of nanoparticles inside the body (Clift et al. 2011). Additionally, it is difficult to use *in vitro* system for identifying some endpoints such as histological alterations and the impact on the immune system (Nel et al. 2012). However it is certainly important for both *in vitro* and *in vivo* tests that the exposure dose of nanoparticles used for experiments is derived from the actual scenario, and the nanoparticles are well dispersed while dispersant is biocompatible (Hurt et al. 2006).

3.2 Characterization of Nanoparticles

In order to measure toxicological endpoints, it requires an initial characterization of the test substance prior to any toxicity screening. For nanotoxicology, it is also imperative to carry out characterization for nanoparticles before conducting experiments. However, distinguished from the common chemical toxicants, nanoparticles demand a comprehensive characterization on their physicochemical propertied, including size distribution, shape, surface area, crystallinity, purity, agglomeration state, surface charge, solubility, *etc.* (Table 1). But it is difficult to

conduct a complete characterization of nanoparticles, because in most toxicology laboratories the facilities are not fully comprehensive. Therefore, sometimes it is the availability of facilities that determines the type of characterization performed rather than the design or the aim of the experiments.

Among all parameters, size is the most important considered for characterization, which plays a critical role in nanotoxicity. Light microscopies are favoured techniques in the biological science, but they are difficult to adapt for nanotoxicity studies as the size scale of nanostructure lies below optical resolution limits. Thus, the most commonly used techniques includes scanning electron microscopy (SEM), transmission electron microscopy (TEM), dynamic light scattering (DLS) and atomic force microscopy (AFM). Electron microscopy is a simple technique that can directly measure the size and morphology of the particle, as well as the size distribution. However this technique has some disadvantages that it is quite time-consuming and requires specific sample preparation. Moreover, the measurement is carried in a vacuum condition with dry samples, which may alter the property of the samples. Thus it is not able to analyse the samples in dispersion. By contrast, the AFM is a cost-efficient technique that can perform the characterization in air or in liquid dispersions. It can provide information on many physical properties, such as size, morphology and surface state. Technique of DLS is straightforward to measure hydrodynamic diameter under the conditions closer to the exposure situation. But it usually gives a larger size than the other techniques, due to the solvent layer outside the particles is calculated including.

In many toxicity investigations of nanoparticles, there is a primary limitation that it lacks quantification of the nanoparticles concentrations in the test media. It is

suggested that it requires a quantification measurement at the beginning and the end of experiments when a specific dose is adopted. Recently, the quantification measurements of nanoparticles in the aqueous phase have been conducted most commonly in experiments with C60 fullerenes. This is because C60 can be simply measured under ultraviolet-visible (UV/vis) spectroscopy following toluene extraction (Hungerbuehler et al. 1993; Tervonen et al. 2010). However, the concentrations of CNTs in aqueous phase are limited to nominal concentrations; fractions of CNTs appear commonly in the dispersion. Nevertheless, other techniques such as spectrofluorometric determination, thermal optical transmittance, and radioactivity measurements for radioactively labelled nanoparticles, are available for quantification measurements (Petersen and Henry 2012).

In general, other parameters of the nanoparticles also require characterisation to correlate to the toxicity, and many methods still need optimization and development, especially for new types of nanoparticles in aqueous dispersion, while extensive experience can be gained from the fields of fundamental colloid chemistry or other scientific area.

Table 1 Characterisation techniques for nanoparticles

Techiniques	Parameters	Limitations or advantages
Electron microscopy (Scanning electron microscopy) (Transmission electron microscopy)	Size Size distribution shape agglomeration	1) Analyse sample under high vacuum 2) Samples require drying; not capable of aqueous samples 3) It is time-consuming 4) It requires a sufficient amount of nanoparticles for size distribution analysis 5) SEM usually possesses a lower resolution than TEM
Dynamic light scattering	Size (Size distribution agglomeration	1) The measured size is larger than the real size 2) It is not compatible for carbon nanotubes 3) It is compatible for aqueous samples
Atomic force microscopy	Size Size distribution morphology	1) It is no necessary to conduct analysis in vacuum 2) It is cost-effective 3) It is grater for statistical size distributions
Energy dispersive spectrometer	Elemental composition	1) It can identify the purity of nanopartciles 2) It can determine the chemical composition, including metal catalyst residue
Inductively coupled plasma mass spectroscopy	Elemental composition	1) It is highly sensitive 2) The analysis is rapid

3.3 Dispersion of nanoparticles for toxicity tests

It is one of the key facts in toxic assessment of the carbon nanoparticles (CNPs) both *in vitro* and *in vivo* of how to disperse CNPs in toxic test, because the aggregation or agglomeration of CNPs in culture media or vehicles complicates the interpretation of the toxicity test results. It has been shown that unstable and agglomerated nanoparticles dispersions used in toxicity tests could result in inaccurate data for nanotoxicity and even cause misleading conclusions (Jiang et al. 2009). It was also found that the hydrodynamic size of the nanoparticles is often larger than the primary size when dispersed in liquids. Thus, it is important to understand the behaviours of nanoparticles under different solution conditions prior to the toxicity assessments, and this will highly facilitate these investigations.

The weak or strong forces among the molecules or atoms, respectively, including van der Waals forces, electrostatic forces, and sintered bonds, tend to give a rise to the agglomerate and aggregate for nanomaterials (Porter et al. 2008; Sager et al. 2007). Especially, the van der Waals interaction energy of tube-tube contact that bundles CNTs is relatively high, which makes CNT dispersion one of the most important challenges for the widespread industrial application of CNTs (Girifalco and Hodak 2002; Girifalco et al. 2000; Madni et al. 2010). Agglomeration is defined as the collection of weakly bound particles or aggregates or mixture of both, which is found to result in external surface areas is nearly equal to the sum of the surface areas of the individual components. However, aggregation is defined as the collection of strongly bonded or fused particles, which causes that the external surface areas possibly shrink in comparison to the sum of calculated surface areas of the individual components. This indicates that aggregates are held by strong forces, such as covalent bonds. Therefore, agglomerations are more loosely bound particles, which may be because of

the high ionic strength shielding the nanoparticles charge repulsion, while aggregations represent highly tight bound or fused particles, and it alters the size, surface area and the physicochemical property of the nanoparticles (Jiang et al. 2009; Keller et al. 2010).

The nanomaterials are dramatically different form their bulk ones in terms of the physicochemical property. Agglomerations appear to have a high impact on the biological effects of nanoparticles by contrast to the well-dispersed ones. It was found that dispersed SWCNTs could significantly inhibit the proliferation of BEAS-2B cells, while non-dispersed SWCNTs had no effect on the cells (Wang et al. 2010). Thus how to disperse nanoparticles is also one of the most important determinants in the toxic test for CNPs (Bihari et al. 2008; Buford et al. 2007; Foucaud et al. 2007; Vippola et al. 2009; Warheit 2006). What is more important? The dispersant used for CNPs itself should have no adverse effects on the test system. For example, the dispersant should not exert toxic effect on the cell lines, microorganisms and animals used in the test, or the effects are eliminated to minimum extend if there's no better choice. However, it is a tough job to find a good dispersant for the CNPs toxic tests meeting the requirements of biocompatibility, dispensability and dispersion stability.

Fullerenes C60 were the first artificial nanomaterial and gained much attention. Aqueous C60 can be generated by using water or other vehicle solvent. Previously, tetrahydrofuran (THF) has been used to prepare aqueous C60 as a vehicle solvent in toxicology studies (Deguchi et al. 2001; Lovern and Klaper 2006; Oberdörster 2004b). However THF can change the surface charge of C60 particles, and THF can still be retained in C60 aggregates (Brant et al. 2005). This could possibly lead to false positive results in the toxic test of C60, because of that the actual toxicity result from

the presence of THF or its degradation products were neglected. This speculation was later determined by investigation conducted on larval zebrafish that a THF degradation product (γ-butyrolactone) played a key role in the toxic effects rather than that induced by C60 (Henry et al. 2007).

Despite the solvent, CNPs can also be suspended using a range of natural and synthetic polymers and surfactants such as natural organic matter (NOM), sodium dodecyl sulphate (SDS), polyvinylpyrrolidone (PVP), and polyethyleneimine (PEI). The role that these surface coatings have in CNP toxicity is not yet well understood, but limited numbers of studies have investigated this topic using *Daphnia magna* (Edgington et al. 2010; Petersen et al. 2011a). Researchers also turned their eyes to other dispersant for CNPs, such as distilled water, dimethylsulfoxide (DMSO), a 1,2-dipalmitoyl-sn-glycero-3-phosphocholine (DPPC) solution, bovine serum albumin (BSA) and Tween 80, and it suggested that appropriate dispersants were proposed according to the type of CNT (Kim et al. 2011). In addition, it is important to test the dispensability, dispersion stability, and biocompatibility of the selected dispersant prior to the toxicity evaluations, and also an optimised dispersing protocol is required.

Table 2 Possible obstacles in the dispersion method for nanoparticles

Dispersion approach	Disadvantages
Using solvent or chemical dispersants	1) The possible toxicity of the solvent or dispersants; 2) The residue solvent or dispersants in nanoparticles, *e.g.*, tetrahydrofuran in fullerene C60; 3) A solvent control is required; 4) Solvent or dispersant may change the characteristics of the nanoparticles, such as shape, surface chemistry.
Ultra-sonication	1) It may break the carbon nanotubes into small pieces by high energy, or it can damage the surface of nanoparticles; 2) Long time sonication may generate lots of heart and increase the temperature 3) Only using sonication may not maintain the dispersion of nanoparticles for a long period.
Stirring	1) It often takes very long time; 2) It may break the nanotubes or alter the surface of the nanoparticles; 3) Only using stirring may not maintain the dispersion of nanoparticles for a long period.

4. Biospectroscopy

Spectroscopy is a powerful technique, which is traditionally used by chemists and physicists to identify the unknown molecular entities. With the spectroscopic instruments updated, spectroscopy shows its ability to characterise biochemical components in complex bio-samples and it has been introduced to many biological research laboratories, where biospectroscopy starts. Conventional bio-assays are usually time-consuming and labour-intensive; especially it requires expertise training on the sample preparation and test conduction. Additionally, some agents used in these bio-assays are expensive. In contrast with these traditional techniques, biospectroscopy provides a rapid, label-free analytical route for biological research. Particularly, it can save time and labour, and only requires a minimum amount of training for experiment conduction. Mainly there are two spectroscopic approaches employed in the biospectroscopy: infrared (IR) and Raman spectroscopy (Figure 4).

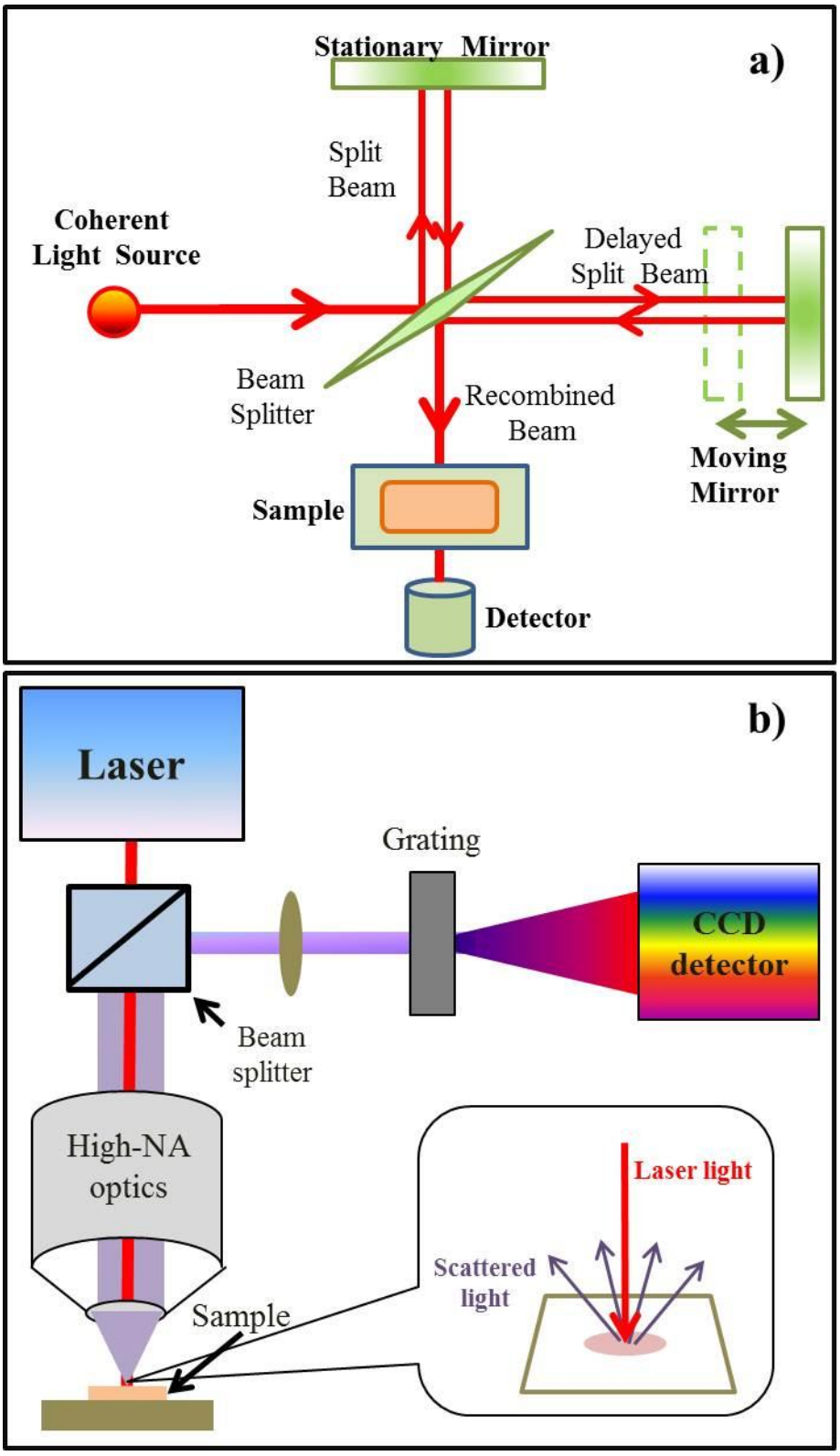

Figure 4 A brief illustration of spectroscopic instrument **a**) FTIR; **b**) Raman.

4.1 Infrared spectroscopy

Biomolecules are characterised by IR spectroscopy due to the IR absorption of the vibration movements (*e.g.*, bending, stretching, wagging or scissoring) in their chemical bonds. IR absorption occurs at a specific wavenumber corresponding to the specific energy of the vibrational movement. Thus, peaks in the IR spectra particularly present identical chemical bond in the samples. For biospectroscopy, the mid-infrared (MIR) spectroscopy (4000-400 cm^{-1} in wavenumbers) is commonly used. In contrast to the near-infrared (NIR), MIR contains fundamental vibrational transitions rather than overtones. This means MIR can provide inherently higher signal intensities given the increased absorption cross-section. Furthermore, within MIR, the range of 1800-900 cm^{-1} is regarded as the biochemical fingerprint region for bio-samples, because this region can generate identifiable peaks at specific absorption frequencies, such as Amide I (~1650 cm^{-1}), Amide II (~1550 cm^{-1}), Amide III (~1260 cm^{-1}), carbohydrates (~1155 cm^{-1}), glycogen (~1030 cm^{-1}), lipids (~1750 cm^{-1}), asymmetric phosphate stretching vibrations ($\nu_{as}PO_2$; ~1225 cm^{-1}), symmetric phosphate stretching vibrations (ν_sPO_2; ~1225 cm^{-1}) and protein phosphorylation (~970 cm^{-1})(Kelly et al. 2011).

Fourier-transform infrared (FTIR) spectrometer is widely applied in biological studies. The most used IR spectroscopic methods are transmission, transflection and attenuated total reflection (ATR) (Figure 5). On transmission mode, infrared beam is directly passed. Transflection is another method, where IR beam is reflected off by an IR-reflective surface [such as that found on low-emissivity (Low-E) slides], travels back through the sample to the detector. In these two modes, the beam is travelling through the absorbing sample, thus it requires short pathlengths in the samples. This means the thickness of the samples is quite critical; too thick will cause too long

pathlength of IR beam in sample, which would result in all the IR radiation being absorbed by the sample and none reaching the detector. Utilizing the same principle, but based on a different pathway, ATR-FTIR spectroscopy directing the infrared light at an interface between an infrared transparent material with a high refractive index called the internal reflection element (IRE, *e.g.*, a prism made of ZnSe, diamond, silicon or germanium) and a sample on the surface of the IRE. Because in this situation the angle of incidence of the IR beam is greater than the critical angle, total internal reflection occurs consequently. At the reflecting surface, a standing wave of radiation (*i.e.*, an evanescent wave) is established, and this evanescent wave interacts with the sample, attenuating the infrared beam of light exiting the IRE back to detector. The depth of penetration for the evanescent wave in a sample is dependent on the angle of incidence and the refractive indices of both the IRE and the sample. It is typically in the range of 0.5-2 μm (Kazarian and Chan 2013). However, since the evanescent wave reaches deeper site in the sample than the depth of penetration, it should be noted that absorbance information is obtained from the sample beyond this range (Kazarian and Chan 2010).

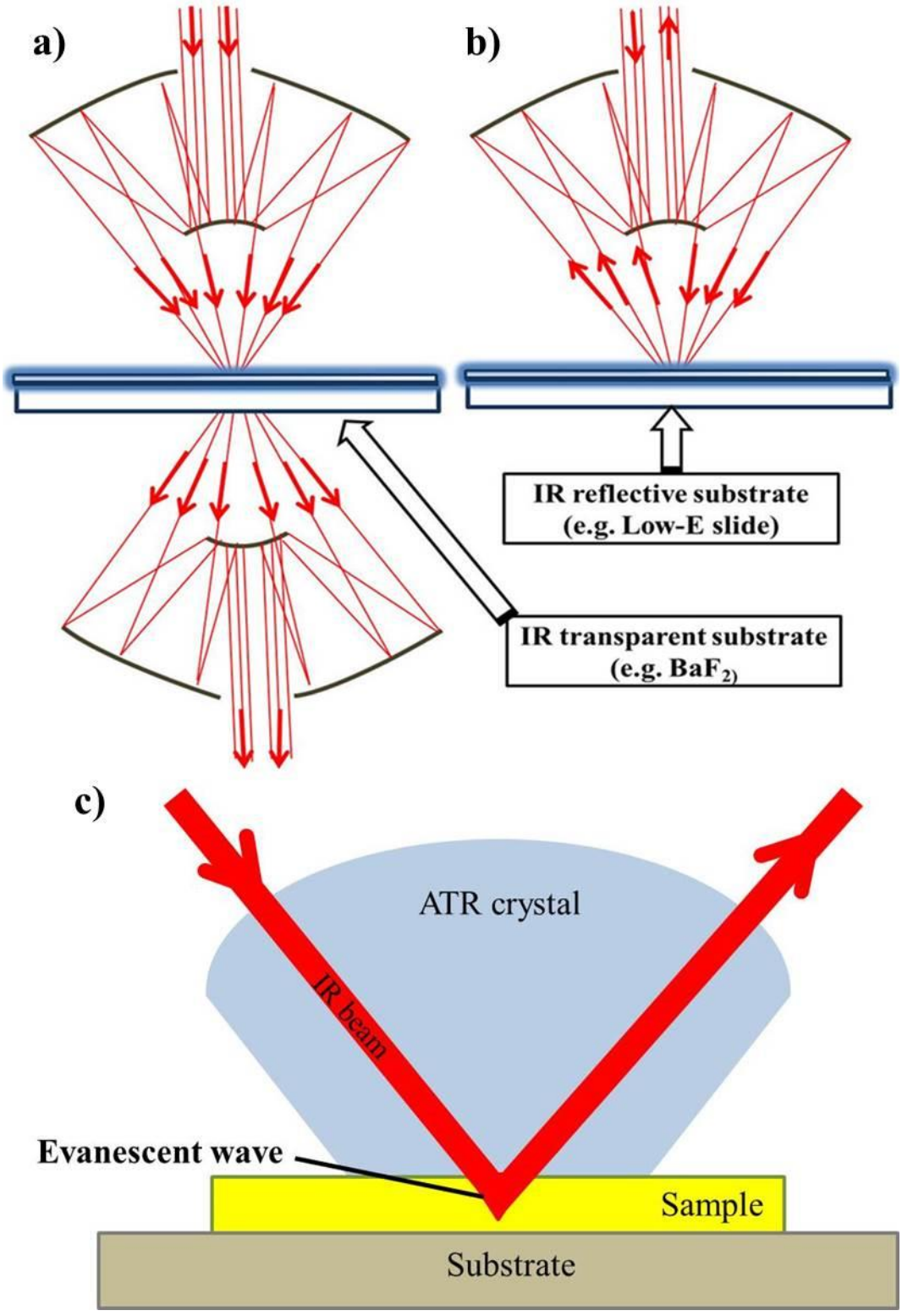

Figure 5 A brief illustration of FTIR mode **a**) transmission; **b**) transflection; **c**) ATR-FTIR spectroscopy.

The combination of FTIR with optical microscopy has been frequently used for imaging. Due to the property of the IR spectroscopy, FTIR microscopy is a useful non-destructive and label-free molecular imaging tool, providing chemical specificity of mid-infrared spectroscopy with spatial specificity (Bhargava 2012). In this approach, an absorption spectrum is regarded as a molecular fingerprint of sample at every pixel, and biochemical information can be extracted from each spectrum that can be correlated with known biochemical structure. Conventional IR microscope is coupled to interferometers equipped with globar sources, and image maps are obtained by raster scanning with single-point detectors. This means the conventional IR microscope has the drawback that the acquisition time for a high-resolution microspectroscopic map is highly time-consuming. Thus, a synchrotron beam is employed to replace the thermal IR source, in order to improve the signal-to-noise ratio (SNR) and spatial resolution (Miller and Dumas 2006; Nasse et al. 2011). Furthermore, a focal plane array (FPA) multichannel detector is used instead of the single element detector to accelerate data acquisition through parallel detection in benchtop instruments (Baker et al. 2014). It is now determined that the coupling of synchrotron light with a wide-field FPA detector can highly increase the SNR of spectral data by contrast to the conventional one (Hirschmugl and Gough 2012).

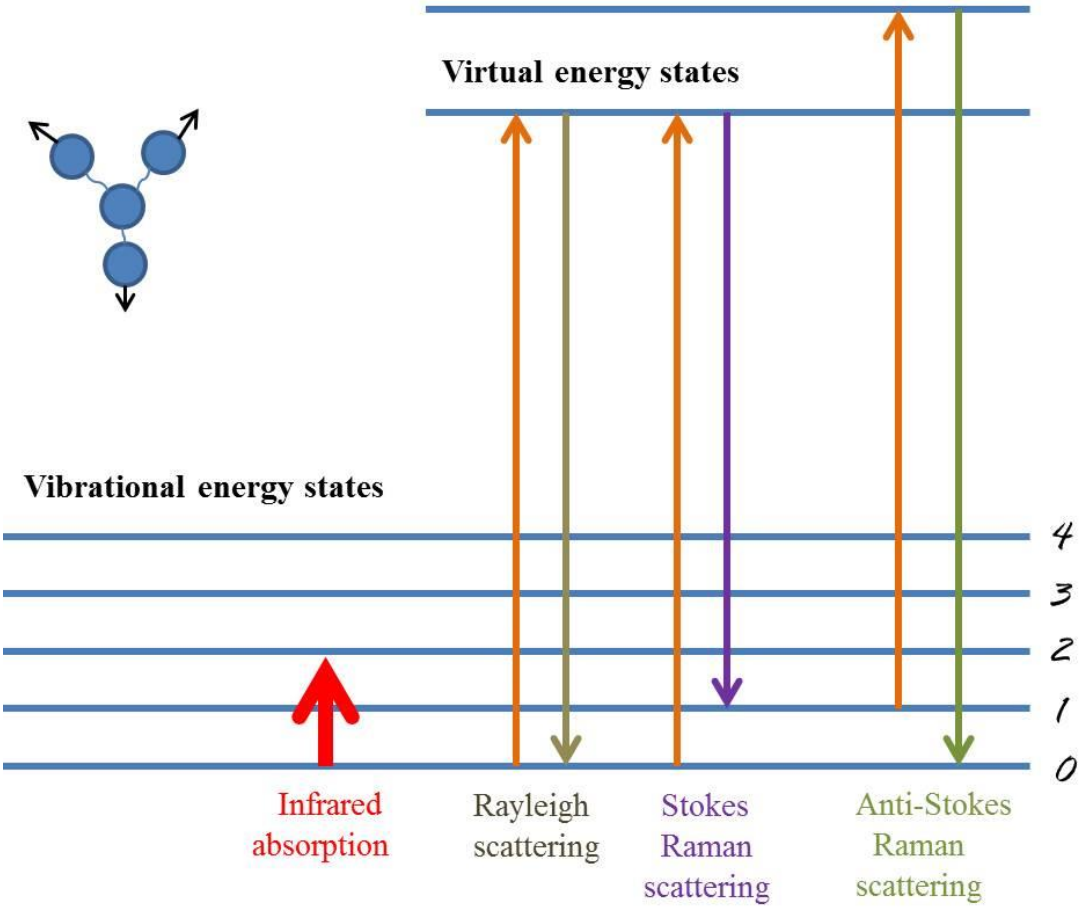

Figure 6 A brief illustration of vibrational spectroscopic theory.

4.2 Raman spectroscopy

Raman is a scattering technique, measuring the interaction when the photon from a monochromatic light source (*i.e.*, laser) encounters the chemical bond in molecules (Figure 6). Following the light photons are absorbed and released back, the vibrational energy of the molecules are also caused to increase and decrease subsequently. In this situation, sometimes the molecules do not return back to its previous energy state, there will be a frequency shift occurring in the released photon in order to maintain the energy balance. This phenomenon of shift is inelastic scattering or so-called Raman scattering (Kneipp et al. 1999). However, this does not occur efficiently; the incidence is less than 1% of the total photons absorbed by the molecules. The back-ward light is then filtered that only the Raman scattering reaches the detector and generate a spectrum.

For chemical analysis, IR spectroscopy is currently the most used vibrational spectroscopy technique, mainly because it is higher intrinsic sensitive and much cheaper for instrument when compared with the Raman spectroscopy. However, in biological systems, IR spectroscopy has a severe disadvantage that there is a strong absorbance of the ever-present water (Ellis and Goodacre 2006). Although NIR with less sensitivity is not limited by water to the same e, the bands in NIR region are mostly overtones and combination bands, which are too broad to serve as convenient identifiers of complex systems (Wang and Mizaikoff 2008). Such a situation leaves Raman spectroscopy as the most suitable vibrational spectroscopy of biological systems.

The major advantage distinguished from IR spectroscopy is that Raman spectroscopy is rather oblivious to aqueous environments (Krafft et al. 2009). The Raman cross-

section of water is very small. Furthermore, progress has been made in Raman instrumentation, including higher sensitive detectors, more efficient rejection filters, and improved collection system. This step forward has bridged up much of gaps in the sensitivity and cost between IR and Raman spectroscopy. Nevertheless, by the nature of how Raman spectroscopy works, the basic disadvantage of normal Raman spectroscopy is its inherent weak intensity and corresponding low sensitivity. This is still an obstacle for the routine use of Raman. This disadvantage is especially distinct in biological systems, because here many of the target biocompounds are present at low concentrations. Additionally, due to its unselective nature to the various molecules present in the biological samples, Raman often generates highly congested spectra, that are usually very difficult to analyze. Besides, normal Raman often encounters a strong fluorescence background, giving rise to deteriorate the quality of the spectra, and bring down the signal-to-noise ratio (SNT).

4.3 Surface-enhanced Raman spectroscopy

When using the normal Raman, one often encounters a strong fluorescence background (intrinsic or impurity-originating) that deteriorates the quality of the spectra, and adversely affects the signal-to-noise (S/N) ratio. Surface-enhanced Raman spectroscopy (SERS) (Figure 7), by its nature of enhancing the Raman cross-sections, can provides intense spectra and help us overcome these disadvantages of normal Raman. It provides us a rapid and highly sensitive tool to detect chemical structure information for the application in biological research. SERS significantly improves the S/N ratio by the ability of SERS-active substrates to quench fluorescence.

The field of SERS has started since it was first time recognized that Raman spectra of sub monolayer coverage of molecules could be acquired on electrochemically roughed

coinage metal surfaces (Albrecht and Creighton 1977; Jeanmaire and Van Duyne 1977). Although research struggle was paid, the mechanism underlying the highly enhanced spectra by SERS is not completely understood yet. In general the enhancement factors for SERS, as compared to normal Raman scattering, are mainly attributed to two mechanisms: an electromagnetic enhancement mechanism and a chemical enhancement (charge-transfer)) mechanism (Campion and Kambhampati 1998; Moskovits 1985). Plasmon, so called as the collective excitation of the electron gas of a conductor, its energy on a smooth surface is bound to the surface. Thus, on a suitably roughened surface, the plasmon with a perpendicular component is created. When exciting radiation (laser beam) interacts with the surface, the plasmon energy causes the Raman process to occur in the analyte molecule. Then the energy is transferred back into the plasmon, and also into the scattered radiation, which is shifted in frequency by the energy transferred to the nuclei in the Raman process, is detected by the spectrometer. Generally, the electromagnetic field of the radiation at the surface can be greatly enhanced under conditions of surface plasmon excitation, and both the incident laser field and the scattered Raman field are amplified via their interaction with the surface, and these constitute the electromagnetic SERS mechanism (Campion and Kambhampati 1998). Charge-transfer (chemical) enhancement, regarded as a second enhancement mechanism, operates independently from the electromagnetic mechanism. In this situation, the molecule is bound to the metal surface to form a charge transfer complex. When the exciting radiation interacts with the metal, form an electron–hole arises and energy is transferred to the analyte through the new metal to the bonds of the molecule. While the Raman process occurs on the analyte, and the energy is then transferred back into the metal for scattering, and an enhanced signal will be detected. For highly optimized surfaces, the total

SERS enhancement factor may approach ~ 10^{10}–10^{11} (Sharma et al. 2012). This makes SERS an ultrasensitive detection tool; even the single molecule level can be detected (Camden et al. 2008; Kneipp et al. 1997). It is generally acknowledged that the electromagnetic effect make a much greater contribution to the enhancement by contrast to the charge-transfer effect. Additionally, electromagnetic enhancement is regarded as a nonselective amplifier for Raman scattering by all molecules adsorbed on a particular surface (Hering et al. 2008). However, as the dominant contributor to most SERS processes is the electromagnetic enhancement mechanism, the maximum SERS enhancing region decreases dramatically rapidly with distance (r^{-10} for spheres), and the largest enhancement can be found only in a few nanometre closest to the Au nanoparticle surface (Stiles et al. 2008).

The success of SERS is highly reliant on the interaction between the analyte molecule and the surface of plasmonic substrates. Usually, gold (Au), silver (Ag), or copper (Cu) are used as the classic SERS substrates. Due to their stable physicochemical property, Au and Ag are most often used SERS substrates. Since surface plasmons have to be excited by the incident laser beam, the excitation wavelength for a SERS experiment must be adapted to the plasmon wavelength of the respective metal and also to the nanostructure of the metal surface, which also has an effect on the plasmon resonance wavelength (Campion and Kambhampati 1998). Thus, SERS excitation lines cover mainly the visible spectral region and the near infrared (NIR) wavelength range (Stiles et al. 2008). With the development of SERS, novel SERS substrates have been introduced, including Au and Ag nanoparticles with various shapes and even with coating to form the shell-isolated nanoparticle (Li et al. 2010), such as Au-Ag core-shell particle (Cao et al. 2001), SiO_2 coating Au nanoparticle colloids (Lu et al. 2002), 2D Ag nanoparticle arrays (Cho et al. 2012), and nano-Au film (Wang et al. 2009).

Beyond Au and Ag, other metals including the alkali metals (Li, Na, K, Rb, and Cs), Al, Ga, In, Pt, Rh, and metal alloys have been explored in the applications for plasmonic substrates for SERS (Sharma et al. 2012). And applications of novel nanomaterials such as graphene (Huang et al. 2010; Ren et al. 2011; Zhang et al. 2011) and quantum dots (Kulakovich et al. 2002; Quagliano 2004) have recently been reported as well.

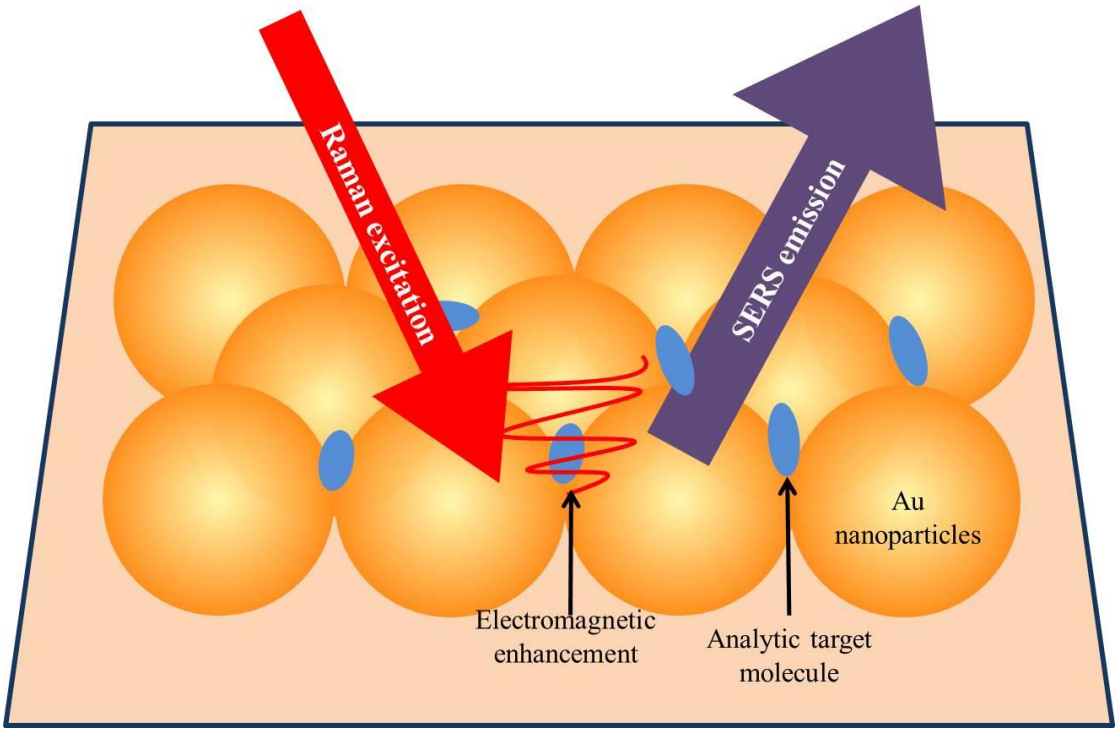

Figure 7 A brief illustration of SERS.

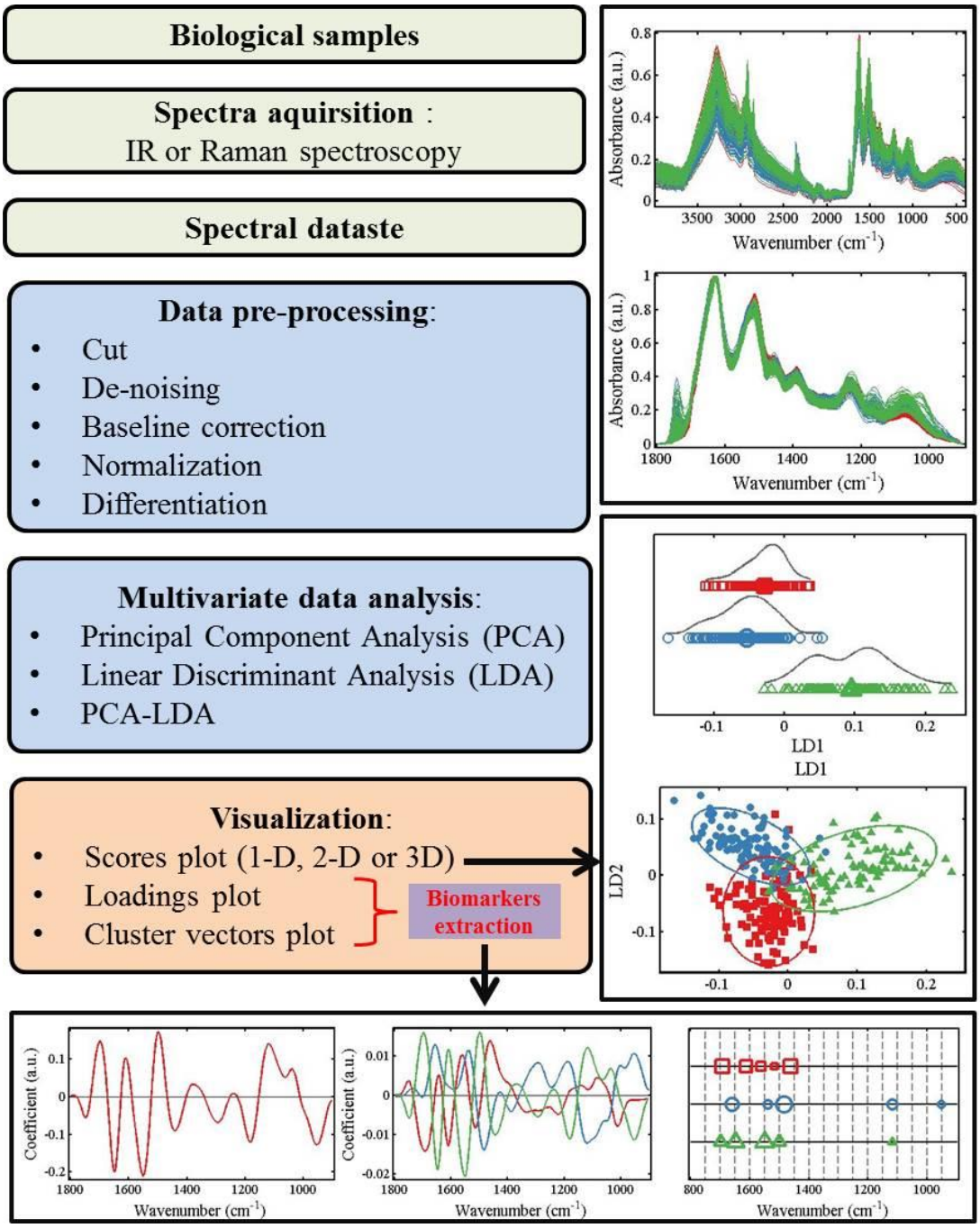

Figure 8 A brief introduction on workflow of spectroscopy analysis.

5. Spectroscopic Data analysis

The using spectroscopic techniques in biological research can generate tremendous amount of data. And the advancement of the spectroscopic instrumentation has even led to an explosive growth in stored or transient data. All these data provide us massive information on the biochemical constituents in the biological samples such as DNA/RNA, proteins, carbohydrates and lipids. Owing to the heterogeneous nature of bio-molecules, the spectroscopic data derived from biological samples are complex and diverse. This means that tiny differences in these data may contain critical information. Thus, it is difficult to interpret the information in the spectra by a simple data-analysis method. To overcome these intricacies and gain a deeper insight into the data, it is urgent to introduce new and automated methods for the spectral data analysis (Figure 8).

5.1 Pre-processing for spectra

Spectral data pre-processing is an important step in workflow of the spectral data analysis (Figure 8). And it has been regarded as an indispensable part involving specific processing procedures performed on the raw spectral data. It is recognised that the a proper pre-processing data is the basis for a better performing of the quantitative and classification models on data when compared with that solely using the raw data (Heraud et al. 2006; Liu et al. 2003). Generally, a proper data pre-processing could help improve the robustness and accuracy of subsequent quantitative and classification analysis; format the data to be better understood by researchers and computer; detect and remove the outliers and trends; and cut out the irrelevant or redundant information by feature selection (Lasch 2012).

5.1.1 Pre-processing in IR spectra

For the repeatability and reproducibility of the spectra, quality test is performed on the dataset firstly, which can be also considered as outliers test. The outliers are the "wrong" measurements that are unsuitable for data analysis, which may be resulted from instrument saturation (too high absorption because of excessive sample thickness), instrument malfunction, atmospheric changes, gas contamination, excessive scattering or dispersion phenomena, and excessive noise (Trevisan et al. 2012). The quality test can help us check for the absorption bands of atmospheric water vapour, samples thickness, and the spectral signal-to-noise ratio (SNR). The water vapour disturbance in the spectra now can be successfully compensated by the software (*e.g.*, OPUS) (Naumann 2008). According to the quality test, the outliers could be then removed.

5.1.1.1 Normalisation

The use of normalization allows an effective comparison in classification analysis of the IR spectra derived from heterogeneous sets of samples. Normalisation can be applied to minimize the impacts of varying optical pathlength on the spectra, to compensate for the intensity variations of the IR source, or to correct for the different sample thickness or concentrations.

During the IR spectra acquisition, spectral baseline could be distorted due to the scattering problems or IR absorption by the supporting substrates in transmission and transflection FTIR, or the change of instrumental factors. In each situation, a baseline correction is required to make the spectral parameter more accurately (Mazet et al. 2005). There are numerous methods suggested for the baseline correction, while most

of them are mainly based on the distinct principles and algorithms, and aim to minimize unwanted spectral offsets, broad baseline distortions, and positive or negative slopes. For example, rubberband baseline correction can be used to achieve baseline correction; it can stretch the spectra down such a minimal area of the spectral region to fit a convex polygonal line and then subtract spectra from the original spectrum. Differentiation is also used as a means for both bassline correction and to resolve overlapped bands, which frequently occurs in IR spectra. First-order differentiation is most frequently used single pre-processing step, while the second-order one is applied together with vector normalisation. However, the differentiation at each order can enhance the spectral noise by one order of magnitude(Trevisan et al. 2012). For de-noising, Savizky-Golay (S-G) smoothing and Wavelet de-noising (WDN) can be used. WDN utilizes non-linear filtering implemented through multi-scale decomposition and thresholding (Trevisan et al. 2012). WDN method is considered as a better alternative, especially for the spectra that contain sharp peaks (*i.e.*, Raman spectroscopy).

In some cases, differences in the sample thickness or concentration can be the main cause of the spectral variation among samples (Shin and Markey 2006). To minimize these adverse impacts, the spectra need to be scaled to match a specific criterion. Most occasionally, if there is such a peak consistently presenting in all spectra in the dataset, normalisation to a particular peak can be applied. For examples, spectra can be normalised to amide I peak (~ 1650 cm^{-1}) or amide II peak (~ 1550 cm^{-1}). When there is no apparently consistent peak across the spectra, vector normalisation is often applied following the differentiation, or area normalisation could be used as well.

5.1.2 Pre-processing in Raman spectra

Generally, most of the pre-processing methods employed on the IR spectra can be shared using the Raman spectral data. Many studies suggest that there are no principle differences on the applicability of quality test, baseline correction, and normalisation methods between the Raman and IR spectra. However, for exceptions, it is not necessary to take the correction water vapour and resonant Mei scattering into account during the pre-processing on Raman spectra. But it is more important to notice that a lower SNR often occurs in Raman spectra of biological samples. For this fact, it is particular important to introduce de-noising methods in the Raman spectra pre-processing. Due to the nature of the Raman instrument, a sharp and intense cosmic ray artefact would occur in the spectra by random, and the fluorescence back frequently turn up in the spectra in the same wavelength region with the Raman signal. Thus, the pre-processing in Raman spectra focus on the methodologies to the disadvantages of cosmic ray and strong florescence background (Lasch 2012).

Cosmic ray could be generated when the high-energy cosmic particles hit the charged-coupled devices (CCD), which is used as the sensitive integrating detector in Raman spectrometers. This cosmic ray may then superimpose on the Raman signals. A few methods have been carried out to eliminate the occurrence of the cosmic ray (Li and Dai 2011; Zhang and Ben-Amotz 2002; Zhao 2003). As the cosmic ray are usually sharp and intense peaks superimposed in the raw spectra. Thus, following a simple correction the spectra containing cosmic ray can be easily found out and discarded.

By contrast to the random occurrence of cosmic ray, it is ubiquitous for the fluorescence background in Raman spectra. The fluorescence background is intense; in some cases it can reach 10^6-10^8 times more intense than Raman scattering (Mosier-

Boss et al. 1995). Therefore, software-based methods have been developed for fluorescence background correction, which comprising purely mathematical or chemometric techniques. Among the mathematical methods, polynomial baseline fitting is the most commonly used, due to its advantages of speed, simplicity and convenience (Zhao et al. 2007). When using this approach it is important to define the polynomial order sufficiently low that it can not only reduce the complexity of the fit model but also avoid over-fitting. The usual polynomial order values vary between 4 and 6 (Zhao et al. 2007).

5.2 Feature extraction

Feature means the input variable; the absorbance intensities at each wavenumber collected by the spectrometer can be regarded as the total variables in the dataset for input to the multivariate data analysis. The feature extraction can be simply understood as the procedure to produce a small number of variables which still keep the main key information for the original whole set of the wavenumber-variables. Thus, multivariate data-analysis techniques have been employed in the feature extraction process. Multivariate data analysis involves in the mathematical, statistical and computer science to efficiently extract useful information from the spectral data.

5.2.1 Principal Component Analysis

Principle component analysis (PCA) is an unsupervised data analysis technique employed to reduce dimensionality and generate a visualization of the data (Kelly et al. 2011). PCA is a commonly technique that based on evaluating the total variances within a dataset via Eigen analysis. PCA method is projecting a higher dimensional data matrix "X" (matrix "X" consisting of ***m*** object rows and ***n*** variable columns, $m \times$

n matrix; ***m*** objects are observations [*i.e.*, spectra] and ***n*** variables are measurements [*i.e.*, wavenumber]) onto a low component subspace; It is a linear transformation of the wavenumber dataset operated by the PCA loadings matrix (Kelly et al. 2011). And the loadings vectors (commonly called principal components [PCs]) within this matrix are eigenvectors of the covariance matrix of the data. These PCs are obtained by calculating the eigenvectors and eigenvalues of the covariance matrix obtained from the data matrix. The eigenvector with the highest eigenvalue gives rise to the first PC (PC1), which is lying on the direction of greatest variance in the data. "PC1" is the direction (axis) that maximizes the longitudinal (along axis) variance or the axis that minimizes the squared projection (transverse) distances. All PCs are orthogonal to each other, which mean each loading forms an angle of 90 °with all the other loadings. Thus, the PCs are completely uncorrelated and independent.

For an X-matrix ($m \times n$), the largest number of PCs is either one less than the number of objects (m-1) or equal to the number of variables (n), depending on which ever is smaller (Gautam et al. 2015). However, the higher-orders of the PCs are regarded as noise factors which contain useless noise component for the spectral dataset. To understand importance of the PCs order, "percentage of variance explained" has been used to determine this (Westerhuis et al. 1998). Usually there is a steep increase in percentage of variance explained, followed by a flat line. No matter how many spectral channels there are, the relevant information (spectral variance) can be explained by the first few dominant PCs while repeated information is present in various spectral channels. Commonly, the first three PCs were selected (each contributes higher than 5% percentage of variance with total cumulative value of above 90 %) for optimum visualization of the spread of the data.

PCA is undoubtable a powerful dimension-reduction data analysis technique with capability of identifying some important structural information in the data, and it is the fundamental basis of many other multivariate data analysis technique. However, PCA is only capable of recognising total variance regarding a whole dataset, but without the capability to identify within-group and among-group variance due to the fact that it is an unsupervised procedure (Wang and Mizaikoff 2008). Often, in order to interpret the complex biochemical information from vibrational spectroscopic techniques, it requires further data analysis using supervised procedures like LDA, PLS, PCR etc.

5.2.2 Linear Discriminant Analysis

LDA is a supervised technique which forms linear combinations of variables dependent on differences between the classes in the data set (Kelly et al. 2011). In LDA method, data can be projected into the new dimensional space using these axes found with LDA. In the new dimensional space, each observation would have fewer variables and at the same time observations belonging to the same class will form lumps (clusters) and each cluster would be clearly differentiated from the other. A particular feature of LDA is that it may achieve maximum separation between classes over the within class by carefully establishing the discriminant function(Kelly et al. 2011). Following LDA applied, the data set will have only c - 1 variables, where c is the number of data classes. The Euclidean distance (ED) or Mahalanobis distance (MD) is usually calculated. Based on the distance of the unknown samples to the centre of each class, they are used in LDA to classify unknown ones. In order to establish a reliable classifier using LDA, it requires a much higher number of objects than that of variables (Wang and Mizaikoff 2008). Hence, it is necessary to do data reduction on the spectra dataset prior to applying LDA method.

5.2.3 PCA-LDA

It is very useful to combine both PCA and LDA approaches (called PCA-LDA model). The PCA-LDA model improves the efficiency of classification as it automatically finds the most diagnostically significant features. PCA is applied to the original dataset first, and only the first few principal component scores are retained for further LDA. The resulting Linear Discriminant scores matrix represents compactly the original data and very efficiently differentiates one class from another. However, there is one important factor for consideration that how many PCs to include when applying LDA following PCA. Too few PCs will cause an information missing for the spectral dataset, while too many will increase the amount of noise in the data, and may lead to LDA overfitting (Kelly et al. 2011). Commonly, 10 factors is a compromise on both situations, since that more than 99% of variance is captured in the first 10 PCs, while more than 20 PCs includes too much noise (Kemsley 1996). Similar to PCA, loading analysis can also be performed using the PC-LDA model, where each LD loading can be represented as a linear combination of PC Loadings. Thus, it can be used to understand and identify specific vibrational bands corresponding for the differences between classes (Gautam et al. 2015).

5.3 Visualisation of the processed spectral data

Following the multivariate data analysis, most of the information in the spectra has been extracted. Resulting scores and loadings plots provide a visual representation and interpretation of variables responsible for any difference. To simple see the differences between the groups, using the factor scores resulting from the analysis could easily draw dimensional scores plots graph (*e.g.*, 1-, 2-, or 3-D scatter plots) (Figure 8), which facilitate the visualisation of the segregations between classes

(Llabjani et al. 2009; Llabjani et al. 2010). Furthermore, coefficients of loadings vectors of either technique can be plotted against the wavenumber axis to reveal the contributions of each wavenumber to form each corresponding factor for class separation and compactness, because the loadings vectors have the same resolution as the original spectra. Additionally, the loadings can also show which the most distinguishing wavenumbers are. Each distinguished wavenumber is then related to the corresponding biochemical and identified as a potential biomarker to specific category.

It is the fact that loadings vectors are found to be more informative when they "pass through" data points instead of pointing toward void space (Martin et al. 2007). Thus, a cluster vector approach is developed, a geometric construction that can be applied to any of the linear techniques described, while it is more often employed following PCA-LDA (Kelly et al. 2011). There is only one cluster vector for each data class by contrast to the loadings vectors. Each cluster vector is the vector that points from the origin to the centre of its corresponding data class in the vector space spanned by the loadings vectors. The centre of a given class is calculated by taking the average between all points belonging to the class. However, when it requires comparing the objective groups with the control ones, this approach will bring inconvenience to identify the biomarker differences in the objective groups compared to the control ones, because in this approach the "control" class itself has a cluster vector. In order to overcome this disadvantages, the cluster vector for the "control" class is transformed to the zero vector by shifting the origin of the factors space to the centre of the "control" cluster (Llabjani et al. 2010), whereas the other cluster vectors express comparisons of data classes against their corresponding vehicle control. This approach is particularly useful when there are many classes and interpretation of the scores and

loadings plots is both complex and subjective. To simplify the identification of the main biomarkers for each class, cluster vector peak plots were used to indicate the first few highest peaks in the cluster vector plots (Llabjani et al. 2011).

6. Aims and objectives

This thesis is mainly consisting of four research projects, which are focusing on utilisation of biospectroscopy in the toxicity assessment of the four types CNPs both *in vitro* and *in vivo*, as well as a cooperative project of using IR spectroscopy to identify the alteration in MCF-7cells by Benzo[*a*]pyrene. The main objectives of the four projects are listed below:

- To investigate the dose-response effects of the three CNPs (C60, short and long MWCNTs) in MCF-7 cells at a low dose treatment by using ATR-FTIR and Raman spectroscopy (Chapter 3).
- To assess the nanotoxicity of the four types CNPs (C60, short and long MWCNTs, SWCNTs) in zebrafish with a low-dose chronic exposure and detect alterations in tissues by ATR-FTIR and Raman spectroscopy (Chapter 4).
- To investigate the nanotoxicity of the four types CNPs in A549 cells with biospectroscopic techniques of ATR-FTIR and SERS (Chapter 5).
- To explore the binary effects of C60 and B[*a*]P in two cell lines (gill cells and MCF-7 cells) by using FTIR microscope (Chapter 6).

References

Aiken, G.R., Hsu-Kim, H. and Ryan, J.N. 2011. Influence of Dissolved Organic Matter on the Environmental Fate of Metals, Nanoparticles, and Colloids. Environ. Sci. Technol. 45, 3196-3201.

Albrecht, M.G. and Creighton, J.A. 1977. Anomalously intense Raman spectra of pyridine at a silver electrode. J. Am. Chem. Soc. 99, 5215-5217.

Azevedo Costa, C.L., Chaves, I.S., Ventura-Lima, J., Ferreira, J.L.R., Ferraz, L., de Carvalho, L.M. and Monserrat, J.M. 2012. In vitro evaluation of co-exposure of arsenium and an organic nanomaterial (fullerene, C60) in zebrafish hepatocytes. Comp. Biochem. Physiol., Part C: Toxicol. Pharmacol. 155, 206-212.

Bagchi, D., Bagchi, M., Hassoun, E.A. and Stohs, S.J. 1995. In vitro and in vivo generation of reactive oxygen species, DNA damage and lactate dehydrogenase leakage by selected pesticides. Toxicology 104, 129-140.

Baker, M.J., Trevisan, J., Bassan, P., Bhargava, R., Butler, H.J., Dorling, K.M., Fielden, P.R., Fogarty, S.W., Fullwood, N.J., Heys, K.A., Hughes, C., Lasch, P., Martin-Hirsch, P.L., Obinaju, B., Sockalingum, G.D., Sule-Suso, J., Strong, R.J., Walsh, M.J., Wood, B.R., Gardner, P. and Martin, F.L. 2014. Using Fourier transform IR spectroscopy to analyze biological materials. Nature Protocols 9, 1771-1791.

Bakry, R., Vallant, R.M., Najam-ul-Haq, M., Rainer, M., Szabo, Z., Huck, C.W. and Bonn, G.K. 2007. Medicinal applications of fullerenes. Int. J. Nanomed. 2, 639.

Baun, A., Sørensen, S.N., Rasmussen, R.F., Hartmann, N.B. and Koch, C.B. 2008. Toxicity and bioaccumulation of xenobiotic organic compounds in the presence of aqueous suspensions of aggregates of nano-C60. Aquat. Toxicol. 86, 379-387.

Becheri, A., Dürr, M., Lo Nostro, P. and Baglioni, P. 2008. Synthesis and characterization of zinc oxide nanoparticles: application to textiles as UV-absorbers. J. Nanopart. Res. 10, 679-689.

Bello, D., Wardle, B., Yamamoto, N., Guzman deVilloria, R., Garcia, E., Hart, A., Ahn, K., Ellenbecker, M. and Hallock, M. 2009. Exposure to nanoscale particles and fibers during machining of hybrid advanced composites containing carbon nanotubes. J. Nanopart. Res. 11, 231-249.

Benn, T.M. and Westerhoff, P. 2008. Nanoparticle Silver Released into Water from Commercially Available Sock Fabrics. Environ. Sci. Technol. 42, 4133-4139.

Bhargava, R. 2012. Infrared Spectroscopic Imaging: The Next Generation. Appl. Spectrosc. 66, 1091-1120.

Bianco, A., Kostarelos, K. and Prato, M. 2005. Applications of carbon nanotubes in drug delivery. Curr. Opin. Chem. Biol. 9, 674-679.

Bihari, P., Vippola, M., Schultes, S., Praetner, M., Khandoga, A.G., Reichel, C.A., Coester, C., Tuomi, T., Rehberg, M. and Krombach, F. 2008. Optimized dispersion of nanoparticles for biological in vitro and in vivo studies. Part. Fibre Toxicol. 5, 14.

Bouwmeester, H., Lynch, I., marvin, H.J.P., Dawson, K.A., Berges, M., Braguer, D., Byrne, H.J., Casey, A., Chambers, G., Clift, M.J.D., Elia, G., Fernandes, T.F., Fjellsbø, L.B., Hatto, P., Juillerat, L., Klein, C., Kreyling, W.G., Nickel, C., Riediker, M. and Stone, V. 2011. Minimal analytical characterization of engineered nanomaterials needed for hazard assessment in biological matrices. Nanotoxicology 5, 1-11.

Brant, J., Lecoanet, H., Hotze, M. and Wiesner, M. 2005. Comparison of Electrokinetic Properties of Colloidal Fullerenes (n-C60) Formed Using Two Procedures†. Environ. Sci. Technol. 39, 6343-6351.

Buford, M., Hamilton, R., Jr. and Holian, A. 2007. A comparison of dispersing media for various engineered carbon nanoparticles. Part. Fibre Toxicol. 4, 1-9.

Cabiscol, E., Tamarit, J. and Ros, J. 2010. Oxidative stress in bacteria and protein damage by reactive oxygen species. Int. Microbiol. 3, 3-8.

Camden, J.P., Dieringer, J.A., Wang, Y., Masiello, D.J., Marks, L.D., Schatz, G.C. and Van Duyne, R.P. 2008. Probing the Structure of Single-Molecule Surface-Enhanced Raman Scattering Hot Spots. J. Am. Chem. Soc. 130, 12616-12617.

Campion, A. and Kambhampati, P. 1998. Surface-enhanced Raman scattering. Chem. Soc. Rev. 27, 241-250.

Cao, Y., Jin, R. and Mirkin, C.A. 2001. DNA-modified core-shell Ag/Au nanoparticles. J. Am. Chem. Soc. 123, 7961-7962.

Casey, A., Herzog, E., Davoren, M., Lyng, F., Byrne, H. and Chambers, G. 2007a. Spectroscopic analysis confirms the interaction between SWCNT and various dyes commonly used to assess cytotoxicity. Carbon 45, 1425 - 1432.

Casey, A., Herzog, E., Davoren, M., Lyng, F.M., Byrne, H.J. and Chambers, G. 2007b. Spectroscopic analysis confirms the interactions between single walled carbon nanotubes and various dyes commonly used to assess cytotoxicity. Carbon 45, 1425-1432.

Cho, W.J., Kim, Y. and Kim, J.K. 2012. Ultrahigh-Density Array of Silver Nanoclusters for SERS Substrate with High Sensitivity and Excellent Reproducibility. ACS Nano 6, 249-255.

Christian, P., Von der Kammer, F., Baalousha, M. and Hofmann, T. 2008. Nanoparticles: structure, properties, preparation and behaviour in environmental media. Ecotoxicology 17, 326-343.

Clift, M.D., Gehr, P. and Rothen-Rutishauser, B. 2011. Nanotoxicology: a perspective and discussion of whether or not in vitro testing is a valid alternative. Arch. Toxicol. 85, 723-731.

Crouzier, D., Follot, S., Gentilhomme, E., Flahaut, E., Arnaud, R., Dabouis, V., Castellarin, C. and Debouzy, J.C. 2010. Carbon nanotubes induce inflammation but decrease the production of reactive oxygen species in lung. Toxicology 272, 39-45.

Deguchi, S., Alargova, R.G. and Tsujii, K. 2001. Stable Dispersions of Fullerenes, C60 and C70, in Water. Preparation and Characterization. Langmuir 17, 6013-6017.

Dhawan, A. and Sharma, V. 2010. Toxicity assessment of nanomaterials: methods and challenges. Anal. Bioanal. Chem. 398, 589-605.

Edgington, A.J., Roberts, A.P., Taylor, L.M., Alloy, M.M., Reppert, J., Rao, A.M., Mao, J. and Klaine, S.J. 2010. The influence of natural organic matter on the toxicity of multiwalled carbon nanotubes. Environ. Toxicol. Chem. 29, 2511-2518.

Ellis, D.I. and Goodacre, R. 2006. Metabolic fingerprinting in disease diagnosis: biomedical applications of infrared and Raman spectroscopy. Analyst 131, 875-885.

Elsaesser, A. and Howard, C.V. 2012. Toxicology of nanoparticles. Adv. Drug Del. Rev. 64, 129-137.

Ferreira, J.L.R., Lonné, M.N., Fran ça, T.A., Maximilla, N.R., Lugokenski, T.H., Costa, P.G., Fillmann, G., Antunes Soares, F.A., de la Torre, F.R. and Monserrat, J.M. 2014. Co-exposure of the organic nanomaterial fullerene C60 with benzo[a]pyrene in Danio rerio (zebrafish) hepatocytes: Evidence of toxicological interactions. Aquat. Toxicol. 147, 76-83.

Foucaud, L., Wilson, M.R., Brown, D.M. and Stone, V. 2007. Measurement of reactive species production by nanoparticles prepared in biologically relevant media. Toxicol. Lett. 174, 1-9.

Ganesh, R., Smeraldi, J., Hosseini, T., Khatib, L., Olson, B.H. and Rosso, D. 2010. Evaluation of Nanocopper Removal and Toxicity in Municipal Wastewaters. Environ. Sci. Technol. 44, 7808-7813.

Gautam, R., Vanga, S., Ariese, F. and Umapathy, S. 2015. Review of multidimensional data processing approaches for Raman and infrared spectroscopy. EPJ Techn Instrum 2, 1-38.

Girifalco, L.A. and Hodak, M. 2002. Van der Waals binding energies in graphitic structures. Phys. Rev. B 65, 125404.

Girifalco, L.A., Hodak, M. and Lee, R.S. 2000. Carbon nanotubes, buckyballs, ropes, and a universal graphitic potential. Phys.l Rev. B 62, 13104-13110.

Gonzalez, L., Lison, D. and Kirsch-Volders, M. 2008. Genotoxicity of engineered nanomaterials: A critical review. Nanotoxicology 2, 252-273.

Gooding, J.J. 2005. Nanostructuring electrodes with carbon nanotubes: A review on electrochemistry and applications for sensing. Electrochim. Acta 50, 3049-3060.

Gottschalk, F. and Nowack, B. 2011. The release of engineered nanomaterials to the environment. J. Environ. Monit. 13, 1145-1155.

Gottschalk, F., Sonderer, T., Scholz, R.W. and Nowack, B. 2009. Modeled Environmental Concentrations of Engineered Nanomaterials (TiO2, ZnO, Ag, CNT, Fullerenes) for Different Regions. Environ. Sci. Technol. 43, 9216-9222.

Griveau, J.F., Dumont, E., Renard, P., Callegari, J.P. and Le Lannou, D. 1995. Reactive oxygen species, lipid peroxidation and enzymatic defence systems in human spermatozoa. J. Reprod. Fertil. 103, 17-26.

Halliwell, B. 1991. Reactive oxygen species in living systems: Source, biochemistry, and role in human disease. Am. J. Med. 91, S14-S22.

Henry, T.B., Menn, F.-M., Fleming, J.T., Wilgus, J., Compton, R.N. and Sayler, G.S. 2007. Attributing Effects of Aqueous C60 Nano-Aggregates to Tetrahydrofuran Decomposition Products in Larval Zebrafish by Assessment of Gene Expression. Environ. Health Perspect. 115, 1059-1065.

Heraud, P., Wood, B.R., Beardall, J. and McNaughton, D. 2006. Effects of pre-processing of Raman spectra on in vivo classification of nutrient status of microalgal cells. J. Chemom. 20, 193-197.

Hering, K., Cialla, D., Ackermann, K., Dörfer, T., Möller, R., Schneidewind, H., Mattheis, R., Fritzsche, W., Rösch, P. and Popp, J. 2008. SERS: a versatile tool in chemical and biochemical diagnostics. Anal. Bioanal. Chem. 390, 113-124.

Hirschmugl, C.J. and Gough, K.M. 2012. Fourier Transform Infrared Spectrochemical Imaging: Review of Design and Applications with a Focal Plane Array and Multiple Beam Synchrotron Radiation Source. Appl. Spectrosc. 66, 475-491.

Holder, A.L., Goth-Goldstein, R., Lucas, D. and Koshland, C.P. 2012. Particle-Induced Artifacts in the MTT and LDH Viability Assays. Chem. Res. Toxicol. 25, 1885-1892.

Huang, J., Zhang, L., Chen, B., Ji, N., Chen, F., Zhang, Y. and Zhang, Z. 2010. Nanocomposites of size-controlled gold nanoparticles and graphene oxide: Formation and applications in SERS and catalysis. Nanoscale 2, 2733-2738.

Hungerbuehler, H., Guldi, D.M. and Asmus, K.D. 1993. Incorporation of C60 into artificial lipid membranes. J. Am. Chem. Soc. 115, 3386-3387.

Hurt, R.H., Monthioux, M. and Kane, A. 2006. Toxicology of carbon nanomaterials: Status, trends, and perspectives on the special issue. Carbon 44, 1028-1033.

Jeanmaire, D.L. and Van Duyne, R.P. 1977. Surface Raman spectroelectrochemistry: Part I. Heterocyclic, aromatic, and aliphatic amines adsorbed on the anodized silver electrode. J. Electroanal. Chem. Interfacial Electrochem. 84, 1-20.

Jensen, A.W., Wilson, S.R. and Schuster, D.I. 1996. Biological applications of fullerenes. Biorg. Med. Chem. 4, 767-779.

Jia, G., Wang, H., Yan, L., Wang, X., Pei, R., Yan, T., Zhao, Y. and Guo, X. 2005. Cytotoxicity of Carbon Nanomaterials: Single-Wall Nanotube, Multi-Wall Nanotube, and Fullerene. Environ. Sci. Technol. 39, 1378-1383.

Jiang, J., Oberdörster, G. and Biswas, P. 2009. Characterization of size, surface charge, and agglomeration state of nanoparticle dispersions for toxicological studies. J. Nanopart. Res. 11, 77-89.

Johnston, H., Pojana, G., Zuin, S., Jacobsen, N.R., Møller, P., Loft, S., Semmler-Behnke, M., McGuiness, C., Balharry, D., Marcomini, A., Wallin, H., Kreyling, W., Donaldson, K., Tran, L. and Stone, V. 2013. Engineered nanomaterial risk. Lessons learnt from completed nanotoxicology studies: potential solutions to current and future challenges. Crit. Rev. Toxicol. 43, 1-20.

Katz, E. and Willner, I. 2004. Biomolecule-Functionalized Carbon Nanotubes: Applications in Nanobioelectronics. ChemPhysChem 5, 1084-1104.

Kayat, J., Gajbhiye, V., Tekade, R.K. and Jain, N.K. 2011. Pulmonary toxicity of carbon nanotubes: a systematic report. Nanomed. Nanotechnol. Biol. Med. 7, 40-49.

Kazarian, S.G. and Chan, K.L.A. 2010. Micro- and Macro-Attenuated Total Reflection Fourier Transform Infrared Spectroscopic Imaging. Appl. Spectrosc. 64, 135A-152A.

Kazarian, S.G. and Chan, K.L.A. 2013. ATR-FTIR spectroscopic imaging: recent advances and applications to biological systems. Analyst 138, 1940-1951.

Keller, A.A., Wang, H., Zhou, D., Lenihan, H.S., Cherr, G., Cardinale, B.J., Miller, R. and Ji, Z. 2010. Stability and Aggregation of Metal Oxide Nanoparticles in Natural Aqueous Matrices. Environ. Sci. Technol. 44, 1962-1967.

Kelly, J.G., Trevisan, J.l., Scott, A.D., Carmichael, P.L., Pollock, H.M., Martin-Hirsch, P.L. and Martin, F.L. 2011. Biospectroscopy to metabolically profile biomolecular structure: a multistage approach linking computational analysis with biomarkers. J. Proteome Res. 10, 1437-1448.

Kemsley, E.K. 1996. Discriminant analysis of high-dimensional data: a comparison of principal components analysis and partial least squares data reduction methods. Chemometrics Intellig. Lab. Syst. 33, 47-61.

Kim, J., Song, K., Lee, J. and Yu, I. 2011. Evaluation of biocompatible dispersants for carbon nanotube toxicity tests. Arch. Toxicol. 85, 1499-1508.

Kiser, M.A., Ryu, H., Jang, H., Hristovski, K. and Westerhoff, P. 2010. Biosorption of nanoparticles to heterotrophic wastewater biomass. Water Res. 44, 4105-4114.

Kneipp, K., Kneipp, H., Itzkan, I., Dasari, R.R. and Feld, M.S. 1999. Ultrasensitive Chemical Analysis by Raman Spectroscopy. Chem. Rev. 99, 2957-2976.

Kneipp, K., Wang, Y., Kneipp, H., Perelman, L.T., Itzkan, I., Dasari, R.R. and Feld, M.S. 1997. Single Molecule Detection Using Surface-Enhanced Raman Scattering (SERS). Phys. Rev. Lett. 78, 1667-1670.

Krafft, C., Steiner, G., Beleites, C. and Salzer, R. 2009. Disease recognition by infrared and Raman spectroscopy. J. Biophotonics 2, 13-28.

Kroll, A., Pillukat, M., Hahn, D. and Schnekenburger, J. 2012. Interference of engineered nanoparticles with in vitro toxicity assays. Arch. Toxicol. 86, 1123-1136.

Kroll, A., Pillukat, M.H., Hahn, D. and Schnekenburger, J. 2009. Current in vitro methods in nanoparticle risk assessment: Limitations and challenges. Eur. J. Pharm. Biopharm. 72, 370-377.

Kulakovich, O., Strekal, N., Yaroshevich, A., Maskevich, S., Gaponenko, S., Nabiev, I., Woggon, U. and Artemyev, M. 2002. Enhanced Luminescence of CdSe Quantum Dots on Gold Colloids. Nano Lett. 2, 1449-1452.

Lasch, P. 2012. Spectral pre-processing for biomedical vibrational spectroscopy and microspectroscopic imaging. Chemometrics Intellig. Lab. Syst. 117, 100-114.

Lehto, M., Karilainen, T., Róg, T., Cramariuc, O., Vanhala, E., Tornaeus, J., Taberman, H., Jänis, J., Alenius, H., Vattulainen, I. and Laine, O. 2014. Co-Exposure with Fullerene May Strengthen Health Effects of Organic Industrial Chemicals. PLoS ONE 9, e114490.

Li, J.F., Huang, Y.F., Ding, Y., Yang, Z.L., Li, S.B., Zhou, X.S., Fan, F.R., Zhang, W., Zhou, Z.Y., WuDe, Y., Ren, B., Wang, Z.L. and Tian, Z.Q. 2010. Shell-isolated nanoparticle-enhanced Raman spectroscopy. Nature 464, 392-395.

Li, S. and Dai, L. 2011. An Improved Algorithm to Remove Cosmic Spikes in Raman Spectra for Online Monitoring. Appl. Spectrosc. 65, 1300-1306.

Limbach, L.K., Wick, P., Manser, P., Grass, R.N., Bruinink, A. and Stark, W.J. 2007. Exposure of Engineered Nanoparticles to Human Lung Epithelial Cells: Influence of Chemical Composition and Catalytic Activity on Oxidative Stress. Environ. Sci. Technol. 41, 4158-4163.

Liu, K.-Z., Tsang, K.S., Li, C.K., Shaw, R.A. and Mantsch, H.H. 2003. Infrared Spectroscopic Identification of β-Thalassemia. Clin. Chem. 49, 1125-1132.

Liu, Z., Tabakman, S., Welsher, K. and Dai, H. 2009. Carbon nanotubes in biology and medicine: In vitro and in vivo detection, imaging and drug delivery. Nano Research 2, 85-120.

Llabjani, V., Crosse, J.D., Ahmadzai, A.A., Patel, I.I., Pang, W., Trevisan, J., Jones, K.C., Shore, R.F. and Martin, F.L. 2011. Differential Effects in Mammalian Cells Induced by Chemical Mixtures in Environmental Biota As Profiled Using Infrared Spectroscopy. Environ. Sci. Technol. 45, 10706-10712.

Llabjani, V., Jones, K.C., Thomas, G.O., Walker, L.A., Shore, R.F. and Martin, F.L. 2009. Polybrominated Diphenyl Ether-Associated Alterations in Cell Biochemistry as Determined by Attenuated Total Reflection Fourier-Transform Infrared Spectroscopy: a Comparison with DNA-Reactive and/or Endocrine-Disrupting Agents. Environ. Sci. Technol. 43, 3356-3364.

Llabjani, V., Trevisan, J., Jones, K.C., Shore, R.F. and Martin, F.L. 2010. Binary Mixture Effects by PBDE Congeners (47, 153, 183, or 209) and PCB Congeners (126 or 153) in MCF-7 Cells: Biochemical Alterations Assessed by IR Spectroscopy and Multivariate Analysis. Environ. Sci. Technol. 44, 3992-3998.

Lovern, S.B. and Klaper, R. 2006. Daphnia magna mortality when exposed to titanium dioxide and fullerene (C60) nanoparticles. Environ. Toxicol. Chem. 25, 1132-1137.

Lowry, G.V., Gregory, K.B., Apte, S.C. and Lead, J.R. 2012. Transformations of Nanomaterials in the Environment. Environ. Sci. Technol. 46, 6893-6899.

Lu, Y., Yin, Y., Li, Z.-Y. and Xia, Y. 2002. Synthesis and Self-Assembly of Au@SiO2 Core−Shell Colloids. Nano Lett. 2, 785-788.

Madni, I., Hwang, C.-Y., Park, S.-D., Choa, Y.-H. and Kim, H.-T. 2010. Mixed surfactant system for stable suspension of multiwalled carbon nanotubes. Colloids Surf. Physicochem. Eng. Aspects 358, 101-107.

Martin, F.L., German, M.J., Wit, E., Fearn, T., Ragavan, N. and Pollock, H.M. 2007. Identifying Variables Responsible for Clustering in Discriminant Analysis of Data from Infrared Microspectroscopy of a Biological Sample. J. Comput. Biol. 14, 1176-1184.

Martin, F.L., Kelly, J.G., Llabjani, V., Martin-Hirsch, P.L., Patel, I.I., Trevisan, J., Fullwood, N.J. and Walsh, M.J. 2010. Distinguishing cell types or populations based on the computational analysis of their infrared spectra. Nat. Protocols 5, 1748-1760.

Matsuda, S., Matsui, S., Shimizu, Y. and Matsuda, T. 2011. Genotoxicity of Colloidal Fullerene C60. Environ. Sci. Technol. 45, 4133-4138.

Mauter, M.S. and Elimelech, M. 2008. Environmental Applications of Carbon-Based Nanomaterials. Environ. Sci. Technol. 42, 5843-5859.

Mazet, V., Carteret, C., Brie, D., Idier, J. and Humbert, B. 2005. Background removal from spectra by designing and minimising a non-quadratic cost function. Chemometrics Intellig. Lab. Syst. 76, 121-133.

McHedlov-Petrossyan, N.O. 2013. Fullerenes in Liquid Media: An Unsettling Intrusion into the Solution Chemistry. Chem. Rev. 113, 5149-5193.

Meng, H., Xia, T., George, S. and Nel, A.E. 2009. A Predictive Toxicological Paradigm for the Safety Assessment of Nanomaterials. ACS Nano 3, 1620-1627.

Miller, L.M. and Dumas, P. 2006. Chemical imaging of biological tissue with synchrotron infrared light. Biochim. Biophys. Acta, Biomembr. 1758, 846-857.

Monteiro-Riviere, N.A. and Inman, A.O. 2006. Challenges for assessing carbon nanomaterial toxicity to the skin. Carbon 44, 1070-1078.

Monteiro-Riviere, N.A., Inman, A.O. and Zhang, L.W. 2009. Limitations and relative utility of screening assays to assess engineered nanoparticle toxicity in a human cell line. Toxicol. Appl. Pharmacol. 234, 222-235.

Mosier-Boss, P.A., Lieberman, S.H. and Newbery, R. 1995. Fluorescence Rejection in Raman Spectroscopy by Shifted-Spectra, Edge Detection, and FFT Filtering Techniques. Appl. Spectrosc. 49, 630-638.

Moskovits, M. 1985. Surface-enhanced spectroscopy. Rev. Mod. Phys. 57, 783-826.

Nasse, M.J., Walsh, M.J., Mattson, E.C., Reininger, R., Kajdacsy-Balla, A., Macias, V., Bhargava, R. and Hirschmugl, C.J. 2011. High-resolution Fourier-transform infrared chemical imaging with multiple synchrotron beams. Nat Meth 8, 413-416.

Naumann, D. 2008. FT-IR spectroscopy of microorganisms at the Robert Koch Institute: experiences gained during a successful project. pp. 68530G-68530G-68512.

Nel, A., Xia, T., Mädler, L. and Li, N. 2006. Toxic Potential of Materials at the Nanolevel. Science 311, 622-627.

Nel, A., Xia, T., Meng, H., Wang, X., Lin, S., Ji, Z. and Zhang, H. 2012. Nanomaterial Toxicity Testing in the 21st Century: Use of a Predictive Toxicological Approach and High-Throughput Screening. Acc. Chem. Res. 46, 607-621.

Nel, A.E., Madler, L., Velegol, D., Xia, T., Hoek, E.M.V., Somasundaran, P., Klaessig, F., Castranova, V. and Thompson, M. 2009. Understanding biophysicochemical interactions at the nano-bio interface. Nat Mater 8, 543-557.

Nowack, B. and Bucheli, T.D. 2007. Occurrence, behavior and effects of nanoparticles in the environment. Environ. Pollut. 150, 5-22.

Oberdörster, E. 2004a. Manufactured nanomaterials (fullerenes, C60) induce oxidative stress in the brain of juvenile largemouth bass. Environ. Health Perspect. 112, 1058-1062.

Oberdörster, E. 2004b. Manufactured Nanomaterials (Fullerenes, C(60)) Induce Oxidative Stress in the Brain of Juvenile Largemouth Bass. Environ. Health Perspect. 112, 1058-1062.

Pan, B. and Xing, B. 2008. Adsorption Mechanisms of Organic Chemicals on Carbon Nanotubes. Environ. Sci. Technol. 42, 9005-9013.

Park, J.-W., Henry, T.B., Ard, S., Menn, F.-M., Compton, R.N. and Sayler, G.S. 2011. The association between nC60 and 17α-ethinylestradiol (EE2) decreases EE2 bioavailability in zebrafish and alters nanoaggregate characteristics. Nanotoxicology 5, 406-416.

Park, J.-W., Henry, T.B., Menn, F.-M., Compton, R.N. and Sayler, G. 2010. No bioavailability of 17α-ethinylestradiol when associated with nC60 aggregates during dietary exposure in adult male zebrafish (Danio rerio). Chemosphere 81, 1227-1232.

Petersen, E.J. and Henry, T.B. 2012. Methodological considerations for testing the ecotoxicity of carbon nanotubes and fullerenes: Review. Environ. Toxicol. Chem. 31, 60-72.

Petersen, E.J., Pinto, R.A., Mai, D.J., Landrum, P.F. and Weber, W.J. 2011a. Influence of Polyethyleneimine Graftings of Multi-Walled Carbon Nanotubes on their Accumulation and Elimination by and Toxicity to Daphnia magna. Environ. Sci. Technol. 45, 1133-1138.

Petersen, E.J., Zhang, L., Mattison, N.T., O'Carroll, D.M., Whelton, A.J., Uddin, N., Nguyen, T., Huang, Q., Henry, T.B., Holbrook, R.D. and Chen, K.L. 2011b. Potential Release Pathways, Environmental Fate, And Ecological Risks of Carbon Nanotubes. Environ. Sci. Technol. 45, 9837-9856.

Porter, D., Sriram, K., Wolfarth, M., Jefferson, A., Schwegler-Berry, D., Andrew, M.E. and Castranova, V. 2008. A biocompatible medium for nanoparticle dispersion. Nanotoxicology 2, 144-154.

Powers, K.W., Palazuelos, M., Moudgil, B.M. and Roberts, S.M. 2007. Characterization of the size, shape, and state of dispersion of nanoparticles for toxicological studies. Nanotoxicology 1, 42-51.

Quagliano, L.G. 2004. Observation of Molecules Adsorbed on III-V Semiconductor Quantum Dots by Surface-Enhanced Raman Scattering. J. Am. Chem. Soc. 126, 7393-7398.

Ren, L. and Zhong, W. 2010. Oxidation Reactions Mediated by Single-Walled Carbon Nanotubes in Aqueous Solution. Environ. Sci. Technol. 44, 6954-6958.

Ren, W., Fang, Y. and Wang, E. 2011. A Binary Functional Substrate for Enrichment and Ultrasensitive SERS Spectroscopic Detection of Folic Acid Using Graphene Oxide/Ag Nanoparticle Hybrids. ACS Nano 5, 6425-6433.

Sager, T.M., Porter, D.W., Robinson, V.A., Lindsley, W.G., Schwegler-Berry, D.E. and Castranova, V. 2007. Improved method to disperse nanoparticles for in vitro and in vivo investigation of toxicity. Nanotoxicology 1, 118-129.

Savolainen, K., Alenius, H., Norppa, H., Tuomi, T. and Kasper, G. 2010. Risk assessment of engineered nanomaterials and nanotechnologies--a review. Toxicology 269, 92-104.

Sayes, C.M., Reed, K.L. and Warheit, D.B. 2007. Assessing Toxicity of Fine and Nanoparticles: Comparing In Vitro Measurements to In Vivo Pulmonary Toxicity Profiles. Toxicol. Sci. 97, 163-180.

Serpone, N., Dondi, D. and Albini, A. 2007. Inorganic and organic UV filters: Their role and efficacy in sunscreens and suncare products. Inorg. Chim. Acta 360, 794-802.

Sharma, B., Frontiera, R.R., Henry, A.-I., Ringe, E. and Van Duyne, R.P. 2012. SERS: Materials, applications, and the future. Mater. Today 15, 16-25.

Shi, H., Hudson, L.G. and Liu, K.J. 2004. Oxidative stress and apoptosis in metal ion-induced carcinogenesis. Free Radic. Biol. Med. 37, 582-593.

Shin, H. and Markey, M.K. 2006. A machine learning perspective on the development of clinical decision support systems utilizing mass spectra of blood samples. J. Biomed. Inf. 39, 227-248.

Shinohara, N., Matsumoto, K., Endoh, S., Maru, J. and Nakanishi, J. 2009. In vitro and in vivo genotoxicity tests on fullerene C60 nanoparticles. Toxicol. Lett. 191, 289-296.

Shvedova, A.A., Pietroiusti, A., Fadeel, B. and Kagan, V.E. 2012. Mechanisms of carbon nanotube-induced toxicity: Focus on oxidative stress. Toxicol. Appl. Pharmacol. 261, 121-133.

Simon, A., Maletz, S.X., Hollert, H., Schäffer, A. and Maes, H.M. 2014. Effects of multiwalled carbon nanotubes and triclocarban on several eukaryotic cell lines: elucidating cytotoxicity, endocrine disruption, and reactive oxygen species generation. Nanoscale Res Lett, p. 396.

Simon, H.U., Haj-Yehia, A. and Levi-Schaffer, F. 2000. Role of reactive oxygen species (ROS) in apoptosis induction. Apoptosis 5, 415-418.

Smith, C.J., Shaw, B.J. and Handy, R.D. 2007. Toxicity of single walled carbon nanotubes to rainbow trout, (Oncorhynchus mykiss): Respiratory toxicity, organ pathologies, and other physiological effects. Aquat. Toxicol. 82, 94-109.

Song, M., Wang, F., Zeng, L., Yin, J., Wang, H. and Jiang, G. 2014. Co-exposure of Carboxyl-Functionalized Single-Walled Carbon Nanotubes and 17α-

Ethinylestradiol in Cultured Cells: Effects on Bioactivity and Cytotoxicity. Environ. Sci. Technol. 48, 13978-13984.

Stiles, P.L., Dieringer, J.A., Shah, N.C. and Van Duyne, R.P. 2008. Surface-Enhanced Raman Spectroscopy. Annu. Rev. Anal. Chem. 1, 601-626.

Su, Y., Yan, X., Pu, Y., Xiao, F., Wang, D. and Yang, M. 2013. Risks of Single-Walled Carbon Nanotubes Acting as Contaminants-Carriers: Potential Release of Phenanthrene in Japanese Medaka (Oryzias latipes). Environ. Sci. Technol. 47, 4704-4710.

Tervonen, K., Waissi, G., Petersen, E.J., Akkanen, J. and Kukkonen, J.V.K. 2010. Analysis of fullerene-C60 and kinetic measurements for its accumulation and depuration in Daphnia magna. Environ. Toxicol. Chem. 29, 1072-1078.

Trevisan, J., Angelov, P.P., Carmichael, P.L., Scott, A.D. and Martin, F.L. 2012. Extracting biological information with computational analysis of Fourier-transform infrared (FTIR) biospectroscopy datasets: current practices to future perspectives. Analyst 137, 3202-3215.

Trevisan, J., Angelov, P.P., Patel, I.I., Najand, G.M., Cheung, K.T., Llabjani, V., Pollock, H.M., Bruce, S.W., Pant, K., Carmichael, P.L., Scott, A.D. and Martin, F.L. 2010. Syrian hamster embryo (SHE) assay (pH 6.7) coupled with infrared spectroscopy and chemometrics towards toxicological assessment. Analyst 135, 3266-3272.

Turrens, J.F. 2003. Mitochondrial formation of reactive oxygen species. J. Physiol. 552, 335-344.

Vippola, M., Falck, G., Lindberg, H., Suhonen, S., Vanhala, E., Norppa, H., Savolainen, K., Tossavainen, A. and Tuomi, T. 2009. Preparation of nanoparticle dispersions for in-vitro toxicity testing. Hum. Exp. Toxicol. 28, 377-385.

Wörle-Knirsch, J.M., Pulskamp, K. and Krug, H.F. 2006. Oops They Did It Again! Carbon Nanotubes Hoax Scientists in Viability Assays. Nano Lett. 6, 1261-1268.

Wang, L., Castranova, V., Mishra, A., Chen, B., Mercer, R.R., Schwegler-Berry, D. and Rojanasakul, Y. 2010. Dispersion of single-walled carbon nanotubes by a natural lung surfactant for pulmonary in vitro and in vivo toxicity studies. Part. Fibre Toxicol. 7, 31.

Wang, L. and Mizaikoff, B. 2008. Application of multivariate data-analysis techniques to biomedical diagnostics based on mid-infrared spectroscopy. Anal. Bioanal. Chem. 391, 1641-1654.

Wang, Y., Becker, M., Wang, L., Liu, J., Scholz, R., Peng, J., Gösele, U., Christiansen, S., Kim, D.H. and Steinhart, M. 2009. Nanostructured Gold Films for SERS by Block Copolymer-Templated Galvanic Displacement Reactions. Nano Lett. 9, 2384-2389.

Warheit, D.B. 2006. What is currently known about the health risks related to carbon nanotube exposures? Carbon 44, 1064-1069.

Warheit, D.B., Sayes, C.M. and Reed, K.L. 2009. Nanoscale and Fine Zinc Oxide Particles: Can in Vitro Assays Accurately Forecast Lung Hazards following Inhalation Exposures? Environ. Sci. Technol. 43, 7939-7945.

Westerhuis, J.A., Kourti, T. and MacGregor, J.F. 1998. Analysis of multiblock and hierarchical PCA and PLS models. J. Chemom. 12, 301-321.

Wohlleben, W., Brill, S., Meier, M.W., Mertler, M., Cox, G., Hirth, S., von Vacano, B., Strauss, V., Treumann, S., Wiench, K., Ma-Hock, L. and Landsiedel, R. 2011. On the Lifecycle of Nanocomposites: Comparing Released Fragments and their In-Vivo Hazards from Three Release Mechanisms and Four Nanocomposites. Small 7, 2384-2395.

Xia, Q., Yin, J.J., Cherng, S.-H., Wamer, W.G., Boudreau, M., Howard, P.C. and Fu, P.P. 2006. UVA photoirradiation of retinyl palmitate—Formation of singlet oxygen and superoxide, and their role in induction of lipid peroxidation. Toxicol. Lett. 163, 30-43.

Yang, K., Zhu, L. and Xing, B. 2006. Adsorption of Polycyclic Aromatic Hydrocarbons by Carbon Nanomaterials. Environ. Sci. Technol. 40, 1855-1861.

Zhang, D. and Ben-Amotz, D. 2002. Removal of Cosmic Spikes from Hyper-spectral Images Using a Hybrid Upper-Bound Spectrum Method. Appl. Spectrosc. 56, 91-98.

Zhang, Y., Chen, Y., Westerhoff, P. and Crittenden, J. 2009. Impact of natural organic matter and divalent cations on the stability of aqueous nanoparticles. Water Res. 43, 4249-4257.

Zhang, Z., Xu, F., Yang, W., Guo, M., Wang, X., Zhang, B. and Tang, J. 2011. A facile one-pot method to high-quality Ag-graphene composite nanosheets for efficient surface-enhanced Raman scattering. Chem. Commun. 47, 6440-6442.

Zhao, J. 2003. Image Curvature Correction and Cosmic Removal for High-Throughput Dispersive Raman Spectroscopy. Appl. Spectrosc. 57, 1368-1375.

Zhao, J., Lui, H., McLean, D.I. and Zeng, H. 2007. Automated Autofluorescence Background Subtraction Algorithm for Biomedical Raman Spectroscopy. Appl. Spectrosc. 61, 1225-1232.

Chapter 2

Dose-related alterations of carbon nanoparticles in mammalian cells detected using biospectroscopy: Potential for real-world effects

Junyi Li, Rebecca Strong, Júlio Trevisan, Simon W. Fogarty, Nigel J. Fullwood, Kevin C. Jones, and Francis L. Martin

Environmental science & technology, 2013, 47, 10005-10011.

Contribution:

- I acquired the samples required for the project ;
- I prepared processed and acquired all the data and carried out computational analysis;
- I prepared the first draft of the manuscript.

…… ……

Junyi Li Prof. Francis L. Martin

Environmental Science & Technology

Article

pubs.acs.org/est

Dose-Related Alterations of Carbon Nanoparticles in Mammalian Cells Detected Using Biospectroscopy: Potential for Real-World Effects

Junyi Li,[†] Rebecca Strong,[†] Júlio Trevisan,[†] Simon W. Fogarty,[†,‡] Nigel J. Fullwood,[‡] Kevin C. Jones,[†] and Francis L. Martin[†,*]

[†]Centre for Biophotonics, Lancaster Environment Centre, Lancaster University, Lancaster LA1 4YQ, United Kingdom

[‡]Divison of Biomedical and Life Sciences, Faculty of Health and Medicine, Lancaster University, Lancaster LA1 4YQ, United Kingdom

Supporting Information

ABSTRACT: Nanotechnologies generate a wide range of engineered nanomaterials that enter into our ecosystem, especially carbon-based nanoparticles (CNPs). As these novel materials acquire ever increasing numbers of applications, they may pose a risk to organisms, including humans. However, our knowledge of nanoparticle-induced effects remains limited. We are yet to understand the interaction between nanoparticles and organisms, and classical toxicology fails to provide models for risk assessment. Biospectroscopy techniques were employed to identify the effects induced by real-world levels of a panel of CNPs. MCF-7 cells concentrated in S-phase or G_0/G_1-phase were treated for 24 h with short or long multiwalled carbon nanotubes (MWCNTs) or Fullerene (C60) at the following concentrations: 0.0025 mg/L, 0.005 mg/L, 0.01 mg/L, 0.025 mg/L, 0.05 mg/L, and 0.1 mg/L. Attenuated total reflection Fourier-transform infrared (ATR-FTIR) spectroscopy coupled with computational analysis was then applied to interrogate the cells and significant dose-related effects were detected. From derived infrared spectra, distinct spectral biomarkers of cell alteration induced by each CNP type were identified. Additionally, Raman spectroscopy was applied and allowed us to determine that reactive oxygen species (ROS) were generated by CNPs. These observations highlight the potential of biospectroscopy techniques to determine CNP-induced alterations in target mammalian cells at ppb levels.

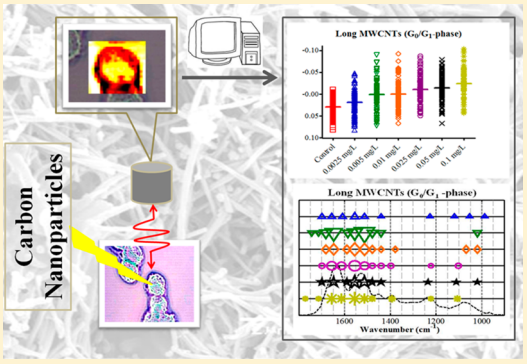

1. INTRODUCTION

Nanomaterials are engineered materials designed to nanoscale size with at least one dimension in the 1−100 nm range. This tiny size gives nanomaterials unique physicochemical properties, resulting in diverse applications in areas such as pharmaceutics and even daily consumable products.[1,2] While the properties of bulk materials and chemical molecules have been well understood, there remains a gap in knowledge in the nanozone between molecule and bulk. Therefore, there is growing concern as to whether these novel materials will pose potential risk in organisms, including humans.[3]

Among the most promising engineered materials, carbon nanotubes (CNTs) and Fullerene (C60) represent two of the most widely investigated carbon nanoparticles (CNPs). Generally, multiwalled carbon nanotubes (MWCNTs) consisting of two or more cylinders of graphite sheets are uniquely small with a high aspect ratio consisting of a diameter at nanometre scale and μm length.[4] C60, with a spherically enclosed structure of 60 carbon atoms, is the most prominent fullerene derivative in general use or under scientific investigation.[5] As it has been predicted that these CNPs will have enormous use, there is no doubt the risk of exposure will increase dramatically for humans and the whole environment.[6] Therefore, assessment of the toxic effects of CNPs is urgently required.

Recently, a range of studies have shown that CNPs generate toxic effects both in vitro and in vivo, such as cell membrane disruption, tissue inflammation, and lung lesions.[7−9] Among the mechanisms involved in CNP toxicology, generation of reactive oxygen species (ROS) is regarded as a major factor.[10] ROS can have a direct impact on the cells or lead to secondary processes causing protein alteration, membrane injury, and even DNA damage.[11] However, some conventional in vitro cytotoxicity assays encounter challenges in investigating nanotoxicology due to the interaction between nanoparticles and the assay itself. Classical dye-based assays such as MTT and neutral red can give invalid results if the dye is adsorbed by or interacts with CNPs.[12] Therefore, the introduction of new methodologies to assess nanotoxicity is required, in addition to the establishment

Received: April 23, 2013
Revised: August 2, 2013
Accepted: August 5, 2013
Published: August 5, 2013

of a new paradigm in conventional assays. In toxicology, dose is an important parameter for both in vitro and in vivo experiments. Although acute effects are likely to be observed following high-dose exposures, understanding the consequences of low-dose exposure over a lifetime is necessary to help understand the possible public health risk of CNPs.

As a powerful noninvasive technique, attenuated total reflection Fourier-transform infrared (ATR-FTIR) spectroscopy can be used to detect alterations induced by chemical agents at environmentally relevant levels within cells.[13,14] An infrared (IR) beam is transmitted through an internal reflection element (IRE; e.g., diamond, zinc selenide, germanium, silicon) in contact with the sample and penetrates a small distance beyond the reflecting surface into the sample.[15] The mid-IR (λ = 2−20 μm) absorbance of cellular biomolecules via vibrational transitions generates biochemical-cell fingerprint spectra (1800−900 cm^{-1}). In particular, peaks are identified as lipid [1750 cm^{-1} (C═O vibration)], Amide I (1650 cm^{-1}), Amide II (1550 cm^{-1}), Amide III (1260 cm^{-1}), and DNA/RNA [1225 cm^{-1} ($\nu_{as}PO_2^-$; asymmetric phosphate stretching vibrations), 1080 cm^{-1} ($\nu_sPO_2^-$; symmetric phosphate stretching vibrations)]. Raman spectroscopy is another noninvasive tool with the ability to detect a wide range of chemical bonds, not only polar bonds. On the basis of a different working theory, Raman can be used as a complement to ATRFTIR spectroscopy. Analyzing the large amount of data derived from IR or Raman spectroscopy is a challenge by conventional methods, but with the help of computational analyses using multivariate techniques including principal component analysis-linear discriminant analysis (PCA-LDA), information can efficiently be extracted from the data.

In this study, we employed ATR-FTIR spectroscopy coupled with computational analysis to investigate dose-related effects of CNPs in mammalian MCF-7 cells. This is an estrogen receptor-positive breast cancer cell line, which has previously been used to investigate toxic effects of either endocrine disruptors or chemicals requiring bioactivation (an excellent characteristic in this regard is that they express phase I and II enzymes).[13] Through this work, we intended to detect alterations in MCF-7 cells following exposure to short or long MWCNTs and Fullerene C60 at concentrations of 0.0025, 0.005, 0.01, 0.025, 0.05, and 0.1 mg/L. The differences in the toxic effects induced by the three CNPs types were also investigated. Additionally, Raman spectroscopy was used to detect the ratio of cysteine-to-protein in order to evaluate reactive oxygen species (ROS) levels in treated cells. Such studies were designed in order to shed insights into CNP-induced toxic mechanisms at environmentally relevant exposure levels.

2. MATERIALS AND METHODS

Chemicals and Nanoparticles. Cell culture consumables were obtained from Invitrogen Life Technologies (Paisley, U.K.). Bovine serum albumin (BSA) obtained from Sigma was ≥98% pure. All CNPs were purchased from Sigma; data regarding their toxicity remains limited, but they are thought to possess asbestos-like properties. Both short and long MWCNTs were >90% pure, while C60 had purity >99.5%. As stated by the company, short MWCNTs were >90% pure with a size of 10−15 nm in diameter and 0.1−10 μm in length. Long MWCNTs were >90% pure as well, but with a larger size, 110−170 nm diameter and 5−9 μm length. C60 had a purity >99.5% and particle diameter of 1 nm. All dispersed CNPs were characterized using scanning electron microscopy (SEM) [JSM 5600 (JEOL)] and images were taken (Figure 1). The two

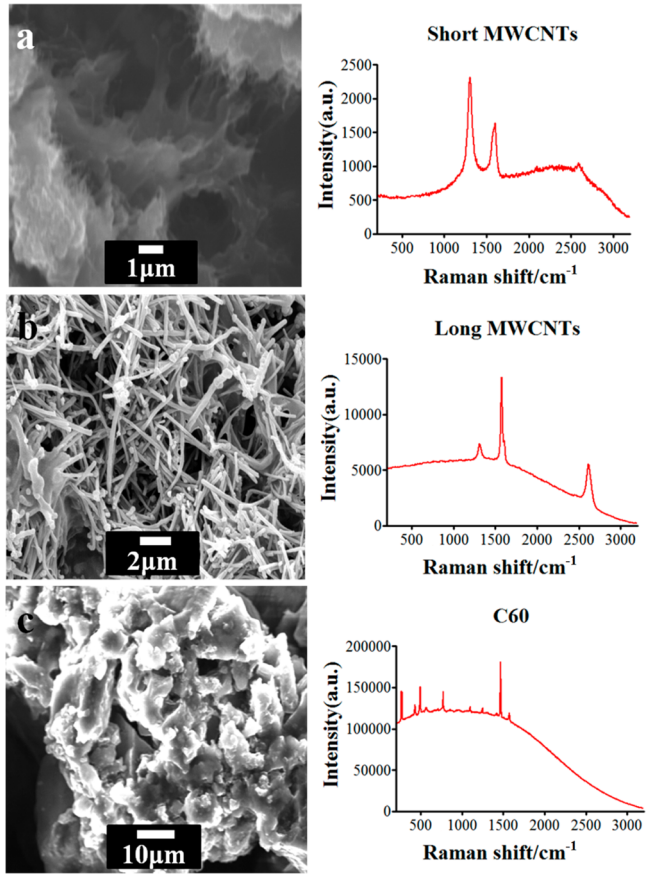

Figure 1. Scanning electron microscopy (SEM) images with corresponding Raman spectra of (a) short MWCNTs; (b) long MWCNTs; and (c) Fullerene (C60).

MWCNTs showed sizes approximating that stated by the company, while C60 appeared almost in agglomeration. Additionally, the CNPs were analyzed by Raman spectroscopy (Renishaw PLC, Gloucestershire, U.K.) with a 785 nm laser, which confirmed their high purity (Figure 1).

Cell Culture. The MCF-7 cell line was grown in Dulbecco's modified essential medium supplemented with 10% heat-inactivated fetal bovine serum (FBS), penicillin (100 U/mL), and streptomycin (100 μg/mL) in a humidified atmosphere with 5% CO_2 in air at 37 °C. MCF-7 cells were routinely cultured in T75 flasks and disaggregated with trypsin (0.05%)/EDTA (0.02%) solution before incorporation into experiments. Following this, cells were immediately resuspended in complete medium and then seeded in T25 flasks, whereupon they were concentrated in either S-phase (grown for 24-h) or G_0/G_1-phase (grown for 96-h) followed by a further-24-h treatment with or without test agents. For each testing protocol, three independent experiments were conducted with either duplicate or triplicate flasks per treatment condition [see Supporting Information (SI)].

CNPs Treatment and ATR-FTIR Spectroscopy. CNPs were suspended in 1% BSA solution in order to assist in suspension and dispersion during treatment, contributing to maximum contact of cells and CNPs. All concentration ranges were diluted with 1% BSA solution from a concentrated stock,

and 50 μL CNPs were delivered to cells in each flask with 5 mL medium. The flasks were gently shaken to make sure the CNPs were well dispersed before being put back in the incubator. Meanwhile, several flasks of cells were exposed to 1% BSA alone as a vehicle control. Following 24-h treatment, cells were again disaggregated into cell suspension and immediately fixed in 70% ethanol for 1 h. Cell samples were then washed three times and applied to glass slides, and allowed to air-dry prior to storage in a desiccator. Cell samples were interrogated using a Bruker TENSOR 27 FTIR spectrometer (Bruker Optics Ltd., Coventry, U.K.) with Helios ATR attachment (containing a diamond IRE; incidence angle of the IR beam: 45°). Instrument settings included 32 scans, 8 cm^{-1} resolution, 2× zero-filling. For each slide, 10 IR spectra were acquired, giving rise to eight data sets (see SI, Table S1). The ATR crystal was cleaned with deionized water and a background was taken prior to starting a new slide. Estimated penetration depth of the IR beam into the sample was calculated at 1.11 and 2.23 μm at 1800 cm^{-1} and 900 cm^{-1}, respectively.[16]

ATR-FTIR spectroscopy gave rise to eight data sets, which were computationally analyzed separately (see SI, Table S1). Data sets DR-1 to DR-6 were generated to study the dose response of nanoparticles, whereas NP-1 and NP-2 allowed for a comparison between the effects of different nanoparticles (see SI, Table S1). Each resulting spectrum had a total of 235 data points within the 1800−900 cm^{-1} region for a 3.84 cm^{-1} spacing.

Data Preprocessing and PCA-LDA. The acquired IR spectral data were processed using the IRootLab toolbox (http://irootlab.googlecode.com)[17] running on MATLAB r2008a (http://www.mathworks.com). Each spectrum was preprocessed by first cutting to the biochemical-cell fingerprint range (1800−900 cm^{-1}), followed by rubberband baseline correction, and normalization to the Amide I peak (around 1650 cm^{-1}). Following preprocessing, cross-calculated PCA-LDA[18] was applied to each data set separately, and the resulting scores and cluster vectors were visualized. PCA-LDA is a composite technique where principal component analysis (PCA) is applied to the spectral data set to reduce the number of variables, and linear discriminant analysis (LDA) is subsequently applied to derive orthogonal variables from which the between-class variance is maximized over the within-class variance.[19] "Cross-calculation" of scores is applied to eliminate the risk of LDA overfitting. It utilizes leave-one-out cross-validation to train the PCA-LDA loadings using $n - 1$ samples (n = number of samples in data set) and subsequently calculate the scores for the remaining sample,[18] repeating until all scores are calculated. The loadings are derived as averages between the n PCA-LDA loadings models. Cluster vectors are derived through pointing from the mean of the control class toward the mean of each treatment class, thus obtaining one vector representing biochemical alterations ("pseudospectrum" wavenumber × coefficient) for each class (excluding Control).[20,21] The number of principal components (PCs) for PCA-LDA was found for each data set separately through an optimization procedure using classification (see SI, Figure S1 and Table S2).

PCA-LDA output data (variables called "PCA-LDA scores") can be visualized as 1-D or 2-D scatterplots ("scores plots"). In these scores plots, nearness between the treatment class and the control class indicates similarity in biochemical structure, while the distance indicates dissimilarity. This allows for a dose−response curve to be derived based on the distance between each treatment mean and the control mean in the scores plot. Interpolation was carried out using cubic splines in Graphpad Prism 4. ANOVA and post hoc tests on PCA-LDA scores were carried out, as well in the same software.

The cluster vectors are derived to study the biomarkers responsible for the biochemical alteration in each class.[22,23] In order to simplify the identification of the alterations induced by chemical agents, the six most important peaks of each cluster vector were detected to derive a "peak locations" plot where the marker size is proportional to the height of its corresponding peak.

Use of Raman Spectra to Assess ROS Level in Cells Induced by CNPs. Raman spectra were recorded using an *In Via* Renishaw Raman spectrometer (Renishaw plc, Gloucestershire, U.K.) equipped with a 785 nm streamline focus laser and a Renishaw-automated 100 nm encoded XYZ stage. The spectrometer's entrance slit of 50 μm combined with a 1200 lines/mm (~1.0 cm^{-1} spectral resolution) diffraction grating dispersing Raman signals onto a master Renishaw Pelletier cooled charge coupled detector (CCD). A white light camera mounted on the microscope was used to visualize the locations of the spectral acquisition. System calibration was carried out using an internal Renishaw silicon calibration source for wavenumber shift. All spectra were acquired using a Leica ×50 objective lens (numeral aperture 0.75), 10 s of 50% laser power (100 mW) exposure with three repeat acquisitions and spectral range covering 2000−500 cm^{-1}. Generally, 30 spectra were obtained from each sample.

Cysteine (Cys) can protect cells from oxidative stress and free radical with its sulfhydryl (-SH) group of high electron-donating capacity.[24] Cysteine and its oxidized form disulfide cystine (CySS) constitute the major redox pools playing an important role in cytoprotection.[25,26] Cys/CySS couple is usually regulated at a homeostatic state in cells, and can be used to indicate the oxidative stress.[27] In this study, raw Raman spectra resulting from the MCF-7 cells treated with or without CNPs were used to calculate the ratio of CySS to protein as a biomarker for ROS level in cells. The intensity at two particular peaks was used to measure the CySS-to-protein ratio. The intensity at 668 cm^{-1} (C−S stretching mode of CySS) was used as a marker for CySS, while that at 1447 cm^{-1} (CH_2 bending mode of protein) was used as a marker for protein.

RESULTS AND DISCUSSION

Throughout the biochemical-cell fingerprint region (1800−900 cm^{-1}) in the raw IR spectra, no differences can be simply observed. However, the use of multivariate computational analysis applied to the large number of the spectra generated allows differences to be more clearly viewed. PCA-LDA scores plots help one visualize the segregation between classes. To avoid overfitting with LDA, we applied a "cross-calculated" version of PCA-LDA (CC PCA-LDA) in this study. Cross-calculated results are nonetheless consistent with direct PCA-LDA results (see SI, Figure S2). Most class separation was seen along LD1, whereas separation was negligible along LD2 for most data sets (see SI, Figures S1). In both methods, clearer category segregation was noted with CNP-treated cells concentrated in G_0/G_1-phase cells compared to those in S-phase [see SI, Figure S2]. To determine whether the treatment groups were significantly different from the corresponding control group, repeated-measures one-way analysis of variance (ANOVA) with Dunnett's post hoc tests were conducted to examine the treated *vs.* control cells in both LD1 and LD2

space (see SI, Figure S2). According to the *P*-value calculated, the CNP-induced effects observed in LD1 space differed significantly ($P < 0.01$) in all treatment groups (Figure 2).

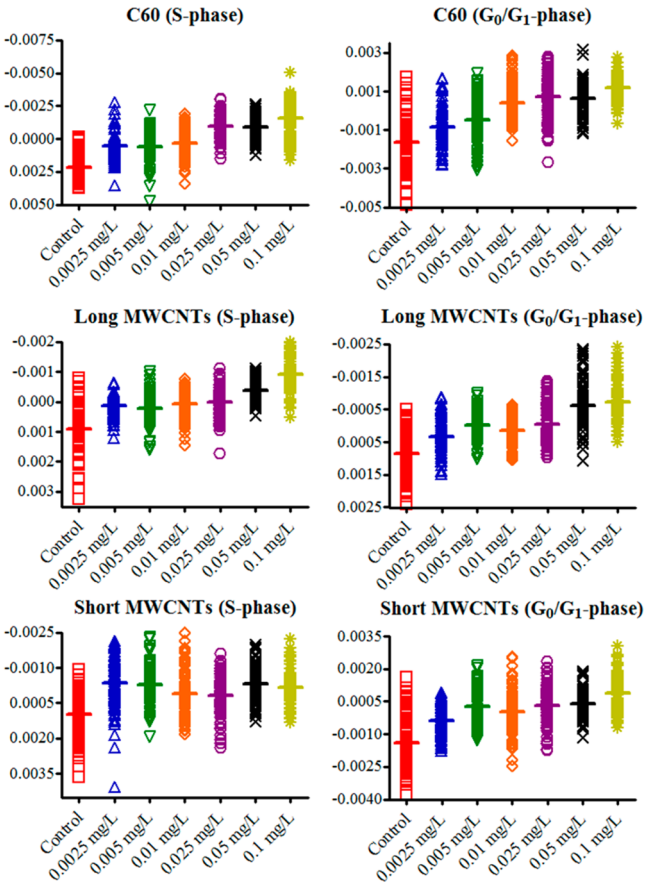

Figure 2. One-dimensional cross-calculated PCA-LDA scores plot in 1st space of infrared (IR) spectra derived from MCF-7 cells (S-phase or G_0/G_1-phase) treated with carbon nanoparticles (CNPs) and concentration compared to the vehicle control. The horizontal line in the center of each plot represents the mean value.

The scores plot in LD1 space clearly shows segregation between each treatment and corresponding control (Figure 2). When MCF-7 cells were treated with CNPs, their response was nonlinear and varied with concentration. The dose−response shows that the response of cells in S-phase was more variable than those concentrated in G_0/G_1-phase. The highest response induced by the three CNPs in cells concentrated in G_0/G_1-phase appeared at the highest concentration treatment, while in the S-phase cells exposed to short MWCNTs the response peak was located at lower concentrations of 0.0025 mg/L. This could be explained as low-dose stimulation and high-dose inhibition of response.[28] These clear low-dose effects observed with exposure to short MWCNTs could be a major concern in hazard assessment.[29]

Figure 3 shows the cluster vectors peaks for the dose−response data sets. Exposure of MCF-7 cells concentrated in S-phase to the three CNPs types suggested that each CNP type shared a similar mode of action, with the induced effects mainly on proteins [Amide I (~1650 cm^{-1}), Amide II (~1550 cm^{-1})], lipid (1705−1750 cm^{-1}), and DNA (~1225 cm^{-1}, ~1080 cm^{-1}). In G_0/G_1-phase cells, similar alterations appeared associated with protein and lipid regions for different CNP

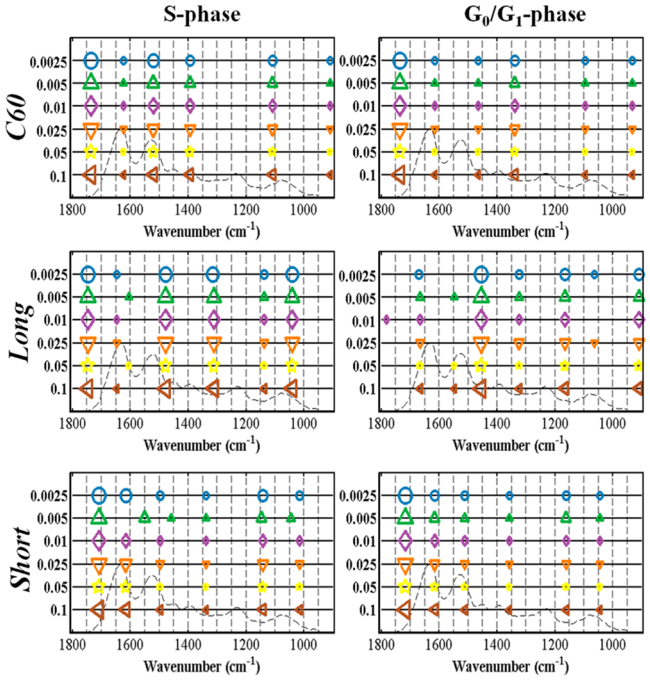

Figure 3. Cluster vectors peaks plot indicating the wavenumber basis for segregation following treatment of MCF-7 cells with CNPs. Each treatment was compared to the control. The size of the symbol in the cluster vector peaks plot is proportional to the height of the corresponding peaks, which are relative to the extent of biochemical alteration compared to the vehicle control. The hint line represents a typical infrared (IR) spectrum of the biochemical-fingerprint region (1800−900 cm^{-1}).

types. However, C60 treatment resulted in a high-level of alterations in the DNA/RNA spectral region in cells in either phase; these effects following exposure to short or long MWCNTs were markedly lower, even to a negligible level compared with those induced by C60.

In order to determine the difference in the toxic effects induced by the three CNPs, another experiment was conducted to test the CNPs on MCF-7 cells (concentrated in S- or G_0/G_1-phase) at a concentration of 0.1 mg/L. Clear segregation was observed in both 1-D and 2-D scores plots, and G_0/G_1-phase cells displayed a clearer segregation between the control and treatment groups (Figure 4a). ANOVA with Newman-Keuls' post hoc test was applied to examine the significance between all pairs of groups in both spaces (see SI, Figure S6). Scores plots in LD1 space showed that the treatment-induced cell alterations ranked as C60 > long MWCNTs > short MWCNTs in both S-phase and G-phase cells (Figure 4b; see SI, Figure S8a). This is contrary to the cytotoxicity test of carbon nanomaterials in alveolar macrophages, which suggested that the effects of MWCNTs are more distinct than those of C60;[30] however, the dose applied was much higher than that employed in our study, which might make a big difference. The cluster vectors plots derived from both CC PCA-LDA and PCA-LDA showed that in both cell cycles all CNPs induced biochemical alterations in MCF-7 cells in the protein region (1690−1400 cm^{-1}) and lipid region (1750−1700 cm^{-1}), while DNA/RNA changes were also evident in the spectral profile (Figure 5; see SI, Figures S7 and S8).

In S-phase cells, exposure to C60 induced specific alterations in protein [~1400 cm^{-1}; e.g., $-COO^-$ (carboxylate)], Amide I (~1650 cm^{-1}), Amide III (~1280 cm^{-1}), and DNA/RNA

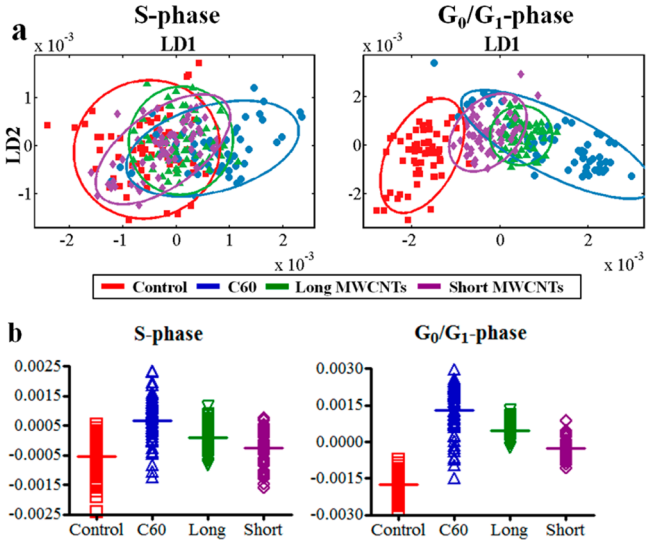

Figure 4. Cross-calculated PCA-LDA scores plots derived from MCF-7 cells (S-phase or G_0/G_1-phase) treated with carbon nanoparticles (CNPs) at concentration of 0.1 mg/L. (a) Scores plots in two dimensions (90% confidence ellipsoids); and (b) Scores plot in 1st space.

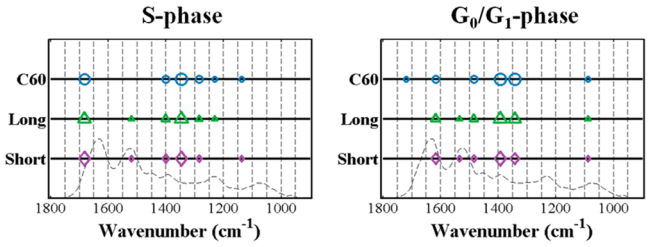

Figure 5. Cross-calculated PCA-LDA cluster vectors peaks plot indicating the wavenumber basis for segregation following treatment of MCF-7 cells with CNPs at concentration of 0.1 mg/L. Each treatment was compared to the control. The size of the symbol in cluster vector peaks plot is proportional to the height of the corresponding peaks, which is relative to the extent of biochemical alteration compared to the vehicle control. The hint line represents a typical infrared (IR) spectrum of the biochemical-fingerprint region (1800–900 cm^{-1}).

(~1225 cm^{-1}; $\nu_{as}PO_2^-$), in ranked order of peak height (Figure 5). According to the cluster vectors peak plot, both long and short MWCNTs induced a similar level of alterations in S-phase cells. The long MWCNTs resulted in specific alterations in protein (~1400 cm^{-1}, $-COO^-$ stretching of amino acids), Amide I (~1650 cm^{-1}), Amide III (~1280 cm^{-1}), DNA/RNA (~1225 cm^{-1}; $\nu_{as}PO_2^-$), and Amide II (~1550 cm^{-1}), while less distinct alterations were induced by short MWCNTs; these latter were associated with Amide I (~1650 cm^{-1}), protein (~1400 cm^{-1}), Amide III (~1280 cm^{-1}), C–O stretch (~1138 cm^{-1}), and Amide II (~1550 cm^{-1}).

In G_0/G_1-phase cells, the main spectral biomarkers altered by C60 included protein (~1400 cm^{-1}), Amide I (~1650 cm^{-1}), lipid (~1720 cm^{-1}), and DNA/RNA (~1080 cm^{-1}; $\nu_sPO_2^-$) (Figure 5). Alterations induced by long or short MWCNTs appeared similar to share the same profile, resulting in alterations in protein (~1400 cm^{-1}), Amide I (~1650 cm^{-1}), DNA/RNA (~1080 cm^{-1}; $\nu_sPO_2^-$) and Amide II (~1550 cm^{-1}). It was observed that short MWCNTs invoked much lower alterations than the other two CNP types tested.

To investigate whether ROS contributed to the toxic effects of different CNPs in MCF-7 cells, Raman spectroscopy was applied to the treated cell samples and CySS-to-protein ratio was calculated from derived spectra. An elevated CySS-to-protein ratio was observed in cells following exposure to CNPs (Figure 6). An ANOVA with Newman-Keuls' post hoc tests

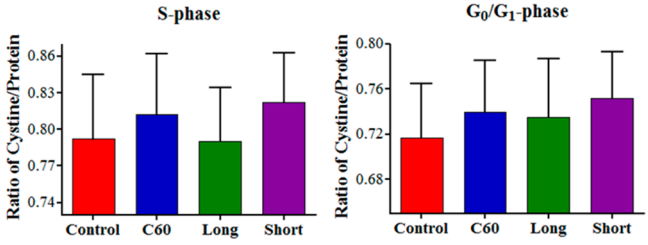

Figure 6. Ratio of CySS (cystine; 668 cm^{-1}) to protein (1447 cm^{-1}) derived from Raman spectra, *mean ± standard deviation.*

was conducted to compare all pairs of the CySS-to-protein ratios of treated groups; significance was observed (see SI, Figure S9). As the elevation of CySS-to-protein ratio is proportional to ROS levels generated in cells, it can be used as a biomarker for this effect. Surprisingly, in both S-phase and G_0/G_1-phase cells, short MWCNTs induced the most pronounced ROS generation, while the IR spectral profiles showed that in G_0/G_1-phase cells short MWCNTs induced much less pronounced effects than the other two CNPs. This may suggest that short MWCNTs exert toxic effects mainly through ROS generation, while effects of long MWCNTs may be induced through other mechanical mechanisms, such as direct contact and damage.

IR spectral profiles indicate that cell components were broadly affected by CNPs, including alterations in protein, lipid, and DNA/RNA. Protein and lipid alterations were highlighted as the most pronounced effects induced by CNPs in MCF-7 cells, which is suggestive that outer cell components are primary cellular targets.[31] Our findings showed that compared with the short or long MWCNTs, C60 was more likely to alter the DNA/RNA region. Even in G_0/G_1-phase cells, which appear to be less susceptible to DNA damage compared with S-phase cells,[32] DNA/RNA alterations following exposure to C60 occurred at a high level. The mechanism of DNA damage here is still not fully understood; it could possibly be as a consequence of the spherical shape and size of C60 nanoparticles. Given its spherical shape coupled with nano-scaled size, C60 may be able to penetrate deeper into areas within cells and exert effects indirectly via ROS generation or other direct pathways. The direct interaction between C60 and DNA/RNA may be an important factor accounting for its propensity to induce DNA/RNA alterations; it has been reported that C60 could be statically hybridized with DNA/RNA and induce structural changes in DNA/RNA,[33] and also that it could interfere with DNA replication leading to DNA damage and even mutation.[34] By contrast the two carbon nanotubes, possessing a much larger size with a long tube shape, have a more limited ability to alter the DNA/RNA region, especially in G_0/G_1-phase cells. Generally, from derived spectral data sets the most pronounced CNP-induced cellular alterations were associated with outer cellular components; this was especially so in cells concentrated in G_0/G_1-phase compared with those concentrated in S-phase. Interestingly, in both S-phase and G_0/G_1-phase cells, the effects of exposure

to short MWCNTs appeared to be much lower than that of long MWCNTs. This is consistent with a study conducted in a THP-1 cell line, which showed that longer CNTs induced a stronger inflammatory response in target cells than shorter ones.[35] It is possible that this may be due to the CNP's morphology. As shown in the SEM images (Figure 1), long MWCNTs with a longer and thicker structure exhibit minimal agglomeration, while short MWCNTs are observed to be more likely to intertwine and agglomerate. Elevated agglomeration could dramatically decrease surface ratio, which plays an important role in the toxic effects of nanoparticles. In G_0/G_1-phase, after 96-h growth, this cell population reached confluence, which may enhance the opportunity of contact between cells and nanoparticles but as well decrease the proportion of nanoparticle quantity to cell number. This could increase the contact between cells and long MWCNTs leading to direct damage in cells, but a higher cell density might dilute the effects of ROS generated from short MWCNTs. Additionally, previous research showed that cells concentrated in G_0/G_1-phase exhibit higher antioxidant enzyme activities compared with those in S-phase,[36] which indicates that cells in G_0/G_1-phase are more likely to protect intracellular components from ROS invasion. However, a high level of protein alterations observed in CNP-exposed G_0/G_1-phase cells still verified their ability to generate ROS.

This study applied biospectroscopy in the investigation of nanotoxicology to detect dose-related effects induced by three CNPs in MCF-7 cells. It was determined that this approach is a novel and powerful tool, capable of identifying the biochemical alterations in cells resulting from exposure to CNPs.[31] Further study could be conducted to reveal more information underlying these alterations. These could include a cytokinesis-block micronucleus assay to assess genotoxicity of CNPs in cells. Additional experiments using biospectroscopy could examine nanoparticle-induced effects in sentinel organisms.

■ ASSOCIATED CONTENT

Supporting Information

Experimental setup for testing of CNPs, optimization of PC number toward classification, and cysteine-to-protein ratio. This material is available free of charge via the Internet at http://pubs.acs.org.

■ AUTHOR INFORMATION

Corresponding Author

*Phone: +44 (0)1524 510206; fax: +44 (0)1524 510217e-mail: f.martin@lancaster.ac.uk.

Notes

The authors declare no competing financial interest.

■ ACKNOWLEDGMENTS

We would like to thank Matthew Riding for assistance in setting up experiments.

■ REFERENCES

(1) Bianco, A.; Kostarelos, K.; Prato, M. Applications of carbon nanotubes in drug delivery. *Curr. Opin. Chem. Biol.* **2005**, *9* (6), 674–679.

(2) Becheri, A.; Dürr, M.; Lo Nostro, P.; Baglioni, P. Synthesis and characterization of zinc oxide nanoparticles: application to textiles as UV-absorbers. *J. Nanopart. Res.* **2008**, *10* (4), 679–689.

(3) Lam, C. W.; James, J. T.; McCluskey, R.; Arepalli, S.; Hunter, R. L. A review of carbon nanotube toxicity and assessment of potential occupational and environmental health risks. *Crit. Rev. Toxicol.* **2006**, *36* (3), 189–217.

(4) Iijima, S. Helical microtubules of graphitic carbon. *Nature* **1991**, *354* (6348), 56–58.

(5) Bakry, R.; Vallant, R. M.; Najam-ul-Haq, M.; Rainer, M.; Szabo, Z.; Huck, C. W.; Bonn, G. K. Medicinal applications of fullerenes. *Int. J. Nanomed.* **2007**, *2* (4), 639–649.

(6) Maynard, A. D.; Baron, P. A.; Foley, M.; Shvedova, A. A.; Kisin, E. R.; Castranova, V. Exposure to carbon nanotube material: Aerosol release during the handling of unrefined single-walled carbon nanotube material. *J. Toxicol. Environ. Health A* **2004**, *67* (1), 87–107.

(7) Hirano, S.; Kanno, S.; Furuyama, A. Multi-walled carbon nanotubes injure the plasma membrane of macrophages. *Toxicol. Appl. Pharmacol.* **2008**, *232* (2), 244–251.

(8) Liu, A.; Sun, K.; Yang, J.; Zhao, D. Toxicological effects of multi-wall carbon nanotubes in rats. *J. Nanoparticle Res.* **2008**, *10* (8), 1303–1307.

(9) Muller, J.; Huaux, F.; Moreau, N.; Misson, P.; Heilier, J.-F.; Delos, M.; Arras, M.; Fonseca, A.; Nagy, J. B.; Lison, D. Respiratory toxicity of multi-wall carbon nanotubes. *Toxicol. Appl. Pharmacol.* **2005**, *207* (3), 221–231.

(10) Nel, A.; Xia, T.; Mädler, L.; Li, N. Toxic potential of materials at the nanolevel. *Science* **2006**, *311* (5761), 622–627.

(11) Elsaesser, A.; Howard, C. V. Toxicology of nanoparticles. *Adv. Drug Delivery Rev.* **2012**, *64* (2), 129–137.

(12) Monteiro-Riviere, N. A.; Inman, A. O.; Zhang, L. W. Limitations and relative utility of screening assays to assess engineered nanoparticle toxicity in a human cell line. *Toxicol. Appl. Pharmacol.* **2009**, *234* (2), 222–235.

(13) Llabjani, V.; Jones, K. C.; Thomas, G. O.; Walker, L. A.; Shore, R. F.; Martin, F. L. Polybrominated diphenyl ether-associated alterations in cell biochemistry as determined by attenuated total reflection Fourier-transform infrared spectroscopy: A comparison with DNA-reactive and/or endocrine-disrupting agents. *Environ. Sci. Technol.* **2009**, *43* (9), 3356–3364.

(14) Llabjani, V.; Crosse, J. D.; Ahmadzai, A. A.; Patel, I. I.; Pang, W.; Trevisan, J.; Jones, K. C.; Shore, R. F.; Martin, F. L. Differential effects in mammalian cells induced by chemical mixtures in environmental biota as profiled using infrared spectroscopy. *Environ. Sci. Technol.* **2011**, *45* (24), 10706–10712.

(15) Walsh, M. J.; German, M. J.; Singh, M.; Pollock, H. M.; Hammiche, A.; Kyrgiou, M.; Stringfellow, H. F.; Paraskevaidis, E.; Martin-Hirsch, P. L.; Martin, F. L. IR microspectroscopy: Potential applications in cervical cancer screening. *Cancer Lett.* **2007**, *246* (1), 1–11.

(16) Trevisan, J.; Angelov, P. P.; Patel, I. I.; Najand, G. M.; Cheung, K. T.; Llabjani, V.; Pollock, H. M.; Bruce, S. W.; Pant, K.; Carmichael, P. L. Syrian hamster embryo (SHE) assay (pH 6.7) coupled with infrared spectroscopy and chemometrics towards toxicological assessment. *Analyst* **2010**, *135* (12), 3266–3272.

(17) Trevisan, J.; Angelov, P. P.; Scott, A. D.; Carmichael, P. L.; Martin, F. L. IRootLab: A free and open-source MATLAB toolbox for vibrational biospectroscopy data analysis. *Bioinformatics* **2013**, *29* (8), 1095–1097.

(18) Riding, M. J.; Trevisan, J.; Hirschmugl, C. J.; Jones, K. C.; Semple, K. T.; Martin, F. L. Mechanistic insights into nanotoxicity determined by synchrotron radiation-based Fourier-transform infrared imaging and multivariate analysis. *Environ. Int.* **2012**, *50*, 56–65.

(19) Duda, R. O.; Hart, P. E.; Stork, D. G. *Pattern Classification*; John Wiley & Sons: New York, 2012.

(20) Martin, F. L.; Kelly, J. G.; Llabjani, V.; Martin-Hirsch, P. L.; Patel, I. I.; Trevisan, J.; Fullwood, N. J.; Walsh, M. J. Distinguishing cell types or populations based on the computational analysis of their infrared spectra. *Nat. Protoc.* **2010**, *5* (11), 1748–1760.

(21) Martin, F. L.; German, M. J.; Wit, E.; Fearn, T.; Ragavan, N.; Pollock, H. M. Identifying variables responsible for clustering in discriminant analysis of data from infrared microspectroscopy of a biological sample. *J. Computat. Biol.* **2007**, *14* (9), 1176–1184.

(22) Kelly, J. G.; Trevisan, J.; Scott, A. D.; Carmichael, P. L.; Pollock, H. M.; Martin-Hirsch, P. L.; Martin, F. L. Biospectroscopy to metabolically profile biomolecular structure: a multistage approach linking computational analysis with biomarkers. *J. Proteome Res.* **2011**, *10* (4), 1437−1448.
(23) Llabjani, V.; Trevisan, J.; Jones, K. C.; Shore, R. F.; Martin, F. L. Binary mixture effects by PBDE congeners (47, 153, 183, or 209) and PCB congeners (126 or 153) in MCF-7 cells: biochemical alterations assessed by IR spectroscopy and multivariate analysis. *Environ. Sci. Technol.* **2010**, *44* (10), 3992−3998.
(24) Go, Y. M.; Jones, D. P. Redox compartmentalization in eukaryotic cells. *Biochim. Biophys. Acta* **2008**, *1780* (11), 1273−1290.
(25) Circu, M. L.; Aw, T. Y. Reactive oxygen species, cellular redox systems, and apoptosis. *Free Radic. Biol. Med.* **2010**, *48* (6), 749−762.
(26) Go, Y.-M.; Park, H.; Koval, M.; Orr, M.; Reed, M.; Liang, Y.; Smith, D.; Pohl, J.; Jones, D. P. A key role for mitochondria in endothelial signaling by plasma cysteine/cystine redox potential. *Free Radic. Biol. Med.* **2010**, *48* (2), 275−283.
(27) Benton, S. M.; Liang, Z.; Hao, L.; Liang, Y.; Hebbar, G.; Jones, D. P.; Coopersmith, C. M.; Ziegler, T. R. Differential regulation of tissue thiol-disulfide redox status in a murine model of peritonitis. *J. Inflamm.* **2012**, *9* (1), 36.
(28) Calabrese, E. J.; Baldwin, L. A. A general classification of U-shaped dose-response relationships in toxicology and their mechanistic foundations. *Hum. Exp. Toxicol* **1998**, *17* (7), 353−364.
(29) Calabrese, E. J.; Baldwin, L. A. Hormesis: U-shaped dose responses and their centrality in toxicology. *Trends Pharmacol. Sci.* **2001**, *22* (6), 285−291.
(30) Jia, G.; Wang, H.; Yan, L.; Wang, X.; Pei, R.; Yan, T.; Zhao, Y.; Guo, X. Cytotoxicity of carbon nanomaterials: Single-wall nanotube, multi-wall nanotube, and fullerene. *Environ. Sci. Technol.* **2005**, *39* (5), 1378−1383.
(31) Riding, M. J.; Martin, F. L.; Trevisan, J.; Llabjani, V.; Patel, I. I.; Jones, K. C.; Semple, K. T. Concentration-dependent effects of carbon nanoparticles in gram-negative bacteria determined by infrared spectroscopy with multivariate analysis. *Environ. Pollut.* **2012**, *163*, 226−234.
(32) Jiao, H.; Allinson, S. L.; Walsh, M. J.; Hewitt, R.; Cole, K. J.; Phillips, D. H.; Martin, F. L. Growth kinetics in MCF-7 cells modulate benzo[*a*]pyrene-induced *CYP1A1* up-regulation. *Mutagenesis* **2007**, *22* (2), 111−116.
(33) Xu, X.; Wang, X.; Li, Y.; Wang, Y.; Yang, L. A large-scale association study for nanoparticle C60 uncovers mechanisms of nanotoxicity disrupting the native conformations of DNA/RNA. *Nucleic Acids Res.* **2012**, *40* (16), 7622−7632.
(34) An, H.; Jin, B. DNA exposure to buckminsterfullerene (C60): Toward DNA stability, reactivity, and replication. *Environ. Sci. Technol.* **2011**, *45* (15), 6608−6616.
(35) Sato, Y.; Yokoyama, A.; Shibata, K.-i.; Akimoto, Y.; Ogino, S.-i.; Nodasaka, Y.; Kohgo, T.; Tamura, K.; Akasaka, T.; Uo, M. Influence of length on cytotoxicity of multi-walled carbon nanotubes against human acute monocytic leukemia cell line THP-1 in vitro and subcutaneous tissue of rats in vivo. *Mol. BioSyst.* **2005**, *1* (2), 176−182.
(36) Oberley, T. D.; Schultz, J. L.; Li, N.; Oberley, L. W. Antioxidant enzyme levels as a function of growth state in cell culture. *Free Radic. Biol. Med.* **1995**, *19* (1), 53−65.

Electronic Supporting Information

Dose-related alterations of carbon nanoparticles in mammalian cells detected using biospectroscopy: potential for real-world effects

*Junyi Li[a], Rebecca Strong[a], Júlio Trevisan[a], Simon W. Fogarty[a,b], Nigel J. Fullwood[b], Kevin C. Jones[a] and Francis L. Martin[a]**

[a]Centre for Biophotonics, Lancaster Environment Centre, Lancaster University, Lancaster LA1 4YQ, UK; [b]Divison of Biomedical and Life Sciences, Faculty of Health and Medicine, Lancaster University, Lancaster LA1 4YQ, UK

*Corresponding author: Prof Francis L Martin PhD; *Email:* f.martin@lancaster.ac.uk; *Tel.:* +44 (0)1524 510206; *Fax:* +44 (0)1524 510217

Summary

- **Number of pages: 14**
- **Number of Figures: 10**
- **Number of Tables: 2**

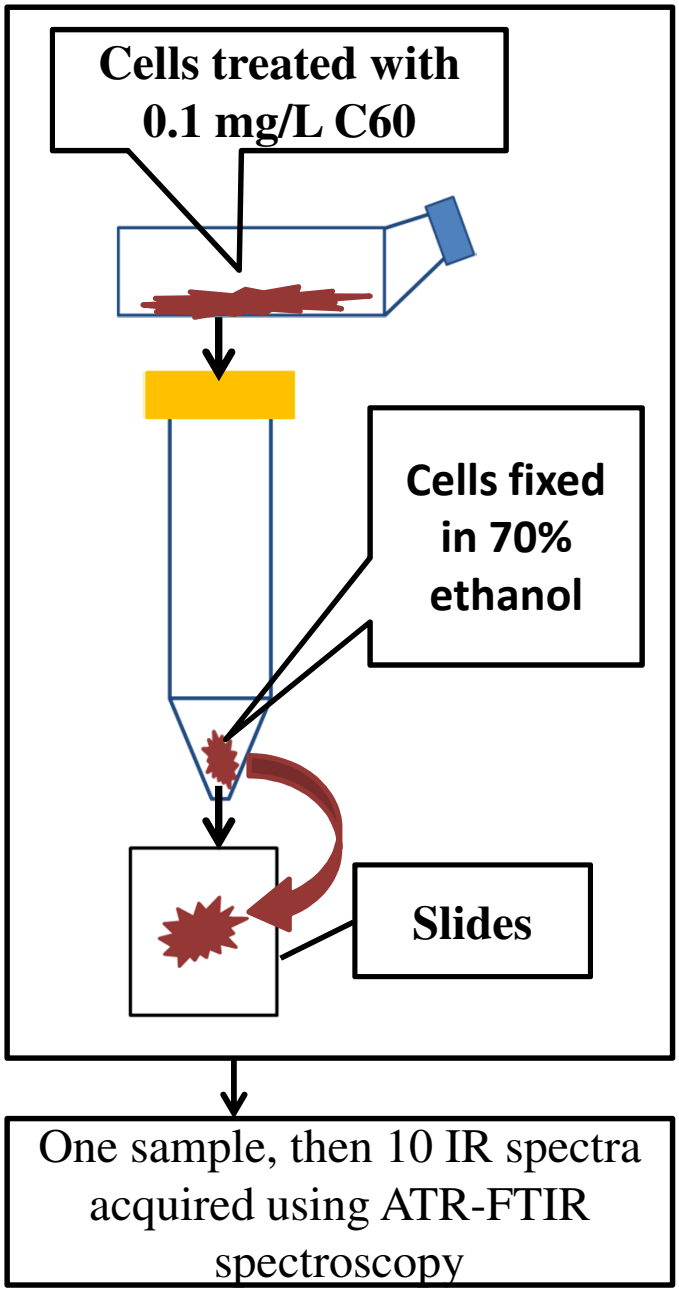

- Each **DR** or **NP** dataset consisted of three independent experiments.

- Each **DR** experiment consisted of 6 treatments and one control (*i.e.*, 7 concentrations), each in triplicate per experiment.
- Each **NP** experiment consisted of 6 treatments and one control (*i.e.*, 7 concentrations), each in duplicate per experiment.

DR: dose response datasets
NP: nanoparticles comparison datasets

Dataset	CNP type	Concentrations	Cell phase	No. samples	No. spectra
DR1	C60	Control, 0.0025, 0.005, 0.01, 0.025, 0.05 and 0.1 mg·L^{-1}	S	63	630
DR2	Long		S	63	630
DR3	Short		S	63	630
DR4	C60		G_0/G_1	63	630
DR5	Long		G_0/G_1	63	630
DR6	Short		G_0/G_1	63	630
NP1	Control, C60, Long, Short	0.1 mg·L^{-1}	S	24	240
NP2			G_0/G_1	24	240
Total				**426**	**4260**

Table S1. Summary of datasets obtained through ATR-FTIR spectroscopy.

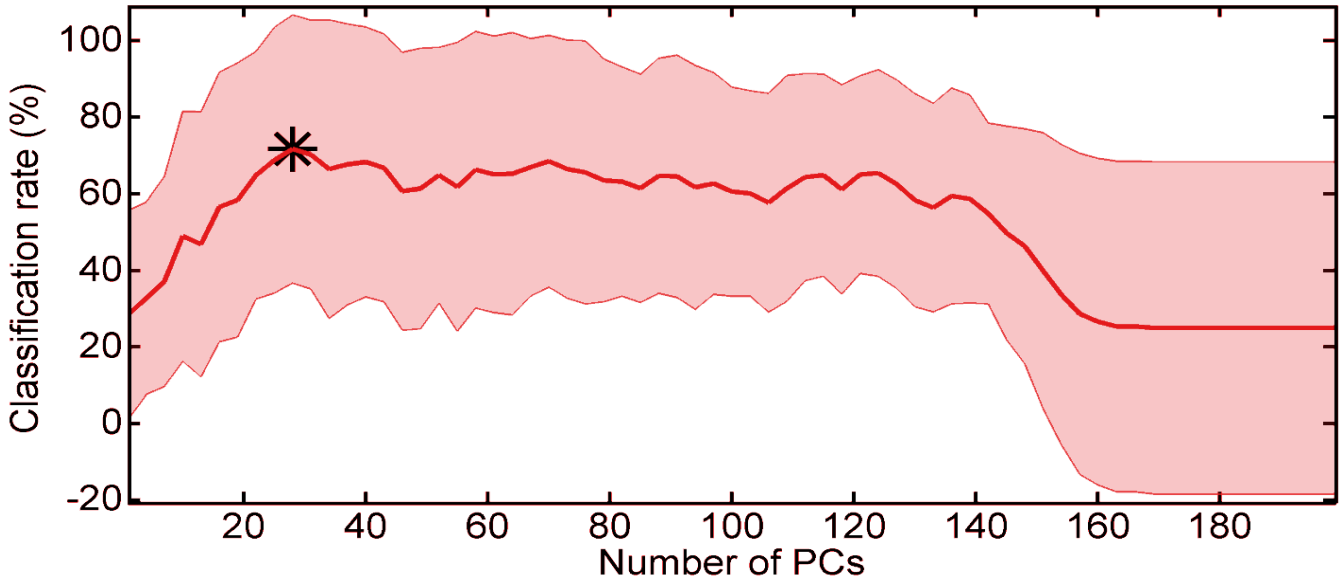

Figure S1. Illustration of optimization of number of principal components (PCs) to use in Cross-Calculated PCA-LDA. The dataset in this illustration was the NP-8 dataset (refer to Table S1). This procedure was repeated similarly with all the other seven datasets. The optimization searches for the optimal number of PCs for the PCA stage of a PCA-LDC classifier [PCA as feature extraction, followed by a Linear discriminant classifier (LDC)]. The search space is from 1 to 199 PCs and the number of PCs with highest average classification rate is selected for Cross-Calculated PCA-LDA. Classification rates were obtained through 10-fold cross-validation. The thick line is the average classification rate, and the hachured area represents the ±standard deviation range.

A step-by-step protocol is available at http://irootlab.googlecode.com, allowing for reproduction of the PCA-LDC optimization on a different dataset.

Dataset	CNP type	Concentrations	No. PCs
DR1	C60 (S-phase)	Control, 0.0025, 0.005, 0.01, 0.025, 0.05 and 0.1 mg·L^{-1}	28
DR2	Long (S-phase)		55
DR3	Short (S-phase)		22
DR4	C60 (G_0/G_1-phase)		28
DR5	Long (G_0/G_1-phase)		58
DR6	Short (G_0/G_1-phase)		28
NP1	All CNPs (S-phase)	0.1 mg·L^{-1}	49
NP2	All CNPs (G_0/G_1-phase)		28

Table S2. Optimal number of principal components (PCs) found for each dataset.

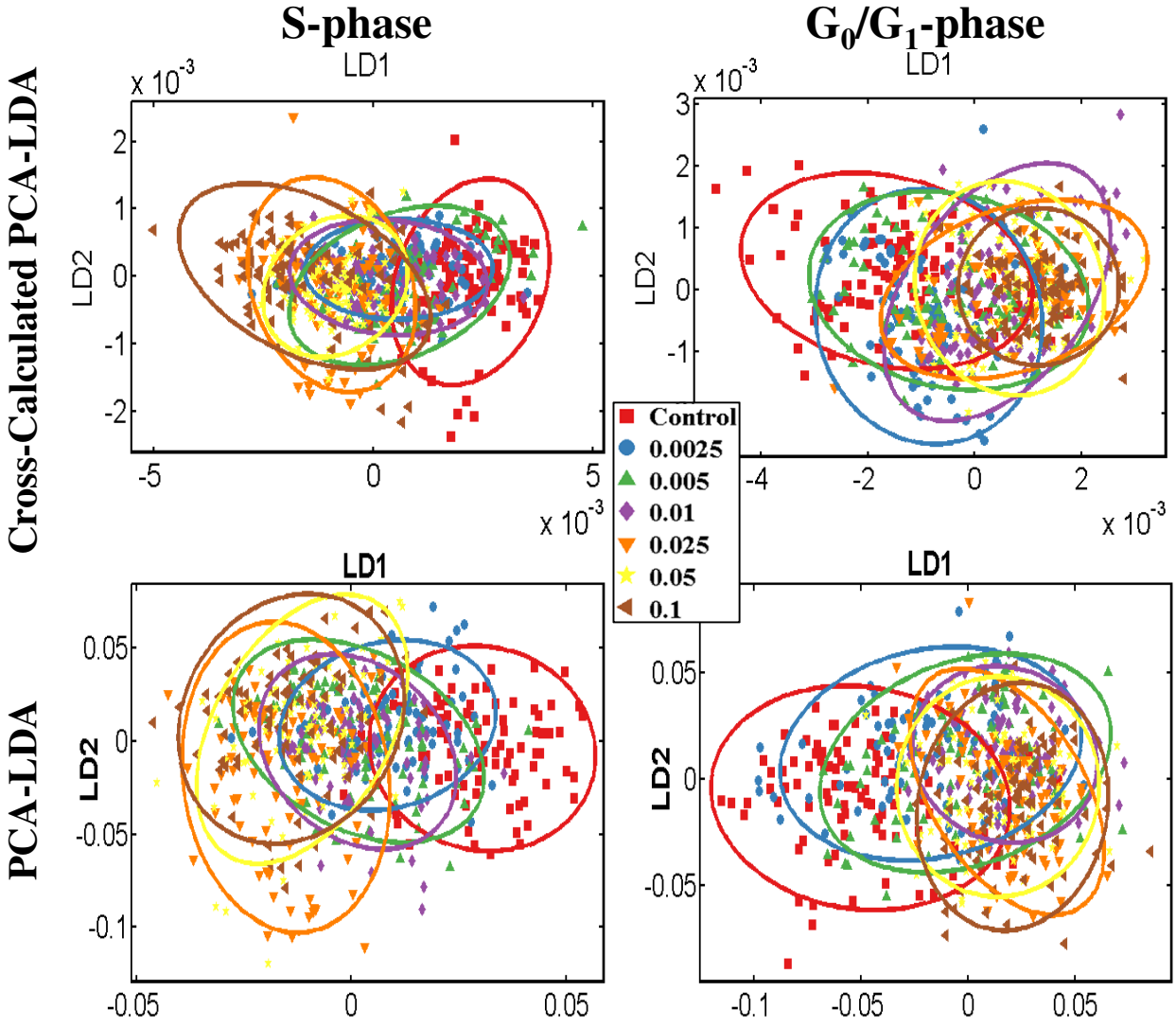

Cells treated with C60 (by *Cross-Calculated PCA-LDA*)

One-way ANOVA with Dunnett's Multiple Comparison Test	S-phase		G_0/G_1-phase	
	LD1	LD2	LD1	LD2
Control *vs*. 0.0025 mg/L	*P <0.01*	*P >0.05*	*P <0.01*	*P <0.01*
Control *vs*. 0.005 mg/L	*P <0.01*	*P >0.05*	*P <0.01*	*P <0.05*
Control *vs*. 0.01 mg/L	*P <0.01*	*P >0.05*	*P <0.01*	*P <0.05*
Control *vs*. 0.025 mg/L	*P <0.01*	*P >0.05*	*P <0.01*	*P >0.05*
Control *vs*. 0.05 mg/L	*P <0.01*	*P >0.05*	*P <0.01*	*P >0.05*
Control *vs*. 0.1 mg/L	*P <0.01*	*P >0.05*	*P <0.01*	*P >0.05*

Cells treated with C60 (by *PCA-LDA*)

One-way ANOVA with Dunnett's Multiple Comparison Test	S-phase		G_0/G_1-phase	
	LD1	LD2	LD1	LD2
Control *vs*. 0.0025 mg/L	*P <0.01*	*P <0.05*	*P <0.01*	*P <0.01*
Control *vs*. 0.005 mg/L	*P <0.01*	*P >0.05*	*P <0.01*	*P <0.01*
Control *vs*. 0.01 mg/L	*P <0.01*	*P >0.05*	*P <0.01*	*P <0.01*
Control *vs*. 0.025 mg/L	*P <0.01*	*P <0.01*	*P <0.01*	*P >0.05*
Control *vs*. 0.05 mg/L	*P <0.01*	*P >0.05*	*P <0.01*	*P >0.05*
Control *vs*. 0.1 mg/L	*P <0.01*	*P <0.01*	*P <0.01*	*P >0.05*

Figure S2. (a) Two-dimensional scores plot (*90% Confidence ellipsoids*) derived from MCF-7 cells treated with ***C60***, with *P-value* for each dimension calculated by one-way ANOVA with Dunnett's post hoc test.

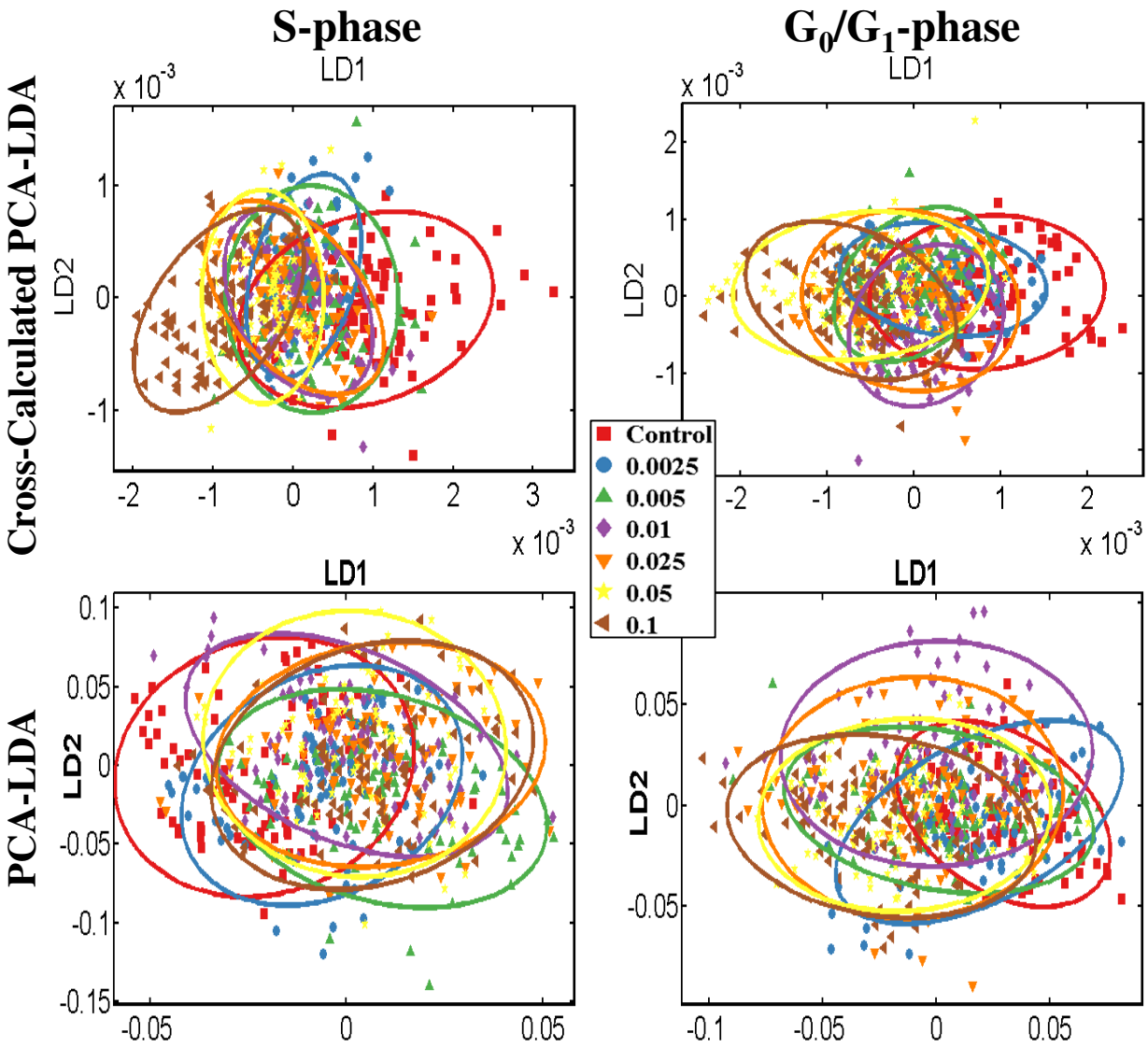

Cells treated with Long MWCNTs (by *Cross-Calculated PCA-LDA*)

One-way ANOVA with Dunnett's Multiple Comparison Test	S-phase		G_0/G_1-phase	
	LD1	LD2	LD1	LD2
Control *vs*. 0.0025 mg/L	*P* <0.01	*P* <0.01	*P* <0.01	*P* >0.05
Control *vs*. 0.005 mg/L	*P* <0.01	*P* >0.05	*P* <0.01	*P* >0.05
Control *vs*. 0.01 mg/L	*P* <0.01	*P* >0.05	*P* <0.01	*P* <0.01
Control *vs*. 0.025 mg/L	*P* <0.01	*P* >0.05	*P* <0.01	*P* >0.05
Control *vs*. 0.05 mg/L	*P* <0.01	*P* >0.05	*P* <0.01	*P* >0.05
Control *vs*. 0.1 mg/L	*P* <0.01	*P* >0.05	*P* <0.01	*P* >0.05

Cells treated with Long MWCNTs (by *PCA-LDA*)

One-way ANOVA with Dunnett's Multiple Comparison Test	S-phase		G_0/G_1-phase	
	LD1	LD2	LD1	LD2
Control *vs*. 0.0025 mg/L	*P* <0.01	*P* >0.05	*P* >0.05	*P* >0.05
Control *vs*. 0.005 mg/L	*P* <0.01	*P* <0.01	*P* <0.01	*P* >0.05
Control *vs*. 0.01 mg/L	*P* <0.01	*P* >0.05	*P* <0.01	*P* <0.01
Control *vs*. 0.025 mg/L	*P* <0.01	*P* >0.05	*P* <0.01	*P* >0.05
Control *vs*. 0.05 mg/L	*P* <0.01	*P* <0.01	*P* <0.01	*P* >0.05
Control *vs*. 0.1 mg/L	*P* <0.01	*P* >0.05	*P* <0.01	*P* >0.05

Figure S2. (b) Two-dimensional scores plot (*90% Confidence ellipsoids*) derived from MCF-7 cells treated with ***Long MWCNTs***, with *P-value* for each dimension calculated by one-way ANOVA with Dunnett's post hoc test.

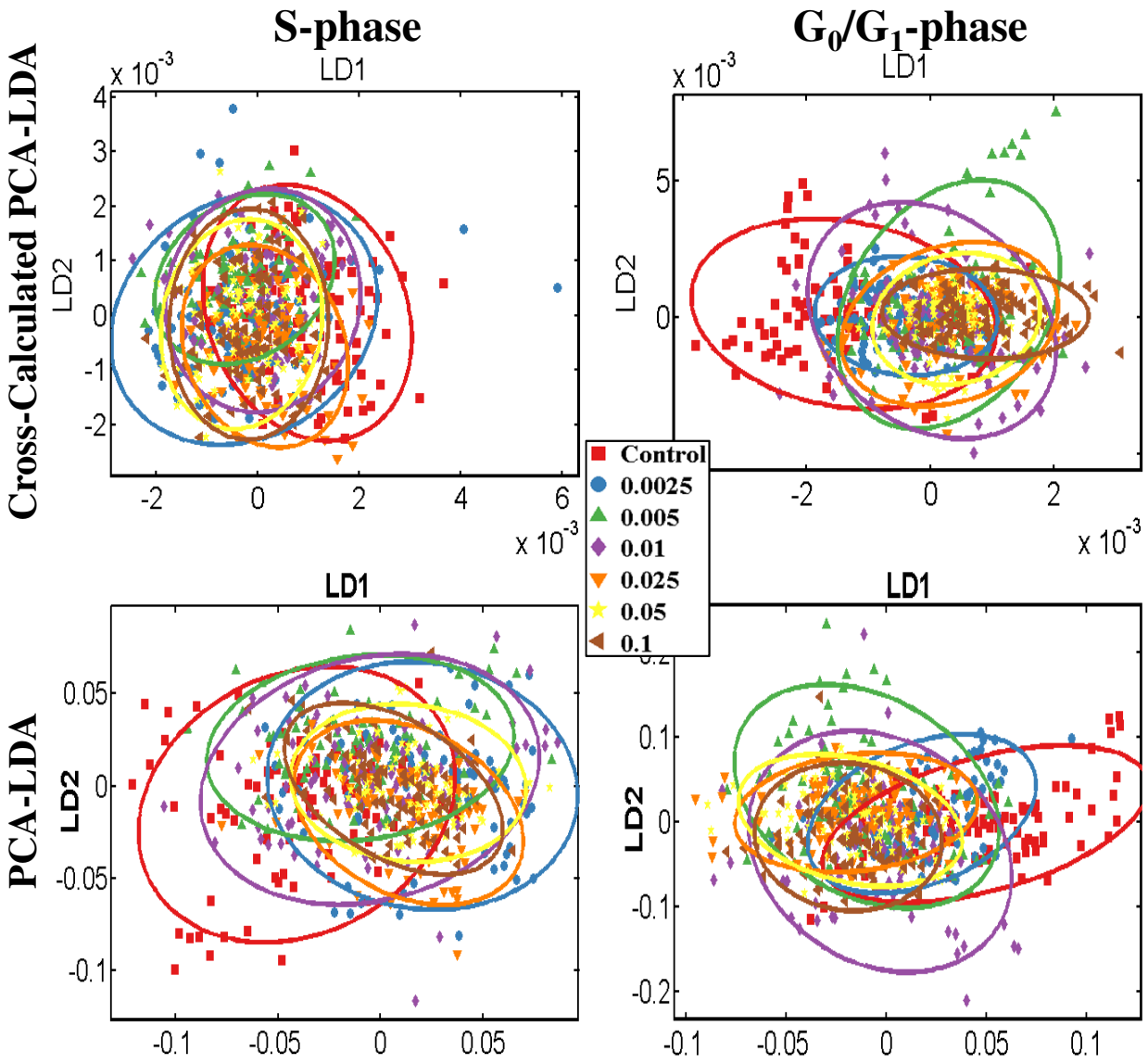

Cells treated with Short MWCNTs (by *Cross-Calculated PCA-LDA*)

One-way ANOVA with Dunnett's Multiple Comparison Test	S-phase		G_0/G_1-phase	
	LD1	LD2	LD1	LD2
Control *vs*. 0.0025 mg/L	*P* <0.01	*P* >0.05	*P* <0.01	*P* >0.05
Control *vs*. 0.005 mg/L	*P* <0.01	*P* <0.01	*P* <0.01	*P* >0.05
Control *vs*. 0.01 mg/L	*P* <0.01	*P* >0.05	*P* <0.01	*P* >0.05
Control *vs*. 0.025 mg/L	*P* <0.01	*P* <0.01	*P* <0.01	*P* >0.05
Control *vs*. 0.05 mg/L	*P* <0.01	*P* >0.05	*P* <0.01	*P* >0.05
Control *vs*. 0.1 mg/L	*P* <0.01	*P* >0.05	*P* <0.01	*P* >0.05

Cells treated with Short MWCNTs (by *PCA-LDA*)

One-way ANOVA with Dunnett's Multiple Comparison Test	S-phase		G_0/G_1-phase	
	LD1	LD2	LD1	LD2
Control *vs*. 0.0025 mg/L	*P* <0.01	*P* >0.05	*P* <0.01	*P* >0.05
Control *vs*. 0.005 mg/L	*P* <0.01	*P* <0.01	*P* <0.01	*P* <0.01
Control *vs*. 0.01 mg/L	*P* <0.01	*P* <0.01	*P* <0.01	*P* <0.01
Control *vs*. 0.025 mg/L	*P* <0.01	*P* >0.05	*P* <0.01	*P* >0.05
Control *vs*. 0.05 mg/L	*P* <0.01	*P* <0.05	*P* <0.01	*P* >0.05
Control *vs*. 0.1 mg/L	*P* <0.01	*P* >0.05	*P* <0.01	*P* >0.05

Figure S2. (c) Two-dimensional scores plot (*90% Confidence ellipsoids*) derived from MCF-7 cells treated with ***Short MWCNTs***, with *P-value* for each dimension calculated by one-way ANOVA with Dunnett's post hoc test.

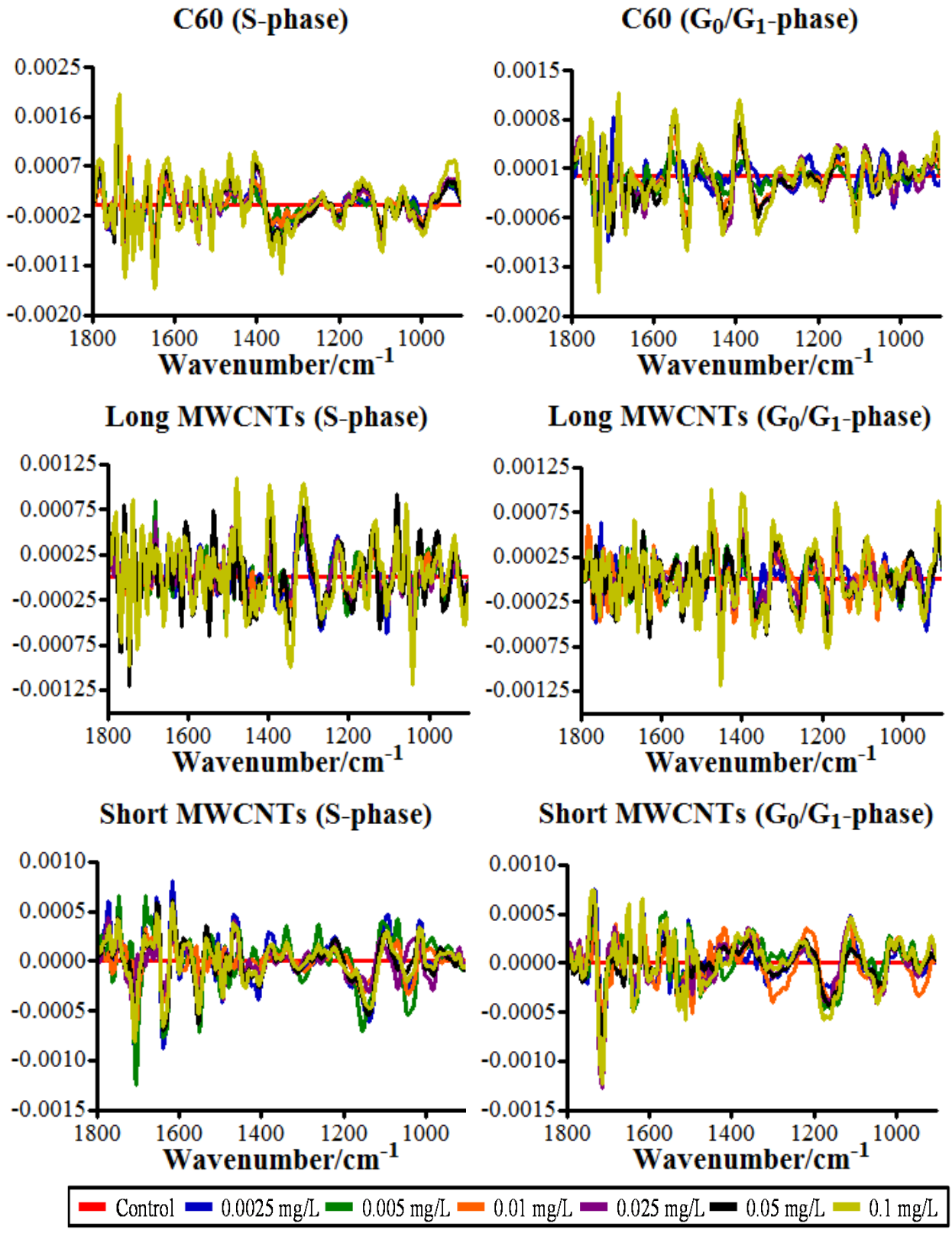

Figure S3. Cluster vectors plot by ***Cross-Calculated PCA-LDA*** indicating the wavenumber basis for segregation following treatment of MCF-7cells with CNPs. Each treatment was compared to the vehicle control. The height of the cluster vector peak is proportional to the extent of biochemical alteration compared to the vehicle control.

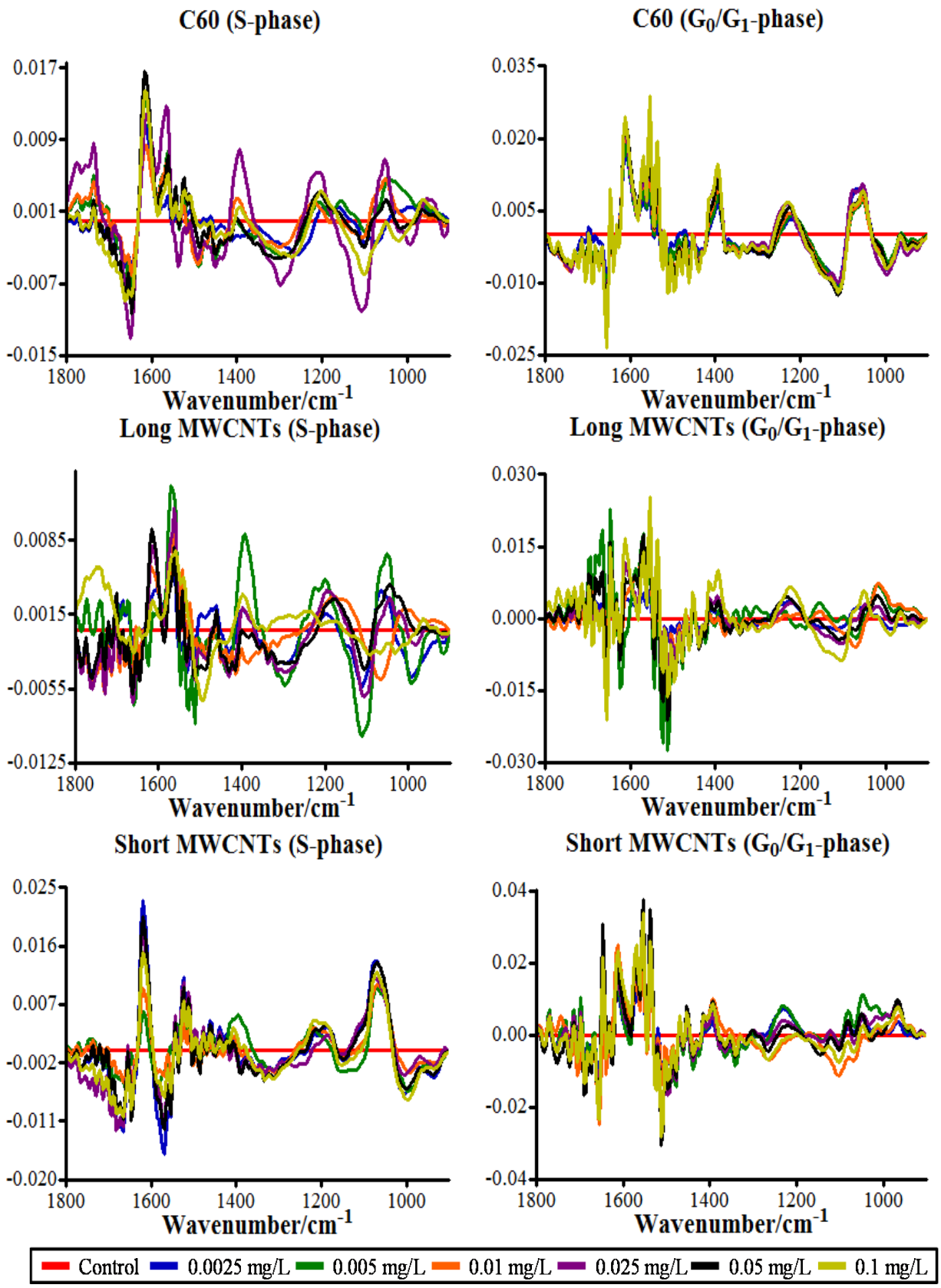

Figure S4. Cluster vectors plot by ***PCA-LDA*** indicating the wavenumber basis for segregation following treatment of MCF-7cells with CNPs. Each treatment was compared to the vehicle control. The height of the cluster vector peak is proportional to the extent of biochemical alteration compared to the vehicle control.

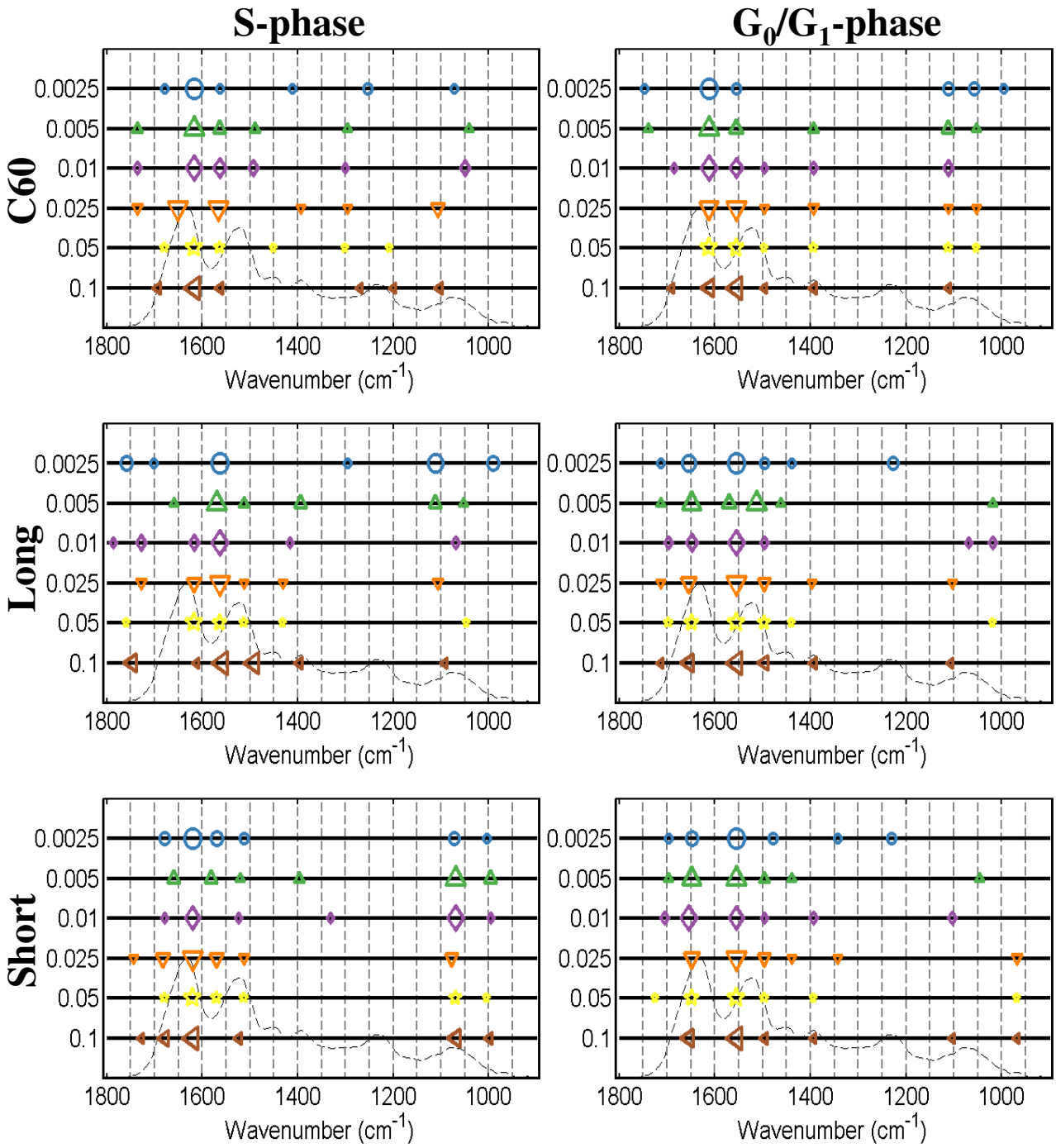

Figure S5. Cluster vectors peaks plot by **PCA-LDA** indicating the wavenumber basis for segregation following treatment of MCF-7 cells with CNPs. Each treatment was compared to the vehicle control. The size of the symbol in cluster vector peaks plot is proportional to the height of the corresponding peaks, which are relative to the extent of biochemical alteration compared to the vehicle control. The hint line represents a typical IR spectrum in the biochemical-fingerprint region (1800 cm^{-1} - 900 cm^{-1}).

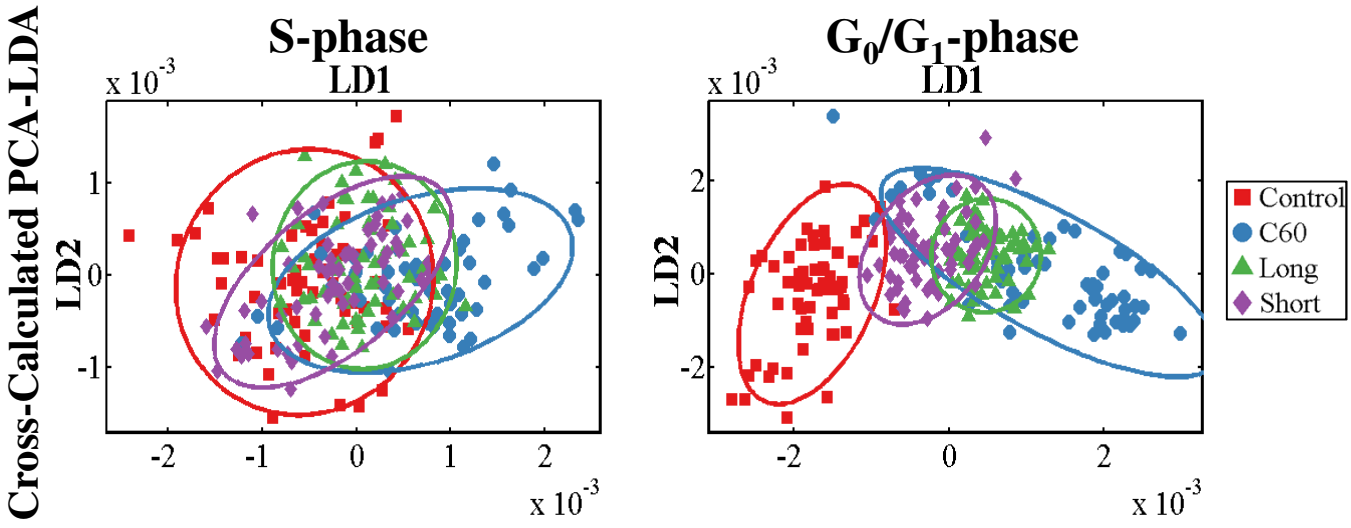

Cross-Calculated PCA-LDA

One-way ANOVA with Newman-Keuls Multiple Comparison Test	S-phase		G_0/G_1-phase	
	LD1	LD2	LD1	LD2
Control *vs.* C60	*P* <0.001	*P* >0.05	*P* <0.001	*P* <0.001
Control *vs.* Long	*P* <0.001	*P* >0.05	*P* <0.001	*P* <0.001
Control *vs.* Short	*P* <0.01	*P* >0.05	*P* <0.001	*P* <0.01
Short *vs.* C60	*P* <0.001	*P* >0.05	*P* <0.001	*P* <0.01
Short *vs.* Long	*P* <0.01	*P* >0.05	*P* <0.001	*P* >0.05
Long *vs.* C60	*P* <0.001	*P* >0.05	*P* <0.001	*P* <0.05

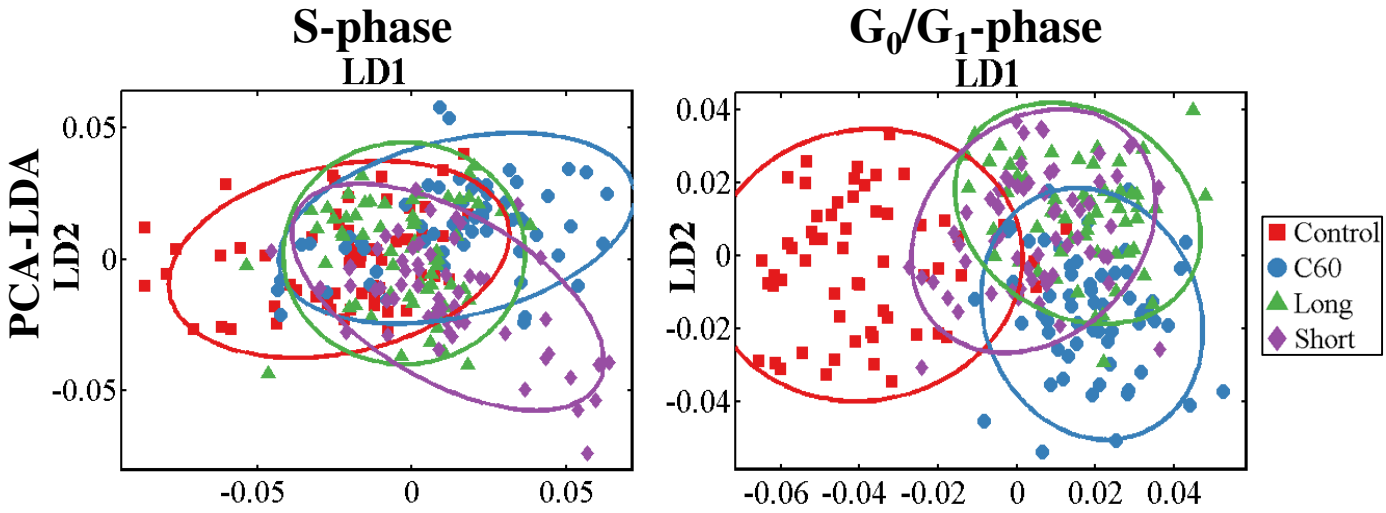

PCA-LDA

One-way ANOVA with Newman-Keuls Multiple Comparison Test	S-phase		G_0/G_1-phase	
	LD1	LD2	LD1	LD2
Control *vs.* C60	*P* <0.001	*P* <0.01	*P* <0.001	*P* <0.001
Control *vs.* Long	*P* <0.001	*P* >0.05	*P* <0.001	*P* <0.001
Control *vs.* Short	*P* <0.001	*P* <0.001	*P* <0.001	*P* <0.01
Short *vs.* C60	*P* >0.05	*P* <0.001	*P* <0.001	*P* <0.001
Short *vs.* Long	*P* <0.01	*P* <0.001	*P* <0.001	*P* >0.05
Long *vs.* C60	*P* <0.001	*P* <0.01	*P* >0.05	*P* <0.001

Figure S6. Two-dimensional scores plot (*90% Confidence ellipsoids*) derived from MCF-7 cells treated with *three Carbon Nanoparticles at 0.1 mg/L*, with *P-value* for each dimension calculated by one-way ANOVA with Newman-Keuls' post hoc test.

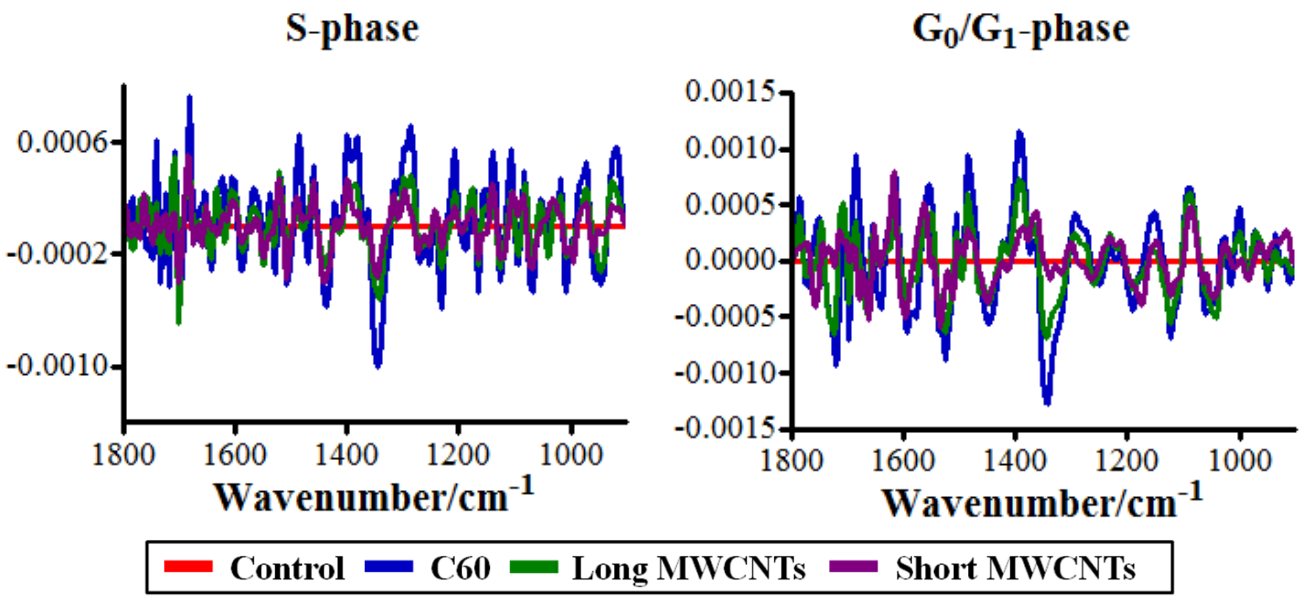

Figure S7. Cluster vectors plot by ***Cross-Calculated PCA-LDA*** derived from MCF-7 cells treated with *three Carbon Nanoparticles at 0.1 mg/L.*

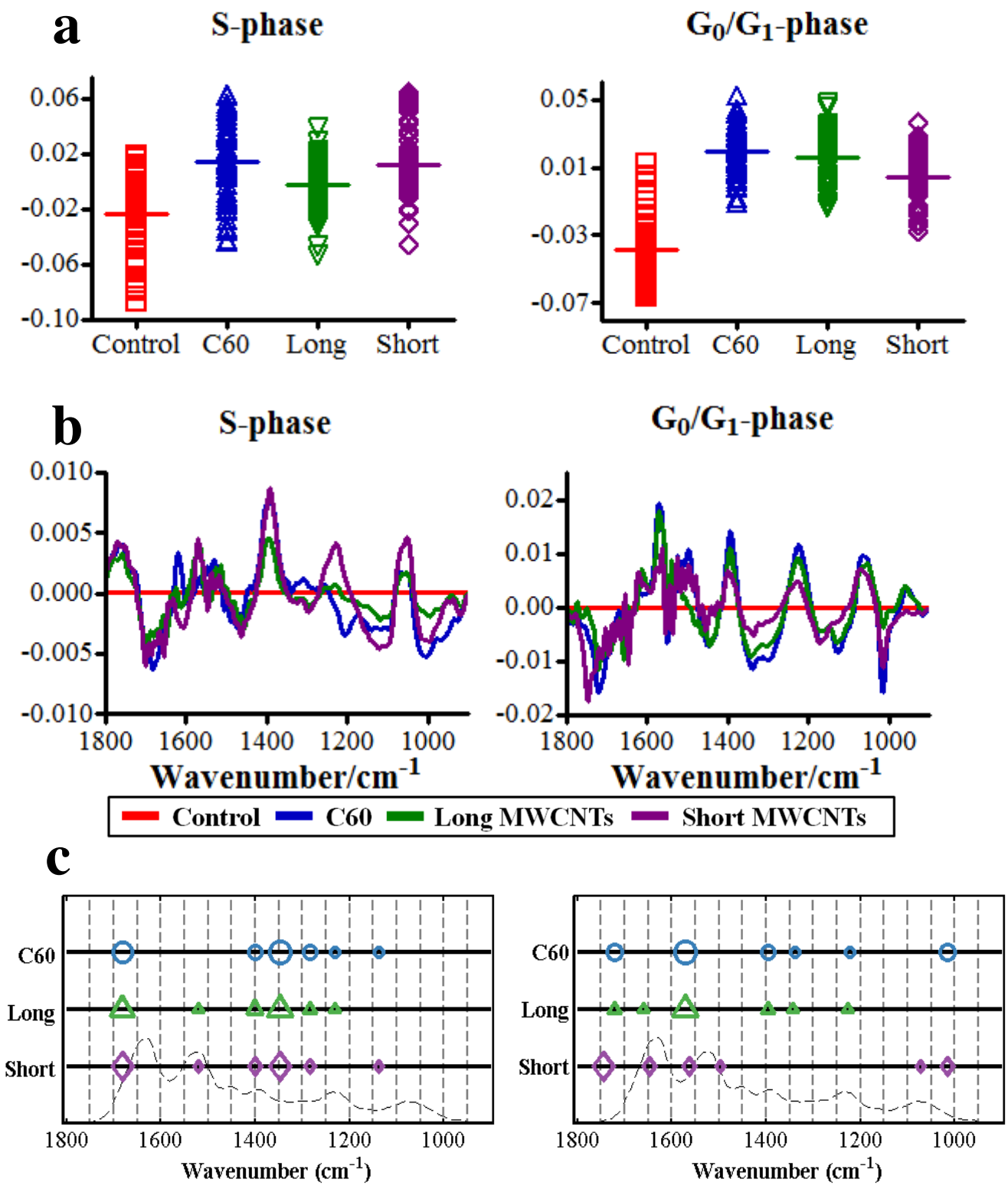

Figure S8. **(a)** One-dimensional scores plot; **(b)** cluster vectors plot; and, **(c)** cluster vectors peak plot derived from MCF-7 cells treated with *three Carbon Nanoparticles at 0.1 mg/L* by ***PCA-LDA***.

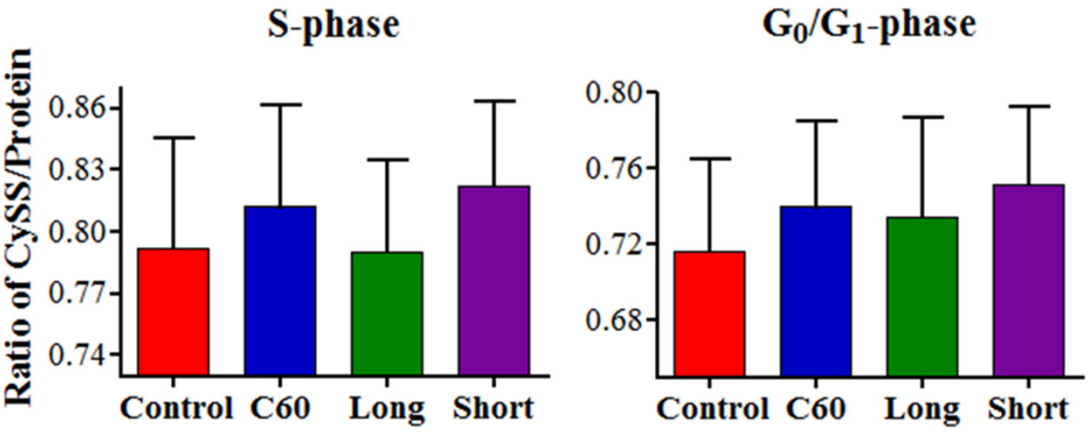

One-way ANOVA with Newman-Keuls' Multiple Comparison Test	*P-value*	
	S-phase	G_0/G_1-phase
Control *vs*. C60	*P <0.001*	*P <0.001*
Control *vs*. Long	*P >0.05*	*P <0.001*
Control *vs*. Short	*P <0.001*	*P <0.001*
C60 *vs*. Long	*P <0.001*	*P >0.05*
C60 *vs*. Short	*P >0.05*	*P <0.05*
Long *vs*. Short	*P <0.001*	*P <0.01*

Figure S9. *P-value* of CySS-to-protein ratio calculated by one-way ANOVA with Newman-Keuls' post hoc test.

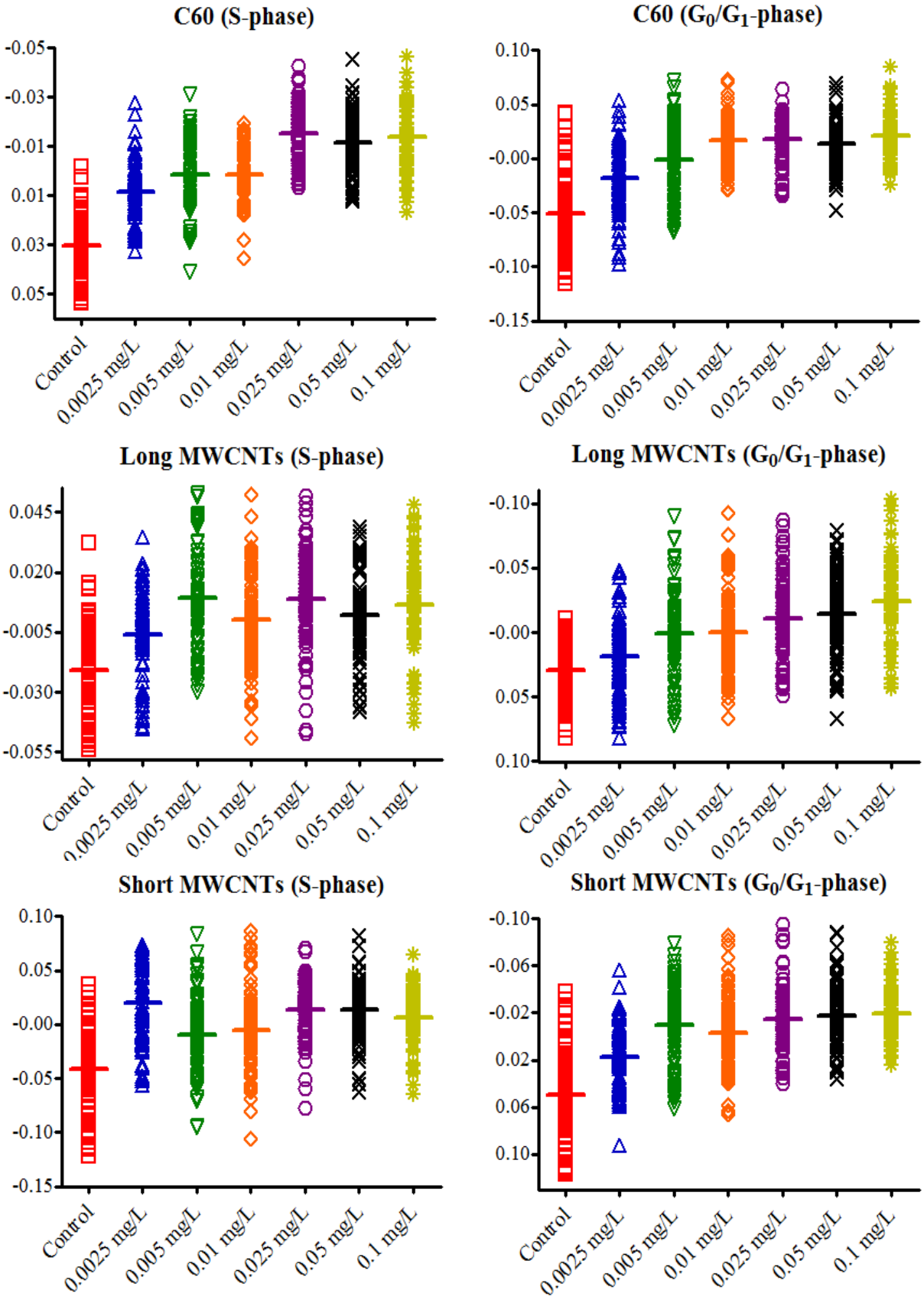

Figure S10. One-dimensional scores plot by ***PCA-LDA*** derived from MCF-7 cells treated with *Carbon Nanoparticles*.

Dose-response curve derived from LD1 space of PCA-LDA with highest response set to 100%

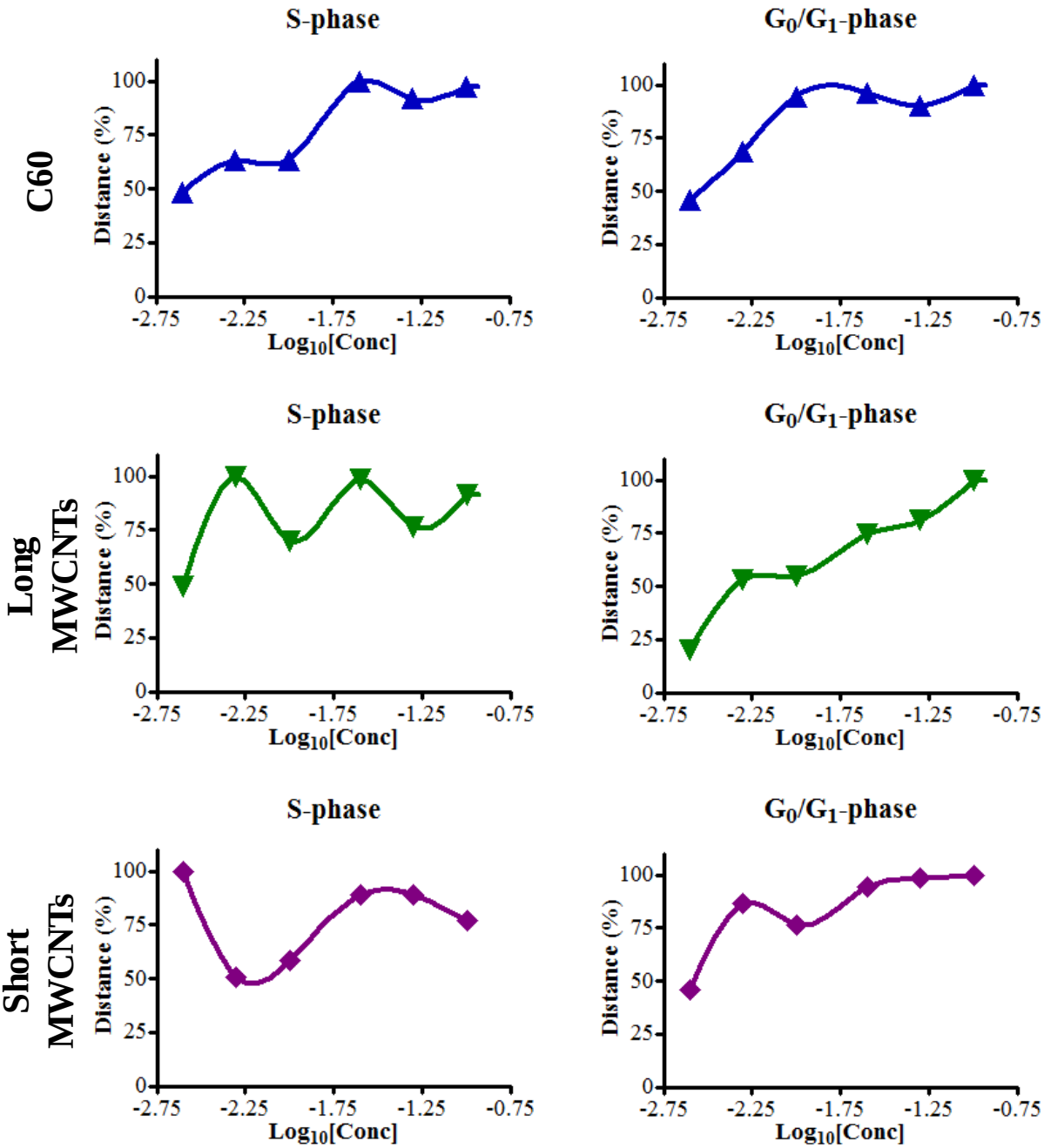

Chapter 3

Real-world carbon nanoparticle exposures induce brain and gonadal alterations in zebrafish (*Danio rerio*) as determined by biospectroscopy techniques

Junyi Li, Guang-Guo Ying, Kevin C. Jones and Francis L. Martin

Analyst, 2015,140, 2687-2695

Contribution:

- I acquired the samples required for the project ;
- I prepared processed and acquired all the data and carried out computational analysis;
- I prepared the first draft of the manuscript.

…… ……

Junyi Li Prof. Francis L. Martin

Analyst

PAPER

View Article Online
View Journal | View Issue

Cite this: *Analyst*, 2015, **140**, 2687

Real-world carbon nanoparticle exposures induce brain and gonadal alterations in zebrafish (*Danio rerio*) as determined by biospectroscopy techniques†

Junyi Li,[a] Guang-Guo Ying,[b] Kevin C. Jones[a] and Francis L. Martin*[a]

Carbon-based nanoparticles (CNPs) have emerged as novel man-made materials with diverse applications, which may present significant risks to organisms. To bridge the gap in our knowledge of nanotoxicology, a number of *in vitro* or *in vivo* studies have been carried out. However, toxicity data remains limited. Herein, we employed a biospectroscopy approach to assess CNP-induced effects in zebrafish (*Danio rerio*). Zebrafish were exposed to Fullerene (C_{60}), long or short multi-walled carbon nanotubes (MWCNTs), or single-walled carbon nanotubes (SWCNTs) for 21 days at two concentrations: 0.1 mg L^{-1} or 0.001 mg L^{-1}. Following exposure, the brain, gills, gonads and liver from zebrafish were interrogated by attenuated total reflection Fourier-transform infrared (ATR-FTIR) or Raman spectroscopy. Computational analysis was then applied to the acquired infrared (IR) spectra, and distinct biochemical segregations between the exposed tissues *vs.* control were observed with spectral biomarkers of alterations identified. In addition, lipid-to-protein ratios in all four tissues were calculated by the IR spectra; unsaturated lipid levels in brain and gonad were assessed by Raman spectroscopy. Marked lipid alterations were observed. These findings show that biospectroscopy approaches have the potential to detect CNP-induced biochemical alterations in zebrafish.

Received 4th December 2014,
Accepted 23rd February 2015

DOI: 10.1039/c4an02227k

www.rsc.org/analyst

1. Introduction

Nanotechnology has introduced a wide range of man-made materials into the environment. Fullerene (C_{60}) and carbon nanotubes (CNTs) are the most promising manufactured carbon-based nanomaterials. With their unique physicochemical properties, these materials offer extraordinary opportunities for applications in industry, biomedicine or everyday life.[1–5] Increasing interest commercially or scientifically is leading to massive production and application of these materials. However, little is known of their potential toxicity, or even how these materials will behave during the manufacturing process and in the environment.[6,7] Consequently, this emerging issue is drawing more and more attention worldwide from scientists and governments.

Increasingly, numerous investigators are examining the toxic interactions of carbon nanoparticles (CNPs) with cells. Jia *et al.* observed that carbon nanomaterials (SWCNTs, MWCNTs or C_{60}) with different geometric structures induce varying levels of cytotoxicity in alveolar macrophages.[8] Additional studies showed that CNPs cause cytotoxicity in HaCat human keratinocytes,[9] human osteoblasts and fibroblasts,[10] and human T-lymphocytes.[11] Other biological models such as bacteria,[12,13] algae,[14] *Daphnia magna*[15] and, even, fish[16] or rats[17] have been employed to study such adverse effects. However, *in vitro* observations do not always faithfully extrapolate to the *in vivo* situation. Also, sometimes conventional assays are limited in their ability to assess nanoparticles.[18] To date, the understanding of CNPs' toxicity remains limited and a paradigm-shifting methodology is required to offset such challenges.

Spectroscopy is increasingly used as a powerful tool in biological research. Infrared (IR) spectroscopy, including attenuated total reflection Fourier-transform infrared (ATR-FTIR) spectroscopy, has been applied in disease diagnosis[19] and toxic assessment of environmental contamination within cells.[20,21] In ATR-FTIR instrumentation, a mid-IR beam (λ = 2–20 μm) is transmitted through an internal reflection element (*e.g.*, diamond, zinc selenide, germanium, silicon) in contact with the samples and penetrates a small distance beyond the sample surface, allowing the generation of bio-

[a]*Centre for Biophotonics, Lancaster Environment Centre, Lancaster University, Lancaster LA1 4YQ, UK. E-mail: f.martin@lancaster.ac.uk; Tel: +44 (0)1524 510206*
[b]*State Key Laboratory of Organic Geochemistry, Guangzhou Institute of Geochemistry, Chinese Academy of Sciences, Guangzhou 510640, China*
†Electronic supplementary information (ESI) available. See DOI: 10.1039/c4an02227k

chemical fingerprint spectra (1800–900 cm^{-1}). Raman spectroscopy is a complimentary spectral method, which can also detect a wide range of chemical bonds in cells and tissues.[22] Some excellent studies have already shown that Raman spectroscopy can also be applied to assess nanotoxicity.[23,24] Such biospectroscopy tools employed in biological investigations may generate a large amount of spectral data, which requires computational analysis in order to extract information.[25]

Previously, we employed ATR-FTIR spectroscopy coupled with computational analysis to detect CNP-induced alterations in MCF-7 cells; dose-related effects were observed.[26] This suggests biospectroscopy as a novel tool capable of identifying the effects of CNPs.[27] Aquatic environments may act as a sink for environmental contaminants including CNPs,[28] and some studies have already reported that single-walled CNTs and C_{60} exert toxic effects in rainbow trout (*Oncorhynchus mykiss*),[29] and that MWCNTs induce toxicity in zebrafish embryos.[30] Thus, it is essential to develop sensitive and reliable methods to assess biological effects of CNPs in fish. Additionally, zebrafish are a well-established model organism widely applied in biological medicine[31] and toxicological assessment.[32] In order to address the limitations of *in vitro* tests and extrapolate to the *in vivo* situation, we conducted tests on zebrafish (*Danio rerio*) following exposure to CNPs and interrogated the tissues using spectroscopy. In this study, zebrafish were exposed to four CNPs (C_{60}, short and long MWCNTs or SWCNTs) at concentrations of 0.1 mg L^{-1} or 0.001 mg L^{-1}. Following 21-day exposure, alterations in tissues including brain, gills, gonads and liver were then assessed *via* biospectroscopy with computational analysis. Our aim was to ascertain real-world CNP effects in a model system.

2. Materials and methods

Chemicals and carbon nanoparticles

Bovine serum albumin (BSA) obtained from Sigma was ≥98%. All CNPs were purchased from Sigma. Short MWCNTs were >90% pure being 10–15 nm in diameter and 0.1–10 μm in length. Long MWCNTs were >90% pure also, but were 110–170 nm in diameter and 5–9 μm in length. C_{60} had a purity >99.5% and particle size of 1 nm. SWCNTs were described as CarboLex AP-grade (the purity of AP-grade products ranges from 50% to 70% by volume); major impurities are carbon nanospheres and carbon-encapsulated catalyst nanoparticles – the diameter was 1.2–1.5 nm. All CNPs were analysed by Raman spectroscopy (Renishaw PLC, UK) with a 785 nm laser, and determined to be of high purity. Additionally, images of CNPs were taken using a scanning electron microscope (SEM) [JSM 5600 (JEOL)] [see ESI Fig. S1†]. CNPs were dispersed in 1% BSA solution with a 15 min ultrasonication and stock solutions were made at concentrations of 100 mg L^{-1} and 1 mg L^{-1}. CNT solutions were stable and well-dispersed, while C_{60} appeared to agglomerate.

Fish maintenance and experimental conditions

All experiments were carried out following approval from the local Institutional Review Board. Zebrafish were maintained in the Aquatic Toxicology Laboratory at the Guangzhou Institute of Geochemistry, Chinese Academy of Sciences. All fish were kept in 50 L flow-through tanks filled with dechlorinated tap water in a temperature-controlled room maintained at 27 ± 1 °C. The room was on a 14 : 10 h light : dark cycle, and fish were fed once a day with a quantity of commercial food at 5% of the wet weight.

Fish exposures were conducted in 10 L glass tanks, and each experimental tank contains 5 L dechlorinated tap water and 4 fish (2 males, 2 females). Prior to exposure, zebrafish in 50 L tanks were randomly transferred to the experimental tank for a 7-day adaptive period. Following this, CNP exposure was initiated and run for 21 days. There were nine randomly assigned tanks for each exposure (control and treatment with one of four CNPs at 0.1 mg L^{-1} or 0.001 mg L^{-1}). Exposure concentrations were chosen based on previous *in vitro* studies,[26] which showed that speculated real-world environmental levels induced alterations in exposed cell populations detectable by biospectroscopy techniques. To minimize contamination, fish were only fed in the morning every day and in the afternoon, each tank was cleaned to eliminate fish faeces and food remains by siphoning the water out of the tanks. Then all tanks were filled with fresh water and treatment. All fish were terminated at the end of the exposure and were sacrificed within seconds by immersion in melting ice prior to body size measurements (weight and length) (see ESI Fig. S2†). From each fish, gills, brain, liver and gonads were independently harvested and fixed in 70% ethanol. Exposure experiments were conducted in triplicate.

Biospectroscopy analysis

Each fixed fish tissue for spectral interrogation was thinly sliced by hand and mounted on IR-reflective low-E slides (Kevley Technologies, USA), allowed to air-dry and stored in a desiccator prior to spectral acquisition. All tissue samples were interrogated using a Bruker TENSOR 27 FTIR spectrometer (Bruker Optics Ltd., UK) equipped with a Helios ATR attachment containing a diamond internal reflection element (IRE). Instrument parameters were set at 32 scans, 16 cm^{-1} resolution. For each slide, 10 IR spectra were acquired at different points across the sample. Prior to starting a new slide, the ATR crystal was cleaned with deionized water and a background taken. Additionally, the brain and gonad tissues from the control group and the high-dose treatment groups for the four CNPs were further interrogated by Raman spectroscopy. Raman spectra were recorded using an *InVia* Renishaw Raman spectrometer (Renishaw plc, UK) equipped with a 785 nm streamline focus laser and a Renishaw-automated 100 nm encoded XYZ stage. The system parameters consisted of 50 μm entrance slit, 830 lines mm^{-1} (~1.69 cm^{-1} spectral resolution) diffraction grating dispersing Raman signal onto a master Renishaw Pelletier cooled charge detector (CCD, 1024 pixel ×

pixel). The system calibration was carried out using an internal Renishaw silicon calibration source for wavenumber shift. A white light camera mounted on the microscope was used to visualize the locations of the spectral acquisition. Spectra were collected using a Leica ×50 objective lens (numeral aperture 0.75) at 50% laser power (≤100 mW prior to lens) of 20-second exposure and spectral range covering 2000–500 cm^{-1}. Approximately 30 spectra were obtained from different sites from each sample.

Data analysis

All spectral data acquired from both ATR-FTIR and Raman spectroscopy were processed using our IRootLab toolbox (http://irootlab.googlecode.com)[33] running on MATLAB r2010a (The MathWorks, Inc., US). IR spectra were pre-processed as follows: cut to 1800–900 cm^{-1} (the biochemical fingerprint range), rubberband baseline correction and normalization to the Amide I peak (1650 cm^{-1}). Computational analysis using multivariate techniques including principal component analysis (PCA) and linear discriminant analysis (LDA) can efficiently analyse such large spectral datasets. Following pre-processing, cross-calculated PCA-LDA was applied to the dataset; information was extracted and visualised as scores plots and cluster vectors. PCA is an unsupervised technique employed to reduce the dimensions of the data, and then the PCA scores are used as input for the subsequent LDA, where the class' information contributes to differentiation of the derived clusters. To eliminate the risk of LDA overfitting, "cross-calculation" was applied to the PCA-LDA scores (see ESI Fig. S3†). It utilizes leave-one-out cross-validation to train the PCA-LDA loadings using n-1 (n = number of spectra in the dataset) samples and subsequently calculates the scores for the remaining sample, repeating this process until all scores are calculated. The loadings are derived as averages between the n PCA-LDA loadings model. Additionally, the number of principal components (PCs) for PCA-LDA was calculated by classification with an optimization procedure. The output data derived from PCA-LDA can be then visualized as 1-D, 2-D or 3-D scatterplots ("scores plots"). In scores plots, nearness between two groups means similarity, while increasing distance indicates dissimilarity. To reveal the biochemical alterations associated with each group in the dataset, PCA-LDA cluster vectors were developed.[25] To simplify the identification of the main biochemical alteration of each group, cluster vectors plots were used to indicate the first eight highest peaks; tentative assignments of the peak wavenumbers are listed (see ESI,† pages 25–46), ranked by peak height.

Lipid accumulation and unsaturated levels in tissues exposed to CNPs

Lipid accumulation in tissues was calculated by measuring the lipid-to-protein ratio using the intensity absorbance at two vibration modes derived from the pre-processed IR spectra. The intensity absorbance at 1400 cm^{-1} corresponding to C═O symmetric stretching of amino acid was used as a protein marker, while the intensity absorbance at 2924 cm^{-1} was associated with $\nu_{as}CH_2$ for lipid. In Raman spectra, the intensity at 1445 cm^{-1} was assigned to CH_2 bending for lipid and the intensity at 1670 cm^{-1} was assigned to ν(C═C) in lipid. The ratio of (C═C)/(CH_2) can be used to calculate the lipid unsaturated level.[34]

Repeated-measures one-way analysis of variance (ANOVA) with Dunnett's post hoc tests were used to examine whether the alteration of the tissues observed in scores plots (LD1 and LD2), and the ratios of lipid/protein and (C═C)/(CH_2) differed significantly between the exposure *vs.* control groups. It's not necessary to transform data to meet the underlying assumption of homogeneity between categories and normality of residuals. *P*-values below 0.05 were considered statistically significant. All ANOVA tests were conducted in GraphPad Prism 4 (GraphPad Software, USA).

3. Results and discussion

When zebrafish were exposed to one of the four CNPs tested, the response for each tissue examined was different and varied with exposure. CNP-specific dose responses compared to the control group were observed in all tissues examined, including brain, gills, gonads and liver (see ESI Fig. S4–S7†). Additionally, ANOVA tests showed that these were significant for the majority of exposures (see ESI Tables S1 and S2†). In the scores plots along the LD1 dimension, most category separation was observed; these simply show the effects for each tissue resulting from two different CNP exposures (Fig. 1 and 2). It is clearly noted that along LD1, the gills and brain exhibit a similar response pattern to the four different CNPs. In contrast, the gonads and liver display an inverse response to these exposures, with the lower dose inducing more pronounced effects than the higher. On a physiologically-based toxicokinetics (PBTK) model, the gills are considered the initial site for uptake and elimination of CNPs, while brain, gonads and liver connected with the gills *via* arterial blood are perturbed by CNPs.[35] It is noted that in zebrafish, blood circulating in veins from the gonads will reach the liver, which may explain why these tissues respond similarly to CNPs. To highlight the main biochemical alterations induced by CNPs, a cluster vectors method was employed following cross-calculated PCA-LDA. CNP exposures generate a range biochemical alterations associated with lipid, protein, glycogen and DNA/RNA (see ESI†).

To reveal the profile of effects induced by CNPs, a dataset was developed to profile alterations in zebrafish tissues following CNP exposures at a concentration of 0.1 mg L^{-1} compared to the control group. Segregation in 2-D cross-calculated PCA-LDA scores plots showed that long MWCNTs, possessing a relatively larger size, exert the most pronounced alterations in the four tissues studied compared to the other three CNPs (Fig. 3). The cluster vectors plots indicate that long MWCNTs-induced effects in tissues are mainly to lipid and protein, with limited alterations in the DNA/RNA region (Fig. 4). However, C_{60} appears to induce a high level of alterations in the DNA/

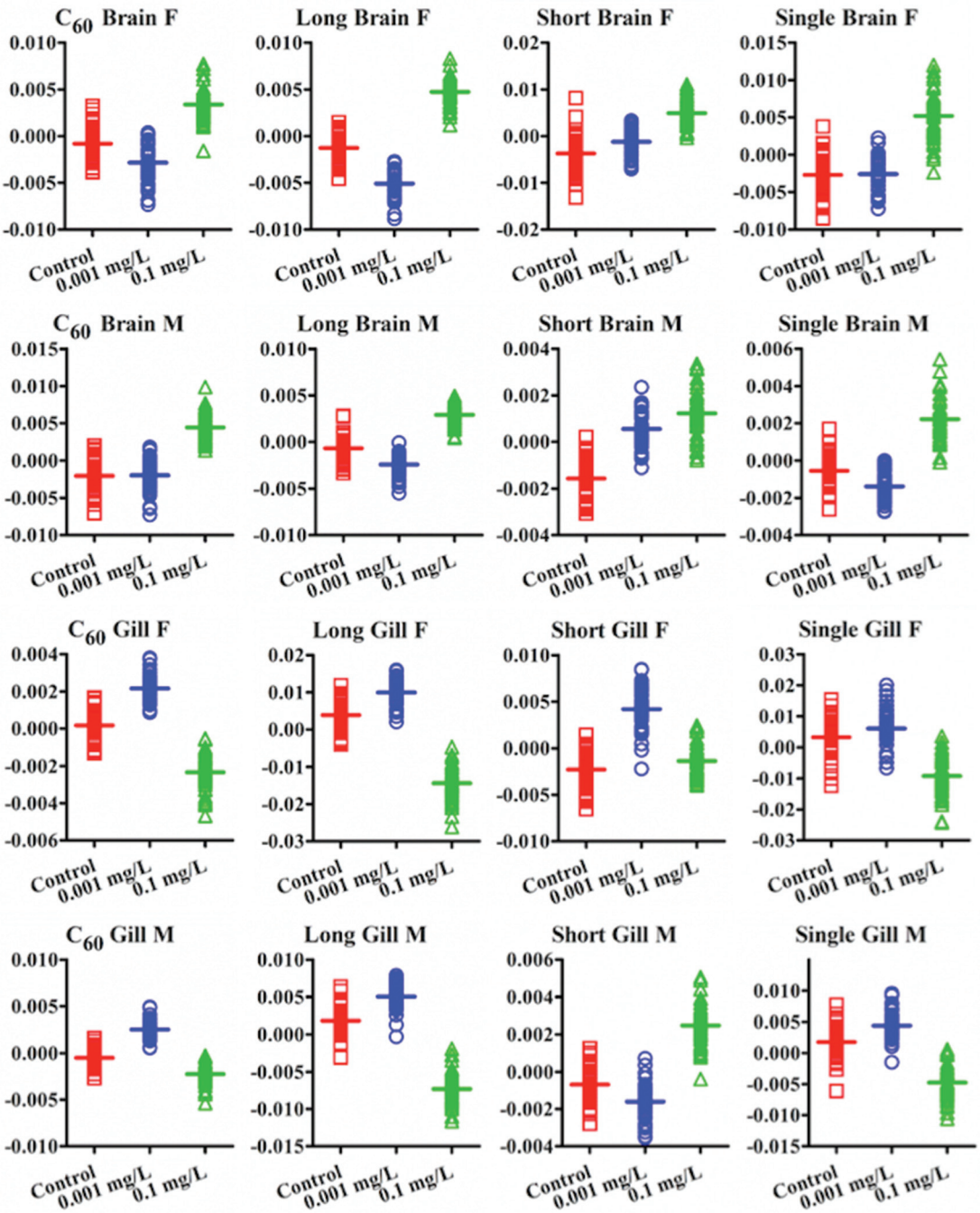

Fig. 1 One-dimensional (1-D) cross-calculated PCA-LDA scores plots in 1st space of infrared (IR) spectra derived from brain or gill of zebrafish [male (M) or female (F)] exposed to carbon nanoparticles (CNPs) at two concentrations compared to the vehicle control. The horizontal line in the centre of each plot represents the mean value. C60, C_{60} (fullerene); long, long MWCNTs; short, short MWCNTs; single, SWCNTs.

RNA region, especially in the brain. SWCNTs- and short MWCNTs-induced alterations in zebrafish appear to be similar. To investigate the brain and gonads further, Raman spectroscopy was employed to interrogate these two tissues; significant post-exposure alterations were again observed.

IR spectra allow an estimation of the lipid-to-protein ratio in tissues. This showed that female fish display a higher lipid-to-protein ratio, except in the gonads. Among all tissue types, male gonads exhibited the highest lipid-to-protein ratio (Fig. 5). Additionally, the unsaturated levels of lipid in brain and gonads were assessed by calculating the ratio of (C=C)/(CH_2) in Raman spectra. It showed that there was a higher unsaturated lipid level in male fish than females (Fig. 6).

As the initial site of uptake and elimination of contamination, the gills would be expected to directly interact with

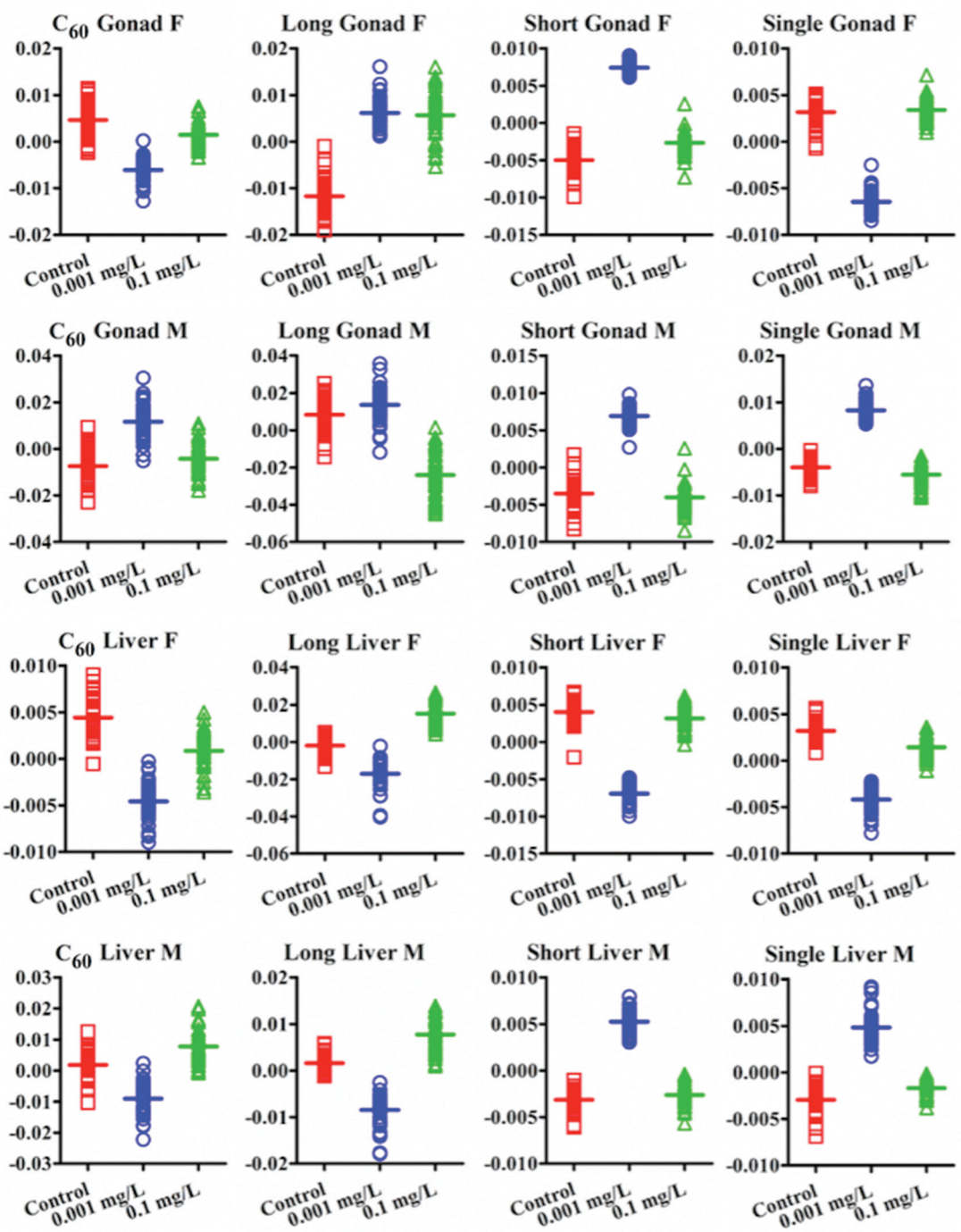

Fig. 2 One-dimensional (1-D) cross-calculated PCA-LDA scores plots in 1st space of infrared (IR) spectra derived from gonad or liver of zebrafish [male (M) or female (F)] exposed to carbon nanoparticles (CNPs) at two concentrations compared to the vehicle control. The horizontal line in the centre of each plot represents the mean value. C60, C_{60} (fullerene); long, long MWCNTs; short, short MWCNTs; single, SWCNTs.

CNPs. Therefore, CNPs would exert effects by direct physical injury and indirectly by generating reactive oxidative species (ROS) and free radicals,[36] resulting in gill inflammation.[37,38] Exposure to CNPs induced significant alterations in Amide I, Amide II, lipid and protein in both female and male fish. Additionally, slight alterations in DNA/RNA region ($\nu_{as}PO_2^-$, ~1225 cm^{-1}; $\nu_sPO_2^-$, ~1080 cm^{-1}) were observed as well. The lipid-to-protein ratio was most highly elevated in gills exposed to long MWCNTs. Short MWCNTs and SWCNTs seemed to elicit a lower lipid-to-protein ratio in gills, while C_{60} showed no significant effect ($P > 0.05$). This suggests that the size of the CNPs plays a major role in inducing inflammation in the gill, with larger sizes causing higher levels of damage.[39] Though it was reported that CNPs would be precipitated on gill mucus,[40]

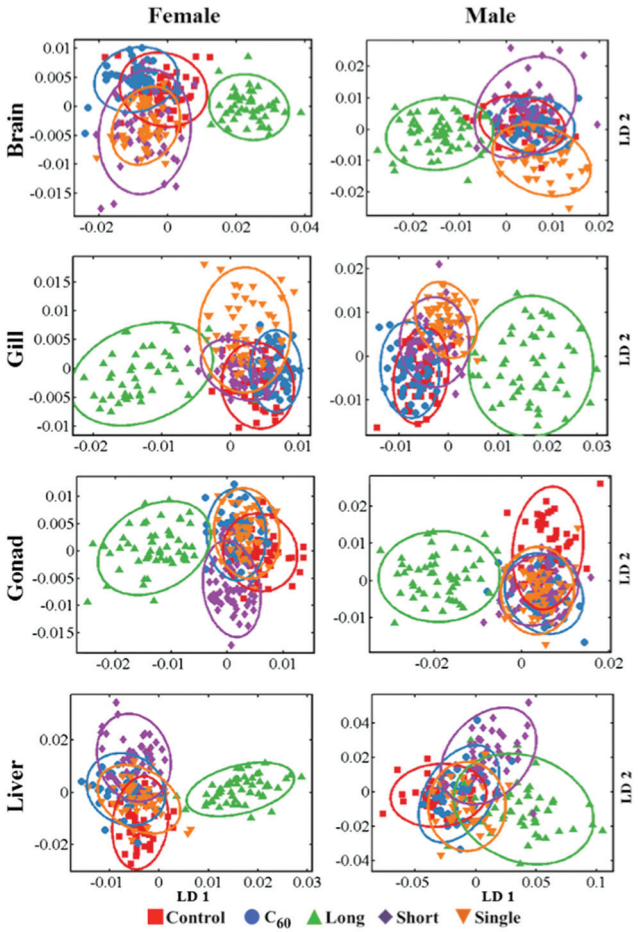

Fig. 3 Cross-calculated PCA-LDA scores plots in 2 dimensions (90% confidence ellipsoids) derived from tissues of zebrafish exposed to carbon nanoparticles (CNPs) at concentration of 0.1 mg L^{-1} and the vehicle control. C60, C_{60} (fullerene); long, long MWCNTs; short, short MWCNTs; single, SWCNTs.

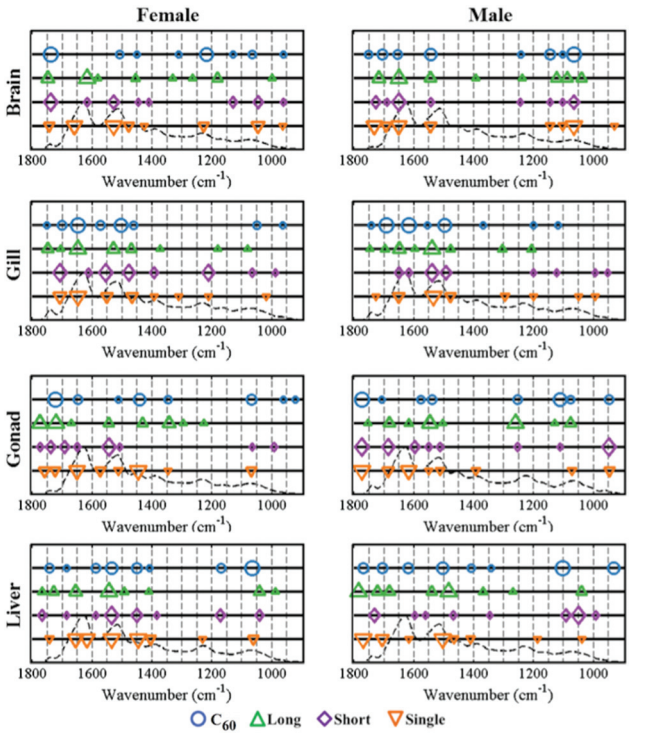

Fig. 4 Cluster vectors peak plots indicating the wavenumber basis for segregation corresponding to the tissues exposed to CNPs (0.1 mg L^{-1}). Each exposed tissue was compared with the vehicle control. The size of the symbol in cluster vectors peaks plot is proportional to the height of the corresponding peaks in the cluster vector plots, which relative to the extent of alteration compared with the vehicle control. The hint line represents a typical IR spectrum of the biochemical-fingerprint region (1800 cm^{-1}–900 cm^{-1}) of the tissue. C60, C_{60} (fullerene); long, long MWCNTs; short, short MWCNTs; single, SWCNTs.

CNPs could still penetrate the gill and be transported into the fish circulation. Even if tight junctions between gill cells dramatically reduce the permeability to CNPs, inflammation factors at the site could still facilitate their transported into the circulation to exert further effects on other organs.

Post-exposure to CNPs, the brain also showed significant alterations. Both IR and Raman spectra showed that long MWCNTs caused the most pronounced alterations in brain for both genders. In contrast, there appeared to be no significant effect of long MWCNTs on the lipid-to-protein ratio compared with control, while C_{60} induced a significant elevation of lipid-to-protein ratio, as well as short MWCNTs and single-walled CNTs. Because of their larger size, it may be difficult for long MWCNTs to penetrate through the tight junctions between the gill cells, which could also limit their ability to cross the blood–brain barrier (BBB).[41] However, with high levels of oxidative stress and even inflammation factors induced by long MWCNTs, they still dramatically altered brain spectral signatures. Raman spectra showed that male fish display higher lipid unsaturated levels than females, which could contribute to the fluidity of the cell membrane. Interestingly, C_{60} caused contrasting effects on unsaturated lipid levels of brain in both genders. In female fish, the unsaturated lipid level was increased, while it was decreased in males, both significantly. As the brain in male fish has a lower lipid-to-protein ratio but higher unsaturated levels compared with that to female fish, it means that the male brain contains less lipid, but possibly greater fluidity due to an elevated content of unsaturated lipid.[42] Thus, it is more likely that the highly lipophilic C_{60} will penetrate further into the lipid region,[43] and exert oxidative damage not only to lipid, but also to further biochemical constituents such as protein and DNA/RNA. However, the three CNTs resulted in a significant increase of unsaturated lipid levels in the female brain, while only SWCNTs caused a significant elevation in males. Due to the lower lipid-to-protein ratio in male brain compared to female, possibly implicating that the male has a thinner layer of lipid, CNPs may exert a wider range of effects in cells. This was exhibited by the IR spectra indicating a trend for CNPs to induce more effects on the DNA/RNA spectral region derived from male brain compared to female. Profiled by both the IR and Raman spectra, all CNPs widely and highly induced alterations in the protein and lipid spectral region. Complimentary to IR, Raman spectra

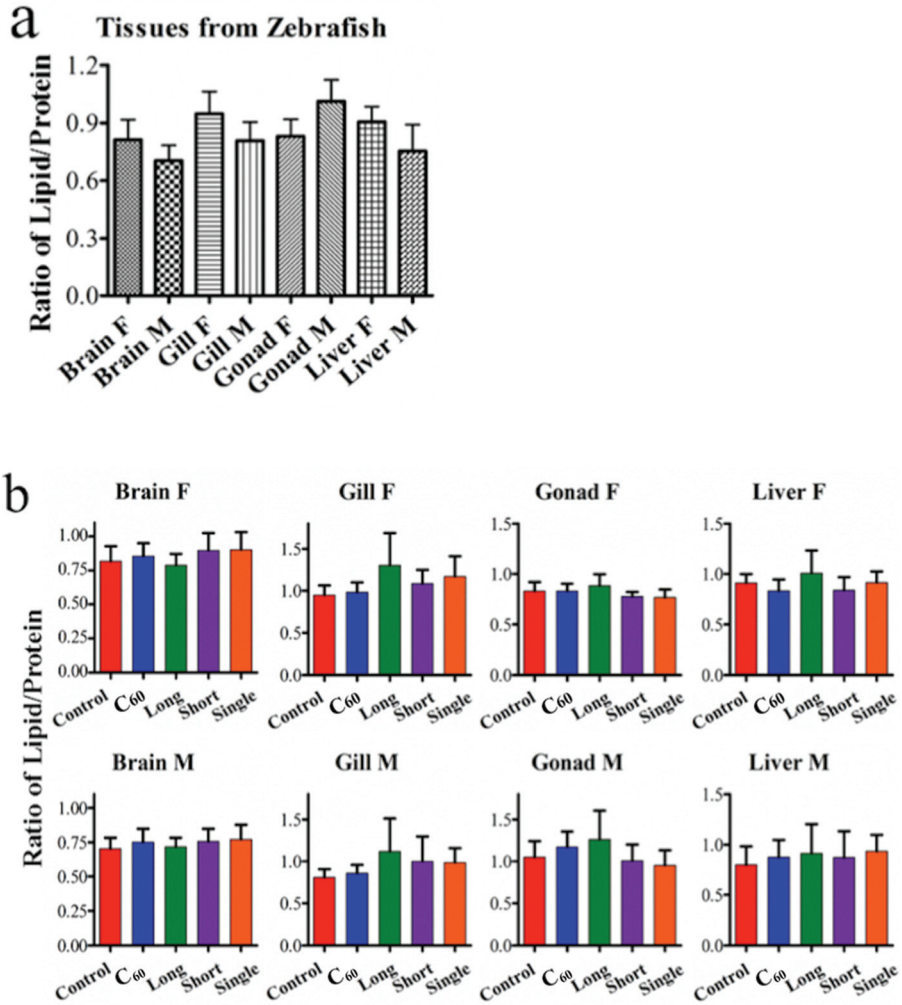

Fig. 5 Ratio of lipid to protein derived from IR spectra, Mean ± standard deviation: (a) Comparison of different tissues from female (F) and male (M) zebrafish without exposure; and, (b) comparison of tissues exposed to CNPs with the control. C60, C_{60} (fullerene); long, long MWCNTs; short, short MWCNTs; single, SWCNTs.

also indicated that CNPs caused significant effects in the spectral range associated with S–S (~524 cm^{-1}), C–S (~662 cm^{-1}) in protein and C=C in lipid (~1655 cm^{-1}). It is accepted that ROS generation is a key pathway in nanoparticle toxicity. High ROS levels could increase the depletion of thiol groups in proteins, especially glutathione (GSH), and increase the oxidized forms such as GSSG.[44,45]

The interference of CNPs in brain could perturb the hypothalamic-pituitary-gonadal axis and affect the gonads further, in addition to direct effects on these tissues. It is evidenced by IR spectra that CNP exposures resulted in significant alterations in lipids, proteins and DNA/RNA. Raman spectra also confirmed this and showed that CNPs could induce alterations associated with C–S (~662 cm^{-1}) in female fish rather than in males. With both higher lipid-to-protein ratios and higher unsaturated lipid levels, male fish are more likely to protect protein from CNP-induced oxidative stress through the antioxidant function at the lipid region. These gonadal alterations would possibly further affect reproductive activity.

As an important organ for active metabolism and detoxification, the liver seems quite sensitive to CNP exposure. IR spectra show that the most pronounced alterations induced by C_{60} were associated with DNA/RNA region ($\nu_s PO_2^-$, ~1080 cm^{-1}) in both genders, followed by alterations located in the protein and lipid spectral regions. Limited effects in DNA/RNA caused from short MWCNTs and SWCNTs were observed as well. In contrast, long MWCNTs seemed to have a weak capability to affect the liver in the DNA/RNA region, but caused significant alterations in lipids and proteins. The lipid-to-protein ratio in liver was significantly elevated by long MWCNTs in both genders. C_{60} and short MWCNTs reduced the lipid-to-protein ratio in female fish, in the absence of significant effects in males, while SWCNTs only elevated that ratio in males. The change in lipid-to-protein ratio in liver could be caused from the direct interference of CNPs, while the lipid accumulation was possibly due to CNP-induced inflammatory stress; long MWCNTs especially appear to disrupt cholesterol trafficking in liver tissue.[46]

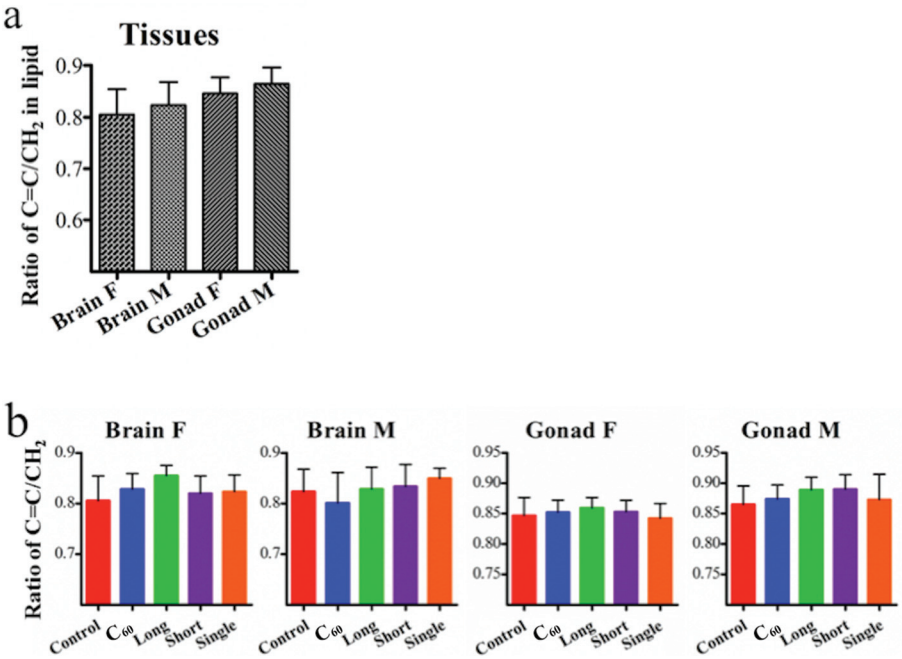

Fig. 6 Ratio of (C=C) to (CH_2) in lipid derived from Raman spectra, Mean ± standard deviation: (a) comparison of brain and gonads in female (F) and male (M) zebrafish without exposure; and, (b) comparison of the tissues (brain and gonads) exposed to CNPs with the control. C60, C_{60} (fullerene); long, long MWCNTs; short, short MWCNTs; single, SWCNTs.

4. Conclusion

Herein, biospectroscopy is presented as a global approach to nanotoxicity assessment, providing one with a profile of CNP-induced alterations. IR and Raman spectra show that CNPs can induce significant alterations in fish, and also highlights the differing effects of four CNPs. Although it could not be shown that the CNPs passed through the bio-barrier (*e.g.*, BBB) and moved to further tissues in fish, such as brain and gonads, the fact that these organs were affected is a key indicator from the perspective of biological effects. Possibly the alterations observed in the brain and gonads demonstrate that CNPs do exert potential toxic effects on both nervous and reproductive systems.[47–50] In addition, the alterations in DNA/RNA spectral regions caused by CNPs, especially by C_{60}, suggested that DNA methylation could be perturbed following the CNP exposure. It is necessary to conduct further investigations to assess the DNA methylation levels in tissues of exposed fish. These effects may be extrapolated to other organisms.[51] Furthermore, future studies need to examine whether the effects of CNPs impact on reproductive activity and test if transgenerational effects might arise.

Acknowledgements

We would like to thank Yanqiu Liang, Yuxia Jiang and Dr Guoyong Huang for their kind assistance in setting up experiments. Funding for the laboratory experiments in this study from the Chinese Academy of Sciences is greatly acknowledged.

References

1 A. W. Jensen, S. R. Wilson and D. I. Schuster, *Bioorg. Med. Chem.*, 1996, **4**, 767–779.
2 R. Bakry, R. M. Vallant, M. Najam-ul-Haq, M. Rainer, Z. Szabo, C. W. Huck and G. K. Bonn, *Int. J. Nanomed.*, 2007, **2**, 639.
3 R. H. Baughman, A. A. Zakhidov and W. A. de Heer, *Science*, 2002, **297**, 787–792.
4 J. M. Planeix, N. Coustel, B. Coq, V. Brotons, P. S. Kumbhar, R. Dutartre, P. Geneste, P. Bernier and P. M. Ajayan, *J. Am. Chem. Soc.*, 1994, **116**, 7935–7936.
5 A. Bianco, K. Kostarelos and M. Prato, *Curr. Opin. Chem. Biol.*, 2005, **9**, 674–679.
6 A. Nel, T. Xia, L. Mädler and N. Li, *Science*, 2006, **311**, 622–627.
7 H. Meng, T. Xia, S. George and A. E. Nel, *ACS Nano*, 2009, **3**, 1620–1627.
8 G. Jia, H. Wang, L. Yan, X. Wang, R. Pei, T. Yan, Y. Zhao and X. Guo, *Environ. Sci. Technol.*, 2005, **39**, 1378–1383.
9 S. K. Manna, S. Sarkar, J. Barr, K. Wise, E. V. Barrera, O. Jejelowo, A. C. Rice-Ficht and G. T. Ramesh, *Nano Lett.*, 2005, **5**, 1676–1684.
10 J. Chłopek, B. Czajkowska, B. Szaraniec, E. Frackowiak, K. Szostak and F. Béguin, *Carbon*, 2006, **44**, 1106–1111.
11 M. Bottini, S. Bruckner, K. Nika, N. Bottini, S. Bellucci, A. Magrini, A. Bergamaschi and T. Mustelin, *Toxicol. Lett.*, 2006, **160**, 121–126.

12 A. Simon-Deckers, S. Loo, M. Mayne-L'hermite, N. Herlin-Boime, N. Menguy, C. Reynaud, B. Gouget and M. Carrière, *Environ. Sci. Technol.*, 2009, **43**, 8423–8429.
13 Z. Tong, M. Bischoff, L. Nies, B. Applegate and R. F. Turco, *Environ. Sci. Technol.*, 2007, **41**, 2985–2991.
14 E. Navarro, A. Baun, R. Behra, N. Hartmann, J. Filser, A.-J. Miao, A. Quigg, P. Santschi and L. Sigg, *Ecotoxicology*, 2008, **17**, 372–386.
15 S. B. Lovern and R. Klaper, *Environ. Toxicol. Chem.*, 2006, **25**, 1132–1137.
16 S. Zhu, E. Oberdörster and M. L. Haasch, *Mar. Environ. Res.*, 2006, **62**(Supplement 1), S5–S9.
17 J. K. Folkmann, L. Risom, N. R. Jacobsen, H. Wallin, S. Loft and P. Møller, *Environ. Health Perspect.*, 2009, **117**, 703–708.
18 A. Kroll, M. H. Pillukat, D. Hahn and J. Schnekenburger, *Eur. J. Pharm. Biopharm.*, 2009, **72**, 370–377.
19 D. I. Ellis and R. Goodacre, *Analyst*, 2006, **131**, 875–885.
20 V. Llabjani, J. Trevisan, K. C. Jones, R. F. Shore and F. L. Martin, *Environ. Sci. Technol.*, 2010, **44**, 3992–3998.
21 V. Llabjani, J. D. Crosse, A. A. Ahmadzai, I. I. Patel, W. Pang, J. Trevisan, K. C. Jones, R. F. Shore and F. L. Martin, *Environ. Sci. Technol.*, 2011, **45**, 10706–10712.
22 J. G. Kelly, J. l. Trevisan, A. D. Scott, P. L. Carmichael, H. M. Pollock, P. L. Martin-Hirsch and F. L. Martin, *J. Proteome Res.*, 2011, **10**, 1437–1448.
23 P. Knief, C. Clarke, E. Herzog, M. Davoren, F. M. Lyng, A. D. Meade and H. J. Byrne, *Analyst*, 2009, **134**, 1182–1191.
24 J. Dorney, F. Bonnier, A. Garcia, A. Casey, G. Chambers and H. J. Byrne, *Analyst*, 2012, **137**, 1111–1119.
25 J. Trevisan, P. P. Angelov, P. L. Carmichael, A. D. Scott and F. L. Martin, *Analyst*, 2012, **137**, 3202–3215.
26 J. Li, R. Strong, J. Trevisan, S. W. Fogarty, N. J. Fullwood, K. C. Jones and F. L. Martin, *Environ. Sci. Technol.*, 2013, **47**, 10005–10011.
27 M. J. Riding, F. L. Martin, J. Trevisan, V. Llabjani, I. I. Patel, K. C. Jones and K. T. Semple, *Environ. Pollut.*, 2012, **163**, 226–234.
28 M. N. Moore, *Environ. Int.*, 2006, **32**, 967–976.
29 T. W. K. Fraser, H. C. Reinardy, B. J. Shaw, T. B. Henry and R. D. Handy, *Nanotoxicology*, 2011, **5**, 98–108.
30 J. Cheng, C. M. Chan, L. M. Veca, W. L. Poon, P. K. Chan, L. Qu, Y.-P. Sun and S. H. Cheng, *Toxicol. Appl. Pharmacol.*, 2009, **235**, 216–225.
31 S. A. Brittijn, S. J. Duivesteijn, M. Belmamoune, L. F. M. Bertens, W. Bitter, J. D. de Bruijn, D. L. Champagne, E. Cuppen, G. Flik, C. M. Vandenbroucke-Grauls, R. A. J. Janssen, I. M. L. de Jong, E. R. de Kloet, A. Kros, A. H. Meijer, J. R. Metz, A. M. van der Sar, M. J. M. Schaaf, S. Schulte-Merker, H. P. Spaink, P. P. Tak, F. J. Verbeek, M. J. Vervoordeldonk, F. J. Vonk, F. Witte, H. Yuan and M. K. Richardson, *Int. J. Dev. Biol.*, 2009, **53**, 835–850.
32 H. Segner, *Comp. Biochem. Physiol., Part C: Toxicol. Pharmacol.*, 2009, **149**, 187–195.
33 J. Trevisan, P. P. Angelov, A. D. Scott, P. L. Carmichael and F. L. Martin, *Bioinformatics*, 2013, **29**, 1095–1097.
34 H. Wu, J. V. Volponi, A. E. Oliver, A. N. Parikh, B. A. Simmons and S. Singh, *Proc. Natl. Acad. Sci. U. S. A.*, 2011, **108**, 3809–3814.
35 A. R. R. Péry, J. Devillers, C. Brochot, E. Mombelli, O. Palluel, B. Piccini, F. Brion and R. Beaudouin, *Environ. Sci. Technol.*, 2013, **48**, 781–790.
36 T. B. Henry, E. J. Petersen and R. N. Compton, *Curr. Opin. Biotechnol.*, 2011, **22**, 533–537.
37 N. Lewinski, V. Colvin and R. Drezek, *Small*, 2008, **4**, 26–49.
38 D. Crouzier, S. Follot, E. Gentilhomme, E. Flahaut, R. Arnaud, V. Dabouis, C. Castellarin and J. C. Debouzy, *Toxicology*, 2010, **272**, 39–45.
39 Y. Sato, A. Yokoyama, K.-i. Shibata, Y. Akimoto, S.-i. Ogino, Y. Nodasaka, T. Kohgo, K. Tamura, T. Akasaka, M. Uo, K. Motomiya, B. Jeyadevan, M. Ishiguro, R. Hatakeyama, F. Watari and K. Tohji, *Mol. BioSyst.*, 2005, **1**, 176–182.
40 C. J. Smith, B. J. Shaw and R. D. Handy, *Aquat. Toxicol.*, 2007, **82**, 94–109.
41 A. Pietroiusti, L. Campagnolo and B. Fadeel, *Small*, 2013, **9**, 1557–1572.
42 C. Chatgilialoglu, C. Ferreri, M. Melchiorre, A. Sansone and A. Torreggiani, *Chem. Rev.*, 2013, **114**, 255–284.
43 E. Oberdörster, *Environ. Health Perspect.*, 2004, **112**, 1058–1062.
44 M. L. Circu and T. Y. Aw, *Free Radical Biol. Med.*, 2010, **48**, 749–762.
45 O. Zitka, S. Skalickova, J. Gumulec, M. Masarik, V. Adam, J. Hubalek, L. Trnkova, J. Kruseova, T. Eckschlager and R. Kizek, *Oncol. Lett.*, 2012, **4**, 1247–1253.
46 K. L. Ma, X. Z. Ruan, S. H. Powis, Y. Chen, J. F. Moorhead and Z. Varghese, *Hepatology*, 2008, **48**, 770–781.
47 G. Bardi, A. Nunes, L. Gherardini, K. Bates, K. T. Al-Jamal, C. Gaillard, M. Prato, A. Bianco, T. Pizzorusso and K. Kostarelos, *PLoS One*, 2013, **8**, e80964.
48 M. Ema, N. Kobayashi, M. Naya, S. Hanai and J. Nakanishi, *Reprod. Toxicol.*, 2010, **30**, 343–352.
49 Y. Bai, Y. Zhang, J. Zhang, Q. Mu, W. Zhang, E. R. Butch, S. E. Snyder and B. Yan, *Nat. Nanotechnol.*, 2010, **5**, 683–689.
50 T.-T. Win-Shwe and H. Fujimaki, *Int. J. Mol. Sci.*, 2011, **12**, 6267–6280.
51 S. Rhiem, M. J. Riding, W. Baumgartner, F. L. Martin, K. T. Semple, K. C. Jones, A. Schäffer and H. M. Maes, *Environ. Pollut.*, 2014, **196C**, 431–439.

Electronic Supplementary Material (ESI) for Analyst.

Electronic Supporting Information

Real-world carbon nanoparticle exposures induce brain and gonadal alterations in zebrafish (*Danio rerio*) as determined by biospectroscopy techniques

Junyi Li[a], *Guangguo Ying*[b], *Kevin C. Jones*[a] *and Francis L. Martin*[a]*

[a] Centre for Biophotonics, Lancaster Environment Centre, Lancaster University, Lancaster LA1 4YQ, UK; [b] State Key Laboratory of Organic Geochemistry, Guangzhou Institute of Geochemistry, Chinese Academy of Science, Guangzhou 510640, China

*Corresponding author: email: f.martin@lancaster.ac.uk; phone: +44 (0)1524 510206; fax: +44 (0)1524 510217

Abbreviations:

C_{60}, fullerene
CNTs, carbon nanotubes
Control, vehicle control
F, female
Long, long MWCNTs
M, male
MWCNTs, multi-walled carbon nanotubes
Short, short MWCNTs
Single, single-walled CNTs

Figure S1 Scanning electron microscopy (SEM) images of **(a)** C_{60} fullerene; **(b)** long MWCNTs; **(c)** short MWCNTs; and, **(d)** single-walled CNTs. For characterization, corresponding Raman spectra are also shown.

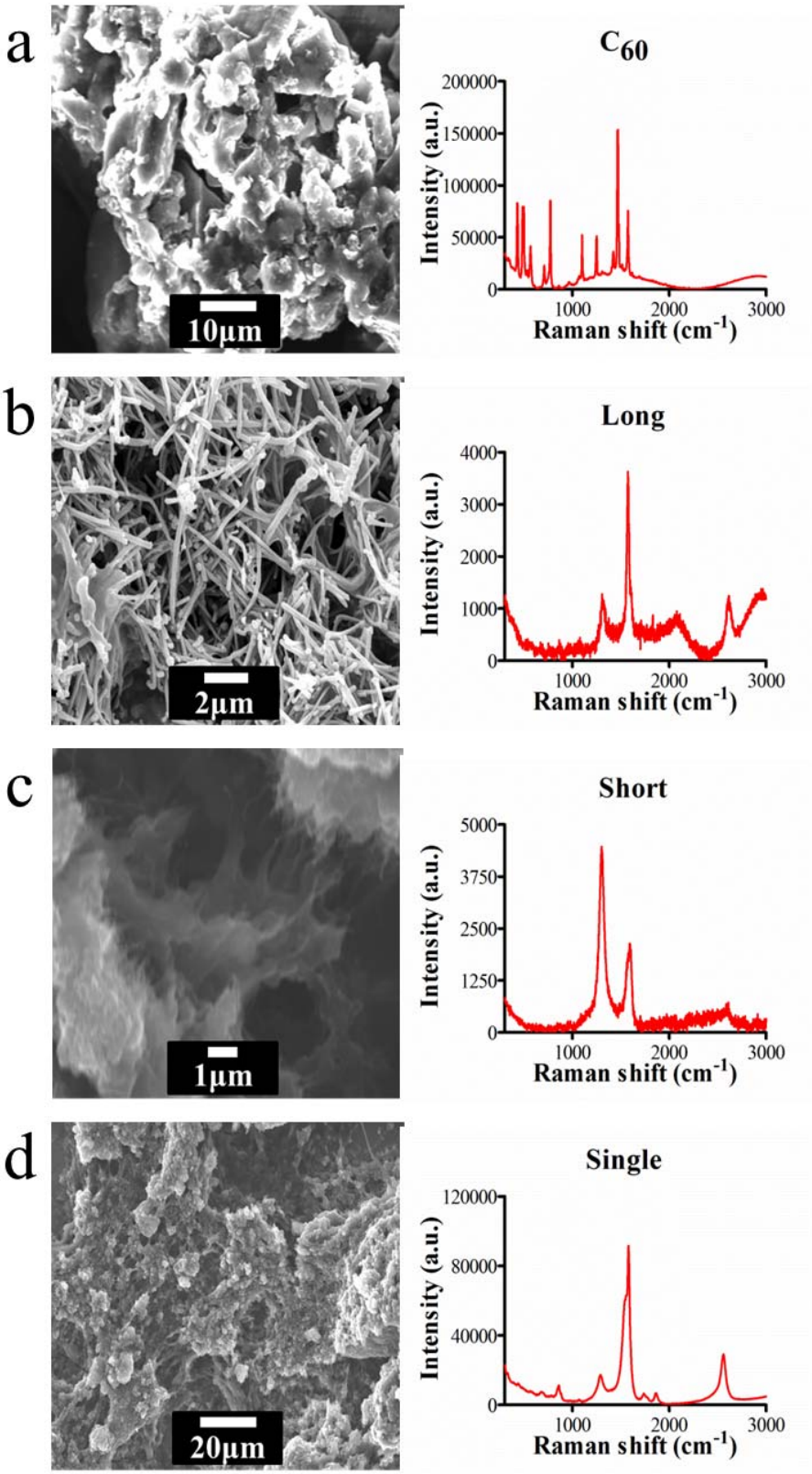

Figure S2 The wet body weight and length of zebrafish.

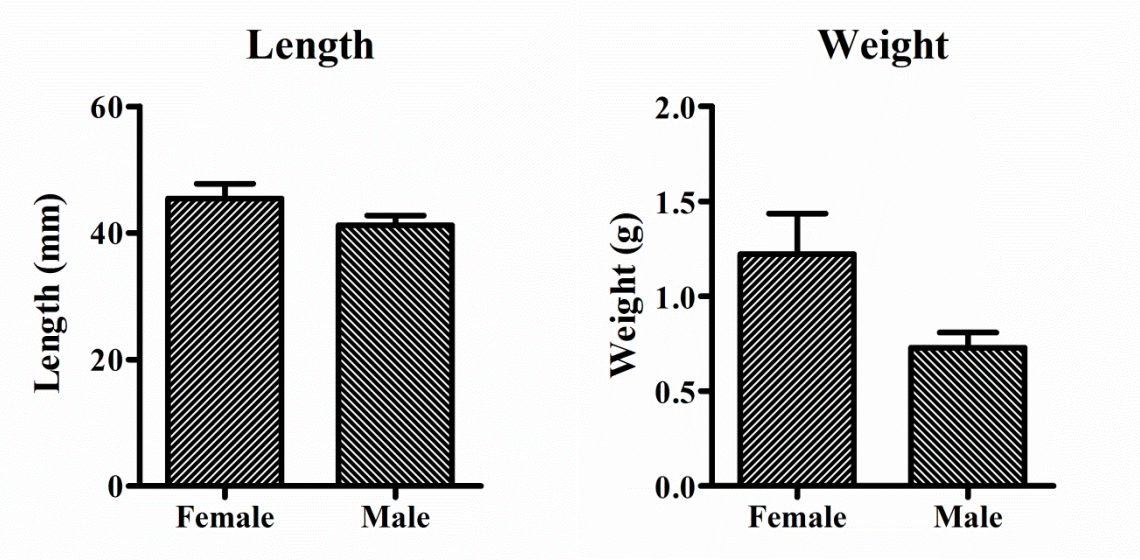

	Female		Male	
	Weight (g)	Length (mm)	Weight (g)	Length (mm)
Mean	1.221	45.431	0.782	41.225
SD	0.214	2.342	0.081	1.533

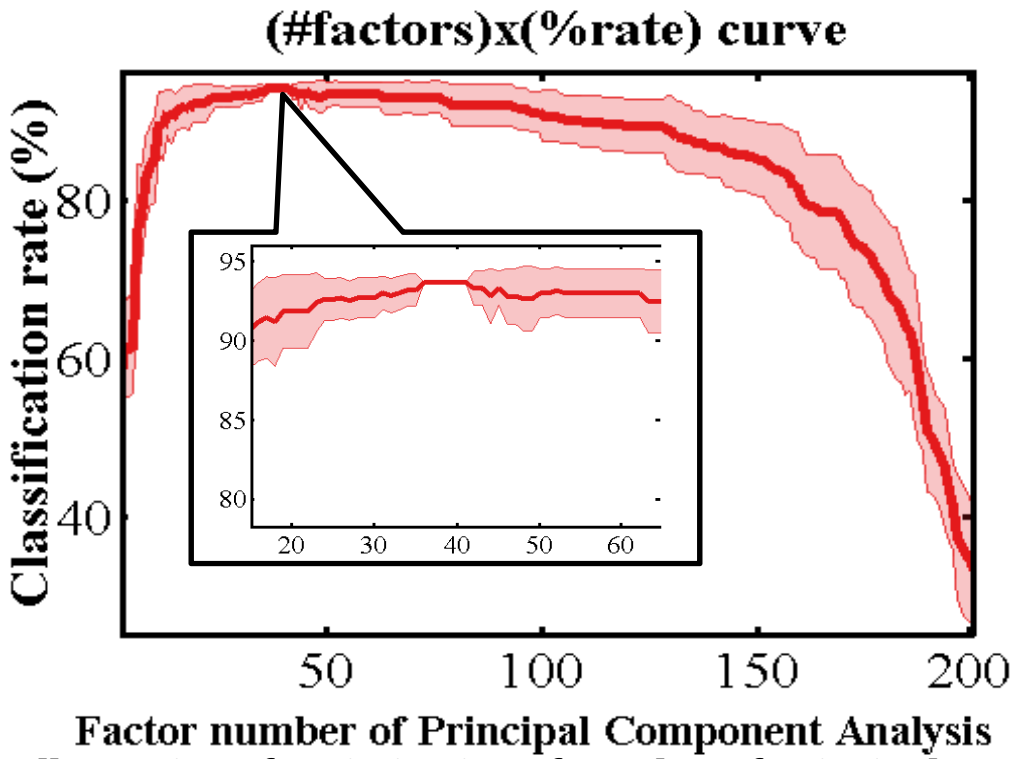

Figure S3. Illustration of optimization of number of principal components (PCs) to use in PCA-LDA. The dataset in this illustration was the NP-8 dataset (refer to Table S1). This procedure was repeated similarly with all the other seven datasets. The optimization searches for the optimal number of PCs for the PCA stage of a PCA-LDC classifier [(PCA as feature extraction, followed by a linear discriminant classifier (LDC)]. The search space is from 1 to 199 PCs and the number of PCs with highest average classification rate is selected for PCA-LDA. Classification rates were obtained through 10-fold cross-validation. The thick line is the average classification rate, and the hachured area represents the ± standard deviation range.

A step-by-step protocol is available at http://irootlab.googlecode.com, allowing for reproduction of the PCA-LDC optimization on a different dataset.

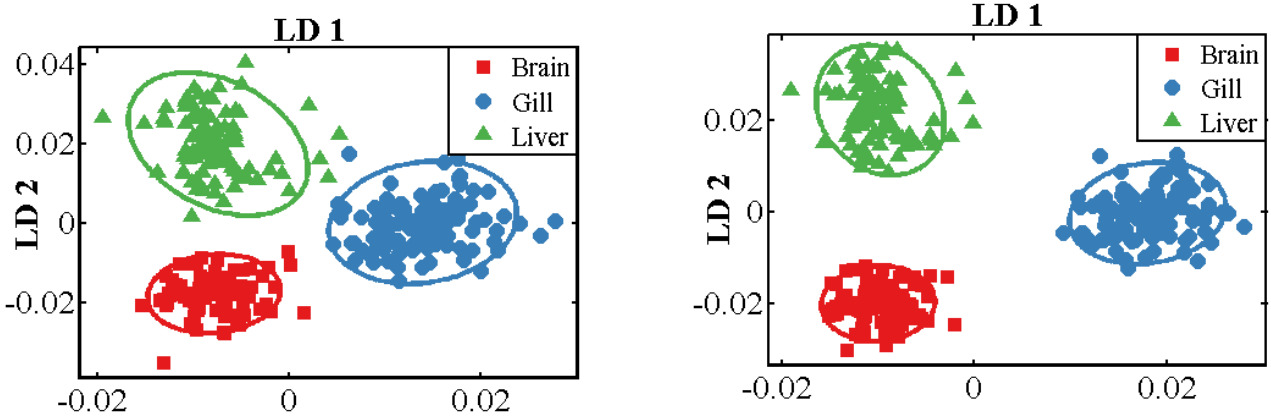

Figure S4 Two-dimensional **cross-calculated PCA-LDA** scores plot (*90% confidence ellipsoids*) derived from zebrafish tissues exposed to **C_{60}** interrogated by **ATR-FTIR spectroscopy**.

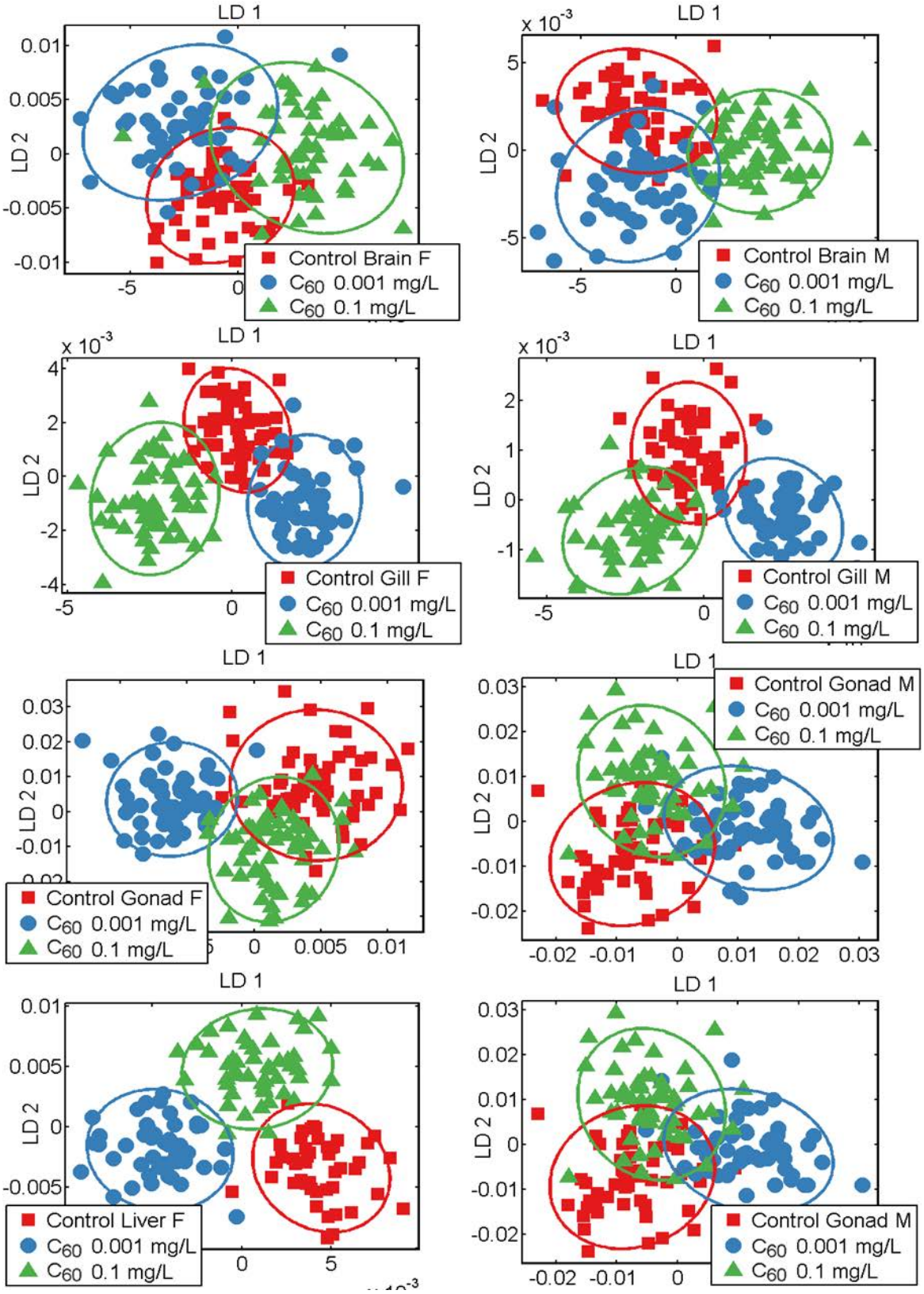

Figure S5 Two-dimensional **cross-calculated PCA-LDA** scores plot (*90% confidence ellipsoids*) derived from zebrafish tissues exposed to **long MWCNTs** interrogated by **ATR-FTIR spectroscopy**.

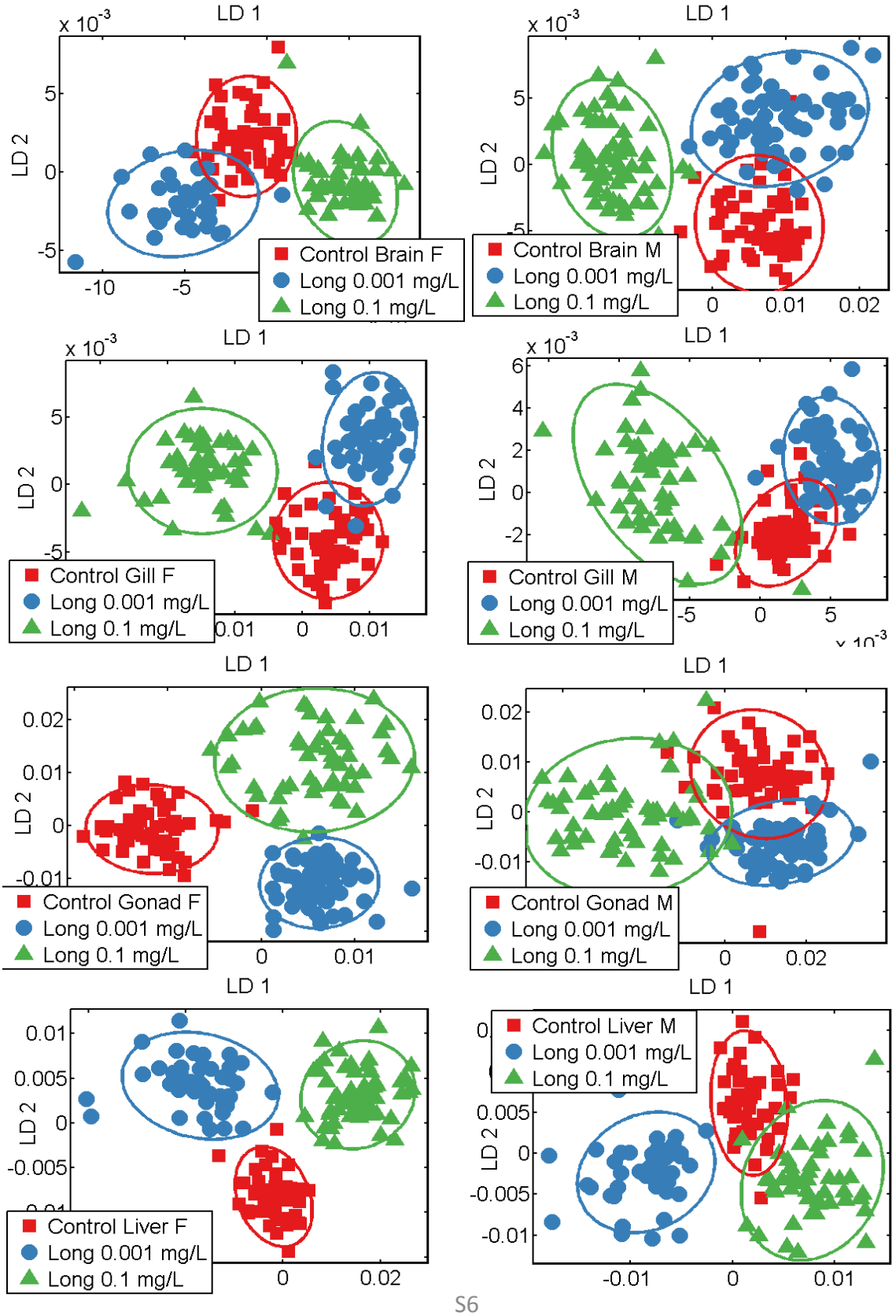

Figure S6 Two-dimensional **cross-calculated PCA-LDA** scores plot (*90% confidence ellipsoids*) derived from zebrafish tissues exposed to **short MWCNTs** interrogated by **ATR-FTIR spectroscopy**.

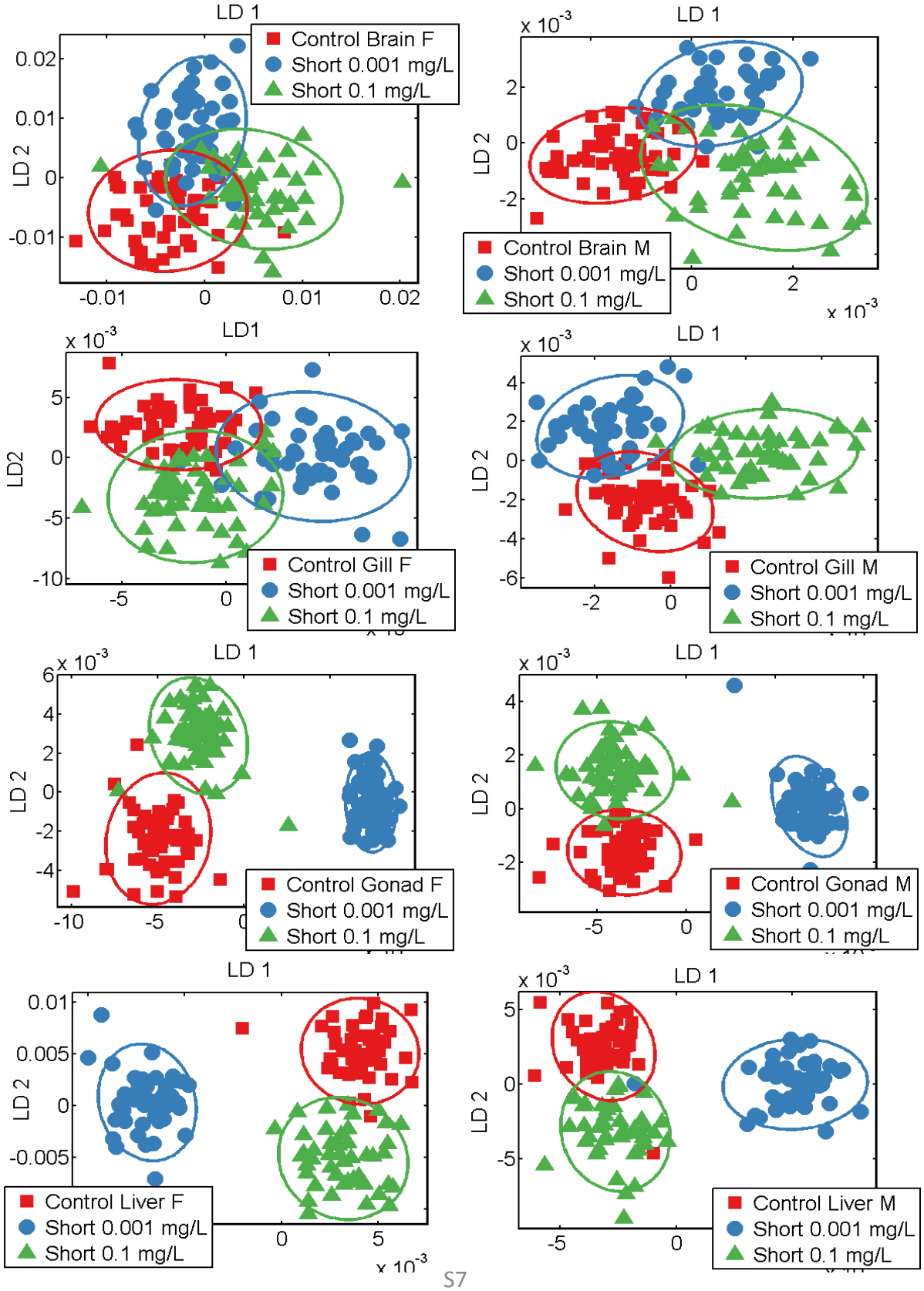

Figure S7 Two-dimensional **cross-calculated PCA-LDA** scores plot (*90% confidence ellipsoids*) derived from zebrafish tissues exposed to **single-walled CNTs** interrogated by **ATR-FTIR spectroscopy**.

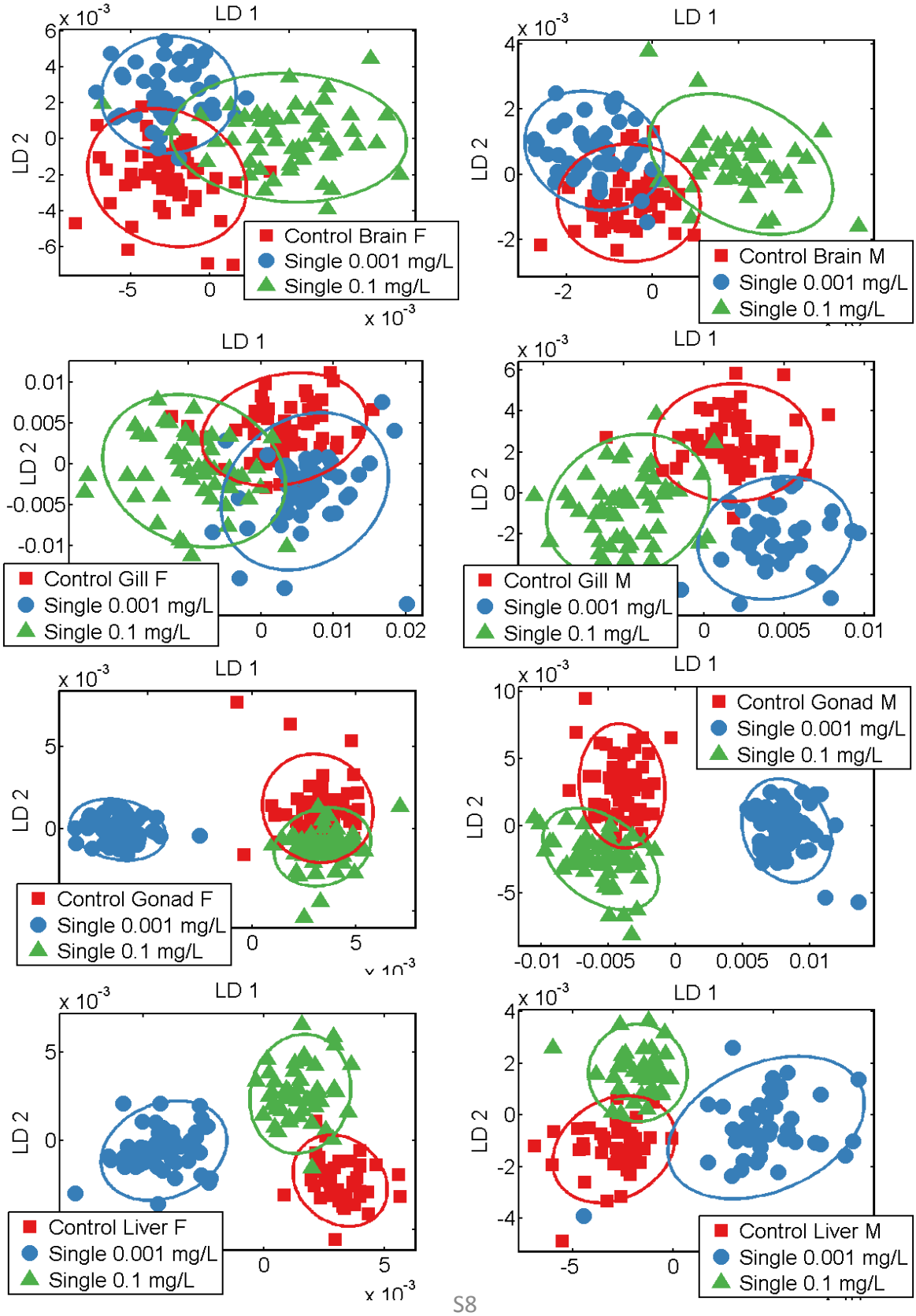

Figure S8 Cross-calculated PCA-LDA cluster vectors plots responsible for the wavenumber basis for segregation of zebrafish **brain, gill, gonads** and **liver** exposed to **C_{60}** or **long MWCNTs** by **ATR-FTIR spectroscopy**. Each treatment was compared to the control. The size of the marker symbol is proportional to the height of corresponding cluster vectors peak.

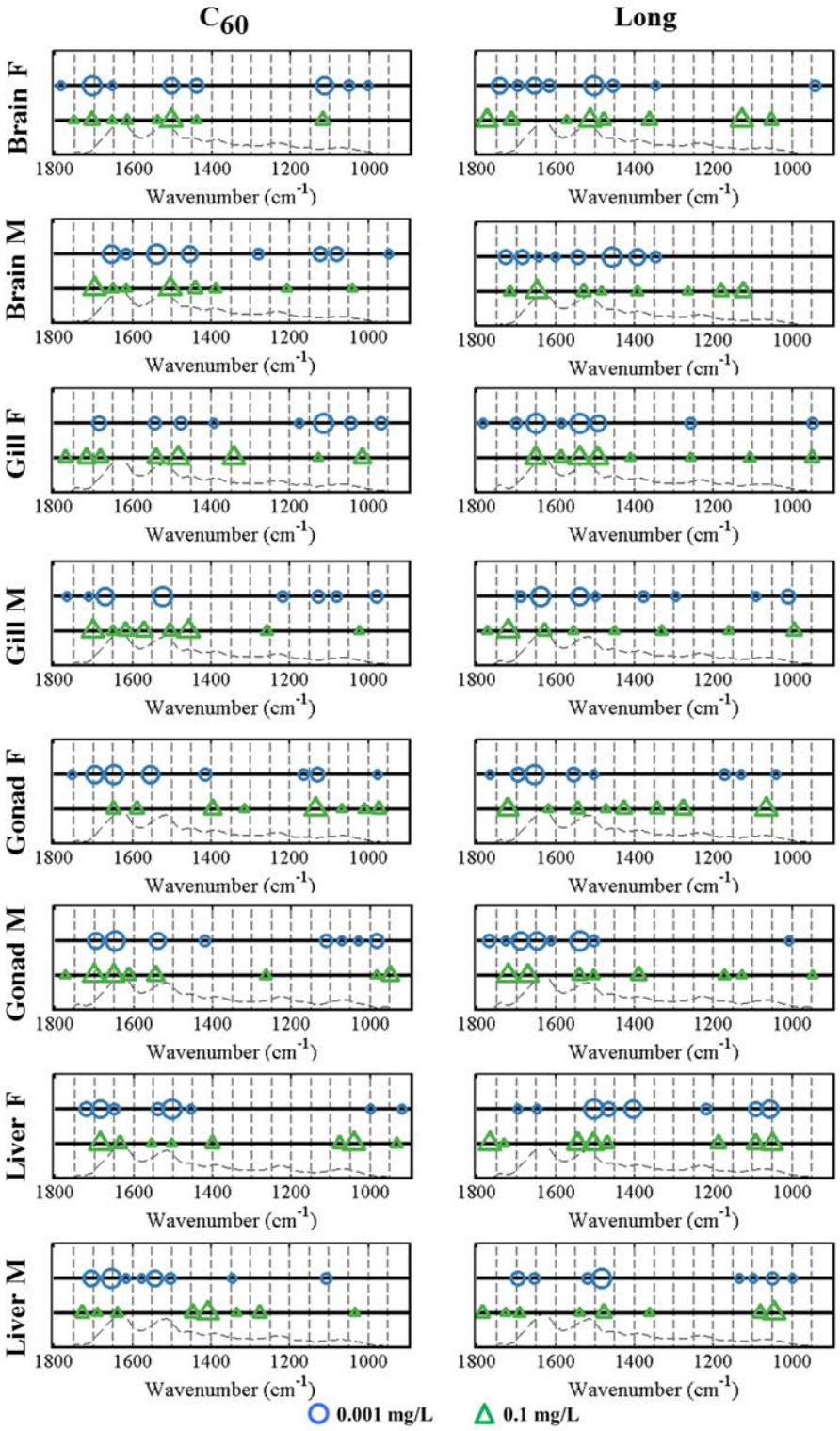

Figure S9 Cross-calculated PCA-LDA cluster vectors plots responsible for the wavenumber basis for segregation of zebrafish **brain, gill, gonads** and **liver** exposed to **short MWCNTs** or **single-walled CNTs** by **ATR-FTIR spectroscopy**. Each treatment was compared to the control. The size of the marker symbol is proportional to the height of corresponding cluster vectors peak.

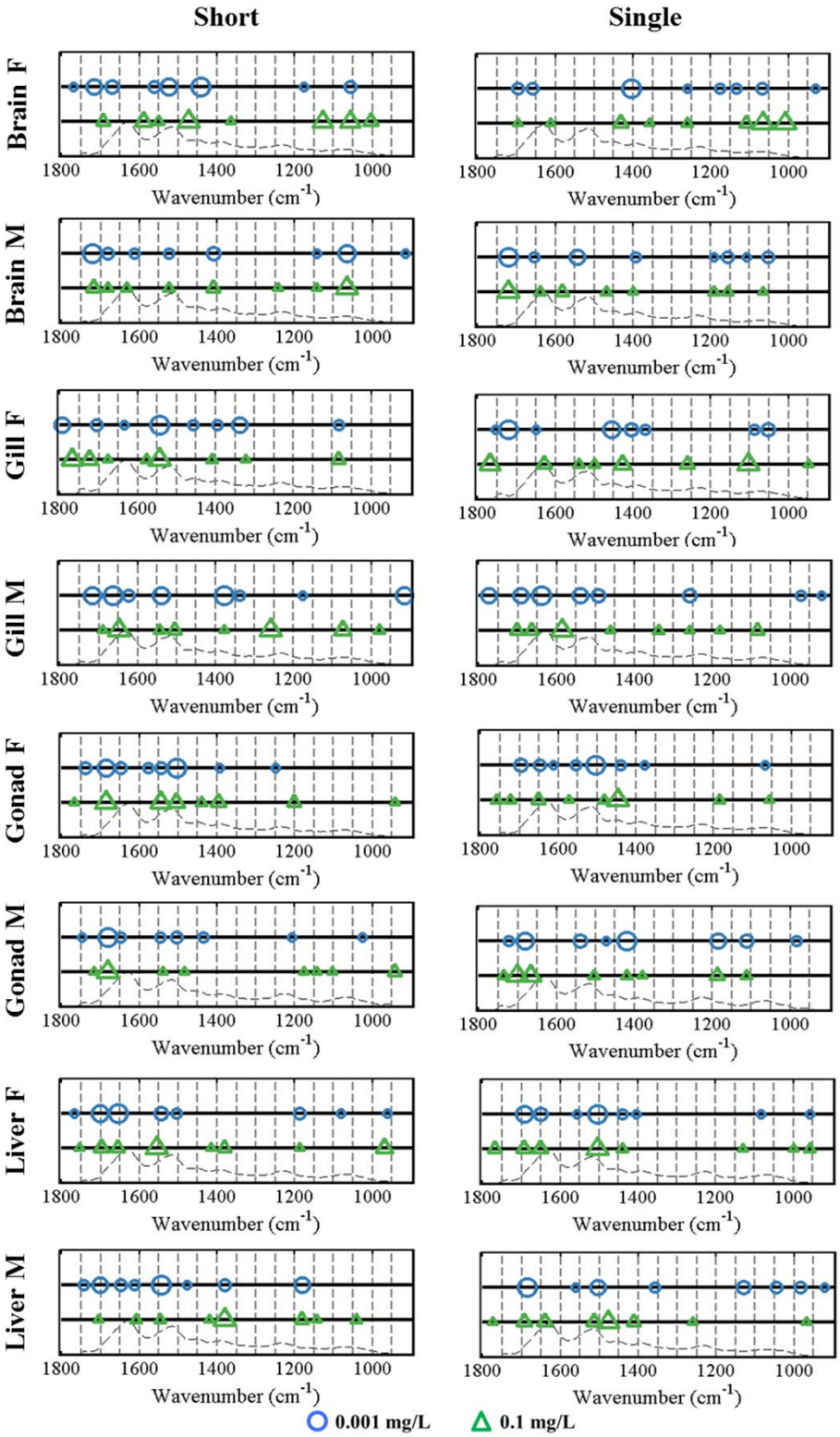

Figure S10 Cross-calculated PCA-LDA cluster vectors plots indicating the wavenumber basis for segregation of zebrafish tissues exposed to C_{60} by **ATR-FTIR spectroscopy**. Each treatment was compared to the control. The height of the cluster vectors peak is proportional to the extent of biochemical alteration compared to the vehicle control.

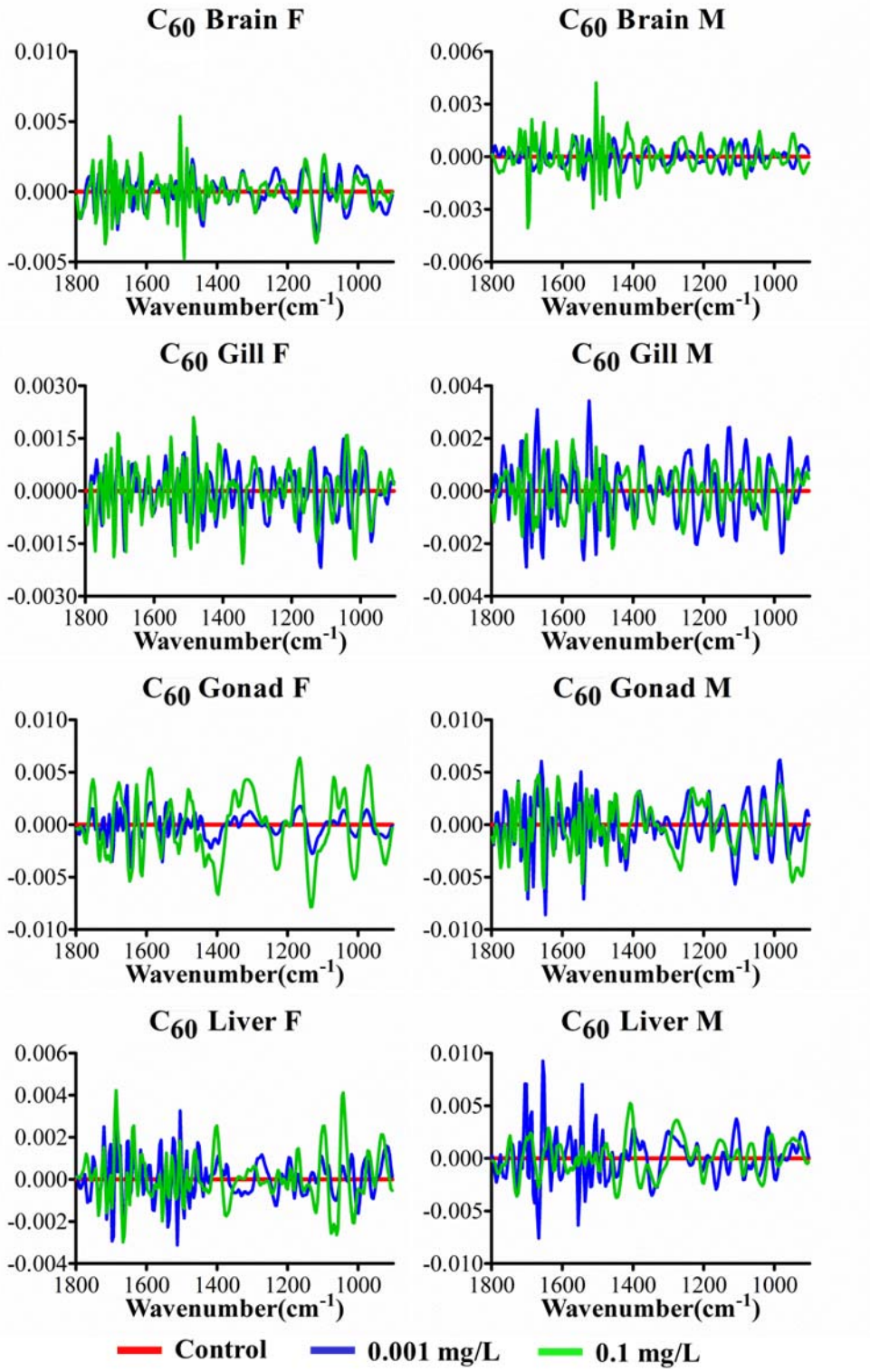

Figure S11 Cross-calculated PCA-LDA cluster vectors plots indicating the wavenumber basis for segregation of zebrafish tissues exposed to **long MWCNTs** by **ATR-FTIR spectroscopy**. Each treatment was compared to the control. The height of the cluster vectors peak is proportional to the extent of biochemical alteration compared to the vehicle control.

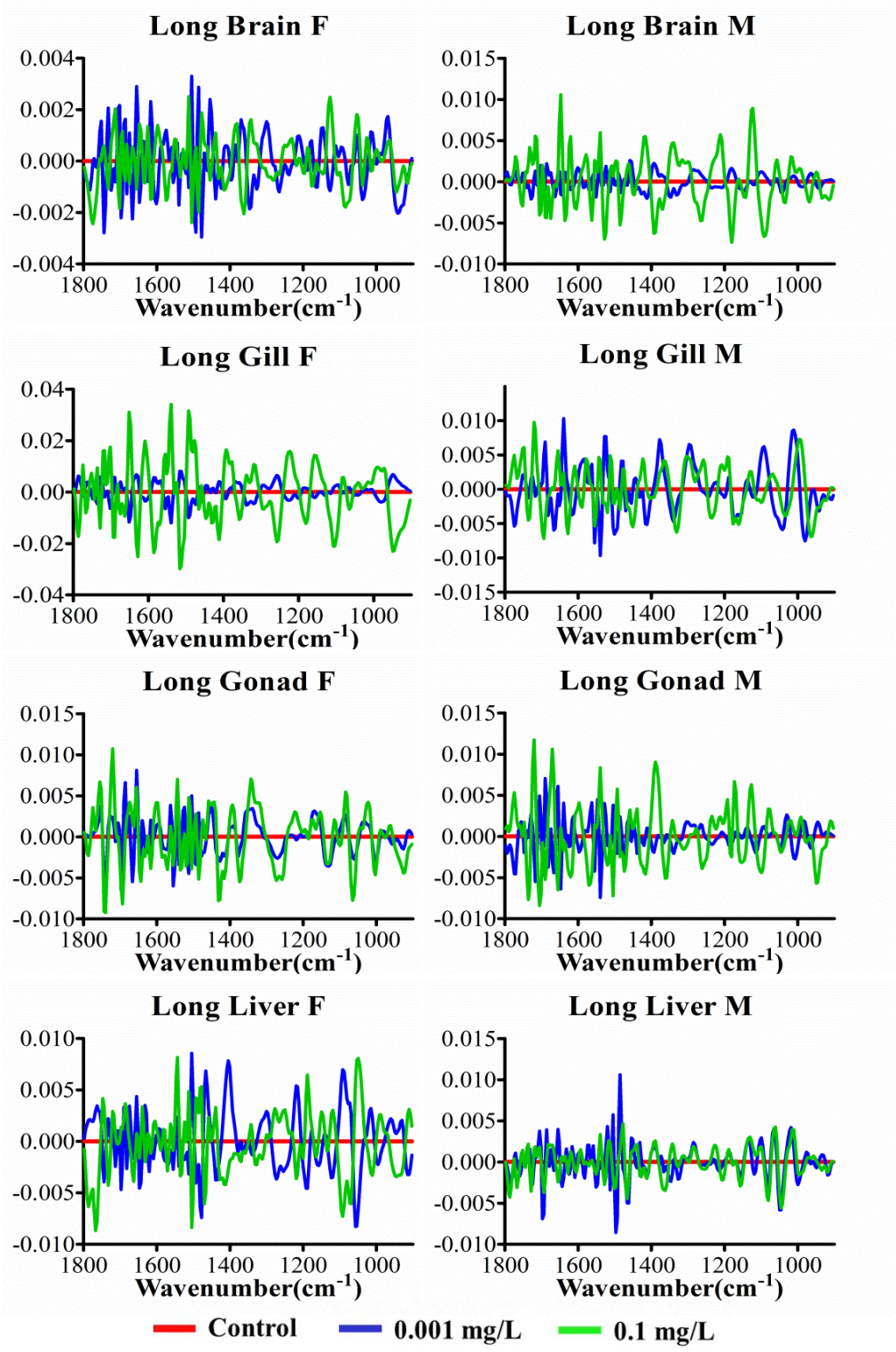

Figure S12 Cross-calculated PCA-LDA cluster vectors plots indicating the wavenumber basis for segregation of zebrafish tissues exposed to **short MWCNTs** by **ATR-FTIR spectroscopy**. Each treatment was compared to the control. The height of the cluster vectors peak is proportional to the extent of biochemical alteration compared to the vehicle control.

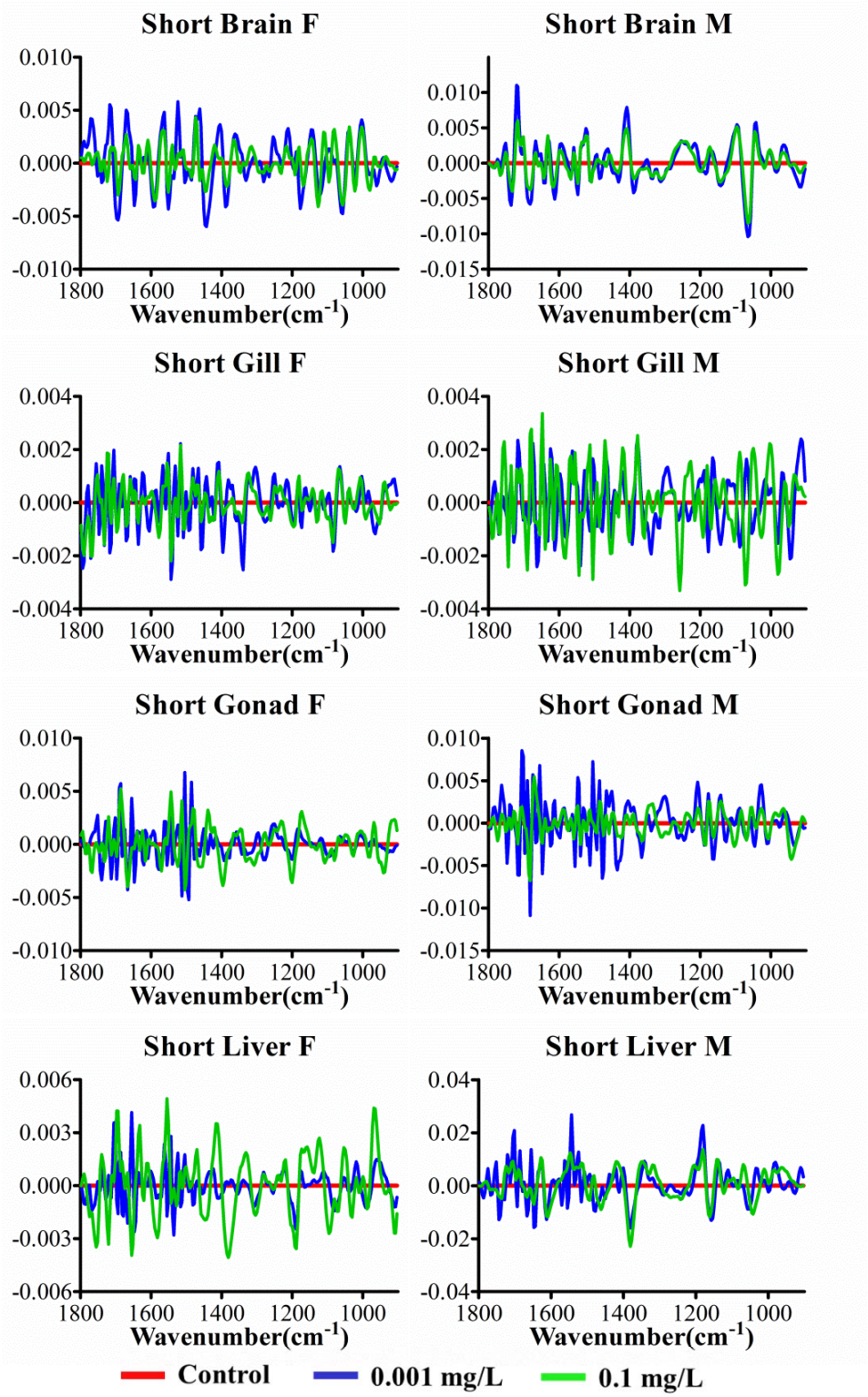

Figure S13 Cross-calculated PCA-LDA cluster vectors plots indicating the wavenumber basis for segregation of zebrafish tissues exposed to **single-walled CNTs** by **ATR-FTIR spectroscopy**. Each treatment was compared to the control. The height of the cluster vectors peak is proportional to the extent of biochemical alteration compared to the vehicle control.

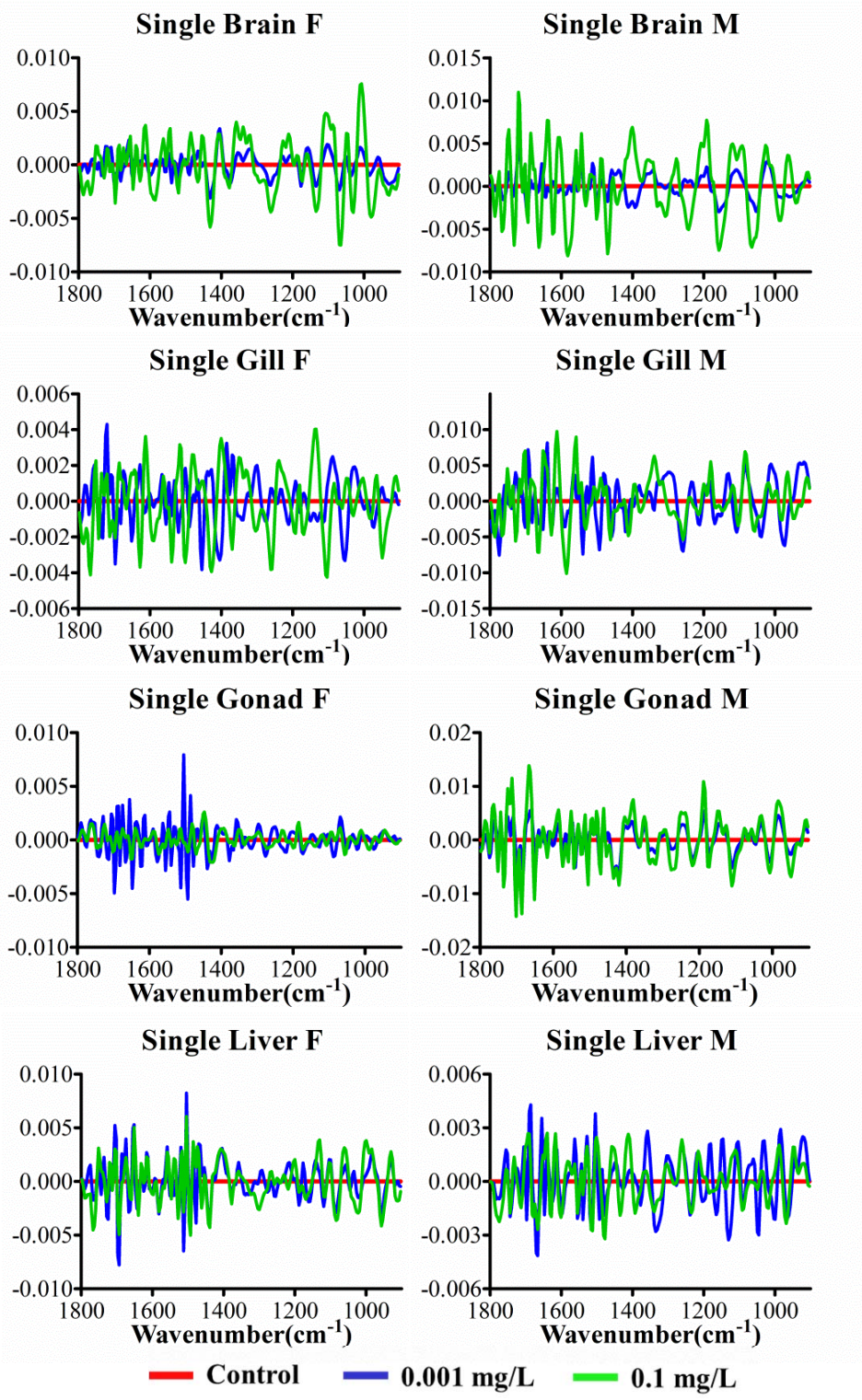

Figure S14 Cross-calculated PCA-LDA cluster vectors plots indicating the wavenumber basis for segregation of zebrafish tissues exposed to **CNPs** by **ATR-FTIR spectroscopy**. Each treatment was compared to the control. The height of the cluster vectors peak is proportional to the extent of biochemical alterations compared to the vehicle control.

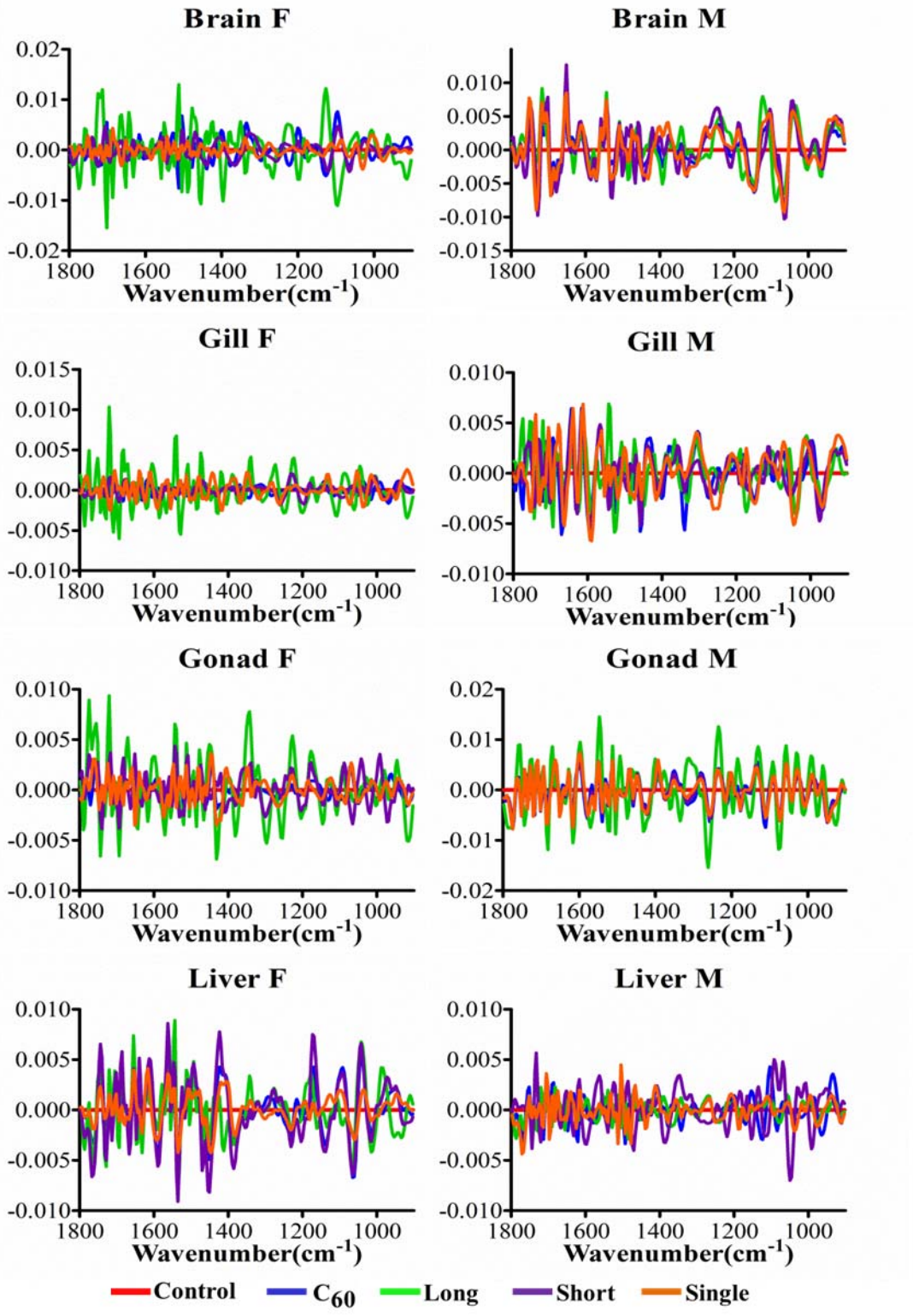

Figure S15 Two-dimension **cross-calculated PCA-LDA** scores plot (*90% confidence ellipsoids*) derived from zebrafish **brain** and **gonad** exposed to **CNPs** at concentration of 0.1 mg/L interrogated by **Raman spectroscopy**.

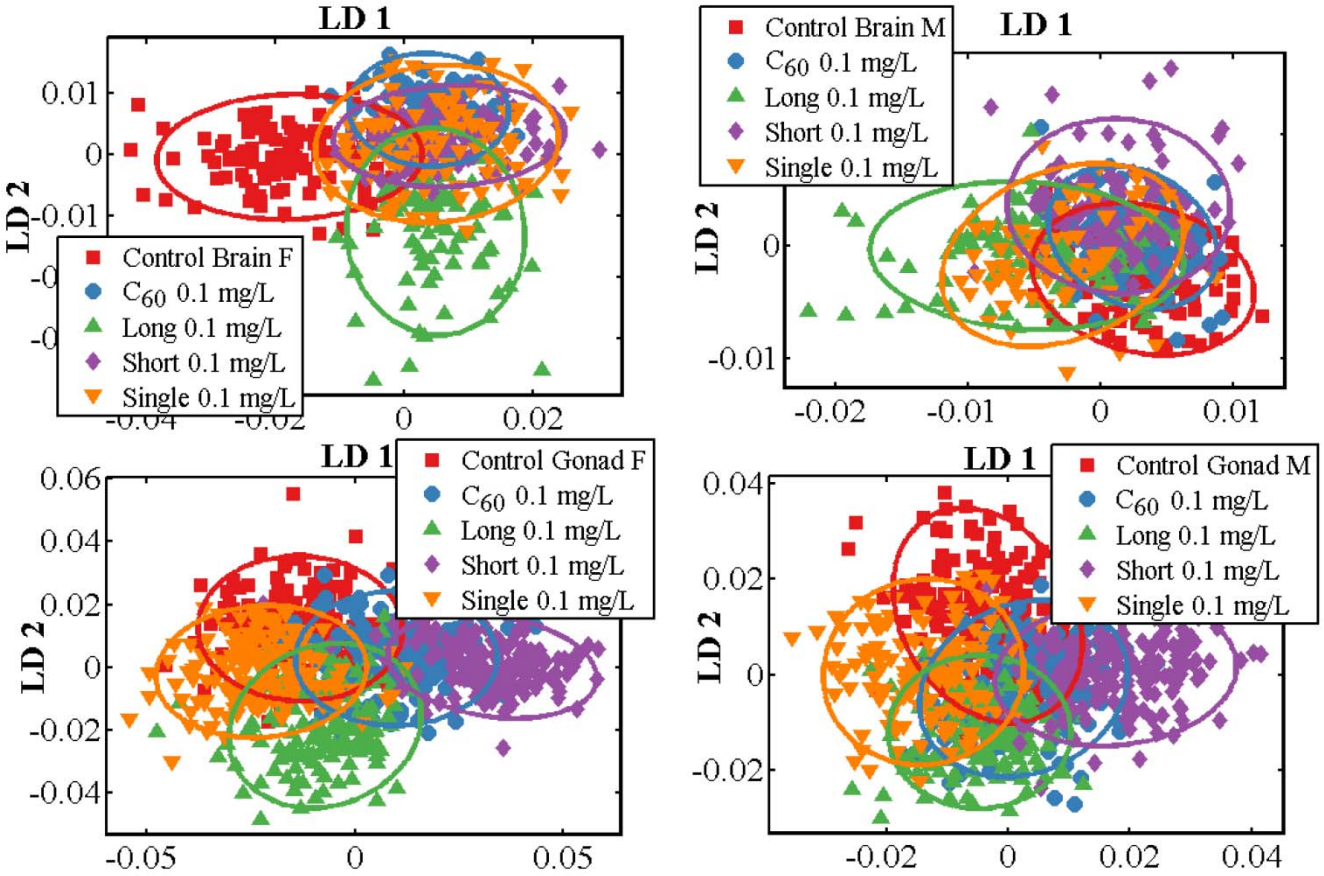

Figure S16 Cross-calculated PCA-LDA cluster vectors plots indicating the wavenumber basis for segregation of zebrafish tissues exposed to **CNPs** at concentration of 0.1 mg/L by **Raman spectroscopy**. Each treatment was compared to the control. The height of the cluster vectors peak is proportional to the extent of biochemical alterations compared to the vehicle control.

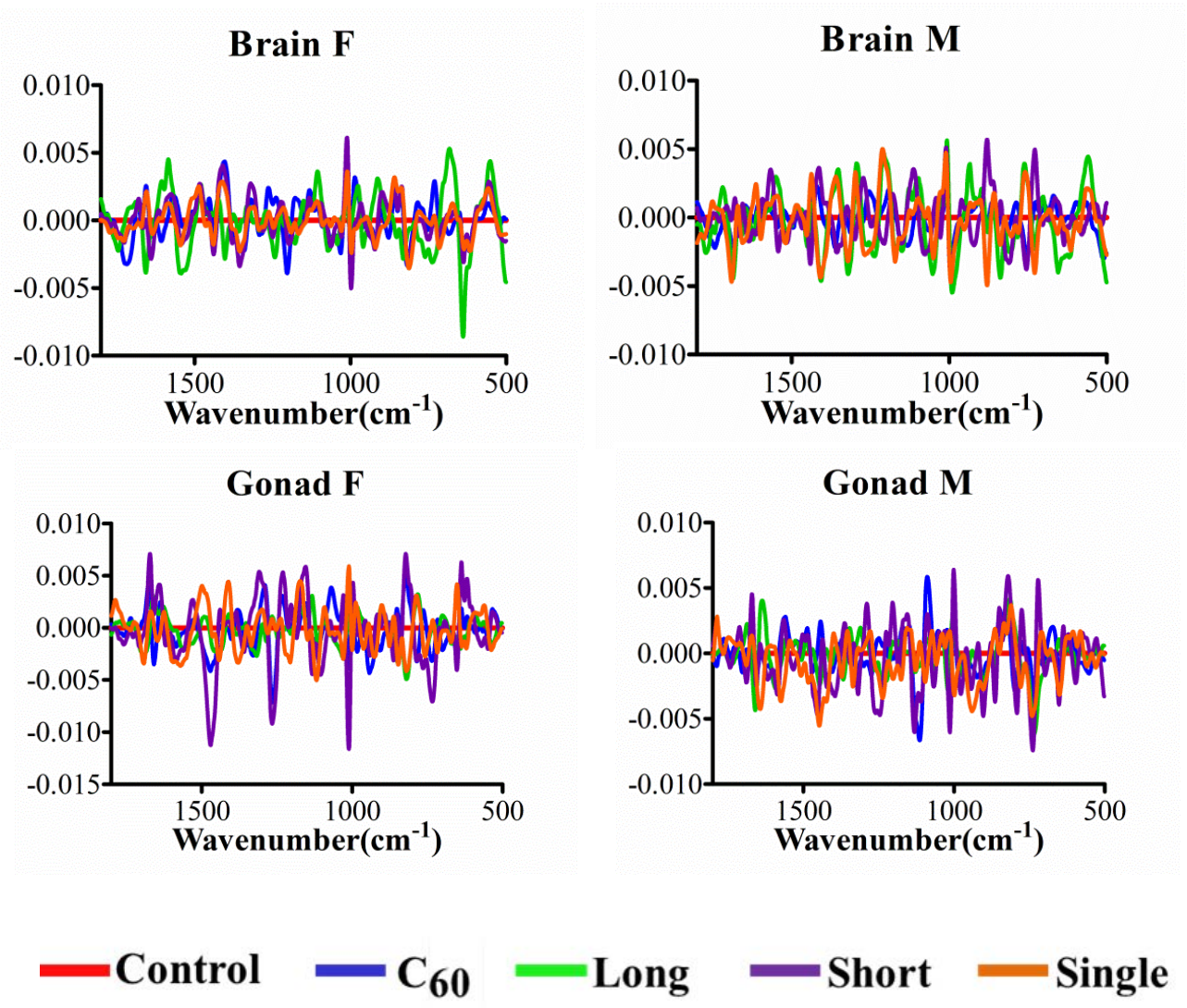

Figure S17 Cross-calculated PCA-LDA cluster vectors plots responsible for the wavenumber basis for segregation of zebrafish **brain** and **gonads** exposed to **CNPs** at concentration of 0.1 mg/L by **Raman spectroscopy**. Each treatment was compared to the control. The size of the marker symbol is proportional to the height of corresponding cluster vectors peak.

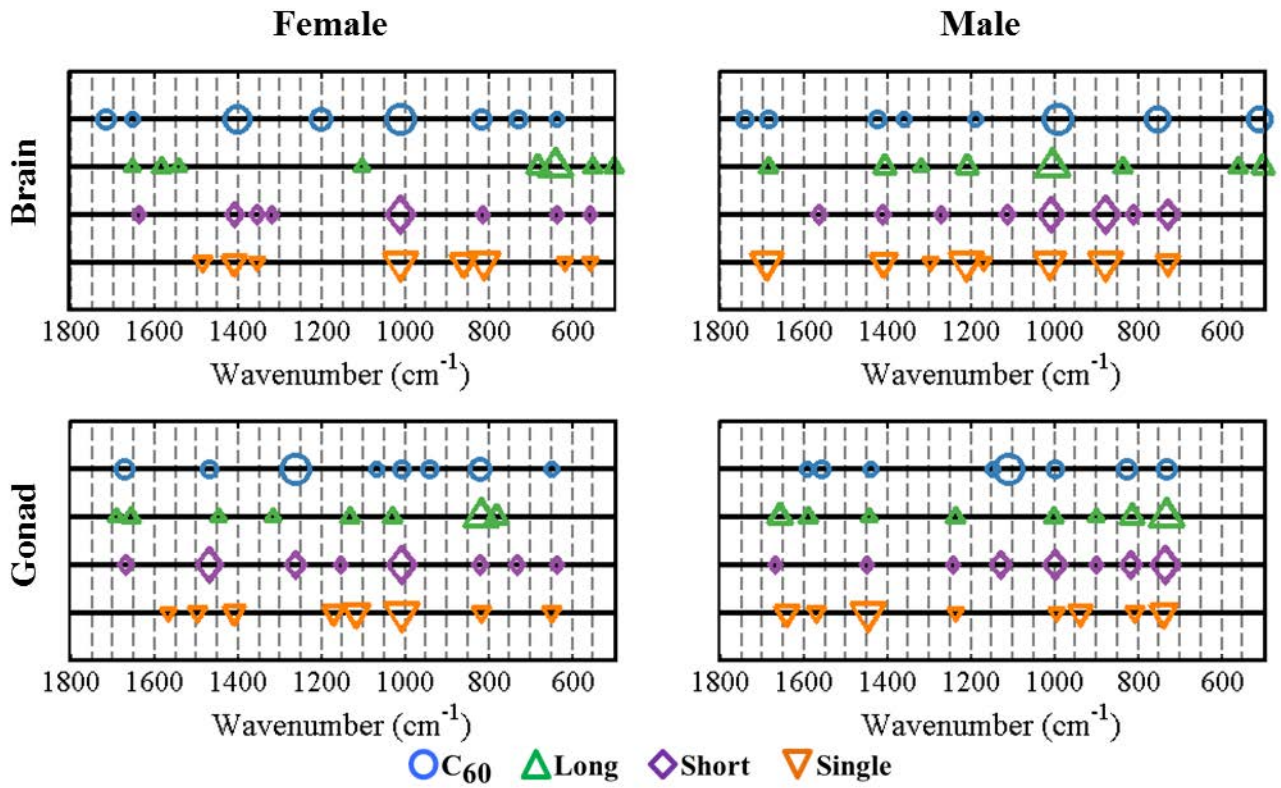

Table S1 *P-value* for each dimension calculated by one-way ANOVA with Dunnett's post-hoc test for 2-D cross-calculated PCA-LDA scores plots.

Tissues of zebrafish exposed to C_{60} (by cross-calculated PCA-LDA) by ATR-FTIR spectroscopy					
One-way ANOVA with Dunnett's Multiple Comparison Test		**Female**		**Male**	
		LD1	LD2	LD1	LD2
Brain	Control *vs.* 0.001 mg/L	*P <0.0001*	*P <0.0001*	*P >0.05*	*P <0.0001*
	Control *vs.* 0.1 mg/L	*P <0.0001*	*P <0.0001*	*P <0.0001*	*P <0.0001*
Gill	Control *vs.* 0.001 mg/L	*P <0.0001*	*P <0.0001*	*P <0.0001*	*P <0.0001*
	Control *vs.* 0.1 mg/L	*P <0.0001*	*P <0.0001*	*P <0.0001*	*P <0.0001*
Gonad	Control *vs.* 0.001 mg/L	*P <0.0001*	*P <0.01*	*P <0.0001*	*P <0.0001*
	Control *vs.* 0.1 mg/L	*P <0.0001*	*P <0.0001*	*P <0.01*	*P <0.0001*
Liver	Control *vs.* 0.001 mg/L	*P <0.0001*	*P <0.001*	*P <0.0001*	*P <0.0001*
	Control *vs.* 0.1 mg/L	*P <0.0001*	*P <0.0001*	*P <0.0001*	*P <0.0001*

Tissues of zebrafish exposed to **Long MWCNTs** (by cross-calculated PCA-LDA) by ATR-FTIR spectroscopy					
One-way ANOVA with Dunnett's Multiple Comparison Test		**Female**		**Male**	
		LD1	LD2	LD1	LD2
Brain	Control *vs.* 0.001 mg/L	*P <0.0001*	*P <0.0001*	*P <0.0001*	*P <0.0001*
	Control *vs.* 0.1 mg/L	*P <0.0001*	*P <0.0001*	*P <0.0001*	*P <0.0001*
Gill	Control *vs.* 0.001 mg/L	*P <0.0001*	*P <0.0001*	*P <0.0001*	*P <0.0001*
	Control *vs.* 0.1 mg/L	*P <0.0001*	*P <0.0001*	*P <0.0001*	*P <0.0001*
Gonad	Control *vs.* 0.001 mg/L	*P <0.0001*	*P <0.0001*	*P <0.001*	*P <0.0001*
	Control *vs.* 0.1 mg/L	*P <0.0001*	*P <0.0001*	*P <0.0001*	*P <0.0001*
Liver	Control *vs.* 0.001 mg/L	*P <0.0001*	*P <0.0001*	*P <0.0001*	*P <0.0001*
	Control *vs.* 0.1 mg/L	*P <0.0001*	*P <0.0001*	*P <0.0001*	*P <0.0001*

Table S2 *P-value* for each dimension calculated by one-way ANOVA with Dunnett's post-hoc test for 2-D cross-calculated PCA-LDA scores plots.

Tissues of zebrafish exposed to **Short MWCNTs** (cross-calculated PCA-LDA) by ATR-FTIR spectroscopy					
One-way ANOVA with Dunnett's Multiple Comparison Test		**Female**		**Male**	
		LD1	LD2	LD1	LD2
Brain	Control *vs.* 0.001 mg/L	*P <0.0001*	*P <0.0001*	*P <0.0001*	*P <0.0001*
	Control *vs.* 0.1 mg/L	*P <0.0001*	*P <0.0001*	*P <0.0001*	*P <0.0001*
Gill	Control *vs.* 0.001 mg/L	*P <0.0001*	*P <0.0001*	*P <0.0001*	*P <0.0001*
	Control *vs.* 0.1 mg/L	*P <0.01*	*P <0.0001*	*P <0.0001*	*P <0.0001*
Gonad	Control *vs.* 0.001 mg/L	*P <0.0001*	*P <0.0001*	*P <0.0001*	*P <0.0001*
	Control *vs.* 0.1 mg/L	*P <0.0001*	*P <0.0001*	*P >0.05*	*P <0.0001*
Liver	Control *vs.* 0.001 mg/L	*P <0.0001*	*P <0.0001*	*P <0.0001*	*P <0.0001*
	Control *vs.* 0.1 mg/L	*P <0.001*	*P <0.0001*	*P <0.01*	*P <0.0001*

Tissues of Zebrafish exposed to **single-walled CNTs** (cross-calculated PCA-LDA) by ATR-FTIR spectroscopy					
One-way ANOVA with Dunnett's Multiple Comparison Test		**Female**		**Male**	
		LD1	LD2	LD1	LD2
Brain	Control *vs.* 0.001 mg/L	*P > 0.05*	*P < 0.0001*	*P < 0.0001*	*P < 0.0001*
	Control *vs.* 0.1 mg/L	*P < 0.0001*	*P < 0.0001*	*P < 0.0001*	*P < 0.0001*
Gill	Control *vs.* 0.001 mg/L	*P < 0.01*	*P < 0.0001*	*P < 0.0001*	*P < 0.0001*
	Control *vs.* 0.1 mg/L	*P < 0.0001*	*P < 0.0001*	*P < 0.0001*	*P < 0.0001*
Gonad	Control *vs.* 0.001 mg/L	*P < 0.0001*	*P < 0.0001*	*P < 0.0001*	*P < 0.0001*
	Control *vs.* 0.1 mg/L	*P > 0.05*	*P < 0.0001*	*P < 0.0001*	*P < 0.0001*
Liver	Control *vs.* 0.001 mg/L	*P < 0.0001*	*P < 0.0001*	*P < 0.0001*	*P < 0.0001*
	Control *vs.* 0.1 mg/L	*P < 0.0001*	*P < 0.0001*	*P < 0.0001*	*P < 0.0001*

Table S3 *P-value* for each dimension calculated by one-way ANOVA with Dunnett's post-hoc test for 2-D cross-calculated PCA-LDA scores plots.

Tissues of zebrafish exposed to CNPs (by cross-calculated PCA-LDA) interrogated by ATR-FTIR spectroscopy					
One-way ANOVA with Dunnett's Multiple Comparison Test		Female		Male	
		LD1	LD2	LD1	LD2
Brain	Control *vs.* C_{60} 0.1 mg/L	*P <0.0001*	*P <0.001*	*P <0.001*	*P >0.05*
	Control *vs.* Long 0.1 mg/L	*P <0.0001*	*P <0.0001*	*P <0.0001*	*P <0.001*
	Control *vs.* Short 0.1 mg/L	*P <0.0001*	*P <0.0001*	*P >0.05*	*P <0.0001*
	Control *vs.* Single 0.1 mg/L	*P <0.0001*	*P <0.0001*	*P <0.0001*	*P <0.001*
Gill	Control *vs.* C_{60} 0.1 mg/L	*P <0.0001*	*P <0.001*	*P <0.001*	*P >0.05*
	Control *vs.* Long 0.1 mg/L	*P <0.0001*	*P <0.001*	*P <0.0001*	*P >0.05*
	Control *vs.* Short 0.1 mg/L	*P <0.0001*	*P <0.001*	*P <0.0001*	*P <0.0001*
	Control *vs.* Single 0.1 mg/L	*P <0.001*	*P <0.0001*	*P <0.0001*	*P <0.0001*
Gonad	Control *vs.* C_{60} 0.1 mg/L	*P <0.0001*	*P <0.0001*	*P >0.05*	*P <0.0001*
	Control *vs.* Long 0.1 mg/L	*P <0.0001*	*P >0.05*	*P <0.0001*	*P <0.0001*
	Control *vs.* Short 0.1 mg/L	*P <0.0001*	*P <0.0001*	*P <0.01*	*P <0.0001*
	Control *vs.* Single 0.1 mg/L	*P <0.0001*	*P <0.0001*	*P <0.01*	*P <0.0001*
Liver	Control *vs.* C_{60} 0.1 mg/L	*P <0.001*	*P <0.0001*	*P <0.0001*	*P >0.05*
	Control *vs.* Long 0.1 mg/L	*P <0.0001*	*P <0.0001*	*P <0.0001*	*P <0.01*
	Control *vs.* Short 0.1 mg/L	*P >0.05*	*P <0.0001*	*P <0.0001*	*P <0.0001*
	Control *vs.* Single 0.1 mg/L	*P >0.05*	*P <0.0001*	*P <0.0001*	*P <0.01*

Table S4 *P-value* for each dimension calculated by one-way ANOVA with Dunnett's post-hoc test for 2-D cross-calculated PCA-LDA scores plots.

Tissues of zebrafish exposed to CNPs (by cross-calculated PCA-LDA) interrogated by **Raman spectroscopy**					
One-way ANOVA with Dunnett's Multiple Comparison Test		Female		Male	
		LD1	LD2	LD1	LD2
Brain	Control *vs.* C_{60} 0.1 mg/L	*P <0.0001*	*P <0.001*	*P >0.05*	*P <0.0001*
	Control *vs.* Long 0.1 mg/L	*P <0.0001*	*P <0.0001*	*P <0.0001*	*P <0.0001*
	Control *vs.* Short 0.1 mg/L	*P <0.0001*	*P <0.0001*	*P <0.001*	*P <0.0001*
	Control *vs.* Single 0.1 mg/L	*P <0.0001*	*P <0.001*	*P <0.0001*	*P <0.0001*
Gonad	Control *vs.* C_{60} 0.1 mg/L	*P <0.0001*	*P <0.0001*	*P <0.0001*	*P <0.0001*
	Control *vs.* Long 0.1 mg/L	*P <0.0001*	*P <0.0001*	*P >0.05*	*P <0.0001*
	Control *vs.* Short 0.1 mg/L	*P <0.0001*	*P <0.0001*	*P <0.0001*	*P <0.0001*
	Control *vs.* Single 0.1 mg/L	*P <0.0001*	*P <0.0001*	*P <0.0001*	*P <0.0001*

Table S5 *P-value* for each dimension calculated by one-way ANOVA with Dunnett's post-hoc test for lipid-to-protein ratios derived from **IR** spectra.

Lipid-to-protein ratios derived from IR spectra following ATR-FTIR spectroscopy			
One-way ANOVA with Dunnett's Multiple Comparison Test		**Female**	**Male**
Brain	Control *vs.* C_{60} 0.1 mg/L	*P <0.01*	*P <0.01*
	Control *vs.* Long 0.1 mg/L	*P >0.05*	*P >0.05*
	Control *vs.* Short 0.1 mg/L	*P <0.001*	*P <0.01*
	Control *vs.* Single 0.1 mg/L	*P <0.0001*	*P <0.001*
Gill	Control *vs.* C_{60} 0.1 mg/L	*P >0.05*	*P >0.05*
	Control *vs.* Long 0.1 mg/L	*P <0.0001*	*P <0.0001*
	Control *vs.* Short 0.1 mg/L	*P <0.001*	*P <0.0001*
	Control *vs.* Single 0.1 mg/L	*P <0.0001*	*P <0.0001*
Gonads	Control *vs.* C_{60} 0.1 mg/L	*P >0.05*	*P <0.001*
	Control *vs.* Long 0.1 mg/L	*P <0.0001*	*P <0.0001*
	Control *vs.* Short 0.1 mg/L	*P <0.0001*	*P >0.05*
	Control *vs.* Single 0.1 mg/L	*P <0.0001*	*P <0.01*
Liver	Control *vs.* C_{60} 0.1 mg/L	*P <0.01*	*P >0.05*
	Control *vs.* Long 0.1 mg/L	*P <0.001*	*P <0.01*
	Control *vs.* Short 0.1 mg/L	*P <0.01*	*P >0.05*
	Control *vs.* Single 0.1 mg/L	*P >0.05*	*P <0.01*

Table S6 *P-value* for each dimension calculated by one-way ANOVA with Newman-Keuls' post-hoc test for lipid-to-protein ratios in different tissues derived from **IR** spectra.

Lipid-to-protein ratios derived from IR spectra following ATR-FTIR spectroscopy								
	Brain F	**Brain M**	**Gill F**	**Gill M**	**Gonads F**	**Gonads M**	**Liver F**	**Liver M**
Brain F		*P <0.0001*	*P <0.0001*	*P >0.05*	*P >0.05*	*P <0.0001*	*P <0.0001*	*P <0.01*
Brain M	*P <0.0001*		*P <0.0001*	*P <0.0001*	*P <0.0001*	*P <0.0001*	*P <0.0001*	*P <0.01*
Gill F	*P <0.0001*	*P <0.0001*		*P <0.0001*	*P <0.0001*	*P <0.001*	*P <0.01*	*P <0.0001*
Gill M	*P >0.05*	*P <0.0001*	*P <0.0001*		*P >0.05*	*P <0.0001*	*P <0.0001*	*P <0.01*
Gonads F	*P >0.05*	*P <0.0001*	*P <0.0001*	*P >0.05*		*P <0.0001*	*P <0.0001*	*P <0.0001*
Gonads M	*P <0.0001*	*P <0.0001*	*P <0.001*	*P <0.0001*	*P <0.0001*		*P <0.0001*	*P <0.0001*
Liver F	*P <0.0001*	*P <0.0001*	*P <0.01*	*P <0.0001*	*P <0.0001*	*P <0.0001*		*P <0.0001*
Liver M	*P <0.01*	*P <0.01*	*P <0.0001*	*P <0.01*	*P <0.001*	*P <0.0001*	*P <0.0001*	

Table S7 *P-value* for each dimension calculated by one-way ANOVA with post-hoc test for $C=C/CH_2$ ratios derived from **Raman** spectra.

Ratio of $C=C/CH_2$ derived from Raman spectra			
One-way ANOVA with Dunnett's Multiple Comparison Test		**Female**	**Male**
Brain	Control *vs.* C_{60} 0.1 mg/L	*P <0.0001*	*P <0.001*
	Control *vs.* Long 0.1 mg/L	*P <0.0001*	*P >0.05*
	Control *vs.* Short 0.1 mg/L	*P <0.01*	*P >0.05*
	Control *vs.* Single 0.1 mg/L	*P <0.0001*	*P <0.001*
Gonad	Control *vs.* C_{60} 0.1 mg/L	*P >0.05*	*P <0.01*
	Control *vs.* Long 0.1 mg/L	*P <0.0001*	*P <0.0001*
	Control *vs.* Short 0.1 mg/L	*P <0.01*	*P <0.0001*
	Control *vs.* Single 0.1 mg/L	*P >0.05*	*P <0.01*

Ratio of $C=C/CH_2$ derived from Raman spectra	
One-way ANOVA with Newman-Keuls' Multiple Comparison Test	***P*-value**
Brain F *vs.* Gonad M	*P <0.0001*
Brain F *vs.* Gonad F	*P <0.0001*
Brain F *vs.* Brain M	*P <0.0001*
Brain M *vs.* Gonad M	*P <0.0001*
Brain M *vs.* Gonad F	*P <0.0001*
Gonad F *vs.* Gonad M	*P <0.0001*

Cluster vectors plots for zebrafish brain tissues derived from IR spectra by cross-calculated PCA-LDA

	Female		Male	
	Wavenumber (cm^{-1})	Tentative assignments	Wavenumber (cm^{-1})	Tentative assignments
C_{60}	1740	Lipid, ν(C=O)	1065	$\nu_s PO_2^-$
	1220	$\nu_{as} PO_2^-$	1543	Amide II
	1065	$\nu_s PO_2^-$	1145	Carbohydrates, ν(C-O)
	1508	Amide II	1710	Lipid, ν(C=O)
	1130	Carbohydrates, ν(C-O)	1655	Amide I
	960	Protein phosphorylation	1750	Lipid, ν(C=O)
	1450	Proteins, $\nu_{as} CH_3$	1103	$\nu_s PO_2^-$
	1312	Amide III	1245	$\nu_{as} PO_2^-$
Long MWCNTs	1616	Amide I	1650	Amide II
	1747	Lipid, ν(C=O)	1716	$\nu_s PO_2^-$
	1180	Carbohydrates, ν(C-O)	1543	Amide II
	1454	Proteins, $\nu_{as} CH_3$	1122	Carbohydrates, ν(C-O)
	1265	Amide III	1087	$\nu_s PO_2^-$
	1000	Protein phosphorylation	1038	Glycogen
	1582	Amide II	1392	$\nu(COO^-)$
	1320	Amide III	1238	$\nu_{as} PO_2^-$
Short MWCNTs	1740	Lipid, ν(C=O)	1650	Amide I
	1530	Amide II	1065	$\nu_s PO_2^-$
	1045	Glycogen	1728	Lipid, ν(C=O)
	1130	Carbohydrates, ν(C-O)	1543	Amide II
	1616	Amide I	1680	Amide I
	960	Protein phosphorylation	1245	Amide III
	1412	Proteins, $\nu_{as} CH_3$	1103	$\nu_s PO_2^-$
	1447	Proteins, $\nu_{as} CH_3$	1145	Carbohydrates, ν(C-O)
Single-walled CNTs	1528	Amide II	1065	$\nu_s PO_2^-$
	1658	Amide I	1732	Lipid, ν(C=O)
	1045	Glycogen	1650	Amide I
	1477	Proteins, $\nu_{as} CH_3$	1543	Amide II
	1744	Lipid, ν(C=O)	1690	Amide I
	1226	$\nu_{as} PO_2^-$	1145	Carbohydrates, ν(C-O)
	964	Protein phosphorylation	1103	$\nu_s PO_2^-$
	1427	Proteins, $\nu_{as} CH_3$	930	Protein phosphorylation

Cluster vectors plots for zebrafish gill tissues derived from IR spectra by cross-calculated PCA-LDA

	Female		Male	
	Wavenumber (cm^{-1})	Tentative assignments	Wavenumber (cm^{-1})	Tentative assignments
C_{60}	1647	Amide I	1616	Amide I
	1504	Amide II	1690	Amide I
	1573	Amide II	1496	Amide II
	1710	Lipid, ν(C=O)	1554	Amide II
	1049	Glycogen	1118	Carbohydrates, ν(C-O)
	1462	Proteins, $\nu_{as}CH_3$	1369	$\nu(COO^-)$
	964	Protein phosphorylation	1199	$\nu_{as}PO_2^-$
	1750	Lipid, ν(C=O)	1743	Lipid, ν(C=O)
Long MWCNTs	1647	Amide I	1539	Amide II
	1528	Amide II	1647	Amide I
	1747	Lipid, ν(C=O)	1477	Proteins, $\nu_{as}CH_3$
	1469	Proteins, $\nu_{as}CH_3$	1700	Lipid, ν(C=O)
	1180	Carbohydrates, ν(C-O)	1207	$\nu_{as}PO_2^-$
	1705	Lipid, ν(C=O)	1303	Amide III
	1080	$\nu_sPO_2^-$	1597	Amide I
	1373	$\nu(COO^-)$	1747	Lipid, ν(C=O)
Short MWCNTs	1710	Lipid, ν(C=O)	1539	Amide II
	1550	Amide II	1492	Proteins, $\nu_{as}CH_3$
	1470	Proteins, $\nu_{as}CH_3$	1650	Amide I
	1211	$\nu_{as}PO_2^-$	1616	Amide I
	1392	$\nu(COO^-)$	952	Protein phosphorylation
	1612	Amide I	995	Protein phosphorylation
	1064	$\nu_sPO_2^-$	1199	$\nu_{as}PO_2^-$
	987	Protein phosphorylation	1122	Carbohydrates, ν(C-O)
Single-walled CNTs	1647	Amide I	1535	Amide II
	1708	Lipid, ν(C=O)	1651	Amide II
	1465	Proteins, $\nu_{as}CH_3$	1447	Proteins, $\nu_{as}CH_3$
	1550	Amide II	1296	Amide III
	1392	$\nu(COO^-)$	995	Amide III
	1018	Glycogen	1050	Glycogen
	1211	$\nu_{as}PO_2^-$	1728	Lipid, ν(C=O)
	1311	Amide III	1200	$\nu_{as}PO_2^-$

Cluster vectors plots for zebrafish gonad tissues derived from IR spectra by cross-calculated PCA-LDA

	Female		Male	
	Wavenumber (cm^{-1})	Tentative assignments	Wavenumber (cm^{-1})	Tentative assignments
C_{60}	1724	Lipid, ν(C=O)	1774	Lipid, ν(C=O)
	1442	Proteins, $\nu_{as}CH_3$	1110	$\nu_s PO_2^-$
	1068	$\nu_s PO_2^-$	948	Protein phosphorylation
	1647	Amide I	1254	Amide III
	1346	$\nu(COO^-)$	1540	Amide II
	1512	Amide II	1076	$\nu_s PO_2^-$
	922	Protein phosphorylation	1477	Amide II
	960	Protein phosphorylation	1708	Lipid, ν(C=O)
Long MWCNTs	1720	Lipid, ν(C=O)	1261	Amide III
	1774	Lipid, ν(C=O)	1546	Amide II
	1342	$\nu(COO^-)$	1681	Amide I
	1430	Proteins, $\nu_{as}CH_3$	1076	$\nu_s PO_2^-$
	1543	Amide II	1616	Amide I
	1226	$\nu_{as} PO_2^-$	1755	Lipid, ν(C=O)
	1296	Amide III	1504	Amide II
	1670	Amide I	1130	Carbohydrates, ν(C-O)
Short MWCNTs	1543	Amide II	948	Protein phosphorylation
	1740	Lipid, ν(C=O)	1774	Lipid, ν(C=O)
	1690	Amide I	1685	Amide I
	1651	Amide I	1597	Amide I
	991	Protein phosphorylation	1512	Amide II
	1774	Lipid, ν(C=O)	1253	Amide III
	1508	Amide II	1550	Amide II
	1064	$\nu_s PO_2^-$	1110	$\nu_s PO_2^-$
Single-walled CNTs	1446	Proteins, $\nu_{as}CH_3$	1774	Lipid, ν(C=O)
	1651	Amide I	1616	Amide I
	1760	Lipid, ν(C=O)	1685	Amide I
	1573	Amide II	945	Protein phosphorylation
	1068	$\nu_s PO_2^-$	1072	$\nu_s PO_2^-$
	1724	Lipid, ν(C=O)	1392	$\nu(COO^-)$
	1512	Amide II	1512	Amide II
	1346	$\nu(COO^-)$	1550	Amide II

Cluster vectors plots for zebrafish liver tissues derived from IR spectra by cross-calculated PCA-LDA

	Female		Male	
	Wavenumber (cm^{-1})	Tentative assignments	Wavenumber (cm^{-1})	Tentative assignments
C_{60}	1064	$\nu_s PO_2^-$	1103	$\nu_s PO_2^-$
	1535	Amide II	1504	Amide II
	1450	Proteins, $\nu_{as} CH_3$	933	Protein phosphorylation
	1743	Lipid, ν(C=O)	1705	Lipid, ν(C=O)
	1168	Carbohydrates, ν(C-O)	1770	Lipid, ν(C=O)
	1589	Amide I	1620	Amide I
	1408	$\nu(COO^-)$	1408	$\nu(COO^-)$
	1685	Amide I	1342	$\nu(COO^-)$
Long MWCNTs	1543	Amide II	1485	Proteins, $\nu_{as} CH_3$
	1654	Amide I	1786	Lipid, ν(C=O)
	1041	Glycogen	1681	Amide I
	1728	Lipid, ν(C=O)	1720	Lipid, ν(C=O)
	1766	Lipid, ν(C=O)	1037	Glycogen
	1492	Proteins, $\nu_{as} CH_3$	1539	Amide II
	987	Protein phosphorylation	1369	$\nu(COO^-)$
	1411	Proteins, $\nu_{as} CH_3$	1269	Amide III
Short MWCNTs	1535	Amide II	1049	Glycogen
	1450	Proteins, $\nu_{as} CH_3$	1732	Lipid, ν(C=O)
	1172	Carbohydrates, ν(C-O)	1092	$\nu_s PO_2^-$
	1766	Lipid, ν(C=O)	1469	Proteins, $\nu_{as} CH_3$
	1041	Glycogen	991	Protein phosphorylation
	1384	$\nu(COO^-)$	1346	$\nu(COO^-)$
	1685	Amide I	1562	Amide II
	1589	Amide I	1597	Amide I
Single-walled CNTs	1446	Proteins, $\nu_{as} CH_3$	1504	Amide II
	1535	Amide II	1770	Lipid, ν(C=O)
	1616	Amide I	1705	Lipid, ν(C=O)
	1654	Amide I	1465	Proteins, $\nu_{as} CH_3$
	1060	$\nu_s PO_2^-$	1411	Proteins, $\nu_{as} CH_3$
	1404	$\nu(COO^-)$	1037	Glycogen
	1743	Lipid, ν(C=O)	1616	Amide I
	1230	$\nu_{as} PO_2^-$	1188	Carbohydrates, ν(C-O)

Cluster vectors plots for zebrafish brain tissues derived from Raman spectra by cross-calculated PCA-LDA

	Female		Male	
	Wavenumber (cm^{-1})	Tentative assignments	Wavenumber (cm^{-1})	Tentative assignments
C_{60}	1008	Phenylalanine	994	Phenylalanine
	1402	Lipid, CH_2	510	Collagen, S-S stretching
	1202	Amide III	753	DNA, nucleic acid
	817	DNA/RNA, phosphodiester	1424	Lipid, CH_2
	1716	Lipid, C=O	1685	Lipid, C=C
	730	DNA, nucleic acid	1743	Lipid, C=O
	635	Protein, *v*(C-S)	1361	Lipid/protein, CH_3/CH_2
	1655	Lipid, C=C	1190	Protein
Long MWCNTs	638	Protein, *v*(C-S)	1006	Phenylalanine
	681	DNA, ring breathing modes	1207	Amide III
	505	Collagen, S-S stretching	506	Collagen, S-S stretching
	1584	Phenylalanine, C=C	1406	Lipid, CH_2
	552	*v*(S-S)	558	*v*(S-S)
	1542	Amide II	1685	Lipid, C=C
	1655	Lipid, C=C	837	Protein
	1105	Carbohydrates	1320	Lipid/protein, CH_3/CH_2
Short MWCNTs	1010	Phenylalanine	879	Protein
	1409	Lipid, CH_2	1009	Phenylalanine
	1354	Lipid/protein, CH_3/CH_2	727	DNA, nucleic acid
	637	Protein, *v*(C-S)	1413	Lipid, CH_2
	814	DNA/RNA, phosphodiester	1112	Carbohydrates
	556	*v*(S-S)	1565	Amide II
	1638	Amide I	810	DNA/RNA, phosphodiester
	1319	Lipid/protein, CH_3/CH_2	1271	Amide III
Single-walled CNTs	1010	Phenylalanine	1211	Amide III
	812	Collagen, C-C stretching	879	Protein
	858	Collagen, C-C stretching	1010	Phenylalanine
	1410	Lipid	1690	Lipid, C=C
	1486	Lipid	1409	Lipid, CH_2
	557	*v*(S-S)	727	DNA, nucleic acid
	1354	Lipid/protein, CH_3/CH_2	1297	Lipid
	616	Protein, *v*(C-S)	1171	Protein

Cluster vectors plots for zebrafish Gonad tissues derived from Raman spectra by cross-calculated PCA-LDA

	Female		Male	
	Wavenumber (cm^{-1})	Tentative assignments	Wavenumber (cm^{-1})	Tentative assignments
C_{60}	1263	Amide III	1111	Carbohydrates
	821	DNA/RNA, phosphodiester	732	DNA, nucleic acid
	1673	Lipid, C=C	826	DNA/RNA, phosphodiester
	940	Protein	998	Phenylalanine
	1469	Lipid, CH_2	1557	Amide II
	1007	Phenylalanine	1593	Phenylalanine
	1068	Carbohydrates	1441	Lipid, CH_2
	650	Protein, *v*(C-S)	1147	Protein
Long MWCNTs	818	DNA/RNA, phosphodiester	732	DNA, nucleic acid
	780	DNA, nucleic acid	1656	Lipid, C=C
	1131	Protein	813	DNA/RNA, phosphodiester
	1658	Lipid, C=C	1002	Phenylalanine
	1030	Phenylalanine	1235	Amide III
	1315	Lipid/protein, CH_3/CH_2	1589	Phenylalanine
	1693	Lipid, C=C	1444	Lipid, CH_2
	1447	Lipid, CH_2	901	Protein
Short MWCNTs	1009	Phenylalanine	736	DNA, nucleic acid
	1469	Lipid, CH_2	1000	Phenylalanine
	1263	Amide III	1129	Carbohydrates
	820	DNA/RNA, phosphodiester	819	DNA/RNA, phosphodiester
	732	DNA, nucleic acid	901	Protein
	1669	Lipid, C=C	1244	Amide III
	635	Protein, *v*(C-S)	1451	Lipid, CH_2
	1153	Protein	1669	Lipid, C=C
Single-walled CNTs	1009	Phenylalanine	1445	Lipid, CH_2
	1117	Carbohydrates	739	DNA, nucleic acid
	1171	Protein	937	Protein
	1409	Lipid, CH_2	1639	Lipid, C=C
	649	Protein, *v*(C-S)	809	DNA/RNA, phosphodiester
	819	DNA/RNA, phosphodiester	1571	Phenylalanine
	1497	Lipid, CH_2	1235	Amide III
	1568	Amide II	996	Phenylalanine

Cluster vectors plots for zebrafish brain exposed to C_{60} at two doses: derived from IR spectra by cross-calculated PCA-LDA

Dose (mg/L)	Female		Male	
	Wavenumber (cm^{-1})	Tentative assignments	Wavenumber (cm^{-1})	Tentative assignments
0.001	1705	Lipid, *v*(C=O)	1539	Amide II
	1114	Carbohydrates, *v*(C-O)	1654	Amide I
	1504	Amide II	1454	Proteins, $v_{as}CH_3$
	1438	Proteins, $v_{as}CH_3$	1080	$v_sPO_2^-$
	1053	Glycogen	1122	Carbohydrates, *v*(C-O)
	1786	Lipid, *v*(C=O)	1280	Amide III
	1003	Glycogen	1616	Amide I
	1654	Amide I	950	Protein phosphorylation
0.1	1504	Amide II	1504	Amide II
	1705	Lipid, *v*(C=O)	1700	Lipid, *v*(C=O)
	1118	Carbohydrates, *v*(C-O)	1438	Proteins, $v_{as}CH_3$
	1616	Amide I	1650	Amide I
	1539	Amide II	1388	$v(COO^-)$
	1750	Lipid, *v*(C=O)	1616	Amide I
	1654	Amide I	1041	Glycogen
	1438	Proteins, $v_{as}CH_3$	1207	$v_{as}PO_2^-$

Cluster vectors plots for zebrafish gill exposed to C_{60} at two doses: derived from IR spectra by cross-calculated PCA-LDA

Dose (mg/L)	Female		Male	
	Wavenumber (cm^{-1})	Tentative assignments	Wavenumber (cm^{-1})	Tentative assignments
0.001	1114	Carbohydrates, *v*(C-O)	1523	Amide II
	1685	Amide I	1670	Amide I
	1543	Amide II	1126	Carbohydrates, *v*(C-O)
	1477	Proteins, $v_{as}CH_3$	980	Protein phosphorylation
	1045	Glycogen	1218	$v_{as}PO_2^-$
	968	Protein phosphorylation	1080	$v_sPO_2^-$
	1392	$v(COO^-)$	1712	Lipid, *v*(C=O)
	1176	Carbohydrates, *v*(C-O)	1766	Lipid, *v*(C=O)
0.1	1485	Proteins, $v_{as}CH_3$	1458	Proteins, $v_{as}CH_3$
	1342	$v(COO^-)$	1701	Lipid, *v*(C=O)
	1014	Glycogen	1570	Amide II
	1716	Lipid, *v*(C=O)	1616	Amide I
	1539	Amide II	1504	Amide II
	1681	Amide I	1257	Amide III
	1770	Lipid, *v*(C=O)	1651	Amide I
	1126	Carbohydrates, *v*(C-O)	1022	Glycogen

Cluster vectors plots for zebrafish gonads exposed to C_{60} at two doses: derived from IR spectra by cross-calculated PCA-LDA

Dose (mg/L)	Female		Male	
	Wavenumber (cm^{-1})	Tentative assignments	Wavenumber (cm^{-1})	Tentative assignments
0.001	1647	Amide I	1647	Amide I
	1554	Amide II	1697	Lipid, ν(C=O)
	1697	Lipid, ν(C=O)	1539	Amide II
	1130	Carbohydrates, ν(C-O)	983	Protein phosphorylation
	1415	Proteins, $\nu_{as}CH_3$	1110	$\nu_s PO_2^-$
	1164	Carbohydrates, ν(C-O)	1419	Proteins, $\nu_{as}CH_3$
	1755	Lipid, ν(C=O)	1029	Glycogen
	975	Protein phosphorylation	1072	$\nu_s PO_2^-$
0.1	1134	Carbohydrates, ν(C-O)	1701	Lipid, ν(C=O)
	1396	$\nu(COO^-)$	1651	Amide I
	972	Protein phosphorylation	1543	Amide II
	1647	Amide I	950	Protein phosphorylation
	1589	Amide I	1612	Amide I
	1010	Glycogen	1265	Amide III
	1068	$\nu_s PO_2^-$	1774	Lipid, ν(C=O)
	1315	Amide III	983	Protein phosphorylation

Cluster vector plots for zebrafish liver exposed to C_{60} at two doses: derived from IR spectra by cross-calculated PCA-LDA

Dose (mg/L)	Female		Male	
	Wavenumber (cm^{-1})	Tentative assignments	Wavenumber (cm^{-1})	Tentative assignments
0.001	1504	Amide II	1654	Amide I
	1685	Amide I	1705	Lipid, ν(C=O)
	1720	Lipid, ν(C=O)	1543	Amide II
	1539	Amide II	1504	Amide II
	1651	Amide I	1107	$\nu_s PO_2^-$
	1454	Proteins, $\nu_{as}CH_3$	1346	$\nu(COO^-)$
	1000	Protein phosphorylation	1577	Amide II
	920	Protein phosphorylation	1616	Amide I
0.1	1685	Amide I	1408	$\nu(COO^-)$
	1041	Glycogen	1446	Proteins, $\nu_{as}CH_3$
	1076	$\nu_s PO_2^-$	1276	Amide III
	1635	Amide I	1728	Lipid, ν(C=O)
	1400	$\nu(COO^-)$	1639	Amide I
	933	Protein phosphorylation	1334	$\nu(COO^-)$
	1554	Amide II	1033	Glycogen
	1504	Amide II	1689	Amide I

Cluster vectors plots for zebrafish brain exposed to long MWCNTs at two doses: derived from IR spectra by cross-calculated PCA-LDA

Dose (mg/L)	Female		Male	
	Wavenumber (cm^{-1})	Tentative assignments	Wavenumber (cm^{-1})	Tentative assignments
0.001	1504	Amide II	1458	Proteins, $\nu_{as}CH_3$
	1654	Amide I	1392	$\nu(COO^-)$
	1743	Lipid, ν(C=O)	1543	Amide II
	1454	Proteins, $\nu_{as}CH_3$	1685	Amide I
	1616	Amide I	1728	Lipid, ν(C=O)
	1697	Lipid, ν(C=O)	1346	$\nu(COO^-)$
	941	Protein phosphorylation	1600	Amide I
	1346	$\nu(COO^-)$	1643	Amide I
0.1	1512	Amide II	1647	Amide I
	1126	Carbohydrates, ν(C-O)	1122	Carbohydrates, ν(C-O)
	1774	Lipid, ν(C=O)	1180	Carbohydrates, ν(C-O)
	1361	$\nu(COO^-)$	1527	Amide II
	1712	Lipid, ν(C=O)	1392	$\nu(COO^-)$
	1477	Proteins, $\nu_{as}CH_3$	1716	Lipid, ν(C=O)
	1053	Glycogen	1485	Proteins, $\nu_{as}CH_3$
	1573	Amide II	1265	Amide III

Cluster vectors plots for zebrafish gill exposed to Long MWCNTs at two doses: derived from IR spectra by cross-calculated PCA-LDA

Dose (mg/L)	Female		Male	
	Wavenumber (cm^{-1})	Tentative assignments	Wavenumber (cm^{-1})	Tentative assignments
0.001	1539	Amide II	1639	Amide I
	1651	Amide I	1539	Amide II
	1492	Proteins, $\nu_{as}CH_3$	1010	Glycogen
	948	Protein phosphorylation	1377	$\nu(COO^-)$
	1257	Amide III	1689	Amide I
	1701	Lipid, ν(C=O)	1296	Amide III
	1789	Lipid, ν(C=O)	1500	Amide II
	1585	Amide I	1091	$\nu_sPO_2^-$
0.1	1539	Amide II	1720	Lipid, ν(C=O)
	1492	Proteins, $\nu_{as}CH_3$	995	Protein phosphorylation
	1651	Amide I	1627	Amide I
	1584	Amide I	1330	$\nu(COO^-)$
	948	Protein phosphorylation	1450	Proteins, $\nu_{as}CH_3$
	1107	$\nu_sPO_2^-$	1554	Amide II
	1257	Amide III	1161	Carbohydrates, ν(C-O)
	1411	Proteins, $\nu_{as}CH_3$	1774	Lipid, ν(C=O)

Cluster vectors plots for zebrafish gonads exposed to long MWCNTs at two doses: derived from IR spectra by cross-calculated PCA-LDA

Dose (mg/L)	Female		Male	
	Wavenumber (cm^{-1})	Tentative assignments	Wavenumber (cm^{-1})	Tentative assignments
0.001	1654	Amide I	1539	Amide II
	1700	Lipid, *v*(C=O)	1689	Amide I
	1554	Amide II	1647	Amide I
	1172	Carbohydrates, *v*(C-O)	1770	Lipid, *v*(C=O)
	1504	Amide II	1504	Amide II
	1130	Carbohydrates, *v*(C-O)	1006	Glycogen
	1766	Lipid, *v*(C=O)	1728	Lipid, *v*(C=O)
	1041	Glycogen	1612	Amide I
0.1	1064	$v_sPO_2^-$	1720	Lipid, *v*(C=O)
	1720	Lipid, *v*(C=O)	1670	Amide I
	1276	Amide III	1388	$v(COO^-)$
	1427	Proteins, $v_{as}CH_3$	1539	Amide II
	1342	$v(COO^-)$	1504	Amide II
	1543	Amide II	1172	Carbohydrates, *v*(C-O)
	1473	Proteins, $v_{as}CH_3$	1126	Carbohydrates, *v*(C-O)
	1620	Amide I	948	Protein phosphorylation

Cluster vectors plots for zebrafish liver exposed to long MWCNTs at two doses: derived from IR spectra by cross-calculated PCA-LDA

Dose (mg/L)	Female		Male	
	Wavenumber (cm^{-1})	Tentative assignments	Wavenumber (cm^{-1})	Tentative assignments
0.001	1504	Amide II	1485	Proteins, $\nu_{as}CH_3$
	1056	$\nu_sPO_2^-$	1697	Lipid, ν(C=O)
	1404	$\nu(COO^-)$	1049	Glycogen
	1091	$\nu_sPO_2^-$	1519	Amide II
	1465	Proteins, $\nu_{as}CH_3$	1654	Amide I
	1218	$\nu_{as}PO_2^-$	1099	$\nu_sPO_2^-$
	1697	Lipid, ν(C=O)	1000	Protein phosphorylation
	1647	Amide I	1134	Carbohydrates, ν(C-O)
0.1	1766	Lipid, ν(C=O)	1054	Glycogen
	1504	Amide II	1080	$\nu_sPO_2^-$
	1543	Amide II	1477	Proteins, $\nu_{as}CH_3$
	1049	Glycogen	1786	Lipid, ν(C=O)
	1091	$\nu_sPO_2^-$	1690	Amide I
	1188	Carbohydrates, ν(C-O)	1728	Lipid, ν(C=O)
	1469	Proteins, $\nu_{as}CH_3$	1361	$\nu(COO^-)$
	1732	Lipid, ν(C=O)	1539	Amide II

Cluster vectors plots for zebrafish brain exposed to short MWCNTs at two doses: derived from IR spectra by cross-calculated PCA-LDA

Dose (mg/L)	Female		Male	
	Wavenumber (cm^{-1})	Tentative assignments	Wavenumber (cm^{-1})	Tentative assignments
0.001	1442	Proteins, $\nu_{as}CH_3$	1720	Lipid, ν(C=O)
	1523	Amide II	1064	$\nu_s PO_2^-$
	1716	Lipid, ν(C=O)	1408	$\nu(COO^-)$
	1670	Amide I	1681	Amide I
	1562	Amide II	1612	Amide I
	1056	$\nu_s PO_2^-$	1523	Amide II
	1176	Carbohydrates, ν(C-O)	914	Protein phosphorylation
	1770	Lipid, ν(C=O)	1141	Carbohydrates, ν(C-O)
0.1	1473	Proteins, $\nu_{as}CH_3$	1064	$\nu_s PO_2^-$
	1126	Carbohydrates, ν(C-O)	1716	Lipid, ν(C=O)
	1056	$\nu_s PO_2^-$	1408	$\nu(COO^-)$
	1589	Amide I	1523	Amide II
	1002	Glycogen	1631	Amide I
	1693	Amide I	1681	Amide I
	1550	Amide II	1242	$\nu_{as} PO_2^-$
	1365	$\nu(COO^-)$	1141	Carbohydrates, ν(C-O)

Cluster vectors plots for zebrafish gill exposed to short MWCNTs at two doses: derived from IR spectra by cross-calculated PCA-LDA

Dose (mg/L)	Female		Male	
	Wavenumber (cm^{-1})	Tentative assignments	Wavenumber (cm^{-1})	Tentative assignments
0.001	1543	Amide II	1377	$\nu(COO^-)$
	1338	$\nu(COO^-)$	1662	Amide I
	1790	Lipid, ν(C=O)	914	Protein phosphorylation
	1705	Lipid, ν(C=O)	1539	Amide II
	1396	$\nu(COO^-)$	1716	Lipid, ν(C=O)
	1083	$\nu_s PO_2^-$	1624	Amide I
	1458	Proteins, $\nu_{as}CH_3$	1338	$\nu(COO^-)$
	1635	Amide I	1176	Carbohydrates, ν(C-O)
0.1	1543	Amide II	1647	Amide I
	1766	Lipid, ν(C=O)	1257	Amide III
	1724	Lipid, ν(C=O)	1072	$\nu_s PO_2^-$
	1083	$\nu_s PO_2^-$	1504	Amide II
	1577	Amide II	1543	Amide II
	1408	$\nu(COO^-)$	979	Protein phosphorylation
	1323	Amide III	1689	Amide I
	1678	Amide I	1377	$\nu(COO^-)$

Cluster vectors plots for zebrafish gonads exposed to short MWCNTs at two doses: derived from IR spectra by cross-calculated PCA-LDA

Dose (mg/L)	Female		Male	
	Wavenumber (cm^{-1})	Tentative assignments	Wavenumber (cm^{-1})	Tentative assignments
0.001	1504	Amide II	1681	Amide I
	1685	Amide I	1504	Amide II
	1647	Amide I	1647	Amide I
	1739	Lipid, ν(C=O)	1435	Proteins, $\nu_{as}CH_3$
	1543	Amide II	1546	Amide II
	1577	Amide II	1207	$\nu_{as}PO_2^-$
	1249	Amide III	1747	Lipid, ν(C=O)
	1392	$\nu(COO^-)$	1026	Glycogen
0.1	1685	Amide I	1681	Amide I
	1543	Amide II	941	Protein phosphorylation
	1504	Amide II	1103	$\nu_sPO_2^-$
	1396	$\nu(COO^-)$	1141	Carbohydrates, ν(C-O)
	1199	$\nu_{as}PO_2^-$	1485	Proteins, $\nu_{as}CH_3$
	1438	Proteins, $\nu_{as}CH_3$	1176	Carbohydrates, ν(C-O)
	941	Protein phosphorylation	1539	Amide II
	1766	Lipid, ν(C=O)	1716	Lipid, ν(C=O)

Cluster vectors plots for zebrafish liver exposed to short MWCNTs at two doses: derived from IR spectra by cross-calculated PCA-LDA

Dose (mg/L)	Female		Male	
	Wavenumber (cm^{-1})	Tentative assignments	Wavenumber (cm^{-1})	Tentative assignments
0.001	1654	Amide I	1543	Amide II
	1701	Lipid, ν(C=O)	1180	Carbohydrates, ν(C-O)
	1543	Amide II	1701	Lipid, ν(C=O)
	1188	Carbohydrates, ν(C-O)	1381	$\nu(COO^-)$
	1504	Amide II	1647	Amide I
	960	Protein phosphorylation	1743	Lipid, ν(C=O)
	1080	$\nu_s PO_2^-$	1612	Amide I
	1766	Lipid, ν(C=O)	1477	Proteins, $\nu_{as}CH_3$
0.1	1554	Amide II	1381	$\nu(COO^-)$
	968	Protein phosphorylation	1180	Carbohydrates, ν(C-O)
	1697	Lipid, ν(C=O)	1546	Amide II
	1381	$\nu(COO^-)$	1608	Amide I
	1654	Amide I	1041	Glycogen
	1188	Carbohydrates, ν(C-O)	1141	Carbohydrates, ν(C-O)
	1415	Proteins, $\nu_{as}CH_3$	1705	Lipid, ν(C=O)
	1755	Lipid, ν(C=O)	1419	Proteins, $\nu_{as}CH_3$

Cluster vectors plots for zebrafish brain exposed to single-walled CNTs at two doses: derived from IR spectra by cross-calculated PCA-LDA

Dose (mg/L)	Female		Male	
	Wavenumber (cm^{-1})	Tentative assignments	Wavenumber (cm^{-1})	Tentative assignments
0.001	1404	$\nu(COO^-)$	1720	Lipid, ν(C=O)
	1068	$\nu_s PO_2^-$	1543	Amide II
	1658	Amide I	1157	Carbohydrates, ν(C-O)
	1697	Lipid, ν(C=O)	1053	Glycogen
	1134	Carbohydrates, ν(C-O)	1654	Amide I
	1176	Carbohydrates, ν(C-O)	1392	$\nu(COO^-)$
	1261	Amide III	1191	$\nu_{as} PO_2^-$
	929	Protein phosphorylation	1107	$\nu_s PO_2^-$
0.1	1006	Glycogen	1720	Lipid, ν(C=O)
	1064	$\nu_s PO_2^-$	1581	Amide II
	1431	Proteins, $\nu_{as} CH_3$	1469	Proteins, $\nu_{as} CH_3$
	1107	$\nu_s PO_2^-$	1191	$\nu_{as} PO_2^-$
	1261	Amide III	1639	Amide I
	1357	$\nu(COO^-)$	1157	Carbohydrates, ν(C-O)
	1612	Amide I	1064	$\nu_s PO_2^-$
	1697	Lipid, ν(C=O)	1400	$\nu(COO^-)$

Cluster vectors plots for zebrafish gill exposed to single-walled CNTs at two doses: derived from IR spectra by cross-calculated PCA-LDA

Dose (mg/L)	Female		Male	
	Wavenumber (cm^{-1})	Tentative assignments	Wavenumber (cm^{-1})	Tentative assignments
0.001	1720	Lipid, ν(C=O)	1639	Amide I
	1454	Proteins, $\nu_{as}CH_3$	1774	Lipid, ν(C=O)
	1053	Glycogen	1539	Amide II
	1404	$\nu(COO^-)$	1693	Amide I
	1369	$\nu(COO^-)$	1257	Amide III
	1087	$\nu_sPO_2^-$	1492	Proteins, $\nu_{as}CH_3$
	1651	Amide I	972	Protein phosphorylation
	1755	Lipid, ν(C=O)	918	Protein phosphorylation
0.1	1103	$\nu_sPO_2^-$	1585	Amide I
	1766	Lipid, ν(C=O)	1662	Amide I
	1427	Proteins, $\nu_{as}CH_3$	1701	Lipid, ν(C=O)
	1261	Amide III	1083	$\nu_sPO_2^-$
	1627	Amide I	1338	$\nu(COO^-)$
	1500	Amide II	1180	Carbohydrates, ν(C-O)
	1539	Amide II	1462	Proteins, $\nu_{as}CH_3$
	948	Protein phosphorylation	1257	Amide III

Cluster vectors plots for zebrafish gonads exposed to single-walled CNTs at two doses: derived from IR spectra by cross-calculated PCA-LDA

Dose (mg/L)	Female		Male	
	Wavenumber (cm^{-1})	Tentative assignments	Wavenumber (cm^{-1})	Tentative assignments
0.001	1504	Amide II	1419	Proteins, $\nu_{as}CH_3$
	1697	Lipid, ν(C=O)	1681	Amide I
	1647	Amide I	1184	Carbohydrates, ν(C-O)
	1554	Amide II	1110	$\nu_s PO_2^-$
	1438	Proteins, $\nu_{as}CH_3$	1539	Amide II
	1612	Amide I	983	Protein phosphorylation
	1068	$\nu_s PO_2^-$	1724	Lipid, ν(C=O)
	1377	$\nu(COO^-)$	1473	Proteins, $\nu_{as}CH_3$
0.1	1446	Proteins, $\nu_{as}CH_3$	1701	Lipid, ν(C=O)
	1651	Amide I	1666	Amide I
	1184	Carbohydrates, ν(C-O)	1188	Carbohydrates, ν(C-O)
	1759	Lipid, ν(C=O)	1735	Lipid, ν(C=O)
	1481	Proteins, $\nu_{as}CH_3$	1110	$\nu_s PO_2^-$
	1724	Lipid, ν(C=O)	1419	Proteins, $\nu_{as}CH_3$
	1056	$\nu_s PO_2^-$	1504	Amide II
	1573	Amide II	1381	$\nu(COO^-)$

Cluster vectors plots for zebrafish liver exposed to single-walled CNTs at two doses: derived from IR spectra by cross-calculated PCA-LDA

Dose (mg/L)	Female		Male	
	Wavenumber (cm^{-1})	Tentative assignments	Wavenumber (cm^{-1})	Tentative assignments
0.001	1504	Amide II	1685	Amide I
	1693	Amide I	1504	Amide II
	1651	Amide I	1130	$\nu(COO^-)$
	1438	Proteins, $\nu_{as}CH_3$	1045	Glycogen
	956	Protein phosphorylation	983	Protein phosphorylation
	1558	Amide II	1357	$\nu(COO^-)$
	1404	$\nu(COO^-)$	921	Protein phosphorylation
	1083	$\nu_sPO_2^-$	1562	Amide II
0.1	1504	Amide II	1477	Proteins, $\nu_{as}CH_3$
	1651	Amide I	1512	Amide II
	1693	Amide I	1639	Amide I
	1766	Lipid, ν(C=O)	1693	Amide I
	1438	Proteins, $\nu_{as}CH_3$	1411	Proteins, $\nu_{as}CH_3$
	956	Protein phosphorylation	968	Protein phosphorylation
	1130	Carbohydrates, ν(C-O)	1261	Amide III
	999	Protein phosphorylation	1774	Lipid, ν(C=O)

Chapter 4

Alterations of A549 cells induced by carbon-based nanoparticles determined by biospectroscopic approach

Junyi Li, Meiping Tian, Li Cui, Heqing Shen, Kevin C. Jones and Francis L. Martin

Manuscript for submission

Contribution:

- I acquired the samples required for the project ;
- I acquired all the data and processed the total spectral dataset;
- I prepared the first draft of the manuscript.

…… ……

Junyi Li Prof. Francis L. Martin

Alterations of A549 cells induced by carbon-based nanoparticles determined by biospectroscopic approach

Junyi Li[a], *Meiping Tian*[b], *Li Cui*[b], *Heqing Shen*[b], *Kevin C. Jones*[a] *and Francis L. Martin*[a]*

[a]Centre of Biophotonics, Lancaster Environment Centre, Lancaster University, Lancaster LA1 4YQ; [b]Key Lab of Urban Environment and Health, Institude of Urban Environment, Chinese Academy of Sciences, Xiamen 361021,China

***Corresponding author** email: f.martin@lancaster.ac.uk; Tel: +44 (0)1524 510206

Abstract

Nanotechnology has introduced us many types of manufactured carbon-based nanoparticles (CNPs), together with a debate on the risks and benefits of these materials. Numerous investigations have been carried out in nanotoxicology, and toxic effects of nanoparticles have been observed by the scientific community. However, there is still a gap in the knowledge of nanotoxicology. In this study, we assessed the global alterations induced by CNPs in A549 cells using biospectroscopic techniques, including attenuated total reflection Fourier-transformation infrared and surface-enhanced Raman spectroscopy. A549 cells were treated with Fullerene (C60), long or short multi-walled carbon nanotubes, or single-walled carbon nanotubes at concentrations of 0.1 mg/L, 0.01 mg/L and 0.001 mg/L. The exposed cells were then interrogated by ATR-FTIR and SERS. Spectra were then processed via computational analysis, and information of biochemical alterations in the treated cells were extracted and visualised. Additionally, global DNA methylation level in the cells exposed to CNPs at 0.1 mg/L was determined by using HPLC-MS and genetic regulators for DNA methylation was checked by quantitative real-time PCR. It was found that CNPs could exert toxic effects in A549 cells, and also contributed to the promotion of global DNA methylation in cells.

Introduction

The rapid development of nanotechnology has introduced numerous nanomaterials with an extraordinary dimension to our world. Consequently, the potential exposure to nanomaterials for public is supposed to increase dramatically. Especially, carbon-based materials (CNMs) are currently used widely in both our daily life and industry[1-4]. Thus, it is urgent to know the health hazards related to their exposure prior to pushing their applications forward[5,6].

Recently, carbon-based materials are one of the most attractive nanomaterials due to their unique physicochemical property with different forms, such as fullerenes (C60), single- and multi-walled carbon nanotubes (MWCNTs). Numerous investigations has been carried out to assess these carbon nanoparticles (CNPs), and toxic effects both *in vitro* and *in vivo* were reported[7-10]. Commonly, generation of reactive oxygen species (ROS) is considered as a major factor involved in the toxicity of CNPs[11]. However, there is still a knowledge gap between nanotoxicology and real-world toxic effects of the CNPs[12]. The applications of conventional toxicology assays in the assessment of nanotoxicity are challenged, and thus new paradigm for these assays is required to be established while novel methodologies are introduced[13].

Raman or attenuated total reflection Fourier-transform infrared (ATR-FTIR) techniques are vibrational spectroscopic approaches capable of deriving biochemical information from biological samples[14]. Vibrational spectroscopy approaches without any specific agents, of the capability to cheaply, rapidly and non-invasively analyze biological samples, have been used to investigate cancer and assess toxic effects of environmental pollution[15-21]. Infrared (IR) spectroscopy is the measurement of the energy absorption of the chemical bond vibrational movement occurring at a specific

energy level. This produces spectra with peaks presenting the chemical bond in the sample. The mid-IR region (1800-900 cm^{-1} in wavenumbers), known as the "biochemical fingerprint" region, is where the majority IR absorption occurs in the biochemical structure. As a scattering technique, Raman spectroscopy has the inherent advantage of being unaffected by aqueous, providing a complementary spectra in samples. Surface-enhanced Raman spectroscopy (SERS), based on the normal Raman, is a technique possessing extremely high detection sensitivity and has a capability of providing fingerprint spectra of various molecules[22,23]. The high detection sensitivity is relying on the strong electromagnetic enhancement, typically produced by Ag or Au NPs, while Raman signals of molecules close to these NPs can be enhanced by more than 6 orders of magnitude[24,25]. This makes SERS an ultrasensitive detection tool; even the single molecule level can be detected[26].

The objective of this study was to perform a cytotoxicity assessment of four types CNPs (C60, Long and Short MWCNTs, single-walled CNTs) by using biospectroscopic techniques. Due to the tiny size, these CNPs can easily become airborne and inhaled and induce pulmonary injury. Hence, A549 cells, a human epithelial-like lung cell line, have been employed as an *in vitro* bio-model in this study. For both *in vitro* and *in vivo* toxicological test, dose is a key parameter to help us know the real-world situation better. Although acute effects are more likely to be observed following the high-dose exposure, recording the consequences of low-dose exposure over a lifetime is necessary to help us understand the possible risk of CNPs for the public. Thus, cells were exposed to CNPs at ppb level with a dose range at the concentration of 0.1 mg/L, 0.01 mg/L and 0.001 mg/L. Following the exposure, ATR-FTIR and SERS were then employed to interrogate the cells. Additionally, the global DNA methylation level in the cells exposed to 0.1 mg/L CNPs was determined by

HPLC-MS, as the disruption of genetic methylation in cells is considered to be linked to diseases such as cancer[27-29]. This study aims to assess the toxic effects induced by CNPs at ppb level.

Results

ATR-FTIR spectral dataset. The spectra derived from ATR-FTIR were inputted to PCA method following an appropriate pre-processing. PCA scores plots help to visualise the segregations among classes displayed as 1-D or 2-D scores plots (supporting information Figure S2). This allows observing a dose-response in the 1-D scores plots from PC1 space (Figure 2), where the scores in PC1 space contribute to most of variance in spectral data. To determine whether the treatment groups were significantly different from the corresponding control group, repeated-measures one-way analysis of variance (ANOVA) with Dunnett's *post hoc* tests were conducted to examine the treated *vs*. the control cells in PC1 space (supporting information Table S4). It showed that in all treatment groups the CNP-induced effects observed in PC1 space differed significantly (P <0.05) from the control group.

Loadings plots derived from the PC1 space identify the distinguishing wavenumbers corresponding for the most important variances in PC1 for each CNP treatment. The first eight primary wavenumbers in each the loadings plot were marked. For each CNP exposure, the wavenumbers ranked as following: 1624, 1658, 1589, 1547,1493, 1709, 1396 and 1103 cm^{-1} in C60 treatment group; 1539, 1501, 1624, 1585, 1662, 1466, 1732 and 1065 cm^{-1} in Long MWCNTs group; 1620, 1547, 1501, 1655, 1585, 1462, 1717 and 1400 cm^{-1} in Short MWCNTs group; and 1508, 1466, 1678, 1732, 1061, 1582, 1018 and 1115 cm^{-1} in SWCNTs group, respectively. These wavenumbers

contributes to most of the segregations in the PC1 space (The tentative assignments were listed in supporting information Table S1).

Another dataset was set up to compare the cellular response when cells were exposed to different types of CNPs at 0.1 mg/L. Following the PCA method, LDA was applied to the dataset as well, which would take the category information into the analytical model. The scores in the first three LD space were used for visualisation (Figure 4a and 4b). The separations between groups were significant. Moreover, cluster vector plots derived from the PCA-LDA result were used to indicate the biochemical alterations in cells induced by different CNPs (Supporting information Figure S4). To simplify the identification of the most pronounced wavenumbers related to the biochemical alterations, peak detector was employed and a cluster vector peak plot was generated (Figure 5a, and the tentative assignments of the first seven wavenumbers were listed in supporting information Table S3).

SERS spectral dataset. Following a similar workflow, the SERS spectral data was properly processed for further analysis. The PC1 scores plots showed significant separations between the treatment groups and the control one (Figure 3, and statistical results in supporting information Table S4). Similarly, the first eight primary wavenumbers in the loadings plots were marked as below: 1454, 1006, 930, 1364, 1621, 1423, 858 and 1487 cm^{-1} for C60 exposure; 1055, 518, 1586, 463, 761, 1522, 625 and 1335 cm^{-1} for Long MWCNTs exposure; 1006, 1456, 1341, 1372, 765, 946, 1718 and 1623 cm^{-1} for Short MWCNTs exposure; and 1623, 442, 1179, 802, 938, 1030, 1417 and 728 cm^{-1} for SWCNTs exposure (The tentative assignments were listed in supporting information Table S2).

Combination approach of PCA-LDA gave rise to the visualisation in both 2-D and 3-D scores plots (Figure 4c and 4d). Significant segregations were observed between the CNPs treatment groups and the control one. Furthermore, cluster vector peak plot displayed the main biochemical alterations induced by different CNPs (Figure 5b, and the tentative assignments of the first seven wavenumbers were listed in supporting information Table S3).

Global DNA methylation level determined by HPLC-MS. The global DNA methylation levels in the A549 cells following CNPs (0.1 mg/L) exposure tended to increase, as it was determined by using HPLC-MS method that the mean level of global genomic methylation was 0.88% in the control group, while the mean values were increased to 0.9967%, 0.9867%, 1.003% and 0.93% following exposure to C60, long or short MWCNTs, and SWCNTs, respectively (Figure 6). The statistical results showed that global DNA methylation level was significantly elevated by C60 (P <0.05) and short MWCNTs (P <0.05) treatment (Statistical results in supporting information Table S5).

Quantitative real-time PCR. Quantitative real-time PCR was used to assess the gene expression level of DNMTs in A549 cells exposed to CNPs at 0.1 mg/L. As a result from CNPs exposure, the expression level of DNMT1 was determined as 1.001 (C60), 0.8905 (Long), 0.9297 (Short), and 0.9284- fold (Single) of the control group. Similarly, the gene expression of DNMT3a was determined as 1.036 (C60), 0.7928 (Long), 0.9018 (Short), and 0.9606- fold (Single) of the control group, and the level of DNMT3b was decreased to 0.9849 (C60), 0.8198 (Long), 0.8171 (Short), and 0.7553-fold (Single) of the control group (Figure 7).

Generally, a down regulating tendency in DNMTs gene transcription in A549 cells following CNPs exposure was observed expect for those by C60. However, significance (P <0.05) was only observed in the downregulation of DNMT3b expression by SWCNTs treatment (Statistical results in supporting information Table S6).

Discussions

When A549 cells were exposed to CNPs, the IR spectra profiled that most of their response was non-linear and varied with concentration except those derived from cells treated with the long MWCNTs (Figure 2). Similarly, Spectral dataset from SERS also indicated highly non-linear response from the cells following exposure (Figure 3).Such non-linear responses were usually associated with the low-dose effects, which is significant in eco-toxicology assessment as environmental contaminations typically emerges at low concentrations. It has determined that biospectroscopy is of the ability to detect non-linear responses or low-dose effects in cells[17,18].

However, more pronounced segregations between exposure groups and the control were observed in SERS scores plot than the IR one (Figure 3). Based on different theory, these two techniques worked on two different ways. The IR spectra is the measurement of absorption after IR beam transmitted into the cells, and thus the spectra collected by ATR-FTIR would be containing the global information of the biochemical constitution in cells. However, the dominant contributor to most SERS processes is the electromagnetic enhancement mechanism, the maximum SERS enhancing region decreases dramatically rapidly with distance (r^{-10} for spheres), and the largest enhancement can be found only in a few nanometre closest to the Au nanoparticle surface[24]. This manifested that most of the signal collected by SERS was

derived from biochemical compounds touched around the surface of Au nanoparticle, which is possibly the cell membrane and the internal biochemical material leaking from cells that may attach to Au nanoparticle during the vortexing. Therefore, SERS reported us a partially information about the cells, but with a much higher sensitivity because of the extremely high enhancement of the Raman signal. These two techniques could be mutually complementary.

In order to determine how the CNPs affected the cells, loadings plots for the PCA of the spectral dataset were employed to highlight the important wavenumbers related to biochemical alterations in exposed cells compared with the control ones. Both the loadings plots derived from the PC1 (Figure 2 and 3) and PC2 (Supporting information) space were used, since loadings in these two PC factors can explain most of variance contributing to the segregations among groups in 2-D scores plots (Supporting information). In each loadings curve, the first eight primary peaks were marked corresponding to the main biomarkers for the dose-response in cells treated with CNPs (All wavenumbers and their tentative assignments were listed in supporting information). The loadings plots for both IR and SERS spectra showed that four types of CNPs shared a similar mode of toxic effects. Dataset derived from IR spectra showed that significant alterations were widely induced in Amide I (~1650 cm^{-1}), Amide II (~1500 cm^{-1}), lipid (~1750 cm^{-1}) and protein (~1400 cm^{-1}) by CNPs, while slight changes in the region of DNA/RNA ($\nu_{as}PO_2^-$, ~1225 cm^{-1}; $\nu_sPO_2^-$, ~1650 cm^{-1}) were observed as well (Figure 2), which suggested that CNPs may exert genotoxicity in cells. Although signal collected by SERS only interpreted partial information in the cells, significant alterations were observed in lipid and Amide I region (ν(C=C), ~1640 cm^{-1}; CH_2 bending, ~1440 cm^{-1}), Phenylalanine (~1001 cm^{-1}) and DNA (~720 cm^{-1}) (Figure 3). All spectral profiles indicated that alterations

induced by CNPs were mainly located in the outer region of cells[21,30]. It is considered that the generation of reactive oxygen species (ROS) and subsequent oxidative stress (OS) is the predominant mechanism leading to nanotoxicity[31,32]. Thus, it could directly or indirectly cause genomic damage inside the cell with no necessity for CNPs to reach the nucleus[33,34].

To compare the toxic effects induced by different types of CNPs, a parallel experiment was carried out that A549 cells were exposed to the four types CNPs at then concentration of 0.1 mg/L. Cells then were then collected for biospectroscopic analysis, and as well as further global DNA methylation assessment. Following the application of PCA-LDA analysis, both 3-D and 2-D scores plots derived from IR and SERS spectra were performed for visualisation (Figure 4). IR spectra indicated that long MWCNTs induced the most pronounced alterations in A549 cells, while C60 seemed to be less harmful to cells; the C60 treated group presented a relatively high overlap with the control group (Figure 4a and 4b). Moreover, the 2-D scores plot derive from the IR spectra also showed that short MWCNTs and SWCNTs exerted toxic effects on cells to a similar extent, but possible presenting a few difference underlying the mechanism due to the significant segregation between these two groups (Figure 4b). This result was consisting with our previous investigations that CNPs with larger size may induce more pronounced alterations[35,36]. In contrast to IR spectra, SERS spectra indicated that short MWCNTs induced the highest response in cells, followed by SWCNTs, and long MWCNTs as ranked, while large overlap between the C60 exposed group and the control group was observed, suggesting that C60 did less harm to cells (Figure 3d). Both spectral dataset determined that C60 was the least toxic one among the four CNPs[37]. In general, cluster vector derived from IR spectra showed that most of the alterations were located in the lipid, Amide I and

protein region, while DNA/RNA region was slightly affected. Both IR and SERS spectra profiled that the most pronounced biochemical alteration in cells after C60 exposure were in lipid region, which could be a result of the sphere shape of the C60 and its relatively lipophilic property. Moreover, the SERS detected high alteration in DNA region (intensity approximately at 760 cm^{-1}) induced by the three types of CNTs. It was possibly due to the factor that CNTs may penetrate the membrane of the cells and caused a leak of internal material in the cells, which may be then detected by SERS.

Beyond the global biochemical information provided by biospectroscopy, global DNA methylation levels in cells treated with CNPs at 0.1 mg/L were measured using HPLC-MS[38]. The results showed that global DNA methylation levels in cells were significantly elevated by C60 and short MWCNTs treatment, while an increasing trend was observed in global genetic methylation ratio of the cells following long MWCNTs and SWCNTs exposure, but without statistically significance (Figure 6, statistical results in supporting information Figure S8). Additionally, utilization of quantitative real-time PCR determined how CNPs impacted on the DNA methylation processing in the cells. As the target genes for q-PCR, the DNMTs are positive regulators for DNA methylation, which can mediate the DNA methylation by catalysing the transfer of a methyl group to DNA. DNMT1 is mainly contributing to maintain the pre-existing methylation pattern during replication, while DNMT3a and DNMT3b are mostly involved in *de novo* methylation[39], which is considered to be implicated in cell growth and differentiation, and also in abnormal methylation in tumorigenesis[40]. Generally, a down regulating tendency in DNMTs gene transcription in A549 cells after CNPs exposure was observed. Based on the statistical calculation, it indicated that only the gene transcription level of DNMT3b was decreased

significantly by SWCNTs. However, this was complicated with the increased global DNA methylation level, while the mechanism still required further investigation.

Conclusion

In this study, biospectroscopy, both ATR-FTIR and SERS, was presented as a novel powerful approach for nanotoxicity assessment, which also provided biochemical information underlying CNPs inducing cellular alterations. Both IR and SERS spectra determined that C60, Long and Short MWCNTs, single-walled CNTs could exert toxic effects in A549 cells and induce alterations in lipid, protein and even the genomic region. Additionally, it was also determined that CNPs at 0.1 mg/L could exert a potential negative impact on the gene expression of DNMTs, but contributed to the global genomic hypermethylation, which suggested that CNPs exposure may contribute to risk of diseases such as cancer[29,41]. Further study could be conducted to investigate how CNPs impact on specific genes.

Methods

Chemicals and carbon nanoparticles

All CNPs were purchased from Sigma. As stated, short MWCNTs were >90% pure being 10-15 nm in diameter and 0.1-10 μm in length. Long MWCNTs were >90% pure also, but were 110-170 nm in diameter and 5-9 μm in length. C60 had a purity >99.5% and particle size of 1 nm. Single-walled CNTs were described as CarboLex AP-grade (the purity of AP-grade products ranges from 50% to 70% by volume); major impurities are carbon nanospheres and carbon-encapsulated catalyst nanoparticles - the diameter was 1.2-1.5 nm. All CNPs were analysed by Raman spectroscopy (Renishaw PLC, Gloucestershire, UK) with a 785 nm laser, and

determined to be of high purity. Additionally, images of CNPs were taken using a scanning electron microscope (SEM) [JSM 5600 (JEOL)] [see Electronic Supporting Information (ESI) Figure S1]. Bovine serum albumin (BSA) obtained from Sigma was ≥98%. CNPs were dispersed in 1% BSA solution with a 15-min ultrasonication bathed in ice water and stock solutions were made at concentrations of 100 mg/L. CNT solutions were stable and well-dispersed, while C60 appeared to agglomerate.

Gold nanoparticles (Au NPs) for SERS were synthesized using trisodium citrate as the reductants (Supporting Information Figure S5), [42,43] which were prepared and characterised by Dr Li Cui in her lab, IUE, China.

Cell culture and CNPs treatment

Human lung epithelial cells, A549 were routinely maintained in RPMI 1640 medium at PH7.2, supplemented with 10% inactivated fetal bovine serum and 1% penicillin/streptomycin and were grown in humidified atmosphere supplied with 5% CO_2 in air at 37℃. A549 cells were cultured in 60mm dishes prior to incorporation into experiments. Following this, cells were disaggregated with trypsin (0.05%)/EDTA (0.02%) solution, and were immediately resuspended in complete medium and seeded in 30mm dishes. Then cells were grown for 24-h to attach and followed by a further 24-h treatment or without test agents. The four CNPs were introduced in the treatment with exposure dose at concentration 0.1 mg/L, 0.01 mg/L and 0.001 mg/L. The control and each exposure group was triplicate.

After exposure, A549 cells were washed three times with cold PBS, scraped and centrifuged at 1000***g*** for 3 min. The resulting cell pellets were fixed with 4% formalin in PBS for 30min. The fixed cells were washed using distilled water and then added to Low-E glass slides (Kevley Technologies, Chesterland, OH, USA), air dried and

stored in desiccator prior to acquirement of ATR-FTIR spectroscopy. For SERS interrogation, the fixed and washed cells were mixed with Au NPs. After vortexing, an aliquot of 10 μL of the mixture were dropped onto a glass slides for SERS measurement.

Spectroscopy acquisition

All A549 cell samples on Low-E slides were interrogated using a Bruker TENSOR 27 FTIR spectrometer (Bruker Optics Ltd., Coventry, UK) equipped with a Helios ATR attachment containing a diamond internal reflection element (IRE). Instrument parameters were set at 32 scans, 8 cm^{-1} resolution. For each slide, 10 IR spectra were acquired at different points across the sample. Prior to starting a new slide, the ATR crystal was cleaned with deionized water and a background was then taken.

SERS spectra were acquired by using a LabRAM Aramis (HORIBA JobinYvon) confocal micro-Raman system equipped with a 1200 g/mm grating, He-Ne 632.8 nm laser (laser power ≤ 70 mW prior to lens). The system calibration was carried out using a silicon calibration source for wavenumber shift. A50X objective (Olympus) with a numerical aperture of 0.55 was used to focus the laser beam and collect Raman signal with a working distance of about 8 mm. In order to reduce the possible damage of laser to cells, DuoScan in the micromapping mode with a scanning area of 30 μm × 30 μm was applied with an acquisition time of 5 s.

Computational analysis of spectral data

Spectral data processing, acquired from both ATR-FTIR and Raman spectroscopy, were performed using IRootLab toolbox (http://irootlab.googlecode.com) running on MATLAB r2010a (The MathWorks, Inc., US)[44]. IR spectra were pre-processed as

followings: cut to 1800-900 cm^{-1} (the biochemical fingerprint range), 2nd differentiation, and vector normalised, While SERS spectra were pre-processed following wavelet de-noising, cut to 400-1800 cm^{-1}, 2nd differentiation, and vector normalised[45]. Computational analysis using multivariate techniques including principal component analysis (PCA) and linear discriminate analysis (LDA) can efficiently analyse the large spectral dataset[46,47]. The main difference between PCA and LDA is that PCA is an unsupervised method, while LDA is a supervised method. PCA looks for projections to maximize variance and LDA looks for projections that maximize the ratio of between-class to within-class scatter[48]. Following pre-processing, PCA was applied to the dataset. PCA, as an unsupervised technique, has capability to reduce the dimensions of the data. Undoubtedly PCA is capable of identifying important information in the spectral data, but it has less discrimination power due to the fact that it is an unsupervised procedure. Often, in order to interpret of the complex biochemical information with labelled classes obtained through vibrational spectroscopic techniques, it requires further data analysis using supervised procedures like LDA. The output data derived from PCA or PCA-LDA can be then visualized as 1-D, 2-D or 3-D scatterplots ("scores plots"). In scores plots, nearness between two groups means similarity, while the distance indicates dissimilarity. To reveal the biochemical alterations associated with each group in the dataset, both loadings plots and cluster vectors[16] were developed. To simplify the identification of the main biochemical alteration of each group, peak detector were used to indicate the first few highest peaks in the loadings plots and cluster vector plots.

Global DNA methylation determined by HPLC-MS

A549 cells exposed to four CNPs at the high dose (0.1 mg/L) were collected, and stored in PBS at -20℃ prior to q-PCR and DNA methylation analysis.

The DNA was extracted from A549 cells by DNeasy Cell Kit (Qiagen, Germany) following the manufacturer's instruction. RNase A was added to the columns in the kit to remove RNA residue. DNA hydrolysis was conducted by using a mixture degradase kit (DNA Degradase Plus, Zymo Research, USA) DNA following the manufacturer's protocol. To confirm the complete hydrolysis of DNA, agarose gel electrophoresis was employed to test the result of the DNA hydrolysis. The DNA hydrolysis mixtures were then stored at -20℃ for mass spectrometric analysis.

To perform chromatographic separation, a Kinetex C_{18} column (100 mm × 4.6 mm, 2.6 μm, Phenomenex, USA) was employed a HPLC system (LC-20AD, Shimadzu, Japan). The injection volume was 20 μL. The mobile phase consisted of water (A) and methanol (B). A gradient elution project was used as follows: 0–0.01 min, 3%B; 0.01–5.00 min, 5%B; 3.00–12.00 min, 50%B; 12.00–15.00 min, 100%B; 15.00–25.00 min, 3%B at a flow rate of 0.5 $mL.min^{-1}$. For the mass spectrometric analysis, an electrospray ionization tandem mass spectrometry (LCMS-8030, Shimadzu, Japan) system was used, operating in positive ionization mode and conditioned at a capillary temperature of 400◦C and medium N_2 curtain gas. Optimized multiple reaction monitoring (MRM) conditions were set up to evaluate dC from m/z 228.1 to 111.9 and 5mdC from m/z 242.1 to 126.0. Data acquisition and processing were performed via Analyst software. The global DNA methylation ratio (MR) was determined by MR = [5-mdC]/([5-mdC] + [dC]).

Quantitative real-time polymerase chain reaction

Total RNAs were extracted using RNeasy@ Mini Kit (Qiagen, Venlo, Netherlands) from cells. Subsequently, reverse transcription of cDNA synthesis was performed with 1 μg total RNA using PrimeScript@ RT reagent kit with gDNA Eraser cDNA synthesis kits (Takara, Otsu, Shiga, Japan). Real-time PCR was carried out in a 20 μL reaction mixture and triplicated, using SYBR Green Master Mix reagents (Roche, Basel, Switzerland) on a Roche LightCycle@ 480llreal-time PCR system following the manufacturer's protocol (95◦C for 10 min followed by 40 cycles at 95◦C for 15 s, and 60◦C for 30 s). The sequences of primers specific for the DNMT1, DNMT3a, DNMT3b, and GAPDH genes were designed using the primer5 software (supporting information Table S7). Gene expression levels were normalised to GAPDH gene expression. The relative levels of each target mRNA transcripts to the control GAPDH were analysed by $2^{-\Delta\Delta Ct}$ method and expressed as fold change.

Statistical analysis

The data are all expressed as the means ±SD. Significant differences among multiple groups were determined using a one-way analysis of variance (ANOVA) followed by Dunnett's *post hoc* tests. Probabilities of $P < 0.05$ were considered as statistically significant. All these tests were conducted in GraphPad Prism 4 (GraphPad Software, USA).

Reference

1 Jensen, A. W., Wilson, S. R. & Schuster, D. I. Biological applications of fullerenes. *Biorg. Med. Chem.* **4**, 767-779, doi:http://dx.doi.org/10.1016/0968-0896(96)00081-8 (1996).

2 Baughman, R. H., Zakhidov, A. A. & de Heer, W. A. Carbon Nanotubes--the Route Toward Applications. *Science* **297**, 787-792, doi:10.1126/science.1060928 (2002).

3 Bianco, A., Kostarelos, K. & Prato, M. Applications of carbon nanotubes in drug delivery. *Curr. Opin. Chem. Biol.* **9**, 674-679, doi:http://dx.doi.org/10.1016/j.cbpa.2005.10.005 (2005).

4 Gooding, J. J. Nanostructuring electrodes with carbon nanotubes: A review on electrochemistry and applications for sensing. *Electrochim. Acta* **50**, 3049-3060, doi:http://dx.doi.org/10.1016/j.electacta.2004.08.052 (2005).

5 Nel, A., Xia, T., Mädler, L. & Li, N. Toxic Potential of Materials at the Nanolevel. *Science* **311**, 622-627, doi:10.1126/science.1114397 (2006).

6 Oberdörster, G., Oberdörster, E. & Oberdörster, J. Nanotoxicology: an emerging discipline evolving from studies of ultrafine particles. *Environ. Health Perspect.*, 823-839 (2005).

7 Warheit, D. B. *et al.* Comparative Pulmonary Toxicity Assessment of Single-wall Carbon Nanotubes in Rats. *Toxicol. Sci.* **77**, 117-125, doi:10.1093/toxsci/kfg228 (2004).

8 Muller, J. *et al.* Respiratory toxicity of multi-wall carbon nanotubes. *Toxicol. Appl. Pharmacol.* **207**, 221-231, doi:http://dx.doi.org/10.1016/j.taap.2005.01.008 (2005).

9 Davoren, M. *et al.* In vitro toxicity evaluation of single walled carbon nanotubes on human A549 lung cells. *Toxicol. In Vitro* **21**, 438-448, doi:http://dx.doi.org/10.1016/j.tiv.2006.10.007 (2007).

10 Smith, C. J., Shaw, B. J. & Handy, R. D. Toxicity of single walled carbon nanotubes to rainbow trout, (Oncorhynchus mykiss): Respiratory toxicity, organ pathologies, and other physiological effects. *Aquat. Toxicol.* **82**, 94-109, doi:http://dx.doi.org/10.1016/j.aquatox.2007.02.003 (2007).

11 Fu, P. P., Xia, Q., Hwang, H.-M., Ray, P. C. & Yu, H. Mechanisms of nanotoxicity: Generation of reactive oxygen species. *J. Food Drug Anal.* **22**, 64-75, doi:http://dx.doi.org/10.1016/j.jfda.2014.01.005 (2014).

12 Kahru, A. & Dubourguier, H.-C. From ecotoxicology to nanoecotoxicology. *Toxicology* **269**, 105-119, doi:http://dx.doi.org/10.1016/j.tox.2009.08.016 (2010).

13 Kroll, A., Pillukat, M. H., Hahn, D. & Schnekenburger, J. Current in vitro methods in nanoparticle risk assessment: Limitations and challenges. *Eur. J. Pharm. Biopharm.* **72**, 370-377, doi:http://dx.doi.org/10.1016/j.ejpb.2008.08.009 (2009).

14 Kelly, J. G. *et al.* Biospectroscopy to metabolically profile biomolecular structure: a multistage approach linking computational analysis with biomarkers. *J. Proteome Res.* **10**, 1437-1448, doi:10.1021/pr101067u (2011).

15 Llabjani, V. *et al.* Polybrominated Diphenyl Ether-Associated Alterations in Cell Biochemistry as Determined by Attenuated Total Reflection Fourier-Transform Infrared Spectroscopy: a Comparison with DNA-Reactive and/or Endocrine-Disrupting Agents. *Environ. Sci. Technol.* **43**, 3356-3364, doi:10.1021/es8036127 (2009).

16 Llabjani, V., Trevisan, J., Jones, K. C., Shore, R. F. & Martin, F. L. Binary Mixture Effects by PBDE Congeners (47, 153, 183, or 209) and PCB Congeners (126 or 153) in MCF-7 Cells: Biochemical Alterations Assessed by IR Spectroscopy and Multivariate Analysis. *Environ. Sci. Technol.* **44**, 3992-3998, doi:10.1021/es100206f (2010).

17 Llabjani, V. *et al.* Differential Effects in Mammalian Cells Induced by Chemical Mixtures in Environmental Biota As Profiled Using Infrared

Spectroscopy. *Environ. Sci. Technol.* **45**, 10706-10712, doi:10.1021/es202574b (2011).

18 Llabjani, V., Trevisan, J., Jones, K. C., Shore, R. F. & Martin, F. L. Derivation by Infrared Spectroscopy with Multivariate Analysis of Bimodal Contaminant-Induced Dose-Response Effects in MCF-7 Cells. *Environ. Sci. Technol.* **45**, 6129-6135, doi:10.1021/es200383a (2011).

19 Patel, I. I. *et al.* High contrast images of uterine tissue derived using Raman microspectroscopy with the empty modelling approach of multivariate curve resolution-alternating least squares. *Analyst* **136**, 4950-4959, doi:10.1039/c1an15717e (2011).

20 Pang, W. *et al.* Identification of benzo[a]pyrene-induced cell cycle-associated alterations in MCF-7 cells using infrared spectroscopy with computational analysis. *Toxicology* **298**, 24-29, doi:10.1016/j.tox.2012.04.009 (2012).

21 Riding, M. J. *et al.* Concentration-dependent effects of carbon nanoparticles in gram-negative bacteria determined by infrared spectroscopy with multivariate analysis. *Environ. Pollut.* **163**, 226-234, doi:http://dx.doi.org/10.1016/j.envpol.2011.12.027 (2012).

22 Hering, K. *et al.* SERS: a versatile tool in chemical and biochemical diagnostics. *Anal. Bioanal. Chem.* **390**, 113-124, doi:10.1007/s00216-007-1667-3 (2008).

23 McNay, G., Eustace, D., Smith, W. E., Faulds, K. & Graham, D. Surface-Enhanced Raman Scattering (SERS) and Surface-Enhanced Resonance Raman Scattering (SERRS): A Review of Applications. *Appl. Spectrosc.* **65**, 825-837 (2011).

24 Stiles, P. L., Dieringer, J. A., Shah, N. C. & Van Duyne, R. P. Surface-Enhanced Raman Spectroscopy. *Annu. Rev. Anal. Chem.* **1**, 601-626, doi:doi:10.1146/annurev.anchem.1.031207.112814 (2008).

25 Sharma, B., Frontiera, R. R., Henry, A.-I., Ringe, E. & Van Duyne, R. P. SERS: Materials, applications, and the future. *Mater. Today* **15**, 16-25, doi:http://dx.doi.org/10.1016/S1369-7021(12)70017-2 (2012).

26 Kneipp, K. *et al.* Single molecule detection using surface-enhanced Raman scattering (SERS). *Phys. Rev. Lett.* **78**, 1667 (1997).

27 Ehrlich, M. DNA methylation in cancer: too much, but also too little. *Oncogene* **21**, 5400-5413 (2002).

28 Esteller, M. & Herman, J. G. Cancer as an epigenetic disease: DNA methylation and chromatin alterations in human tumours. *J. Pathol.* **196**, 1-7, doi:10.1002/path.1024 (2002).

29 Das, P. M. & Singal, R. DNA Methylation and Cancer. *J. Clin. Oncol.* **22**, 4632-4642, doi:10.1200/jco.2004.07.151 (2004).

30 Riding, M. J. *et al.* Mechanistic insights into nanotoxicity determined by synchrotron radiation-based Fourier-transform infrared imaging and multivariate analysis. *Environ. Int.* **50**, 56-65, doi:http://dx.doi.org/10.1016/j.envint.2012.09.009 (2012).

31 Nel, A., Xia, T., Mädler, L. & Li, N. Toxic potential of materials at the nanolevel. *Science* **311**, 622 (2006).

32 Shvedova, A. A., Pietroiusti, A., Fadeel, B. & Kagan, V. E. Mechanisms of carbon nanotube-induced toxicity: Focus on oxidative stress. *Toxicol. Appl. Pharmacol.* **261**, 121-133, doi:http://dx.doi.org/10.1016/j.taap.2012.03.023 (2012).

33 Schuster, G. B. Long-Range Charge Transfer in DNA: Transient Structural Distortions Control the Distance Dependence. *Acc. Chem. Res.* **33**, 253-260, doi:10.1021/ar980059z (2000).

34 Elsaesser, A. & Howard, C. V. Toxicology of nanoparticles. *Adv. Drug Del. Rev.* **64**, 129-137, doi:http://dx.doi.org/10.1016/j.addr.2011.09.001 (2012).

35 Li, J. *et al.* Dose-Related Alterations of Carbon Nanoparticles in Mammalian Cells Detected Using Biospectroscopy: Potential for Real-World Effects. *Environ. Sci. Technol.* **47**, 10005-10011, doi:10.1021/es4017848 (2013).

36 Li, J., Ying, G.-G., Jones, K. C. & Martin, F. L. Real-world carbon nanoparticle exposures induce brain and gonadal alterations in zebrafish (Danio rerio) as determined by biospectroscopy techniques. *Analyst* **140**, 2687-2695, doi:10.1039/c4an02227k (2015).

37 Jia, G. *et al.* Cytotoxicity of Carbon Nanomaterials: Single-Wall Nanotube, Multi-Wall Nanotube, and Fullerene. *Environ. Sci. Technol.* **39**, 1378-1383, doi:10.1021/es048729l (2005).

38 Peng, S.-Y., Zhang, J., Tian, M.-P., Wang, Z.-L. & Shen, H.-Q. Determination of Global DNA Methylation in Biological Samples by Liquid Chromatography-Tandem Mass Spectrometry. *Chinese J. Anal. Chem.* **40**, 1201-1206, doi:http://dx.doi.org/10.1016/S1872-2040(11)60566-5 (2012).

39 Girault, I., Tozlu, S., Lidereau, R. & Bièche, I. Expression Analysis of DNA Methyltransferases 1, 3A, and 3B in Sporadic Breast Carcinomas. *Clin. Cancer Res.* **9**, 4415-4422 (2003).

40 Tian, M. *et al.* Perfluorooctanoic acid induces gene promoter hypermethylation of glutathione-S-transferase Pi in human liver L02 cells. *Toxicology* **296**, 48-55, doi:http://dx.doi.org/10.1016/j.tox.2012.03.003 (2012).

41 Robertson, K. D. DNA methylation and human disease. *Nat Rev Genet* **6**, 597-610, doi:http://www.nature.com/nrg/journal/v6/n8/suppinfo/nrg1655_S1.html (2005).

42 Cui, L., Yao, M., Ren, B. & Zhang, K.-S. Sensitive and Versatile Detection of the Fouling Process and Fouling Propensity of Proteins on Polyvinylidene Fluoride Membranes via Surface-Enhanced Raman Spectroscopy. *Anal. Chem.* **83**, 1709-1716, doi:10.1021/ac102891g (2011).

43 Cui, L. *et al.* In Situ Study of the Antibacterial Activity and Mechanism of Action of Silver Nanoparticles by Surface-Enhanced Raman Spectroscopy. *Anal. Chem.* **85**, 5436-5443, doi:10.1021/ac400245j (2013).

44 Trevisan, J., Angelov, P. P., Scott, A. D., Carmichael, P. L. & Martin, F. L. IRootLab: a free and open-source MATLAB toolbox for vibrational biospectroscopy data analysis. *Bioinformatics* **29**, 1095-1097, doi:10.1093/bioinformatics/btt084 (2013).

45 Trevisan, J., Angelov, P. P., Carmichael, P. L., Scott, A. D. & Martin, F. L. Extracting biological information with computational analysis of Fourier-transform infrared (FTIR) biospectroscopy datasets: current practices to future perspectives. *Analyst* **137**, 3202-3215, doi:10.1039/c2an16300d (2012).

46 Martin, F. L. *et al.* Identifying Variables Responsible for Clustering in Discriminant Analysis of Data from Infrared Microspectroscopy of a Biological Sample. *J. Comput. Biol.* **14**, 1176-1184, doi:10.1089/cmb.2007.0057 (2007).

47 Martin, F. L. *et al.* Distinguishing cell types or populations based on the computational analysis of their infrared spectra. *Nat. Protocols* **5**, 1748-1760, doi:http://www.nature.com/nprot/journal/v5/n11/abs/nprot.2010.133.html#supplementary-information (2010).

48 Gautam, R., Vanga, S., Ariese, F. & Umapathy, S. Review of multidimensional data processing approaches for Raman and infrared spectroscopy. *EPJ Techn Instrum* **2**, 1-38, doi:10.1140/epjti/s40485-015-0018-6 (2015).

Acknowledgment

Funding for the laboratory experiments in this study from the Chinese Academy of Sciences is greatly acknowledged.

Author contribution statement

J.L. conducted the whole experiments. M.T. helped with works on the global DNA methylation by HPLC-MS and gene expression analysis by q-PCR., and the data analysis. L.C. helped on performing SERS on cells samples. H.S. offered suggestions on the experiment and laboratory support for the work. K.C.J. and F.L.M also gave suggestions on the experiment. J.L. wrote the manuscripts and F.L.M. did the final edition.

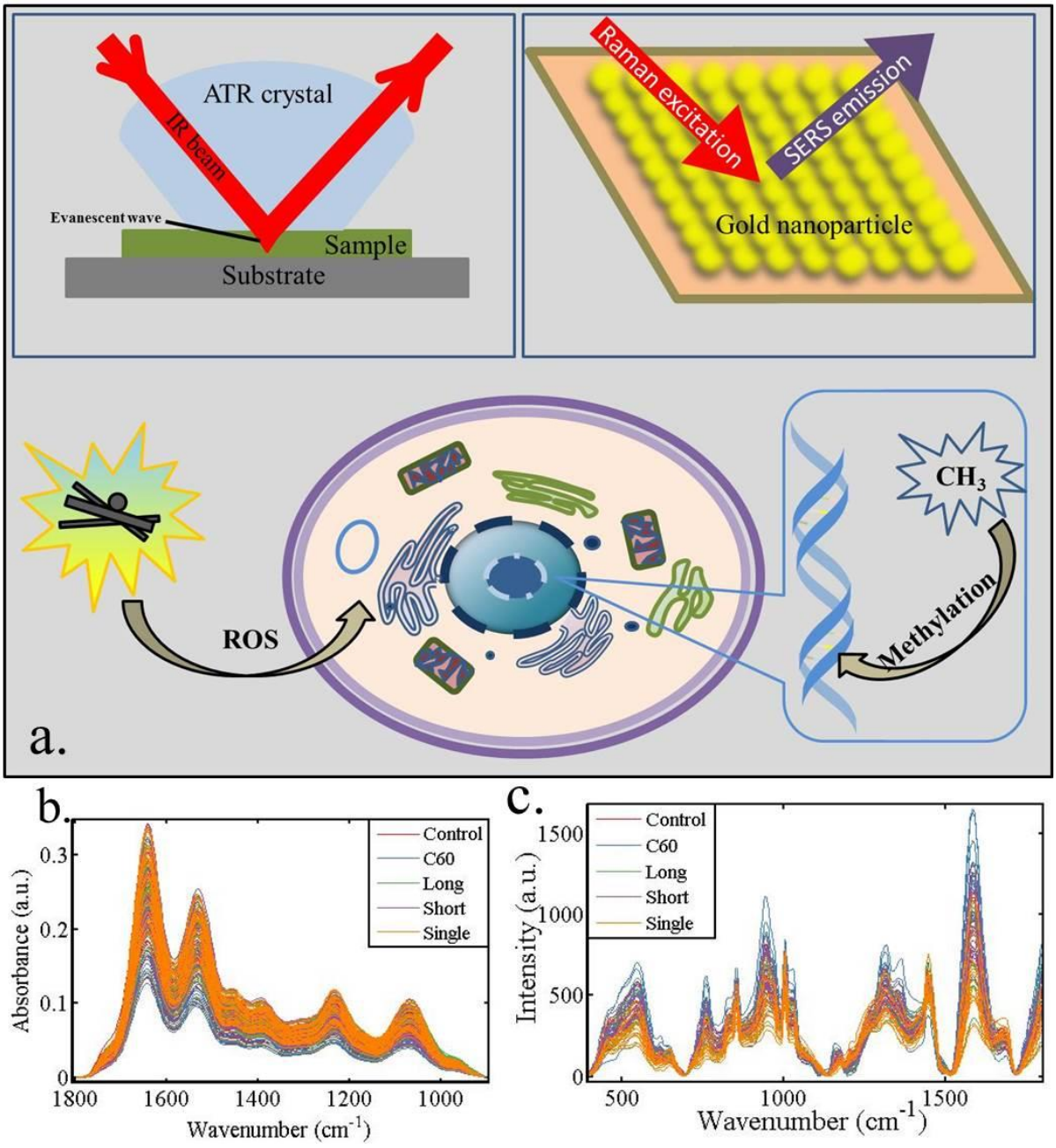

Figure 1. a) General graph for brief introduction of the nanotoxicity and the operation principle of ATR-FTIR and SERS used in this project; b) Raw spectra in "biochemical fingerprint region" from A549 cells collected by ATR-FTIR; c) Raw spectra from A549 cells collected by SERS.

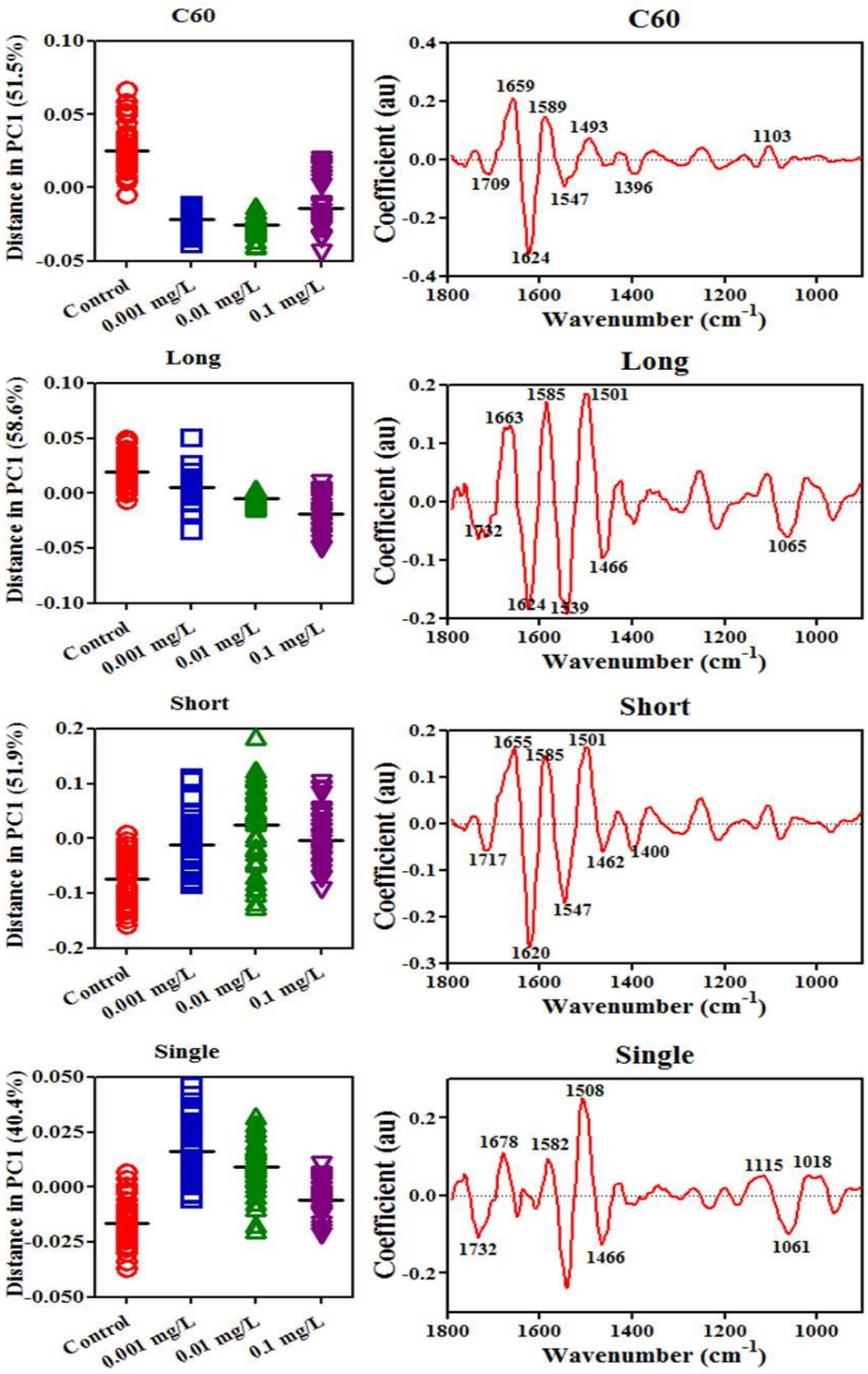

Figure 2. One dimensional (1 D) PCA scores plots in PC1 space of ATR-FTIR spectral dataset derived from A549 cells exposed to carbon nanoparticles at each concentration compared with the vehicle control. Their corresponding loadings plots are on right side.

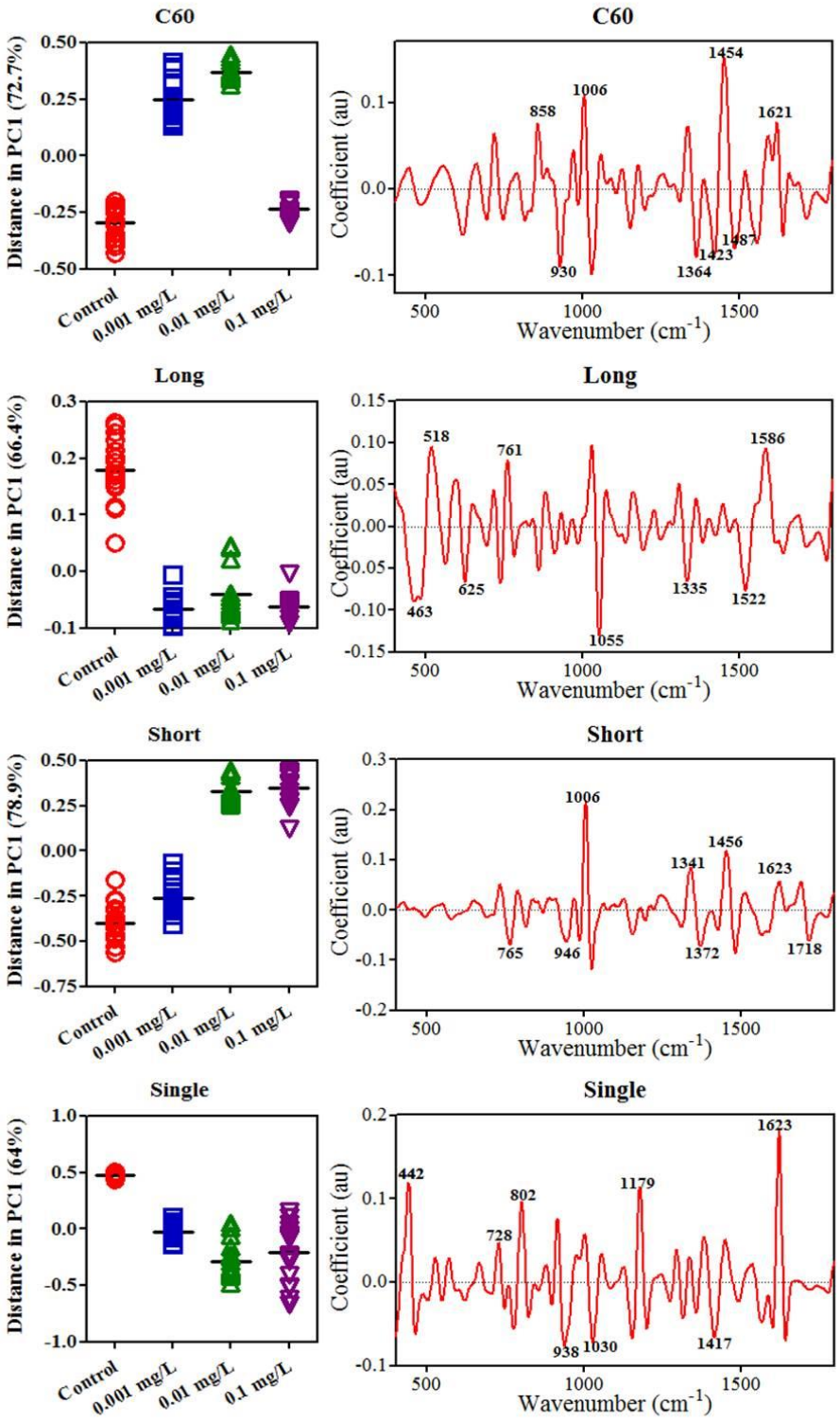

Figure 3. One dimensional (1 D) PCA scores plots in PC1 space of SERS spectral dataset derived from A549 cells exposed to carbon nanoparticles at each concentration

compared with the vehicle control. Their corresponding loadings plots are on right side.

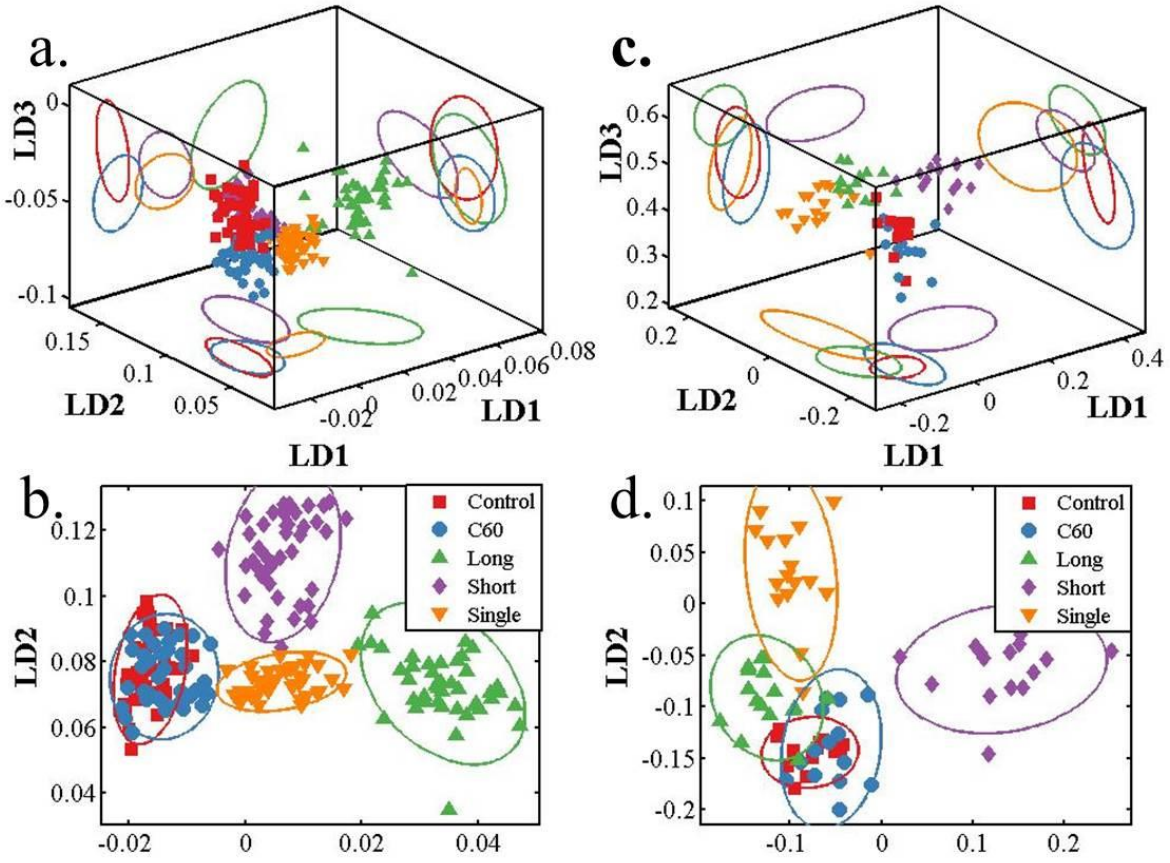

Figure 4. Scores plots by PCA-LDA derived from spectral dataset of the A549 cells exposed to CNPs at 0.1 mg/L compared with the vehicle control (*90% confidence ellipsoids*). **a)** Three dimensional (3 D) and **b)** 2-D PCA-LAD scores plots from the ATR-FTIR spectral dataset; **c)** Three dimensional (3 D) and **d)** 2-D PCA-LAD scores plots from the SERS spectral dataset.

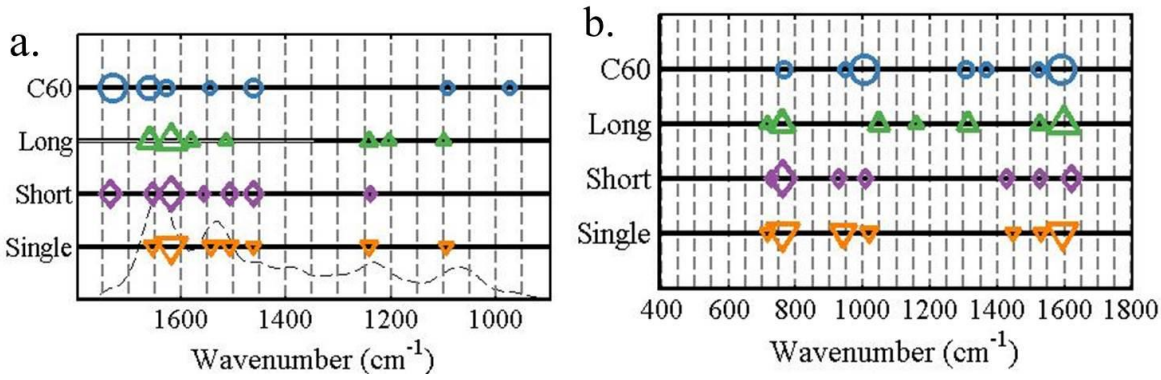

Figure 5. Cluster vector peak plots by PCA-LDA indicating the wavenumber basis for segregation corresponding to A549 cells exposed to CNPs at 0.1 mg/L. Cells exposed to each CNP was compared with the vehicle control. The size of the symbol in cluster vector peaks plot is proportional to the height of the corresponding peaks in the cluster vector plots, which relative to the extent of biochemical alteration compared with the vehicle control. **a**) Cluster vector peak plot derived from ATR-FTIR spectral dataset; **b**) Cluster vector peak plot derived from SERS spectral dataset.

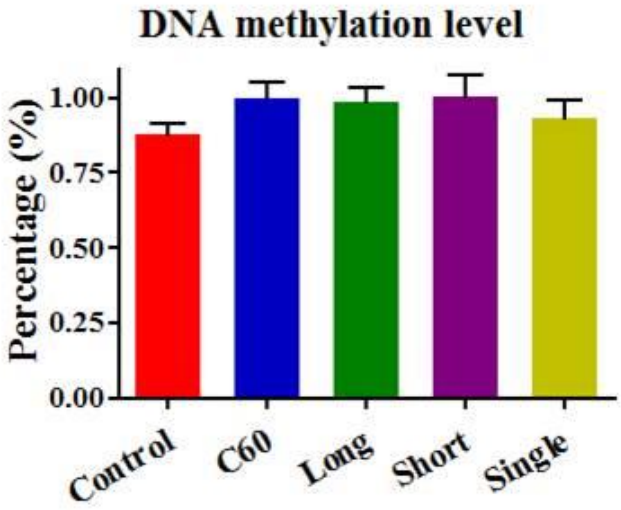

Figure 6. Global DNA methylation levels in A549 cells exposed to CNPs at 0.1 mg/L or without treatment. Values are expressed as means ±SD (n=3)

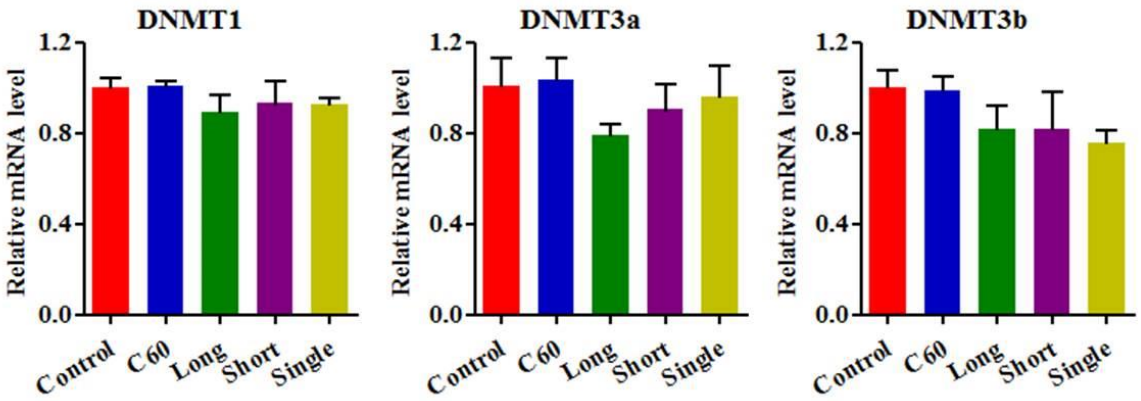

Figure 7. Quantitative real-time polymerase chain reaction analysis of gene expression in A549 cells exposed to CNPs at 0.1 mg/L. Total RNA was isolated, reverse transcribed, and amplified with the specific primers. Relative quantification of each gene expression level was normalized according to GAPDH gene expression. The data of exposure groups were calibrated to the control values (control=1), values are expressed as means ±SD (n=3).

Support information

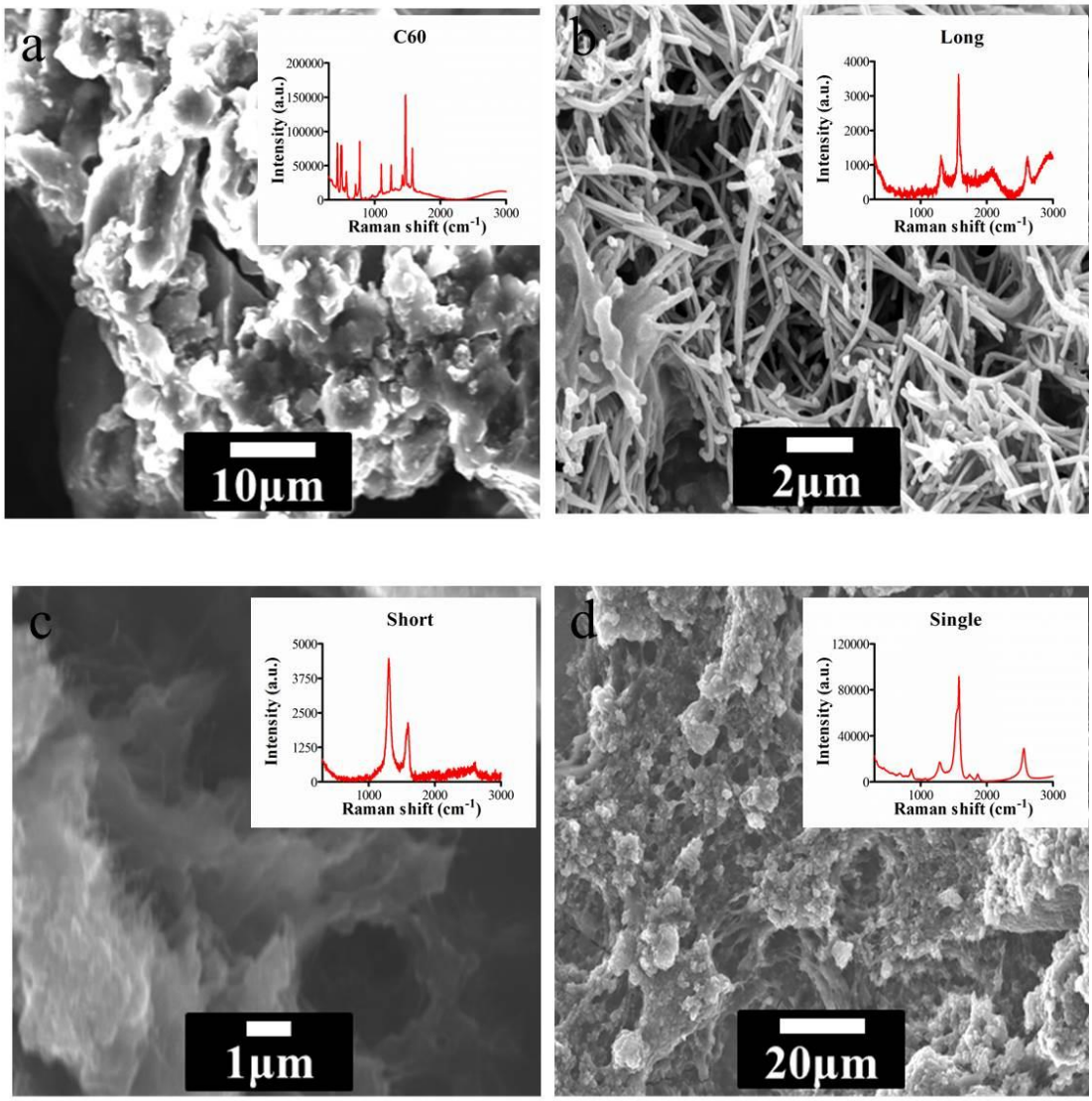

Figure S1. Scanning electron microscopy (SEM) images of **(a)** C60 fullerene; **(b)** Long MWCNTs; **(c)** Short MWCNTs, and **(d)** Single-Walled CNTs with Raman spectra of characterization.

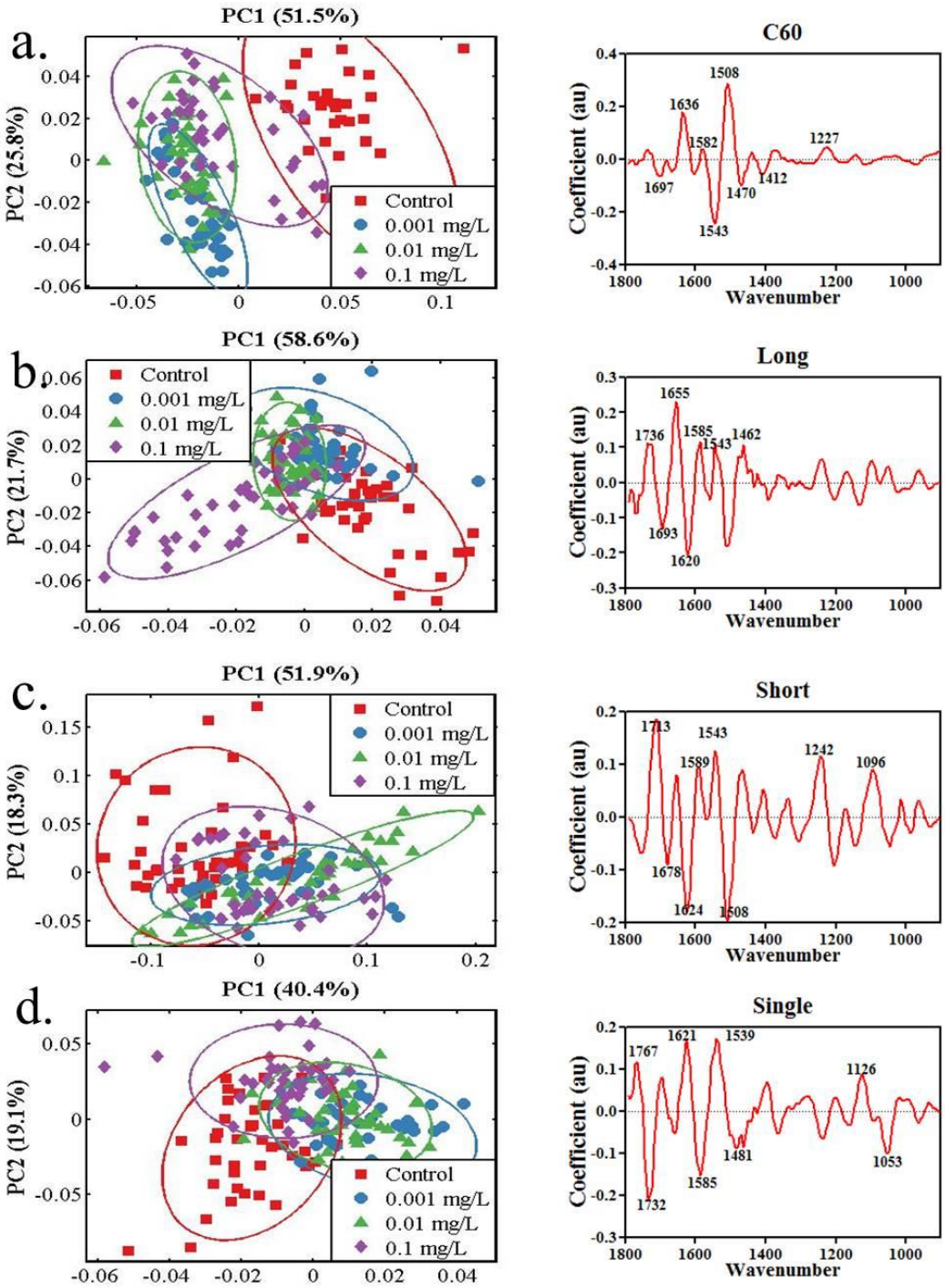

Figure S2. Two-dimension **PCA** scores plots (*90% Confidence ellipsoids*) and loading plots in PC2 derived from A549 cells exposed to CNPs interrogated by **ATR-FTIR**; **a**) C60; **b**) long MWCNTs; **c**) short MWCNTs and **d**) single-walled CNTs.

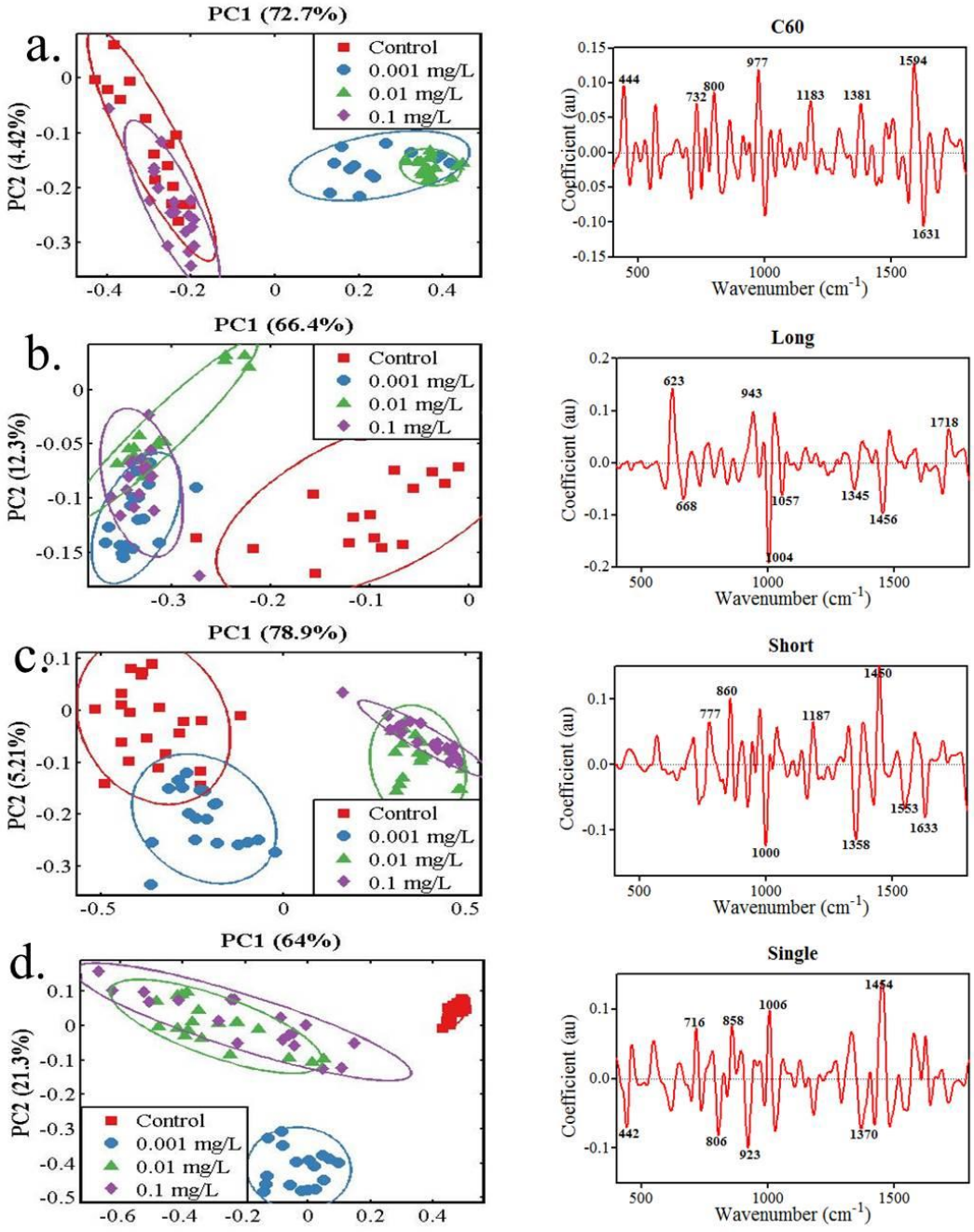

Figure S3. Two-dimension **PCA** scores plots (*90% Confidence ellipsoids*) and loadings plots in PC2 derived from A549 cells exposed to CNPs interrogated by **SERS**; **a**) C60; **b**) long MWCNTs; **c**) short MWCNTs and **d**) single-walled CNTs.

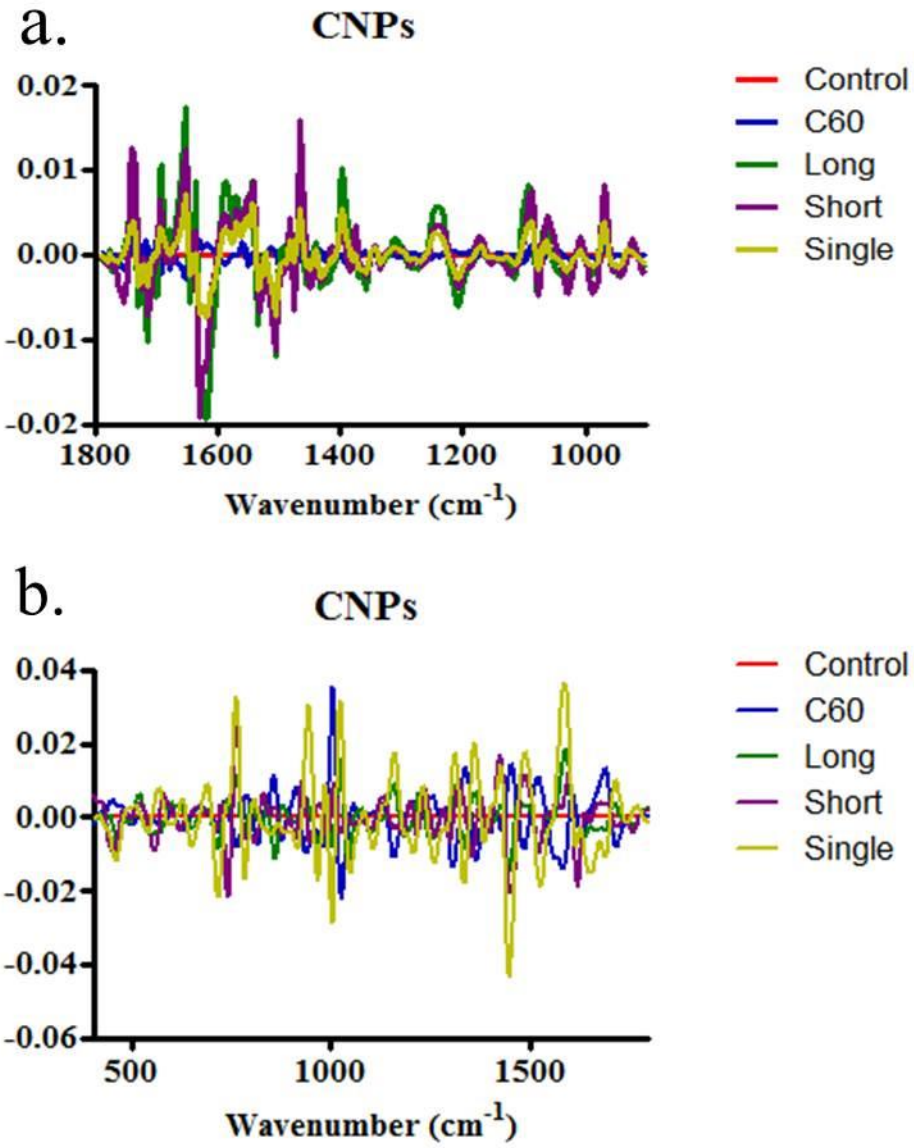

Figure S4. Cluster vector indicating the wavenumber basis for segregation corresponding to A549 cells exposed to CNPs at 0.1 mg/L. Cells exposed to CNPs at 0.1 mg/L was compared with the vehicle control. The height of the cluster vector peak is proportional to the extent of biochemical alteration compared to the vehicle control. Cells were interrogated by **a**) ATR-FTIR; **b**) SERS.

Figure S5.

Synthesis of Au NPs. Au NPs were prepared according to Frens' method.

Briefly,100 mL of 0.01% (wt/vol) $HAuCl_4$ aqueous solution was heated to boil under vigorous stirring,

followed by the immediate addition of 0.6 mL of 1% (wt/vol) trisodium citrate solution. The solution was kept boiling for about 1 h. Then the Au NPs solution cool down for further application.

Prior to being applied with the cell samples, Au NPs solution were washed by de-ion water twice and concentrated using centrifuge.

Table S1 Primary wavenumbers in loadings plots derived from PCA of ATR-FTIR spectral dataset

	PC1		PC2	
	Wavenumber (cm^{-1})	Tentative assignments	Wavenumber (cm^{-1})	Tentative assignments
C60	1624	Amide I	1508	Amide II
	1659	Amide I	1543	Amide II
	1589	Amide I	1636	Amide I
	1547	Amide II	1470	Proteins, $\nu_{as}CH_3$
	1493	Proteins, $\nu_{as}CH_3$	1697	Lipid, ν(C=O)
	1709	Lipid, ν(C=O)	1412	$\nu(COO^-)$
	1396	$\nu(COO^-)$	1227	$\nu_{as}PO_2^-$
	1103	$\nu_sPO_2^-$	1582	Amide II
Long	1539	Amide II	1655	Amide I
	1501	Amide II	1620	Amide I
	1624	Amide I	1508	Amide II
	1585	Amide I	1693	Amide I
	1663	Amide I	1585	Amide I
	1466	Proteins, $\nu_{as}CH_3$	1736	Lipid, ν(C=O)
	1732	Lipid, ν(C=O)	1543	Amide II
	1065	$\nu_sPO_2^-$	1462	Proteins, $\nu_{as}CH_3$
Short	1620	Amide I	1508	Amide II
	1547	Amide II	1713	Lipid, ν(C=O)
	1501	Amide II	1624	Amide I
	1655	Amide I	1543	Amide II
	1585	Amide I	1242	$\nu_{as}PO_2^-$
	1462	Proteins, $\nu_{as}CH_3$	1204	$\nu_{as}PO_2^-$
	1717	Lipid, ν(C=O)	1589	Amide I
	1400	$\nu(COO^-)$	1678	Amide I
Single	1508	Amide II	1732	Lipid, ν(C=O)
	1466	Proteins, $\nu_{as}CH_3$	1539	Amide II
	1678	Amide I	1624	Amide I
	1732	Lipid, ν(C=O)	1585	Amide I
	1061	$\nu_sPO_2^-$	1767	Lipid, ν(C=O)
	1582	Amide II	1053	Glycogen
	1018	Glycogen	1126	ν(CO)
	1114	ν(CO)	1481	Proteins, $\nu_{as}CH_3$

Table S2 Primary wavenumbers in loadings plots derived from PCA of SERS spectral dataset

	PC1		PC2	
	Wavenumber (cm^{-1})	Tentative assignments	Wavenumber (cm^{-1})	Tentative assignments
C60	1454	Lipid, CH2	1594	Lipid, C=C
	1006	Phenylalanine	977	Protein
	930	Protein	1631	Lipid, C=C
	1364	Tryptophan, protein	444	Glycogen
	1621	Lipid, C=C	800	DNA, nucleic acid
	1423	Lipid, CH2	1183	Protein
	858	Collagen	1382	Tryptophan, protein
	1487	Lipid, CH2	732	DNA, nucleic acid
Long	1055	Protein	1004	Phenylalanine
	518	*v*(S-S)	623	*v*(C-S)
	1586	*v*(C=C)	944	Protein
	463	Glycogen	1456	Lipid, CH2
	761	DNA, nucleic acid	668	Protein, *v*(C-S)
	1522	-C=C-, Amide II	1718	Lipid, *v*(C=O)
	625	Protein, *v*(C-S)	1057	Collagen
	1335	Lipid/protein,	1345	Lipid/protein,
Short	1006	Phenylalanine	1450	Lipid, CH2
	1456	Lipid, CH2	1000	Phenylalanine
	1341	Lipid/protein,	1358	Lipid/protein,
	1372	Tryptophan, protein	860	Collagen
	765	DNA, nucleic acid	1633	Lipid, C=C
	946	Protein	777	DNA, nucleic acid
	1718	Lipid, *v*(C=O)	1553	-C=C-, Amide II
	1623	Lipid, C=C	1187	Protein
Single	1623	Lipid, C=C	1454	Lipid, CH2
	442	Glycogen	923	Protein
	1179	Protein	1006	Phenylalanine
	801	DNA, nucleic acid	806	DNA, nucleic acid
	938	Protein	858	Collagen
	1030	Phenylalanine	716	DNA, nucleic acid
	1417	Lipid, CH2	1370	Tryptophan, protein
	728	DNA, nucleic acid	442	Glycogen

Table S3 Cluster vector peaks plot derived from PCA-LDA of spectral dataset

	ATR-FTIR		SERS	
	Wavenumber (cm^{-1})	Tentative assignments	Wavenumber (cm^{-1})	Tentative assignments
C60	1732	Lipid, ν(C=O)	1590	ν(C=C)
	1663	Amide I	1004	Phenylalanine
	1462	Proteins, $\nu_{as}CH_3$	765	DNA, nucleic acid
	1628	Amide I	1308	Lipid/protein,
	1092	$\nu_s PO_2^-$	1524	-C=C-, Amide II
	1547	Amide II	1366	Tryptophan, protein
	972	Protein	946	Protein
Long	1620	Amide I	1596	C=N/C=C, protein
	1659	Amide I	761	DNA, nucleic acid
	1582	Amide II	1047	Glycogen
	1242	$\nu_{as}PO_2^-$	1313	Lipid/protein,
	1204	$\nu_{as}PO_2^-$	1525	-C=C-, Amide II
	1516	Amide II	716	DNA, nucleic acid
	1099	$\nu_s PO_2^-$	1160	Protein
Short	1620	Amide I	759	DNA, nucleic acid
	1736	Lipid, ν(C=O)	1621	Lipid, C=C
	1462	Proteins, $\nu_{as}CH_3$	1428	Lipid, CH2
	1655	Amide I	1008	Phenylalanine
	1508	Amide II	928	Protein
	1558	Amide II	1526	-C=C-, Amide II
	1238	$\nu_{as}PO_2^-$	726	DNA, nucleic acid
Single	1620	Amide I	761	DNA, nucleic acid
	1508	Amide II	1594	C=N/C=C, protein
	1543	Amide II	944	Protein
	1655	Amide I	1020	Phenylalanine
	1242	$\nu_{as}PO_2^-$	1448	Lipid, CH2
	1096	$\nu_s PO_2^-$	1530	-C=C-, Amide II
	1462	Proteins, $\nu_{as}CH_3$	716	DNA, nucleic acid

Table S4 Scores plots in PC1 space following PCA analysis of spectra derived from A549 cells exposed to CNPs

One-way ANOVA with Dunnett's Multiple Comparison Test		C60	Long	Short	Single
ATR-FTIR	Control *vs.* 0.001 mg/L	*P <0.001*	*P <0.001*	*P <0.001*	*P <0.001*
	Control *vs.* 0.01 mg/L	*P <0.001*	*P <0.001*	*P <0.001*	*P <0.001*
	Control *vs.* 0.1 mg/L	*P <0.001*	*P <0.001*	*P <0.001*	*P <0.001*
SERS	Control *vs.* 0.001 mg/L	*P <0.001*	*P <0.001*	*P <0.001*	*P <0.001*
	Control *vs.* 0.01 mg/L	*P <0.001*	*P <0.001*	*P <0.001*	*P <0.001*
	Control *vs.* 0.1 mg/L	*P <0.05*	*P <0.001*	*P < 0.001*	*P <0.001*

Table S5 Global DNA methylation levels of A549 cells exposed to CNPs (0.1 mg/L) assessed by HPLC-MS

One-way ANOVA with Dunnett's Multiple Comparison Test	C60	Long	Short	Single
Control *vs.* CNP	*P <0.05*	*P >0.05*	*P <0.05*	*P >0.05*

Table S6 Relative mRNA level of A549 cells exposed to CNPs (0.1 mg/L) assessed by q-PCR

One-way ANOVA with Dunnett's Multiple Comparison Test		C60	Long	Short	Single
DNMT1	Control *vs.* CNP	*P >0.05*	*P >0.05*	*P >0.05*	*P >0.05*
DNMT3a	Control *vs.* CNP	*P >0.05*	*P >0.05*	*P >0.05*	*P >0.05*
DNMT3b	Control *vs.* CNP	*P >0.05*	*P >0.05*	*P >0.05*	*P <0.05*

Table S7 Sequence of primers used for quantitative RT-PCR

Gene	Primer sequence (5´-3´)	Product size (bp)
DNMT1	F: TACCTGGACGACCCTGACCTC	103
	R: CGTTGGCATCAAAGATGGACA	
DNMT3a	F: TATTGATGAGCGCACAAGAGAGC	111
	R: GGGTGTTCCAGGGTAACATTGAG	
DNMT3b	F: GGCAAGTTCTCCGAGGTCTCTG	113
	R: TGGTACATGGCTTTTCGATAGGA	
GAPDH	F: GGAGAAGGCTGGGGCTCAT	230
	R: TGATGGCATGGACTGTGGTC	

Chapter 5

Co-exposure of Fullerene C60 with benzo[*a*]pyrene in cells: alterations were determined by Fourier-transformation infrared

Junyi Li, Lixin Hu, Guangguo Ying, Kevin C. Jones and Francis L. Martin

Manuscript for submission

Contribution:

- I acquired the samples required for the project ;
- I acquired and processed all the data from samples;
- I prepared the first draft of the manuscript.

…… ……

Junyi Li Prof. Francis L. Martin

Co-exposure of Fullerene C60 with benzo[*a*]pyrene in cells: biological effects were determined by Fourier-transformation infrared

Junyi Li[a], *Lixin Hu*[b], *Guang-guo Ying*[b], *Kevin C. Jones*[a] *and Francis L. Martin*[a]*

[a]Centre for Biophotonics, Lancaster Environment Centre, Lancaster University, Lancaster LA1 4YQ, UK; [b]State Key Laboratory of Organic Geochemistry, Guangzhou Institute of Geochemistry, Chinese Academy of Science, Guangzhou 510640, China

Corresponding author email: f.martin@lancaster.ac.uk; phone: +44 (0)1524 510206; fax: +44 (0)1524 510217

TOC graph

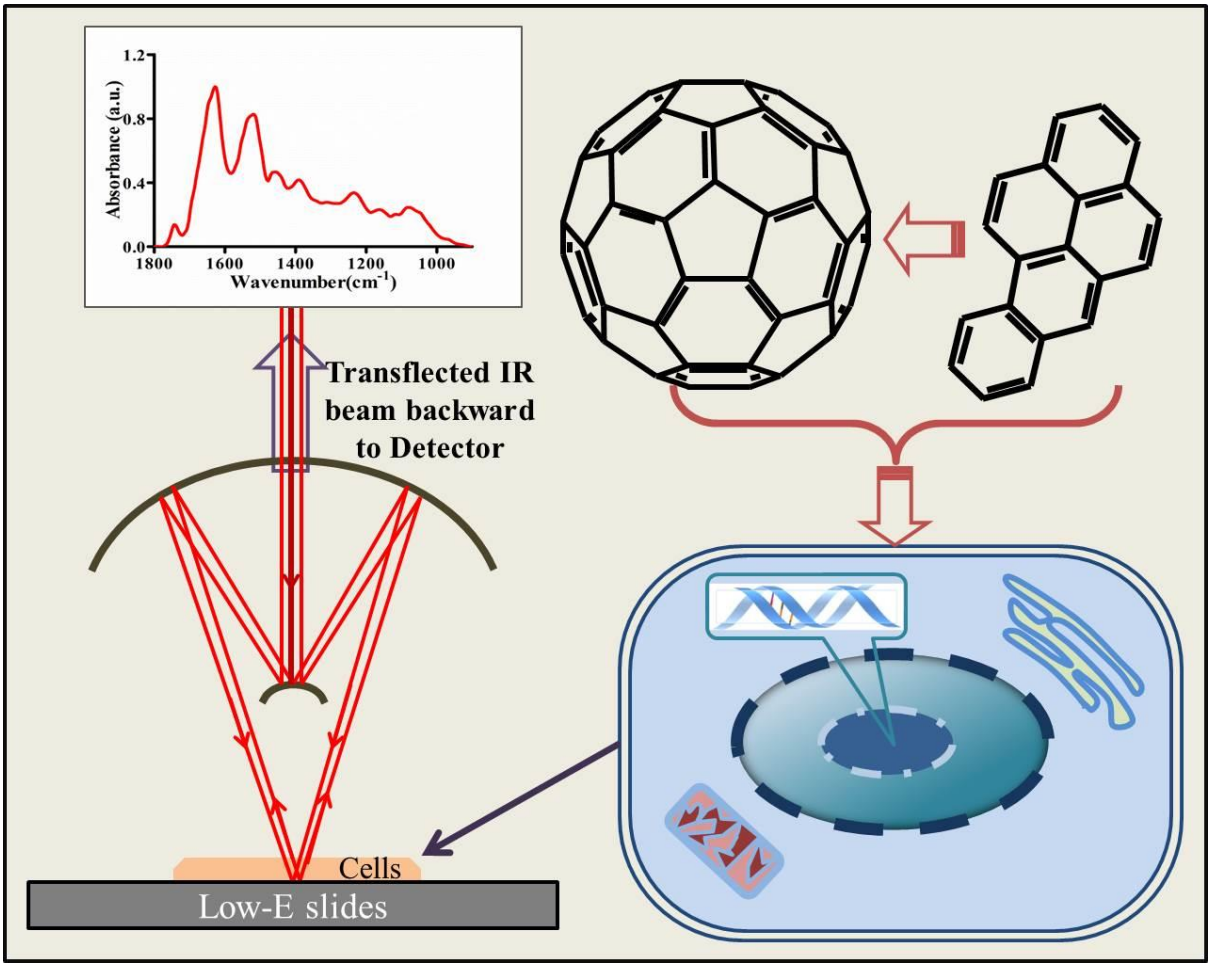
Absorbance (a.u.)
1.2
0.8
0.4
0.0
1800
1600
1400
1200
1000
Wavenumber(cm-1)
Transflected IR
beam backward
to Detector
Cells
Low-E slides

Abstract

The fullerene C60 is one of the most promising manufactured carbon-based nanoparticles, and with the wide applications it could possibly release into the environment. However, C60 is likely to associate with other substances in environment that are toxic. The interaction with C60 can impact on the environmental fate, transport and bioavailability of the toxicants in organism, which is largely unknown. Benzo[*a*]pyrene (B[*a*]P) is one of the most common polycyclic aromatic hydrocarbons (PAHs) among the environmental persistent organic pollutions. When B[*a*]P interacts with C60, the association may affect the biological effects of NPs *per se* or that of B[*a*]P. Thus, in this study two cell lines were employed in such an investigation to explore the biological impacts of the co-exposure of C60 and B[*a*]P. Post-exposure cells were then interrogated using a Fourier-transformation infrared (FTIR) microscope. By employing subsequent computational analysis including principal component analysis (PCA) and linear discriminant analysis (LDA), data reduction is achieved to allow for visualisation of cellular differentiation and the identification of wavenumber-related biomarkers corresponding to cellular biochemical alterations. The results indicated that low-dose C60 could increase the toxicity of B[*a*]P, while C60 at a high concentration could limit the toxicity of B[*a*]P.

Introduction

With the rise of nanotechnology, there has been a rapid increase in the use of nanoparticles in commercial applications. However, there is little known of the fate and behaviour of engineered nanoparticles in the environment, and concerns have emerged on the potential impact to health for human.[1, 2] Furthermore, quantitative analytical methods are required to determine environmental concentrations and enable both effect and exposure assessments. Many methods still need optimization and development, especially for new types of nanoparticles.[3-6] To date, these disadvantages contribute to the inclusive to the current data about the safety risk of the nanoparticles.

Fullerene C60, the first manufactured nanoparticle, possesses unique physical and chemical properties, which makes it a candidate substance for many nanotechnological applications in the industrial and medical fields.[7-10] However, its extremely small size, unique conformation, large surface area, and propensity for surface modification raise possibility that C60 could pose a hazard to humans and other living organisms, which has been assessed and determined by numerous scientific groups[11]. It seems that the cytotoxicity of C60 differs on the type of cells used and how C60 test suspensions are prepared[12, 13].

Despite the debate on the acute toxicity induced by nanoparticles, emerging concerns about release of nanopartilces into environment that it may not only potentially affect biological systems, but also could interact with other substance (*e.g.*, pollution compounds) as co-contamination. Consequently, the nanopartilces could affect the fate, transportation and bioavailability of the pollution compounds by co-contamination. In aquatic environment, contamination compounds can accumulate in

aqueous nanoparticles and this accumulation appears to affect the physicochemical property of both nanoparticles and the co-contamination.[14] Investigations showed that nanoparticles seemed to behaviour highly reactive to interaction with the other compounds. Furthermore, researchers found that nano-silica could facilitate the uptake of the metals by the cells, and induced higher damage in cells than that induced by metal or nano-silica alone.[15] This type of delivery mechanism was so called 'Trojan horse' effects. In another case, it was found that nano-TiO_2 enhanced the bioaccumulation and toxicity of copper in *Daphnia magna*.[16] Similar situations occurred mainly in metal nanoparticles with heavy metal. However, studies investigating the co-contamination on carbon-based nanoparticles seemed to be less conclusive. Recent studies showed that carbon nanomaterials could highly interact with the chemical compounds in the environment.[17-19] Single-walled carbon nanotubes were found to act as a contaminants carrier and enhance the accumulation of phenanthrene in fish digestive track.[20] However, another study suggested that co-exposure with carboxyl-functionalized single-walled carbon nanotubes could significantly inhibit the bioactivity of adsorbed 17α-Ethinylestradiol (EE2) in cultured cells.[21]

Among the persistent organic pollutions, polycyclic aromatic hydrocarbons (PAHs) are a large class of widespread organic compounds with two or more fused aromatic rings and they have a relatively low solubility in water, but are highly lipophilic.[22] Benzo[a]pyrene (B[a]P) is one of the most important PAHs, and it has been identified as being highly carcinogenic. Although B[a]P itself does not exhibit carcinogenic activity, it is a potent ligand for the aryl hydrocarbon receptor (AhR), which may mediate teratogenic and carcinogenic effects of certain environmental pollutants.[23] In cells, B[a]P can bind to AhR and activate it to induce further response, or it is

effectively metabolised by several xenobiotic metabolizing enzymes in cells to B[*a*]P-7,8-diol-9,10-epoxide (BPDE), which is its main ultimate carcinogenic forms, and can forms adducts with DNA.[24-26]

It is highly possible that the carbon-based nanomaterials would actively interact with PAHs and form co-contamination in the environment. In order to understand how this kind of co-exposure will impact on the toxicity, C60 with B[*a*]P was employed to co-expose on cells. The toxic effects in cells were then assessed using a biospetroscipic method; post-exposure cell samples were interrogated by a Fourier-transformation infrared (FTIR) microscope. Such biospectroscopy technique provides us a rapid, bio-agent free and non-destructive method for biological analysis.[27] Therefore, IR spectroscopy has been widely applied in biological researches, such as disease diagnosis[28], stem cell research[29] and toxic assessment[30]. The mid-IR region (4000-400 cm^{-1}) is specific for biological application and it provides us abundant chemical bond information in the 'biochemical-fingerprint' region (1800-900 cm^{-1}), which can generate identifiable peaks at specific absorption frequencies, such as Amide I (~1650 cm^{-1}), Amide II (~1550 cm^{-1}), Amide III (~1260 cm^{-1}), carbohydrates (~1155 cm^{-1}), glycogen (~1030 cm^{-1}), lipids (~1750 cm^{-1}), asymmetric phosphate stretching vibrations ($\nu_{as}PO_2$; ~1225 cm^{-1}), symmetric phosphate stretching vibrations ($\nu_{s}PO_2$; ~1225 cm^{-1}) and protein phosphorylation (~970 cm^{-1}).[31] Overall, coupled with computational multivariate analysis FTIR spectroscopy can be used as sensitive tool for toxic test.

In this study, two cell lines, including a gill cell line and a mammalian cell line (MCF-7) were used to conduct the co-exposure of C60 with B[*a*]P, and the response in cells following exposure were later determined using FTIR spectroscopy. According our

previous investigations, three relative low doses were employed in the co-exposure for B[*a*]P and C60 (respectively, B[*a*]P exposure concentration at 10^{-6} M, 10^{-7} M and 10^{-8} M; C60 at 0.1 mg/L, 0.01 mg/L and 0.001 mg/L).[32, 33]This study aimed to gain an insight into the toxicity of the two agents and the influence of co-exposure on the bioavailability.

Materials and Methods

Chemicals and carbon nanoparticles

All test agents were purchased from Sigma. Benzo[*a*]pyrene was HPLC-grade (>96%) and existing as powder, while dimethyl sulfoxide (DMSO) used as solvent was GC-grade (≥99.5%). Bovine serum albumin (BSA) was also obtained from Sigma was ≥98% pure.

Fullerene C60 used in the study was also from Sigma. As stated, C60 had a purity >99.5% and particle size of 1 nm, and was analysed by Raman spectroscopy (Renishaw PLC, Gloucestershire, UK) with a 785 nm laser, and determined to be of high purity. Additionally, images of C60 were taken using a scanning electron microscope (SEM) [JSM 5600 (JEOL)] [see Electronic Supporting Information (ESI) Figure S1].

Benzo[*a*]pyrene was dissolved using DMSO, and stock solutions were made at the concentration of 10^{-3} M, 10^{-4} M and 10^{-5} M. C60 were dispersed in 1% BSA solution following a 15-min ultrasonication in ice-water bath and stock solutions were made at concentrations of 100 mg/L, 10 mg/L and 1 mg/L. Agglomerate could be observed in the solution due to its lipophilic property. To ensure a homogeneous mixture of chemical agents, solvent and exposure medium, and as well to avoid any solvent

specific effects, stock solutions and exposure medium were mixed prior to application to the cells. In this case, as CNPs and B[*a*]P were dispersed in 1% BSA solution and DMSO respectively, each experimental medium finally contain 0.1% (vol/vol) 1% BSA solution and DMSO as a background control. Therefore an experimental medium containing 0.1% (vol/vol) 1% BSA solution and DMSO without test agents were used as a vehicle control. All these experimental medium were prepared 72 h prior to cell exposure and stored in fridge, which allowed the absorption equilibrium of B[*a*]P onto C60.

Cell culture

Human breast cancer MCF-7 cells were cultured in Dulbecco's modified essential medium (DMEM) supplemented with 10% heat-inactivated foetal bovine serum, penicillin (100 U/mL), and streptomycin (100 μg/mL). MCF-7 Cells were maintained in the incubator of a humidified atmosphere with 5% CO_2 in air at 37℃. The gill cells for primary cultures were derived from gills of rainbow trout (*Oncorhynchus mykiss*) [34]. The cells were cultured with Leibovitz's L-15 culture media supplemented with 10% heat-inactivated foetal bovine serum, penicillin (100 U/mL), and streptomycin (100 μg/mL) as well. These gill cells were maintained without CO2 incubation in free gas exchange with air at an optimal temperature (~ 18℃). All these two cell lines were routinely cultured in 75 cm^2 cell culture flasks. MCF-7 cells were split twice a week, while gill cells were split once a week.

CNPs exposure

For MCF-7 cells, the same medium was used for incubation before and during exposure (namely exposure medium), while L15 medium was used only for gill cell

growing prior to exposure, but a different medium, L15/ex was then introduced as the experimental medium during exposure. L-15/ex medium was firstly introduced in the exposure experiment on RTgill-w1 cell line, which was determined also capable for the gill cells employed in this study. L15/ex medium contains only salts, galactose and pyruvate to provide an isotonic environment and a source of energy and as such is fully defined[35, 36]. Bioavailability of test chemicals in this in vitro system is not influenced by a serum component. Binding of hydrophobic test chemicals to constituents of serum was suggested to contribute to the systematic deviation of mammalian cell viability versus fish acute toxicity depending on the chemicals' octanol−water partition coefficient (Kow) and is also a likely cause of underestimation of fish acute toxicity in previous investigations using fish cell lines[36].

For exposure, cells were directly grown on Low-E slides (Kevely Technologies, OH, USA) in the 45 mm culture dishes. Prior to cell seed, Low-E slides were immersed in ethanol for 30 mins. Following rinsed in sterile water, Low-E slides were then stored in empty culture dishes and dried in incubator. Confluent cells were disaggregated with trypsin (0.05%)/EDTA (0.02%) solution, and were immediately resuspended in complete medium. Cells were then seeded to the culture dishes and allowed to attach on the slides and to form a cell layer on the Low-E slides. After 72 h, the original medium was removed and experimental medium containing test agents or not was added. After 24-h incubation, the cells were grown on the Low-E slides were rinsed in PBS and then fixed in 4% formalin in PBS for 30 min. Once fixed, the slides were rinsed in PBS and followed by a quick wash (~ 3 seconds) in distilled water. Following air-drying overnight, the slides were stored in a desiccator until spectroscopic interrogation.

Spectroscopy analysis

All cell samples on Low-E slides were interrogated using a Bruker TENSOR 70 FTIR spectrometer (Bruker Optics Ltd., Germany) equipped with a HYPERION 1000 microscope containing a liquid nitrogen cooled detector. Instrument parameters were set at 32 scans, 8 cm^{-1} resolution. For each slide, about 20 IR spectra were acquired at different points across the sample. Prior to starting a new slide or after each ten spectra, a background was taken.

Spectral data acquired from FTIR spectroscopy, were processed by using IRootLab toolbox (http://irootlab.googlecode.com) running on MATLAB r2010a (The MathWorks, Inc., US). IR spectra were pre-processed by as follows: cut to 1800-900 cm^{-1} (the biochemical fingerprint range), rubberband baselined, and normalisation to Amide I peak. Computational analysis using multivariate techniques including principal component analysis (PCA) and linear discriminant analysis (LDA) can efficiently analyse the large spectral dataset. Following pre-processing, PCA was applied to the spectral dataset. PCA is an unsupervised technique employed to reduce the dimensions of the data. Undoubtedly PCA is capable of identifying some important biochemical information in the spectral data. However, it has less discrimination power due to the fact that it is an unsupervised procedure. In order to interpret the complex biochemical information obtained through vibrational spectroscopic techniques it requires further data analysis by using supervised procedures such as LDA, PLS, HCA *etc*. Thus, the output data derived from PCA was then input into LDA analysis[37]. The first ten PC factors of PCA were used for LDA analysis since that more than 99% of variance is captured in the first10 PCs[31].

Multivariate analysis results were visualized either as scores plots and/or cluster vectors plot. In scores plots, nearness between two groups means similarity, while the distance indicates dissimilarity[38, 39]. Cluster vectors plot from PCA-LDA was develop to help reveal the biochemical alterations associated with each group in the dataset. To simplify the identification of the main biochemical alteration of each group, cluster vector peak plots were used to indicate the first 7 highest peaks in the cluster vector plots.

Result and discussion

Following exposure to the test agents, cells were harvested and interrogated by FTIR. The interrogation under FTIR microscope gave rise to a large spectral dataset containing 12 classed groups, which were labelled according the treatments as: Control, C60 0.1 mg/L, C60 0.01 mg/L, C60 0.001 mg/L, B[*a*]P at 10^{-8} M, B[*a*]P at 10^{-7} M, B[*a*]P at 10^{-6} M, Mix1 (C60 0.001 mg/L & B[*a*]P at 10^{-6} M), Mix2 (C60 0.01 mg/L & B[*a*]P at 10^{-6} M), Mix3 (C60 0.1 mg/L & B[*a*]P at 10^{-6} M), Mix4 (C60 0.1 mg/L & B[*a*]P at 10^{-7} M), and Mix5 (C60 0.1 mg/L & B[*a*]P at 10^{-8} M).

As specific wavenumbers in IR spectra can be used as marker of biochemical compounds in cells, the intensity absorbance at such a wavenumber in the IR spectra following simply processed (including baseline corrected and normalized) could be used for assessment of alterations in cells. The intensity absorbance at 1400 cm^{-1} was used as a protein marker as it corresponds to C=O symmetric stretching of amino acids and 1740 cm^{-1} is associated with C=O stretching vibrations of lipids. Thus, the protein-to-lipid ratio using the intensity absorbance at these two vibration modes were calculated to assess cell proliferation after exposure[38]. Similarly, other absorbance ratio were employed including: intensity absorbance ratio of 1650 cm^{-1} to 1084 cm^{-1}

as ratio of protein/nucleic acid (1650 cm^{-1} corresponding to Amide I in protein; 1084 cm^{-1} corresponding to symmetric phosphate stretching for DNA/RNA)[40], and intensity ratio of (996 cm^{-1})/(966 cm^{-1}) used as RNA/DNA ratio[40, 41].

The tendency elevated protein-to-lipid ratio indicated that all test agents tend to result active cell proliferation[42]. However, the statistical results listed that most of the treatment in gill cells significantly activated cell proliferation compared with the control, while in MCF-7cells only exposure of Mix4 caused significant proliferation (Figure1a and statistical results in supporting information Table S1). In contrast to the protein-to-lipid ratio, the protein-to-nucleic acid ratio displayed a downregulation by the most exposures in gill cells except for the Mix3 (Figure1b and statistical results in supporting information Table S2). Whereas, the pattern of protein-to-nucleic acid ratio in MCF-7 was complicated; only treatment of 60 0.1 mg/L, Mix4 and Mix5 significantly reduced protein-to-nucleic acid level, while it was significantly elevated by Mix1 (Figure1b and statistical results in supporting information Table S2). Moreover, the ratio of RNA/DNA (Figure1c and statistical results in supporting information Table S3) manifested by IR spectra suggested that in gill cells treatment with C60 at 0.01 mg/L and 0.1 mg/L could significantly reduce RNA/DNA level, which potentially indicated an inhibition in gene expression, while B[*a*]P of 10^{-8} M, Mix1, Mix4 and Mix5 showed capability of stimulation in gene expression. However, the change trend of RNA/DNA level in MCF-7 cells following exposure was different from that in gill cells, especially for the treatment of C60. It was found that RNA/DNA level in MCF-7 cells was significantly increased only by treatment with B[*a*]P at 10^{-7} M and 10^{-6} M, as well as Mix4.

As the mid-IR spectra from the multi-constituent biological samples are rich of biochemical information and greatly complex, using simple intensity absorbance ratio (peak-to-peak ratio) is inadequate for interpretation of the complex biological alteration[43]. Thus, multivariate data-analysis techniques (computational analysis) were employed to help with the bio-information extraction in spectral dataset from the interrogated samples[44, 45]. Combination of different groups consisted a few datasets with emphasis on different purpose to explore the cellular toxicity resulted from single treatment or binary treatment. When the spectral dataset was processed by computational analysis, alterations induced by both single agent and binary mixture were determined. Based on the PCA-LDA, dimensional (1-, 2-, or 3-D) scores plots were performed for visualisation using the first three LD factors, where most segregations among groups were observed. The first two factors were particularly displayed in 1-D scores plot with their corresponding loadings plot, which identifies the wavenumbers responsible for segregation of scores of spectral clusters following exposure. Additionally, cluster vector plot was applied in the dataset of binary mixture exposure so that the global alterations in cells induced by each treatment could be identified compared with the control group.

When the spectral dataset containing whole groups was inputted into PCA-LDA method, 3-D scores plots were performed for visualisation. However, it was difficult to recognise the segregation in 3-D or 2-D scores plot as too many groups involving in the dataset (supporting information). Thus, displaying the first two LD scores in 1-D plots gave rise to a clear global view of segregations among groups (Figure 2). For both LD1 and LD2 space, the corresponding loadings plots were displayed with the first seven primary wavenumbers marked. In LD1 space, the wavenumbers derived from the spectral dataset of gill cells ranked as: 1232 (DNA/RNA, $\nu_{as}PO_2^-$), 1709

(Lipid), 1664 (Amide I), 1070 (DNA/RNA, $\nu_s PO_2^-$), 985 (Protein phosphorylation), 1417 (amino acid, $\nu[COO^-]$), and 1556 (Amide II), while those from MCF-7 cells were similar with gill cells: 1101 (DNA/RNA, $\nu_s PO_2^-$), 1508 (Amide II), 1026 (Glycogen), 1566 (Amide II), 983 (Protein phosphorylation), 1406 (amino acid, $\nu[COO^-]$), and 1712 (Lipid); namely, these wavenumbers corresponding to specific biochemical structures could be used as multi biomarkers in the assessment, in which importance of biomarkers weigh the pronounced extent of wavenumbers in loadings plot. However, in LD2 space the loadings plots for each cell line laid emphasis to different biomarkers; pronounced wavenumbers in loadings plot from gill cells were mainly located in the DNA/RNA region (~1250-1000 cm^{-1}), while counterparts in MCF-7 cells mostly appeared to be in lipid and protein (Amide I) region (~1750-1500 cm^{-1}). For gill cells, significant alterations were observed between the exposed groups and the control in both LD1 and LD2 space, except for that with treatment of Mix3 (statistical results in supporting information Table S4). From this global view, it was found that binary treatment with both high dose of B[*a*]P and C60 was likely to result a highly reduced effects in gill cells, while exposure of a high dose mixed with a low dose could greatly enhanced the toxicity in gill cells. As MCF-7 exposed to the test agents, a similar response mode was presented in 1-D scores plots of both LD space.

The dataset of the control group and those from single treatment with either C60 or B[*a*]P was performed to explore the toxicity of single agent. When cells were exposed to C60, both gill cells and MCF-7 cells were likely to show a linear dose-response in the LD1 space (Figure 3). It also showed that gill cells were significantly affected by C60 at each dose in both LD spaces, while MCF-7 cells only with treatment of 0.1 mg/L in LD1 space and treatment of 0.01 mg/L in LD2 space appeared to be significantly altered (statistical results in supporting information Table S4). In LD1

loadings plot derived from gill cells, the most pronounced wavenumbers were related to amide I, glycogen, DNA/RNA, and lipid regions (Figure 3a and supporting information Table S6). It is similar for MCF-7 cells that segregations in LD1 were mostly resulted from alterations in amide I, lipid, amide II and DNA/RNA region (Figure 3c and supporting information Table S8). These spectral profiles indicated that C60 was capable to induce alterations in outer cellular structures (lipid and protein), but also in the internal materials of DNA/RNA, namely genotoxicity[46, 47]. It is suggested that the genotoxicity of C60 was possibly caused by a reactive oxygen species (ROS) pathway[48].

However, B[*a*]P treatment was likely to result a non-linear dose-response in both cell lines, and in both LD space the significant segregations were observed in the treated groups compared with the control group, except that the group of gill cells exposed to B[*a*]P at 10^{-8} M (Figure 3b & 3d and supporting information Table S4). B[*a*]P is specifically targeting to induce alterations in the DNA/RNA, as loadings plots in both LD1 and LD2 showed obviously pronounced peaks in the wavenumbers corresponding to the biochemical structure of DNA/RNA in cells. This indicated that B[*a*]P was a genotoxic compound inducing DNA damage[25, 49], which is consist with previous studies in our group[32]. Moreover, a low-dose effects was observed in cells following B[*a*]P exposure.

In order to look insight into the mechanism underlying the action of the binary exposure in cells, specific groups were put together as an associated dataset for further analysis. In these dataset, cluster vector plot was employed to indicate the pronounced wavenumbers corresponding for biochemical alterations in each treated cell group compared to the control one. When spectral data from C60 0.1 mg/L, B[*a*]P 10^{-6} M

and their mixture were processed by computational analysis, the 2-D and 3-D scores plots derived from PCA-LDA were performed for visualisation (Figure 4). For gill cells, both the 2-D scores plot and cluster vector plot showed that the treatment of B[*a*]P 10^{-6} M lead to the most pronounced alterations in cells, which mostly appeared to be in the DNA/RNA region, while C60 exerted a lower extent of toxicity in cells (Figure 4a). However, the 1-D scores plots (supporting information) in the first two LD space indicated that co-exposure of these two treatment could dramatically reduce their toxic action in cells, but it still showed a slight genotoxicity, which was indicated by the cluster vector. The similar situation occurred in the dataset of MCF-7 cells (Figure 4b). Cluster vector plot showed that all treatment caused wide alterations in cells including lipid, protein and DNA/RNA, and it was found that both C60 0.1 mg/L and B[*a*]P 10^{-6} M induced highly remarkable alteration in cells, while the treatment of Mix3 displayed a relatively limited toxic action. Additionally, the cluster vector peak C60 tended to induced higher alteration in the protein rather than in the DNA/RNA, while B[*a*]P affected cell with emphasis on the DN/RNA region. However, the cluster vector peak plot suggested that the toxic action of the co-exposure was likely to be limited in the lipid and protein region of MCF-7 cells.

In addition, extra dataset were also performed to explore the differences of the alterations in cells when the binary treatment varied. When gill cells were treated with both C60 and B[*a*]P, the alterations in cells were observed to be elevated with the dose of C60 decreased (B[*a*]P kept at 10^{-6} M) (Figure 5). As it was showed in cluster vector plot, the Mix3 (C60 0.001 mg/L and B[*a*]P 10^{-6} M) caused the most distinct alteration in cells, and the cluster vector showed that its toxic action seems to be a combination of that from C60 and B[*a*]P, while it was even highly enhanced. However, when it kept the dose of C60 at 0.1 mg/L and decrease the dose of the B[*a*]P, the toxic effects

would increase but quite limited by contrast to that from C60 (Figure 6). Toxic mechanism revealed by cluster vector suggested that co-exposure of high dose C60 with low dose B[*a*]P could induce alterations in protein and DNA/RNA region at a similar extent. Additionally, the toxic action of the co-exposure appeared to be similar in the MCF-7 cells. The only thing to make it a bit different is that higher alterations in DNA/RNA region were observed as MCF-7 cell are mammalian cells and more sensitive to the genotoxicity of B[*a*]P. Therefore, it evidenced that high concentration of C60 could limit the toxicity of B[*a*]P.

Conclusion

In general, the biological effects resulted from the binary exposure of contamination compounds exposure are quite complicated and it is difficult to predicted[50]. Particularly, when the nanoparticles encounter the chemical compounds in the environment, this issue become more intractable[51], as it requires taking more factors into account[52]. Moreover, the binary effect of C60 co-exposure with other chemical compounds is a controversial issue. It was reported that association of Hg^{2+} with C60 could increase the bioavailability of Hg^{2+} in Zebrafish[53]. Similar investigation also determined that co-exposure with C60 fullerene may strengthen the health effects of organic industrial chemicals[54]. Another study in ZF-L cells that also focused on the co-exposure of C60 and B[*a*]P (only using one higher dose of C60 at 1.0 mg/L in co-exposure) suggested that C60 could elicited toxicity by increasing the intake of B[*a*]P[55]. While a few other studies draw a different conclusion. Another research group observed that the association between nC60 and 17α-ethinylestradiol (EE2) reduced EE2 bioavailability in zebrafish[56, 57]. Additionally, Yang *et al.* reported lower histological damage induced by fluoroanthene when co-exposed with fullerene under

UV radiation[58]. In this study, the spectral data indicated that low dose of C60 could elevate the toxicity of B[*a*]P, while high concentration of C60 could limit the toxicity of B[*a*]P. The biospectroscopic method also interpreted the toxic action mode of the test agents at such a low dose, both the single treatment and the binary ones. However, the mechanism underlying the different actions from co-exposure with diverse combinations of the two agents still requires further investigation.

Acknowledgements

Funding for the laboratory experiments in this study from the Chinese Academy of Sciences is greatly acknowledged.

References

1. Kahru, A.; Dubourguier, H.-C., From ecotoxicology to nanoecotoxicology. *Toxicology* **2010,** *269*, (2–3), 105-119.

2. Savolainen, K.; Alenius, H.; Norppa, H.; Tuomi, T.; Kasper, G., Risk assessment of engineered nanomaterials and nanotechnologies--a review. *Toxicology* **2010,** *269*, (2-3), 92-104.

3. Monteiro-Riviere, N. A.; Inman, A. O.; Zhang, L. W., Limitations and relative utility of screening assays to assess engineered nanoparticle toxicity in a human cell line. *Toxicol. Appl. Pharmacol.* **2009,** *234*, (2), 222-235.

4. Crane, M.; Handy, R.; Garrod, J.; Owen, R., Ecotoxicity test methods and environmental hazard assessment for engineered nanoparticles. *Ecotoxicology* **2008,** *17*, (5), 421-437.

5. Hassellöv, M.; Readman, J.; Ranville, J.; Tiede, K., Nanoparticle analysis and characterization methodologies in environmental risk assessment of engineered nanoparticles. *Ecotoxicology* **2008,** *17*, (5), 344-361.

6. Aschberger, K.; Micheletti, C.; Sokull-Klüttgen, B.; Christensen, F. M., Analysis of currently available data for characterising the risk of engineered nanomaterials to the environment and human health — Lessons learned from four case studies. *Environ. Int.* **2011,** *37*, (6), 1143-1156.

7. Hughes, G. A., Nanostructure-mediated drug delivery. *Nanomed. Nanotechnol. Biol. Med.* **2005,** *1*, (1), 22-30.

8. Singh, R.; Lillard Jr, J. W., Nanoparticle-based targeted drug delivery. *Exp. Mol. Pathol.* **2009,** *86*, (3), 215-223.

9. Montellano, A.; Da Ros, T.; Bianco, A.; Prato, M., Fullerene C60 as a multifunctional system for drug and gene delivery. *Nanoscale* **2011,** *3*, (10), 4035-4041.

10. Zakharian, T. Y.; Seryshev, A.; Sitharaman, B.; Gilbert, B. E.; Knight, V.; Wilson, L. J., A Fullerene−Paclitaxel Chemotherapeutic: Synthesis, Characterization,

and Study of Biological Activity in Tissue Culture. *J. Am. Chem. Soc.* **2005,** *127*, (36), 12508-12509.

11. Aschberger, K.; Johnston, H. J.; Stone, V.; Aitken, R. J.; Tran, C. L.; Hankin, S. M.; Peters, S. A. K.; Christensen, F. M., Review of fullerene toxicity and exposure – Appraisal of a human health risk assessment, based on open literature. *Regul. Toxicol. Pharmacol.* **2010,** *58*, (3), 455-473.

12. Spohn, P.; Hirsch, C.; Hasler, F.; Bruinink, A.; Krug, H. F.; Wick, P., C60 fullerene: A powerful antioxidant or a damaging agent? The importance of an in-depth material characterization prior to toxicity assays. *Environ. Pollut.* **2009,** *157*, (4), 1134-1139.

13. Xia, X. R.; Monteiro-Riviere, N. A.; Riviere, J. E., Intrinsic biological property of colloidal fullerene nanoparticles (nC60): Lack of lethality after high dose exposure to human epidermal and bacterial cells. *Toxicol. Lett.* **2010,** *197*, (2), 128-134.

14. Christian, P.; Von der Kammer, F.; Baalousha, M.; Hofmann, T., Nanoparticles: structure, properties, preparation and behaviour in environmental media. *Ecotoxicology* **2008,** *17*, (5), 326-343.

15. Limbach, L. K.; Wick, P.; Manser, P.; Grass, R. N.; Bruinink, A.; Stark, W. J., Exposure of Engineered Nanoparticles to Human Lung Epithelial Cells: Influence of Chemical Composition and Catalytic Activity on Oxidative Stress. *Environ. Sci. Technol.* **2007,** *41*, (11), 4158-4163.

16. Fan, W.; Cui, M.; Liu, H.; Wang, C.; Shi, Z.; Tan, C.; Yang, X., Nano-TiO2 enhances the toxicity of copper in natural water to Daphnia magna. *Environ. Pollut.* **2011,** *159*, (3), 729-734.

17. Pan, B.; Xing, B., Adsorption Mechanisms of Organic Chemicals on Carbon Nanotubes. *Environ. Sci. Technol.* **2008,** *42*, (24), 9005-9013.

18. Pan, B.; Lin, D.; Mashayekhi, H.; Xing, B., Adsorption and Hysteresis of Bisphenol A and 17α-Ethinyl Estradiol on Carbon Nanomaterials. *Environ. Sci. Technol.* **2008,** *42*, (15), 5480-5485.

19. Li, X.; Gámiz, B.; Wang, Y.; Pignatello, J. J.; Xing, B., Competitive Sorption Used To Probe Strong Hydrogen Bonding Sites for Weak Organic Acids on Carbon Nanotubes. *Environ. Sci. Technol.* **2015**.

20. Su, Y.; Yan, X.; Pu, Y.; Xiao, F.; Wang, D.; Yang, M., Risks of Single-Walled Carbon Nanotubes Acting as Contaminants-Carriers: Potential Release of Phenanthrene in Japanese Medaka (Oryzias latipes). *Environ. Sci. Technol.* **2013,** *47*, (9), 4704-4710.

21. Song, M.; Wang, F.; Zeng, L.; Yin, J.; Wang, H.; Jiang, G., Co-exposure of Carboxyl-Functionalized Single-Walled Carbon Nanotubes and 17α-Ethinylestradiol in Cultured Cells: Effects on Bioactivity and Cytotoxicity. *Environ. Sci. Technol.* **2014,** *48*, (23), 13978-13984.

22. Srogi, K., Monitoring of environmental exposure to polycyclic aromatic hydrocarbons: a review. *Environ Chem Lett* **2007,** *5*, (4), 169-195.

23. Bock, K. W., Aryl hydrocarbon or dioxin receptor: Biologic and toxic responses. In *Reviews of Physiology, Biochemistry and Pharmacology, Volume 125*, Springer Berlin Heidelberg: 1994; Vol. 125, pp 1-42.

24. Baird, W. M.; Hooven, L. A.; Mahadevan, B., Carcinogenic polycyclic aromatic hydrocarbon-DNA adducts and mechanism of action. *Environ. Mol. Mutagen.* **2005,** *45*, (2-3), 106-114.

25. Xue, W.; Warshawsky, D., Metabolic activation of polycyclic and heterocyclic aromatic hydrocarbons and DNA damage: A review. *Toxicol. Appl. Pharmacol.* **2005,** *206*, (1), 73-93.

26. Nebert, D. W.; Dalton, T. P., The role of cytochrome P450 enzymes in endogenous signalling pathways and environmental carcinogenesis. *Nat. Rev. Cancer* **2006,** *6*, (12), 947-960.

27. Baker, M. J.; Trevisan, J.; Bassan, P.; Bhargava, R.; Butler, H. J.; Dorling, K. M.; Fielden, P. R.; Fogarty, S. W.; Fullwood, N. J.; Heys, K. A.; Hughes, C.; Lasch, P.; Martin-Hirsch, P. L.; Obinaju, B.; Sockalingum, G. D.; Sulé-Suso, J.; Strong, R. J.;

Walsh, M. J.; Wood, B. R.; Gardner, P.; Martin, F. L., Using Fourier transform IR spectroscopy to analyze biological materials. *Nat. Protocols* **2014,** *9*, (8), 1771-1791.

28. Ellis, D. I.; Goodacre, R., Metabolic fingerprinting in disease diagnosis: biomedical applications of infrared and Raman spectroscopy. *Analyst* **2006,** *131*, (8), 875-885.

29. Walsh, M. J.; Fellous, T. G.; Hammiche, A.; Lin, W.-R.; Fullwood, N. J.; Grude, O.; Bahrami, F.; Nicholson, J. M.; Cotte, M.; Susini, J.; Pollock, H. M.; Brittan, M.; Martin-Hirsch, P. L.; Alison, M. R.; Martin, F. L., Fourier Transform Infrared Microspectroscopy Identifies Symmetric PO2− Modifications as a Marker of the Putative Stem Cell Region of Human Intestinal Crypts. *Stem Cells* **2008,** *26*, (1), 108-118.

30. Corte, L.; Rellini, P.; Roscini, L.; Fatichenti, F.; Cardinali, G., Development of a novel, FTIR (Fourier transform infrared spectroscopy) based, yeast bioassay for toxicity testing and stress response study. *Anal. Chim. Acta* **2010,** *659*, (1–2), 258-265.

31. Kelly, J. G.; Trevisan, J. l.; Scott, A. D.; Carmichael, P. L.; Pollock, H. M.; Martin-Hirsch, P. L.; Martin, F. L., Biospectroscopy to metabolically profile biomolecular structure: a multistage approach linking computational analysis with biomarkers. *J. Proteome Res.* **2011,** *10*, (4), 1437-1448.

32. Pang, W.; Li, J.; Ahmadzai, A. A.; Heppenstall, L. D.; Llabjani, V.; Trevisan, J.; Qiu, X.; Martin, F. L., Identification of benzo[a]pyrene-induced cell cycle-associated alterations in MCF-7 cells using infrared spectroscopy with computational analysis. *Toxicology* **2012,** *298*, (1–3), 24-29.

33. Li, J.; Strong, R.; Trevisan, J.; Fogarty, S. W.; Fullwood, N. J.; Jones, K. C.; Martin, F. L., Dose-Related Alterations of Carbon Nanoparticles in Mammalian Cells Detected Using Biospectroscopy: Potential for Real-World Effects. *Environ. Sci. Technol.* **2013,** *47*, (17), 10005-10011.

34. Walker, P. A.; Bury, N. R.; Hogstrand, C., Influence of Culture Conditions on Metal-Induced Responses in a Cultured Rainbow Trout Gill Epithelium. *Environ. Sci. Technol.* **2007,** *41*, (18), 6505-6513.

35. Schirmer, K.; Chan, A. G. J.; Greenberg, B. M.; Dixon, D. G.; Bols, N. C., Methodology for demonstrating and measuring the photocytotoxicity of fluoranthene to fish cells in culture. *Toxicol. In Vitro* **1997,** *11*, (1–2), 107-119.

36. Tanneberger, K.; Rico-Rico, A.; Kramer, N. I.; Busser, F. J. M.; Hermens, J. L. M.; Schirmer, K., Effects of Solvents and Dosing Procedure on Chemical Toxicity in Cell-Based in Vitro Assays. *Environ. Sci. Technol.* **2010,** *44*, (12), 4775-4781.

37. Gautam, R.; Vanga, S.; Ariese, F.; Umapathy, S., Review of multidimensional data processing approaches for Raman and infrared spectroscopy. *EPJ Techn Instrum* **2015,** *2*, (1), 1-38.

38. Llabjani, V.; Trevisan, J.; Jones, K. C.; Shore, R. F.; Martin, F. L., Derivation by Infrared Spectroscopy with Multivariate Analysis of Bimodal Contaminant-Induced Dose-Response Effects in MCF-7 Cells. *Environ. Sci. Technol.* **2011,** *45*, (14), 6129-6135.

39. Llabjani, V.; Crosse, J. D.; Ahmadzai, A. A.; Patel, I. I.; Pang, W.; Trevisan, J.; Jones, K. C.; Shore, R. F.; Martin, F. L., Differential Effects in Mammalian Cells Induced by Chemical Mixtures in Environmental Biota As Profiled Using Infrared Spectroscopy. *Environ. Sci. Technol.* **2011,** *45*, (24), 10706-10712.

40. Andrus, P. G., Cancer monitoring by FTIR spectroscopy. *Technol Cancer Res Treat* **2006,** *5*, (2), 157-167.

41. Sahu, R. K.; Argov, S.; Salman, A.; Huleihel, M.; Grossman, N.; Hammody, Z.; Kapelushnik, J.; Mordechai, S., Characteristic Absorbance of Nucleic Acids in the Mid-IR Region as Possible Common Biomarkers for Diagnosis of Malignancy. *Technol Cancer Res Treat* **2004,** *3*, (6), 629-638.

42. Mourant, J. R.; Yamada, Y. R.; Carpenter, S.; Dominique, L. R.; Freyer, J. P., FTIR Spectroscopy Demonstrates Biochemical Differences in Mammalian Cell Cultures at Different Growth Stages. *Biophys. J.* **2003,** *85*, (3), 1938-1947.

43. Wang, L.; Mizaikoff, B., Application of multivariate data-analysis techniques to biomedical diagnostics based on mid-infrared spectroscopy. *Anal. Bioanal. Chem.* **2008,** *391*, (5), 1641-1654.

44. Trevisan, J.; Angelov, P. P.; Patel, I. I.; Najand, G. M.; Cheung, K. T.; Llabjani, V.; Pollock, H. M.; Bruce, S. W.; Pant, K.; Carmichael, P. L.; Scott, A. D.; Martin, F. L., Syrian hamster embryo (SHE) assay (pH 6.7) coupled with infrared spectroscopy and chemometrics towards toxicological assessment. *Analyst* **2010,** *135*, (12), 3266-3272.

45. Trevisan, J.; Angelov, P. P.; Carmichael, P. L.; Scott, A. D.; Martin, F. L., Extracting biological information with computational analysis of Fourier-transform infrared (FTIR) biospectroscopy datasets: current practices to future perspectives. *Analyst* **2012,** *137*, (14), 3202-3215.

46. Dhawan, A.; Taurozzi, J. S.; Pandey, A. K.; Shan, W.; Miller, S. M.; Hashsham, S. A.; Tarabara, V. V., Stable Colloidal Dispersions of C60 Fullerenes in Water: Evidence for Genotoxicity†. *Environ. Sci. Technol.* **2006,** *40*, (23), 7394-7401.

47. Folkmann, J. K.; Risom, L.; Jacobsen, N. R.; Wallin, H.; Loft, S.; Møller, P., Oxidatively damaged DNA in rats exposed by oral gavage to C60 fullerenes and single-walled carbon nanotubes. *Environ. Health Perspect.* **2009,** *117*, (5), 703-708.

48. Wang, F.; Jin, C.; Liang, H.; Tang, Y.; Zhang, H.; Yang, Y., Effects of fullerene C60 nanoparticles on A549 cells. *Environ. Toxicol. Pharmacol.* **2014,** *37*, (2), 656-661.

49. Castaño, A.; Becerril, C., In vitro assessment of DNA damage after short- and long-term exposure to benzo(a)pyrene using RAPD and the RTG-2 fish cell line. *Mutat. Res. Fundam. Mol. Mech. Mutagen.* **2004,** *552*, (1–2), 141-151.

50. Llabjani, V.; Trevisan, J.; Jones, K. C.; Shore, R. F.; Martin, F. L., Binary Mixture Effects by PBDE Congeners (47, 153, 183, or 209) and PCB Congeners (126 or 153) in MCF-7 Cells: Biochemical Alterations Assessed by IR Spectroscopy and Multivariate Analysis. *Environ. Sci. Technol.* **2010,** *44*, (10), 3992-3998.

51. Canesi, L.; Ciacci, C.; Balbi, T., Interactive effects of nanoparticles with other contaminants in aquatic organisms: Friend or foe? *Mar. Environ. Res.*

52. Baun, A.; Sørensen, S. N.; Rasmussen, R. F.; Hartmann, N. B.; Koch, C. B., Toxicity and bioaccumulation of xenobiotic organic compounds in the presence of

aqueous suspensions of aggregates of nano-C60. *Aquat. Toxicol.* **2008,** *86*, (3), 379-387.

53. Henry, T. B.; Wileman, S. J.; Boran, H.; Sutton, P., Association of Hg2+ with Aqueous (C60)n Aggregates Facilitates Increased Bioavailability of Hg2+ in Zebrafish (Danio rerio). *Environ. Sci. Technol.* **2013,** *47*, (17), 9997-10004.

54. Lehto, M.; Karilainen, T.; Róg, T.; Cramariuc, O.; Vanhala, E.; Tornaeus, J.; Taberman, H.; Jänis, J.; Alenius, H.; Vattulainen, I.; Laine, O., Co-Exposure with Fullerene May Strengthen Health Effects of Organic Industrial Chemicals. *PLoS ONE* **2014,** *9*, (12), e114490.

55. Ferreira, J. L. R.; Lonné, M. N.; França, T. A.; Maximilla, N. R.; Lugokenski, T. H.; Costa, P. G.; Fillmann, G.; Antunes Soares, F. A.; de la Torre, F. R.; Monserrat, J. M., Co-exposure of the organic nanomaterial fullerene C60 with benzo[a]pyrene in Danio rerio (zebrafish) hepatocytes: Evidence of toxicological interactions. *Aquat. Toxicol.* **2014,** *147*, 76-83.

56. Park, J.-W.; Henry, T. B.; Menn, F.-M.; Compton, R. N.; Sayler, G., No bioavailability of 17α-ethinylestradiol when associated with nC60 aggregates during dietary exposure in adult male zebrafish (Danio rerio). *Chemosphere* **2010,** *81*, (10), 1227-1232.

57. Park, J.-W.; Henry, T. B.; Ard, S.; Menn, F.-M.; Compton, R. N.; Sayler, G. S., The association between nC60 and 17α-ethinylestradiol (EE2) decreases EE2 bioavailability in zebrafish and alters nanoaggregate characteristics. *Nanotoxicology* **2011,** *5*, (3), 406-416.

58. Yang, X. Y.; Edelmann, R. E.; Oris, J. T., Suspended C60 nanoparticles protect against short-term UV and fluoranthene photo-induced toxicity, but cause long-term cellular damage in Daphnia magna. *Aquat. Toxicol.* **2010,** *100*, (2), 202-210.

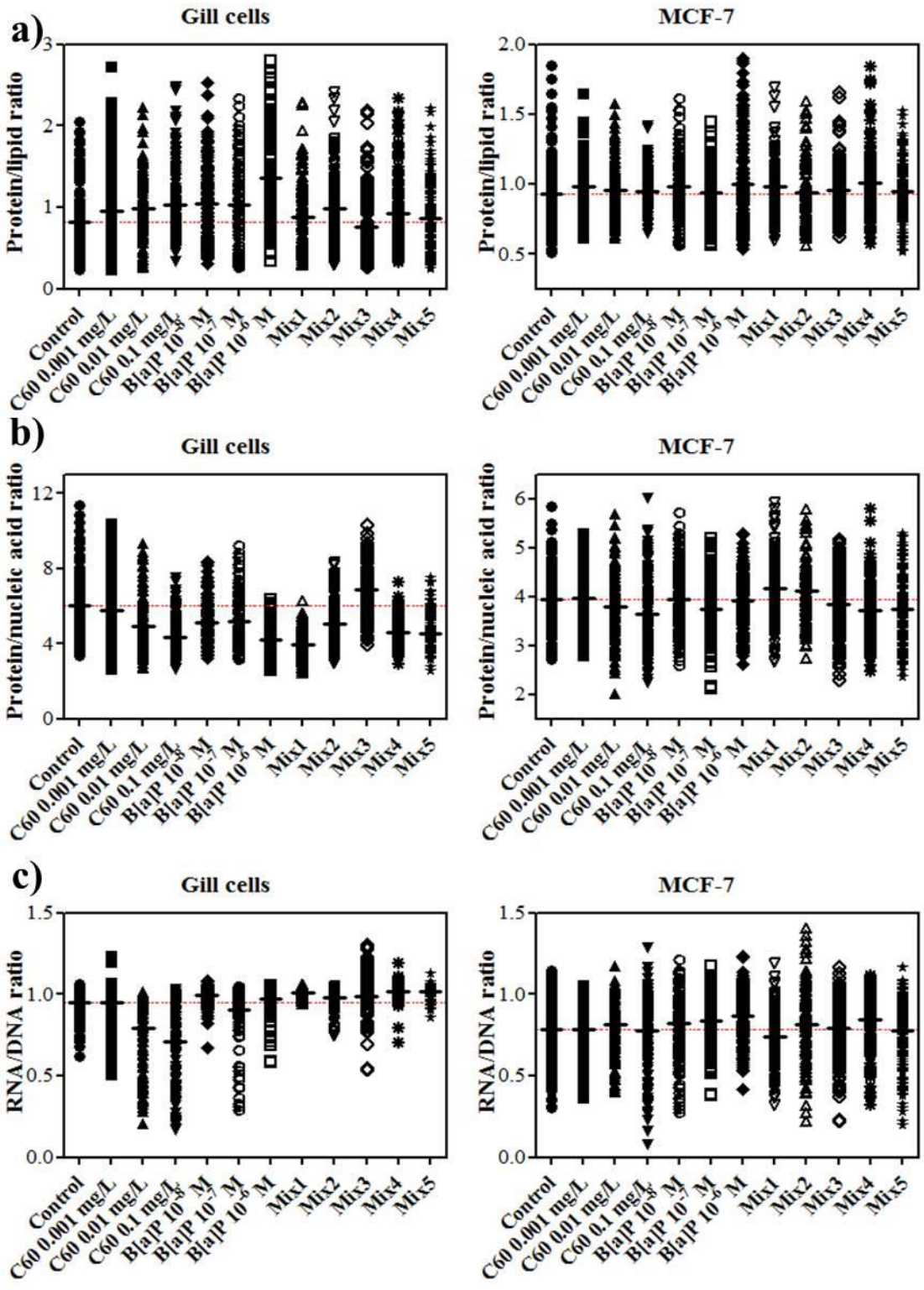

Figure 1. Intensity absorbance ratio derived from IR spectra of the cells a) Ratio of protein to lipid; b) Ratio of protein to nucleic acid; c) Ratio of RNA to DNA.

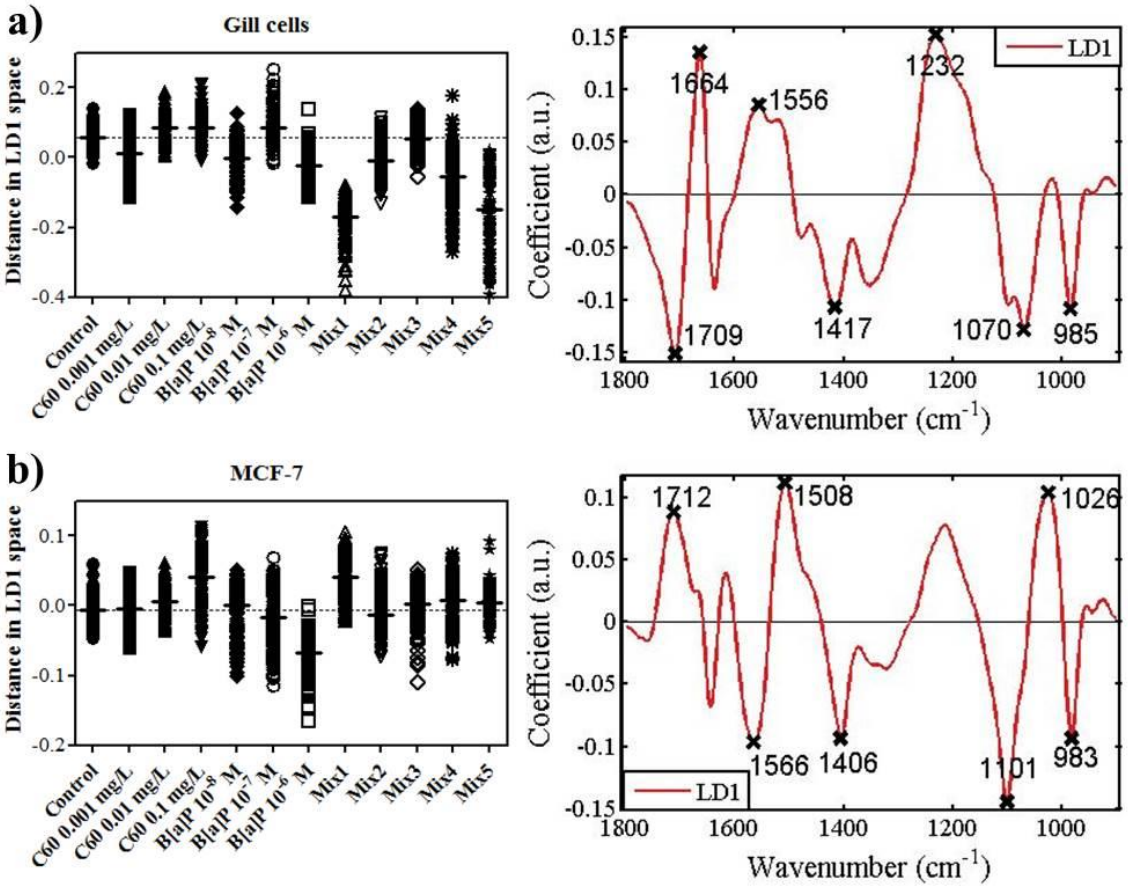

Figure 2. One-D Scores plot in LD1 derived from PCA-LDA of spectral dataset (Dataset Total), with corresponding loading plot. **a**) Gill cells; **b**) MCF-7 cells. BaP, B[*a*]P

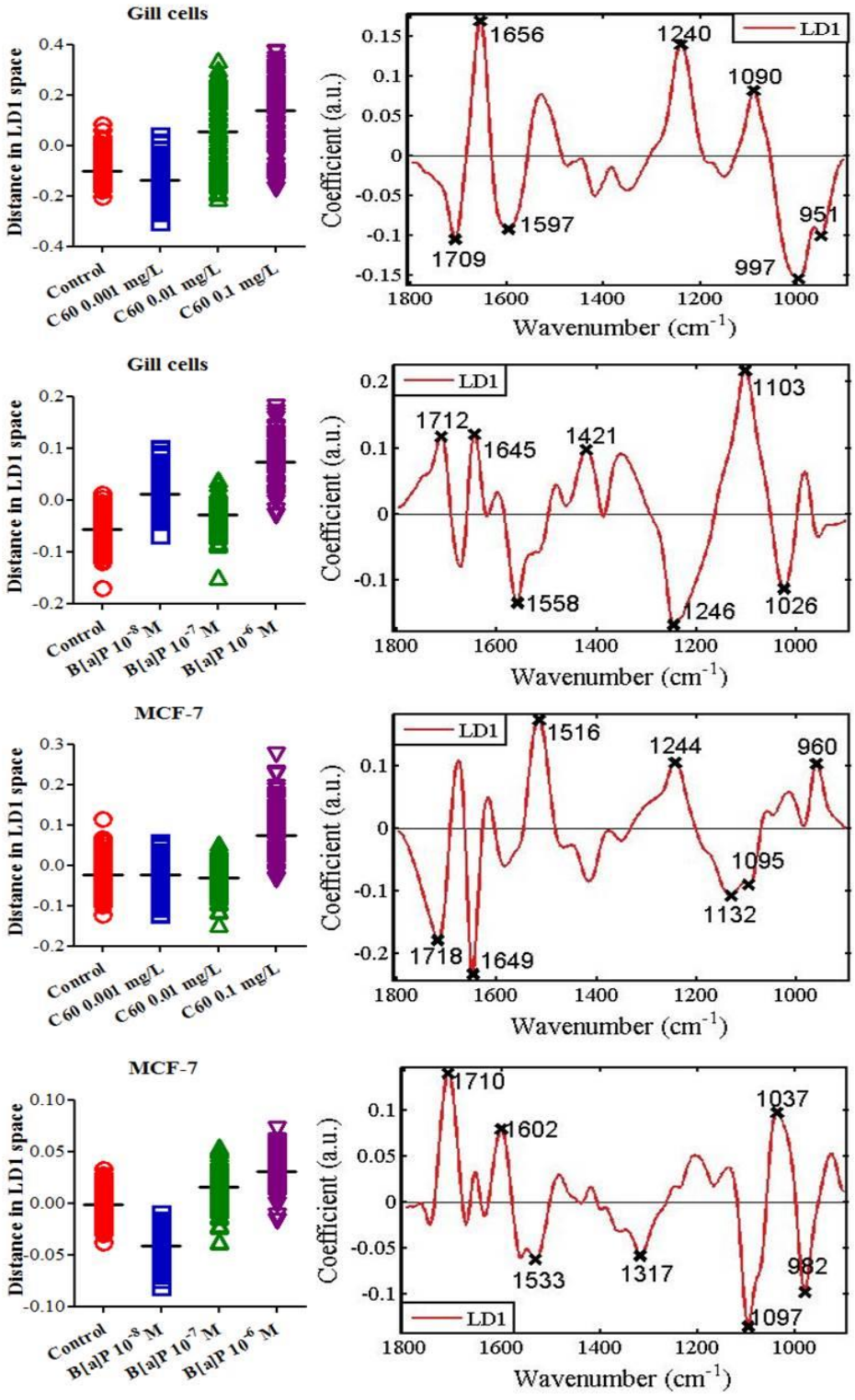

Figure 3. One-D Scores plot in LD1 derived from PCA-LDA of spectral dataset for single treatment, with corresponding loading plot. BaP, B[*a*]P

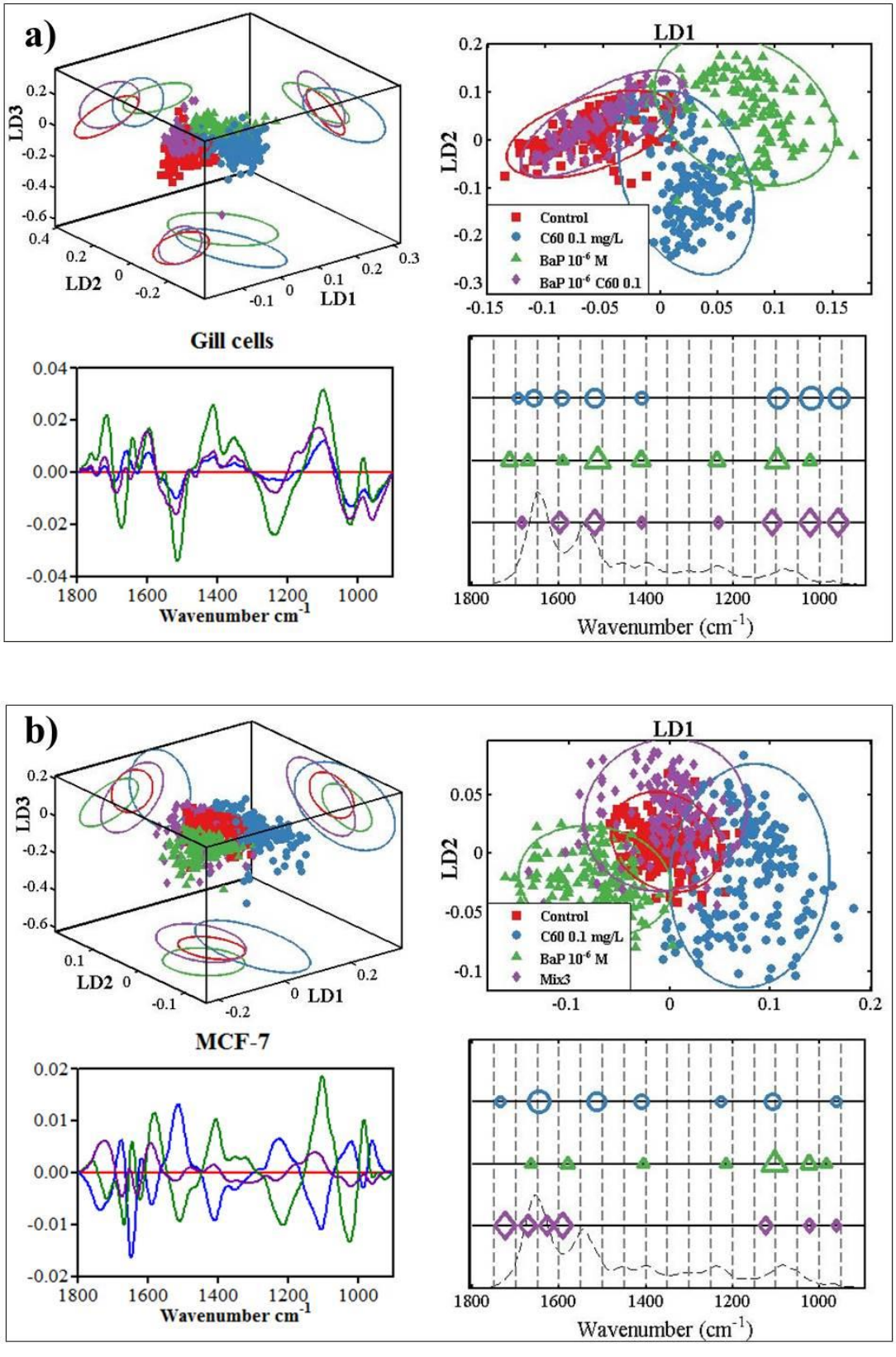

Figure 4. Scores plot and cluster vector derived from PCA-LDA of spectral dataset (Dataset mix). **a**) Gill cells; **b**) MCF-7 cells. BaP, B[*a*]P

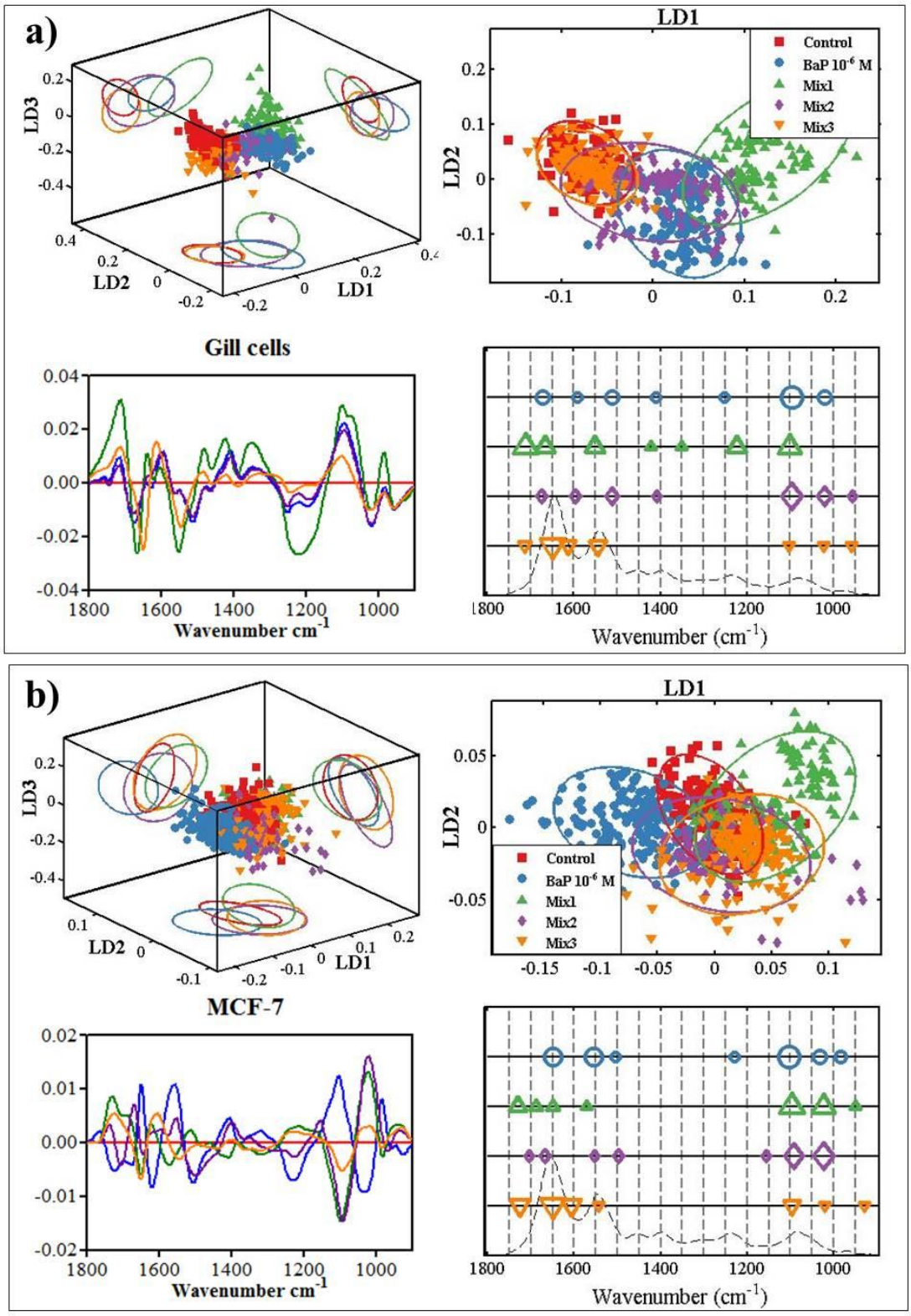

Figure 5. Scores plot and cluster vector derived from PCA-LDA of spectral dataset (Dataset BaPmix). **a**) Gill cells; **b**) MCF-7 cells. BaP, B[*a*]P

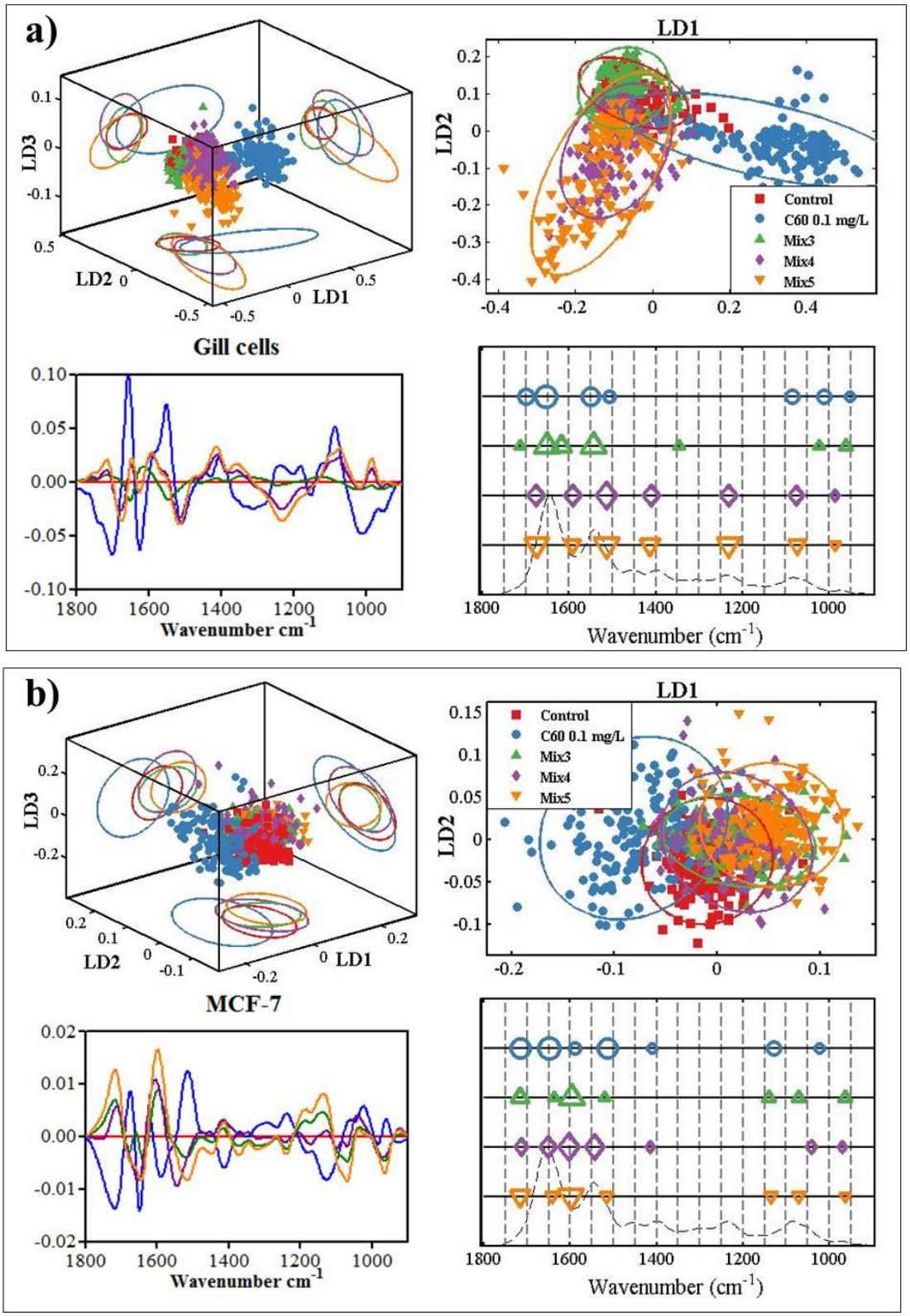

Figure 6. Scores plot and cluster vector derived from PCA-LDA of spectral dataset (Dataset C60mix). **a**) Gill cells; **b**) MCF-7 cells.

Supporting Information

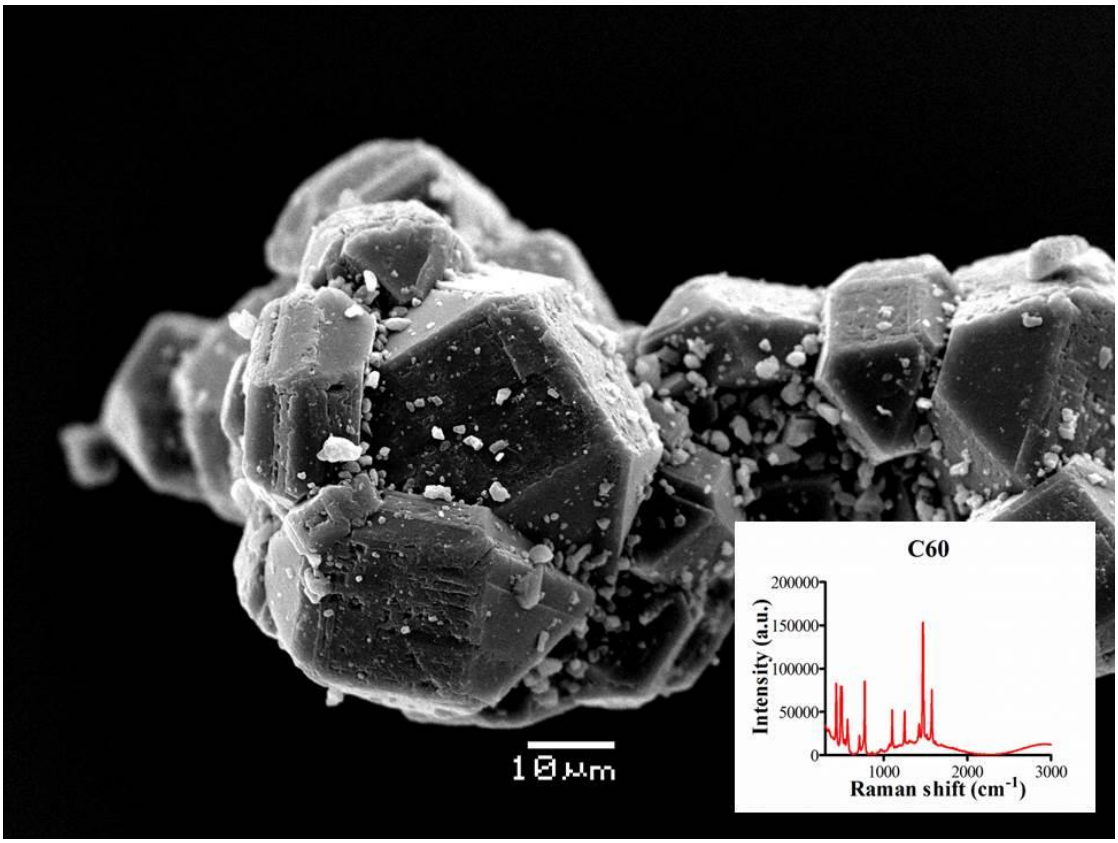

Figure S1. Scanning electron microscopy (SEM) images of fullerene C60 with Raman spectra of characterization.

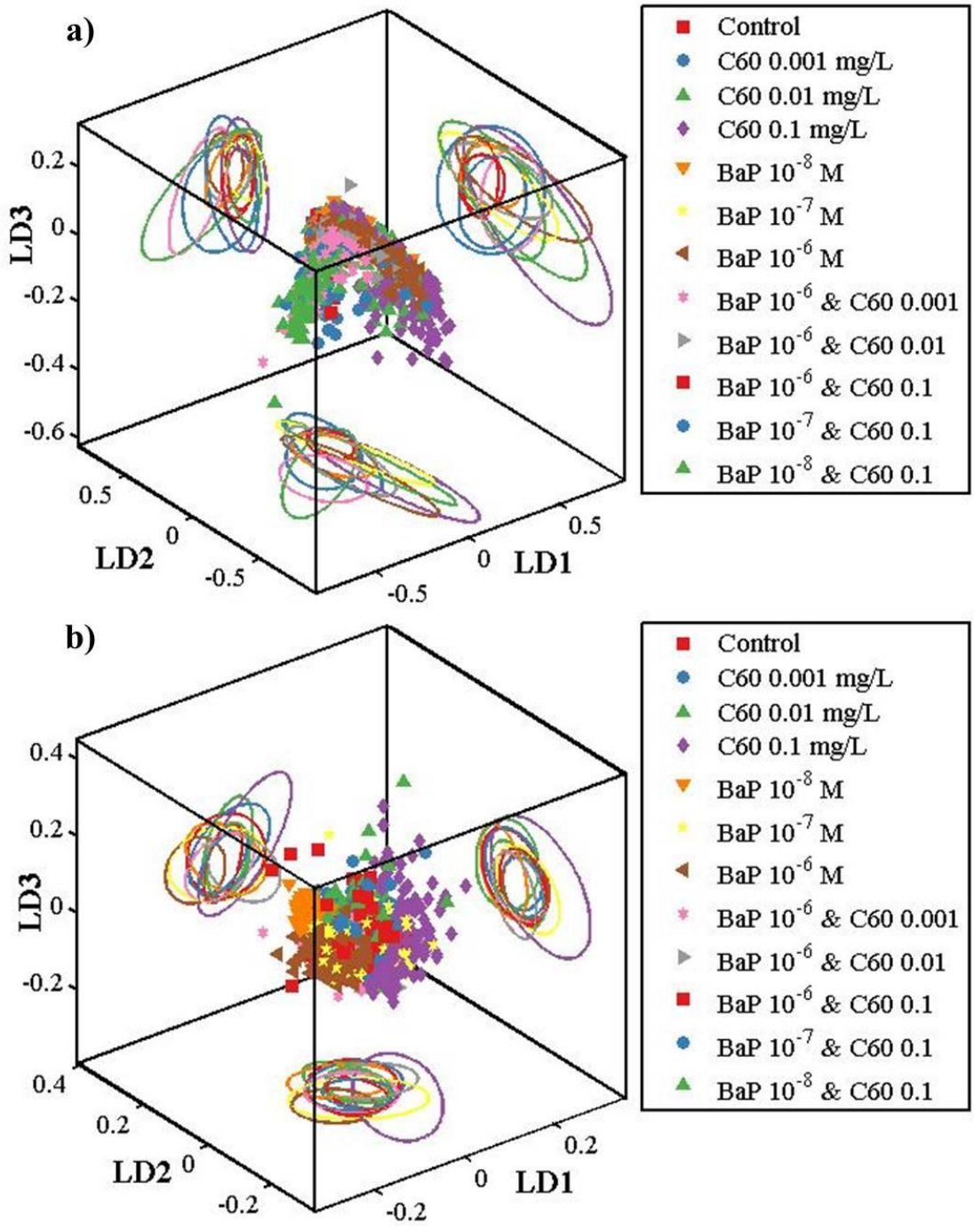

Figure S2. Three-dimension PCA-LDA scores plots (*95% Confidence ellipsoids projected on walls*) derived from post-exposure cells interrogated by FTIR **a**) Gill cells; **b**) MCF-7 cells. BaP, B[*a*]P.

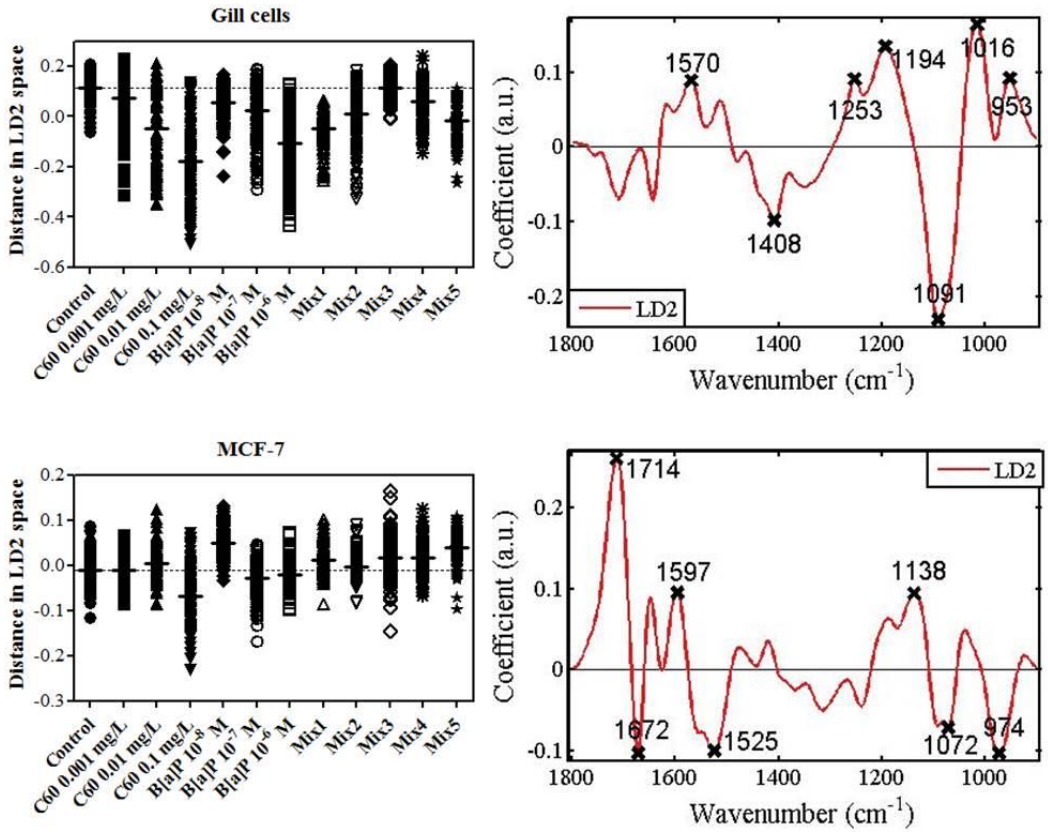

Figure S3. One-D Scores plot in LD2 derived from PCA-LDA of spectral dataset (Dataset Total), with corresponding loading plot. **a**) Gill cells; **b**) MCF-7 cells. BaP, B[*a*]P

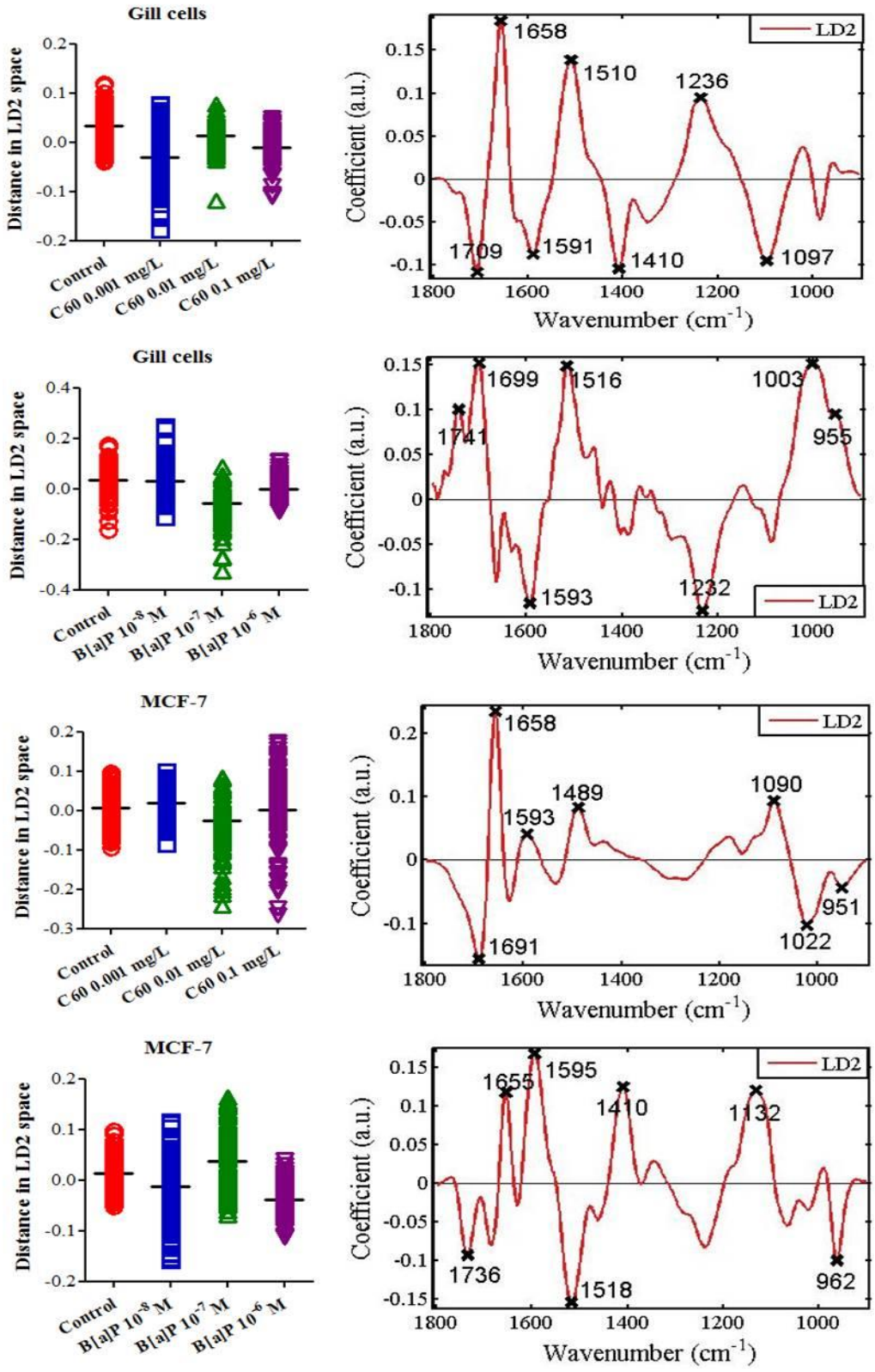

Figure S4. One-D Scores plot in LD2 derived from PCA-LDA of spectral dataset for single treatment, with corresponding loading plot. BaP, B[*a*]P

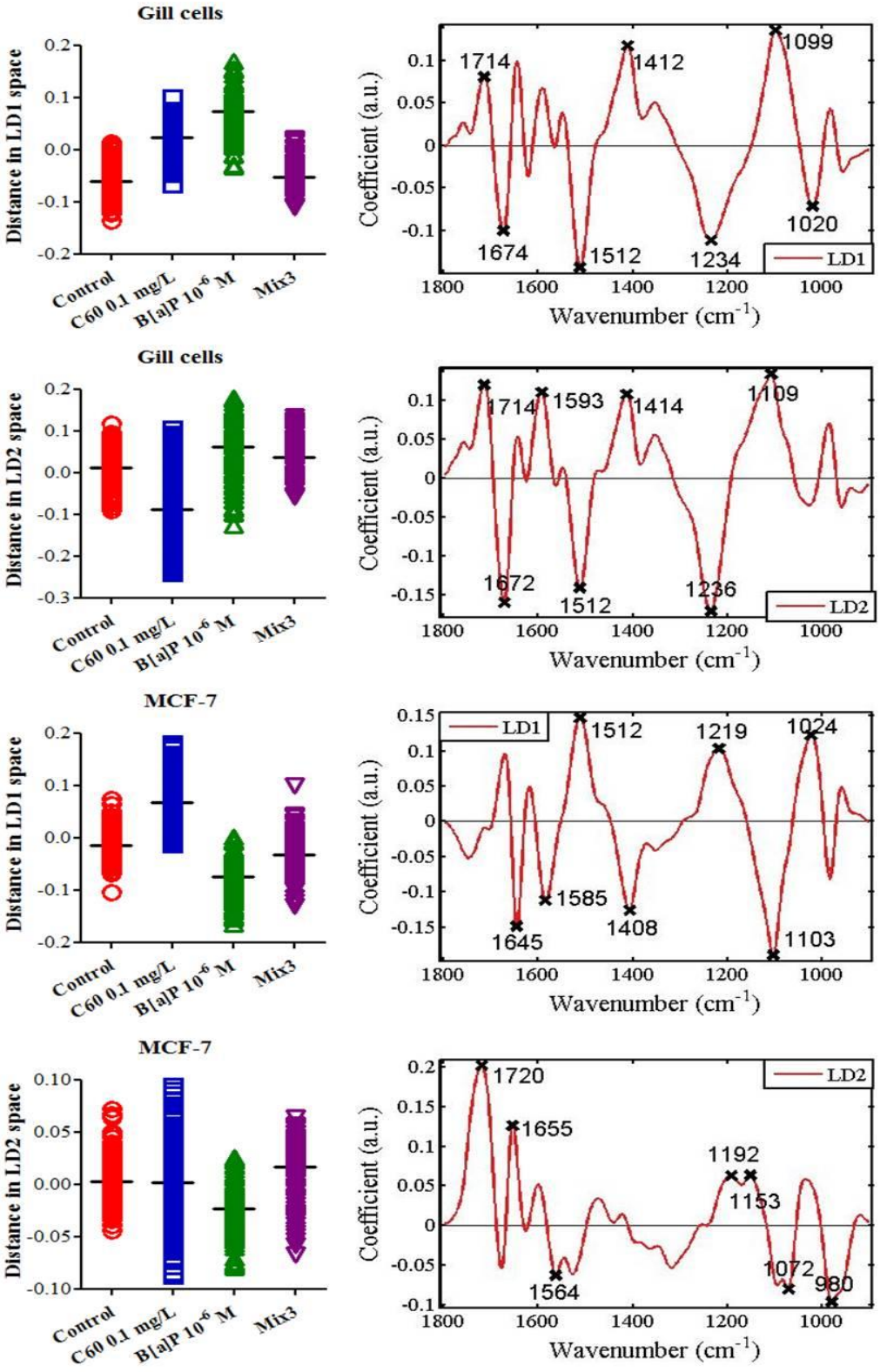

Figure S5. One-D Scores plot derived from PCA-LDA of spectral dataset (Dataset mix), with corresponding loading plot. BaP, B[*a*]P

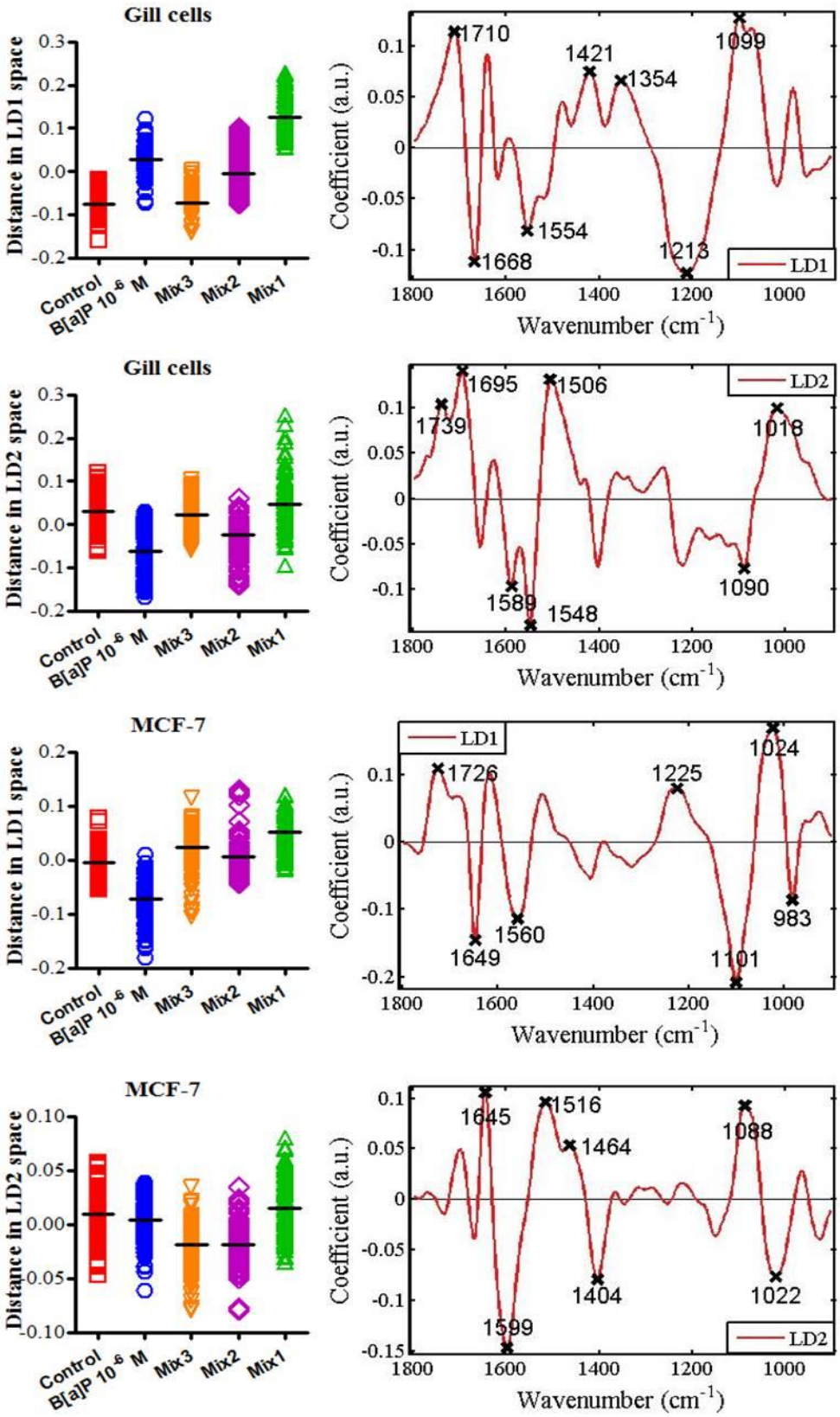

Figure S6. One-D Scores plot derived from PCA-LDA of spectral dataset (Dataset BaPmix), with corresponding loading plot. BaP, B[*a*]P

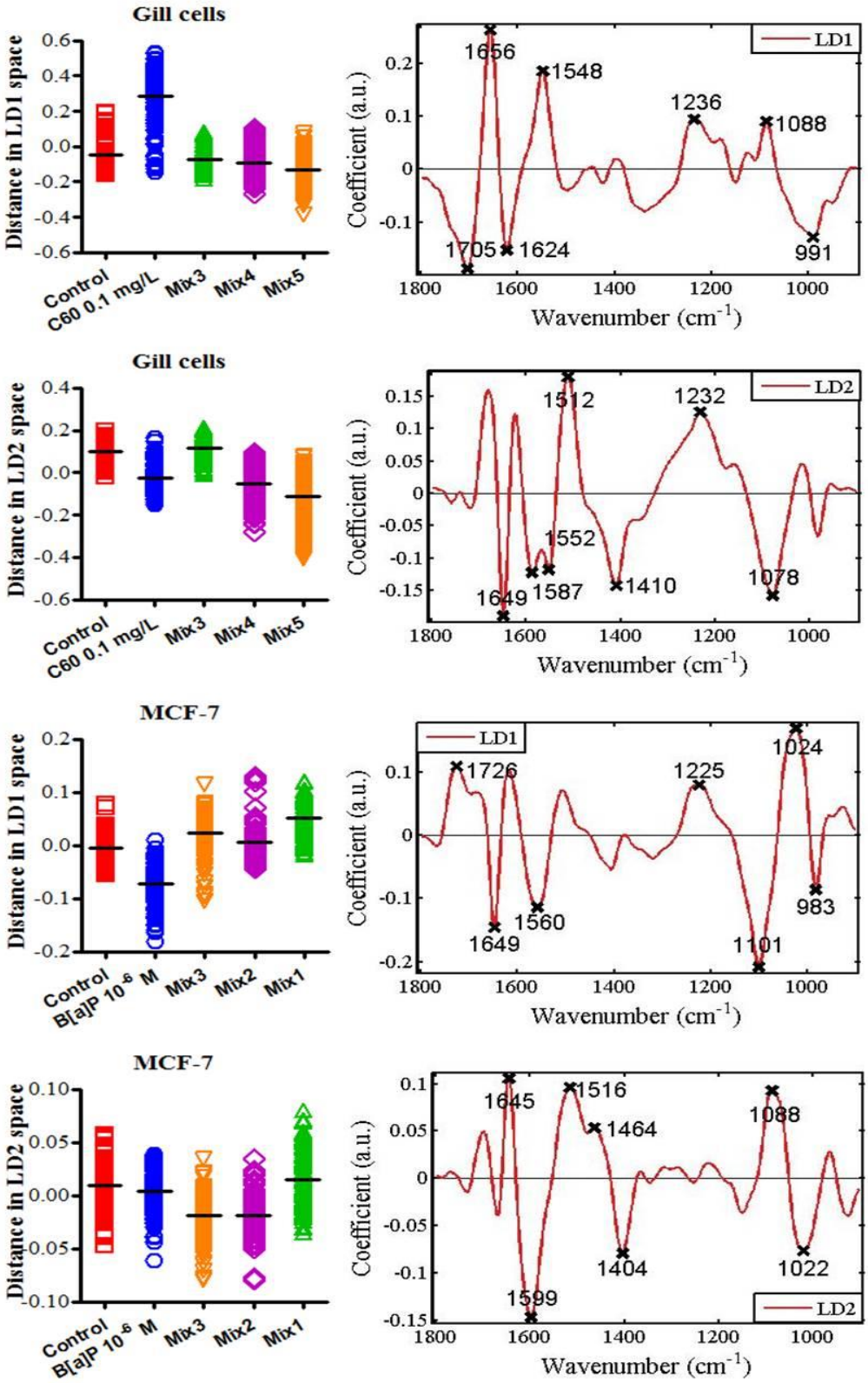

Figure S7. One-D Scores plot derived from PCA-LDA of spectral dataset (Dataset C60mix), with corresponding loading plot. BaP, B[*a*]P

Table S1 Ratio of Protein to Lipid derived from FTIR spectra of cells

One-way ANOVA with Dunnett's Multiple Comparison Test	**Gill cells**	**MCF-7 cells**
Control *vs* C60 0.001 mg/L	*P >0.05*	*P >0.05*
Control *vs* C60 0.01 mg/L	*P <0.05*	*P >0.05*
Control *vs* C60 0.1 mg/L	*P <0.001*	*P >0.05*
Control *vs* B[*a*]P 10^{-8} M	*P <0.001*	*P >0.05*
Control *vs* B[*a*]P 10^{-7} M	*P <0.001*	*P >0.05*
Control *vs* B[*a*]P 10^{-6} M	*P <0.0001*	*P >0.05*
Control *vs* Mix1	*P >0.05*	*P >0.05*
Control *vs* Mix2	*P <0.05*	*P >0.05*
Control *vs* Mix3	*P >0.05*	*P >0.05*
Control *vs* Mix4	*P >0.05*	*P <0.001*
Control *vs* Mix5	*P >0.05*	*P >0.05*

Table S2 Ratio of Protein to Nucleic acid derived from FTIR spectra of cells

One-way ANOVA with Dunnett's Multiple Comparison Test	**Gill cells**	**MCF-7 cells**
Control *vs* C60 0.001 mg/L	*P >0.05*	*P >0.05*
Control *vs* C60 0.01 mg/L	*P <0.0001*	*P >0.05*
Control *vs* C60 0.1 mg/L	*P <0.0001*	*P <0.0001*
Control *vs* B[*a*]P 10^{-8} M	*P <0.0001*	*P >0.05*
Control *vs* B[*a*]P 10^{-7} M	*P <0.0001*	*P >.05*
Control *vs* B[*a*]P 10^{-6} M	*P <0.0001*	*P >0.05*
Control *vs* Mix1	*P <0.0001*	*P <0.05*
Control *vs* Mix2	*P <0.0001*	*P >0.05*
Control *vs* Mix3	*P <0.0001*	*P >0.05*
Control *vs* Mix4	*P <0.0001*	*P <0.05*
Control *vs* Mix5	*P <0.0001*	*P <0.05*

Table S3 Ratio of RNA to DNA derived from FTIR spectra of cells

One-way ANOVA with Dunnett's Multiple Comparison Test	**Gill cells**	**MCF-7 cells**
Control *vs* C60 0.001 mg/L	*P >0.05*	*P >0.05*
Control *vs* C60 0.01 mg/L	*P <0.0001*	*P >0.05*
Control *vs* C60 0.1 mg/L	*P <0.0001*	*P >0.05*
Control *vs* B[*a*]P 10^{-8} M	*P <0.05*	*P >0.05*
Control *vs* B[*a*]P 10^{-7} M	*P >0.05*	*P <0.05*
Control *vs* B[*a*]P 10^{-6} M	*P >0.05*	*P <0.0001*
Control *vs* Mix1	*P <0.001*	*P >0.05*
Control *vs* Mix2	*P >0.05*	*P >0.05*
Control *vs* Mix3	*P >0.05*	*P >0.05*
Control *vs* Mix4	*P <0.0001*	*P <0.05*
Control *vs* Mix5	*P <0.0001*	*P >0.05*

Table S4 Scores plots derived from PCA-LDA of FTIR spectra of cells

One-way ANOVA with Dunnett's Multiple Comparison Test		**Gill cells**		**MCF-7 cells**	
		LD1	LD2	LD1	LD2
Dataset C60	Control vs C60 0.001 mg/L	*P <0.05*	*P <0.0001*	*P >0.05*	*P >0.05*
	Control vs C60 0.01 mg/L	*P <0.0001*	*P <0.0001*	*P >0.05*	*P <0.0001*
	Control vs C60 0.1 mg/L	*P <0.0001*	*P <0.0001*	*P <0.0001*	*P >0.05*
Dataset BaP	Control vs B[*a*]P 10^{-8} M	*P <0.0001*	*P >0.05*	*P <0.0001*	*P <0.0001*
	Control vs B[*a*]P 10^{-7} M	*P <0.0001*	*P <0.001*	*P <0.0001*	*P <0.0001*
	Control vs B[*a*]P 10^{-6} M	*P <0.0001*	*P <0.001*	*P <0.0001*	*P <0.0001*
Dataset total	Control vs C60 0.001 mg/L	*P <0.0001*	*P <0.05*	*P >0.05*	*P >0.05*
	Control vs C60 0.01 mg/L	*P <0.001*	*P <0.0001*	*P <0.001*	*P <0.0001*
	Control vs C60 0.1 mg/L	*P <0.001*	*P <0.0001*	*P <0.0001*	*P <0.0001*
	Control vs B[*a*]P 10^{-8} M	*P <0.0001*	*P <0.0001*	*P >0.05*	*P <0.0001*
	Control vs B[*a*]P 10^{-7} M	*P <0.001*	*P <0.001*	*P <0.05*	*P <0.0001*
	Control vs B[*a*]P 10^{-6} M	*P <0.0001*	*P <0.001*	*P <0.0001*	*P >0.05*
	Control vs Mix1	*P <0.0001*	*P <0.001*	*P <0.0001*	*P <0.0001*
	Control vs Mix2	*P <0.001*	*P <0.0001*	*P >0.05*	*P >0.05*
	Control vs Mix3	*P >0.05*	*P >0.05*	*P >0.05*	*P <0.0001*
	Control vs Mix4	*P <0.0001*	*P <0.0001*	*P <0.0001*	*P <0.0001*
	Control vs Mix5	*P <0.0001*	*P <0.0001*	*P <0.05*	*P <0.0001*

Table S5 Scores plots derived from PCA-LDA of FTIR spectra of cells

One-way ANOVA with Dunnett's Multiple Comparison Test		**Gill cells**		**MCF-7 cells**	
		LD1	LD2	LD1	LD2
Dataset BaPmix	Control vs B[*a*]P 10^{-6} M	*P <0.0001*	*P <0.0001*	*P <0.0001*	*P >0.05*
	Control vs Mix1	*P <0.0001*	*P <0.001*	*P <0.0001*	*P <0.05*
	Control vs Mix2	*P <0.0001*	*P <0.0001*	*P >0.05*	*P <0.0001*
	Control vs Mix3	*P >0.05*	*P >0.05*	*P <0.0001*	*P <0.0001*
Dataset C60mix	Control vs C60 0.1 mg/L	*P <0.0001*	*P <0.0001*	*P <0.0001*	*P <0.0001*
	Control vs Mix3	*P >0.05*	*P >0.05*	*P <0.0001*	*P <0.0001*
	Control vs Mix4	*P <0.001*	*P <0.0001*	*P <0.0001*	*P <0.0001*
	Control vs Mix5	*P <0.0001*	*P <0.0001*	*P <0.0001*	*P <0.0001*
Dataset mix	Control vs C60 0.1 mg/L	*P <0.0001*	*P <0.0001*	*P <0.0001*	*P >0.05*
	Control vs B[*a*]P 10^{-6} M	*P <0.0001*	*P <0.0001*	*P <0.0001*	*P <0.0001*
	Control vs Mix3	*P >0.05*	*P <0.05*	*P <0.0001*	*P <0.0001*

Table S6 Primary wavenumbers in loadings plots derived from PCA-LDA of FTIR spectral dataset (Gill cells)

	LD1		LD2	
	Wavenumber (cm^{-1})	Tentative assignments	Wavenumber (cm^{-1})	Tentative assignments
Dataset C60	1656	Amide I	1658	Amide I
	997	Glycogen	1510	Amide II
	1240	$v_{as}PO_2^-$	1709	Lipid, v(C=O)
	1709	Lipid, v(C=O)	1410	$v(COO^-)$
	951	Protein phosphorylation	1236	$v_{as}PO_2^-$
	1597	Amide I	1097	$v_sPO_2^-$
	1090	$v_sPO_2^-$	1591	Amide I
Dataset BaP	1103	Carbohydrates	1699	Lipid, v(C=O)
	1246	$v_{as}PO_2^-$	1003	Glycogen
	1558	Amide II	1516	Amide II
	1645	Amide I	1232	$v_{as}PO_2^-$
	1712	Lipid, v(C=O)	1593	Amide I
	1026	Glycogen	1741	Lipid, v(C=O)
	1421	$v(COO^-)$	955	Protein phosphorylation
Dataset Total	1232	$v_{as}PO_2^-$	1091	$v_sPO_2^-$
	1709	Lipid, v(C=O)	1016	Glycogen
	1664	Amide I	1194	Collagen
	1070	$v_sPO_2^-$	1408	$v(COO^-)$
	985	Protein phosphorylation	953	Protein phosphorylation
	1417	$v(COO^-)$	1253	$v_{as}PO_2^-$
	1556	Amide II	1570	Amide II

Table S7 Primary wavenumbers in loadings plots derived from PCA-LDA of FTIR spectral dataset (Gill cells)

	LD1		LD2	
	Wavenumber (cm^{-1})	Tentative assignments	Wavenumber (cm^{-1})	Tentative assignments
Dataset C60mix	1656	Amide I	1649	Amide I
	1705	Lipid, *v*(C=O)	1512	Amide II
	1548	Amide II	1078	$v_sPO_2^-$
	1624	Amide I	1410	$v(COO^-)$
	991	Protein phosphorylation	1232	$v_{as}PO_2^-$
	1236	$v_{as}PO_2^-$	1587	Amide I
	1088	$v_sPO_2^-$	1552	Amide II
Dataset BaPmix	1099	$v_sPO_2^-$	1695	Lipid, *v*(C=O)
	1212	$v_{as}PO_2^-$	1548	Amide II
	1710	Lipid, *v*(C=O)	1506	Amide II
	1668	Amide I	1739	Lipid, *v*(C=O)
	1554	Amide II	1018	Glycogen
	1421	$v(COO^-)$	1588	Amide I
	1354	Amide III	1090	$v_sPO_2^-$
Dataset mix	1512	Amide II	1236	$v_{as}PO_2^-$
	1099	$v_sPO_2^-$	1672	Amide I
	1412	$v(COO^-)$	1512	Amide II
	1234	$v_{as}PO_2^-$	1109	Carbohydrates
	1674	Amide I	1714	Lipid, *v*(C=O)
	1714	Lipid, *v*(C=O)	1593	Amide I
	1020	Glycogen	1414	$v(COO^-)$

Table S8 Primary wavenumbers in loadings plots derived from PCA-LDA of FTIR spectral dataset (MCF-7 cells)

	LD1		LD2	
	Wavenumber (cm^{-1})	Tentative assignments	Wavenumber (cm^{-1})	Tentative assignments
Dataset C60	1649	Amide I	1658	Amide I
	1718	Lipid, ν(C=O)	1691	Amide I
	1516	Amide II	1022	Glycogen
	1132	Carbohydrates	1090	$\nu_s PO_2^-$
	1244	$\nu_{as} PO_2^-$	1489	Protein, CH_2
	960	Protein phosphorylation	951	Protein phosphorylation
	1095	$\nu_s PO_2^-$	1593	Amide I
Dataset BaP	1710	Lipid, ν(C=O)	1595	Amide I
	1097	$\nu_s PO_2^-$	1518	Amide II
	1037	Glycogen	1410	$\nu(COO^-)$
	982	Protein phosphorylation	1132	Carbohydrates
	1602	Amide I	1655	Amide I
	1533	Amide II	962	Protein phosphorylation
	1317	Amide III	1736	Lipid, ν(C=O)
Dataset Total	1101	$\nu_s PO_2^-$	1714	Lipid, ν(C=O)
	1508	Amide II	1672	Amide I
	1026	Glycogen	974	Protein phosphorylation
	1566	Amide II	1525	Amide II
	983	Protein phosphorylation	1597	Amide I
	1406	$\nu(COO^-)$	1138	Carbohydrates
	1712	Lipid, ν(C=O)	1072	$\nu_s PO_2^-$

Table S9 Primary wavenumbers in loadings plots derived from PCA-LDA of FTIR spectral dataset (MCF-7 cells)

	LD1		LD2	
	Wavenumber (cm^{-1})	Tentative assignments	Wavenumber (cm^{-1})	Tentative assignments
Dataset C60mix	1716	Lipid, *v*(C=O)	1647	Amide I
	1595	Amide I	1606	Amide I
	1516	Amide II	1093	$v_sPO_2^-$
	1132	Carbohydrates	1026	Glycogen
	1674	Amide I	974	Protein phosphorylation
	1068	$v_sPO_2^-$	1196	Collagen
	962	Protein phosphorylation	1437	$v(COO^-)$
Dataset BaPmix	1101	$v_sPO_2^-$	1599	Amide I
	1024	Glycogen	1645	Amide I
	1649	Amide I	1516	Amide II
	1560	Amide II	1088	$v_sPO_2^-$
	1726	Lipid, *v*(C=O)	1404	$v(COO^-)$
	983	Protein phosphorylation	1002	Glycogen
	1225	$v_{as}PO_2^-$	1464	Protein, CH_2
Dataset mix	1103	$v_sPO_2^-$	1720	Lipid, *v*(C=O)
	1645	Amide I	1655	Amide I
	1512	Amide II	980	Protein phosphorylation
	1408	$v(COO^-)$	1072	$v_sPO_2^-$
	1024	Glycogen	1153	Carbohydrates
	1585	Amide I	1192	Collagen
	1219	$v_{as}PO_2^-$	1564	Amide II

Table S10 Primary wavenumbers in cluster vector plots for PCA-LDA derived from IR spectra

	Gill cells		**MCF-7 cells**	
	Wavenumber (cm^{-1})	Tentative assignments	Wavenumber (cm^{-1})	Tentative assignments
C60 0.1 mg/L	1020	Glycogen	1647	Amide I
	1097	$\nu_s PO_2^-$	1514	Amide II
	956	Protein phosphorylation	1107	Carbohydrates
	1518	Amide II	1410	$\nu(COO^-)$
	1658	Amide I	1736	Lipid, ν(C=O)
	1595	Amide I	1226	$\nu_{as} PO_2^-$
	1411	$\nu(COO^-)$	960	Protein phosphorylation
B[*a*]P 10^{-6} M	1512	Amide II	1098	$\nu_s PO_2^-$
	1099	$\nu_s PO_2^-$	1024	Glycogen
	1412	$\nu(COO^-)$	1581	Amide II
	1236	$\nu_{as} PO_2^-$	1405	$\nu(COO^-)$
	1714	Lipid, ν(C=O)	983	Protein phosphorylation
	1672	Amide I	1214	$\nu_{as} PO_2^-$
	1022	Glycogen	1666	Amide I
B[*a*]P 10^{-6} & C60 0.1	958	Protein phosphorylation	1724	Lipid, ν(C=O)
	1022	Glycogen	1591	Amide I
	1110	Carbohydrates	1672	Amide I
	1518	Amide II	1629	Amide I
	1599	Amide I	1124	Carbohydrates
	1412	$\nu(COO^-)$	1022	Glycogen
	1685	Amide I	960	Protein phosphorylation

Table S11 Primary wavenumbers Cluster vector plots for PCA-LDA derived from IR spectra

	Gill cells		**MCF-7 cells**	
	Wavenumber (cm^{-1})	Tentative assignments	Wavenumber (cm^{-1})	Tentative assignments
B[*a*]P 10^{-6} M	1095	$\nu_s PO_2^-$	1098	$\nu_s PO_2^-$
	1020	Glycogen	1556	Amide II
	1671	Amide I	1648	Amide I
	1512	Amide II	1031	Glycogen
	1410	$\nu(COO^-)$	983	Protein phosphorylation
	1593	Amide I	1504	Amide II
	1252	$\nu_{as} PO_2^-$	1230	$\nu_{as} PO_2^-$
B[*a*]P 10^{-6} & C60 0.001	1710	Lipid, ν(C=O)	1097	$\nu_s PO_2^-$
	1101	Carbohydrates	1022	Glycogen
	1223	$\nu_{as} PO_2^-$	1730	Lipid, ν(C=O)
	1664	Amide I	1648	Amide I
	1550	Amide II	1689	Amide I
	1423	$\nu(COO^-)$	1571	Amide II
	1352	Amide III	948	Protein phosphorylation
B[*a*]P 10^{-6} & C60 0.01	1095	$\nu_s PO_2^-$	1022	Glycogen
	1020	Glycogen	1091	$\nu_s PO_2^-$
	1512	Amide II	1668	Amide I
	1674	Amide I	1498	Amide II
	1597	Amide I	1552	Amide II
	1408	$\nu(COO^-)$	1705	Lipid, ν(C=O)
	956	Protein phosphorylation	1155	Collagen
B[*a*]P 10^{-6} & C60 0.1	1649	Amide I	1648	Amide I
	1545	Amide II	1726	Lipid, ν(C=O)
	1612	Amide I	1606	Amide I
	1712	Lipid, ν(C=O)	1095	$\nu_s PO_2^-$
	1024	Glycogen	1542	Amide II
	1103	Carbohydrates	1020	Glycogen
	958	Protein phosphorylation	929	Protein phosphorylation

Table S12 Primary wavenumbers Cluster vector plots for PCA-LDA of IR spectra

	Gill cells		**MCF-7 cells**	
	Wavenumber (cm^{-1})	Tentative assignments	Wavenumber (cm^{-1})	Tentative assignments
C60 0.1 mg/L	1655	Amide I	1648	Amide I
	1550	Amide II	1716	Lipid, *v*(C=O)
	1699	Lipid, *v*(C=O)	1514	Amide II
	1086	$v_sPO_2^-$	1128	Carbohydrates
	1012	Glycogen	1588	Amide I
	1508	Amide II	1411	$v(COO^-)$
	953	Protein phosphorylation	1023	Glycogen
B[*a*]P 10^{-6} & C60 0.1	1651	Amide I	1597	Amide I
	1545	Amide II	1716	Lipid, *v*(C=O)
	1616	Amide I	1070	$v_sPO_2^-$
	960	Protein phosphorylation	964	Protein phosphorylation
	1024	Glycogen	1140	Carbohydrates
	1712	Lipid, *v*(C=O)	1637	Amide I
	1346	Amide III	1521	Amide II
B[*a*]P 10^{-7} & C60 0.1	1514	Amide II	1604	Amide I
	1591	Amide I	1545	Amide II
	1676	Amide I	1650	Amide I
	1412	$v(COO^-)$	1712	Lipid, *v*(C=O)
	1232	$v_{as}PO_2^-$	1041	Glycogen
	1076	$v_sPO_2^-$	970	Protein phosphorylation
	985	Protein phosphorylation	1415	$v(COO^-)$
B[*a*]P 10^{-8} & C60 0.1	1514	Amide II	1598	Amide I
	1232	$v_{as}PO_2^-$	1716	Lipid, *v*(C=O)
	1673	Amide I	1070	$v_sPO_2^-$
	1413	$v(COO^-)$	1643	Amide I
	1074	$v_sPO_2^-$	1515	Amide II
	1590	Amide I	1136	Carbohydrates
	985	Protein phosphorylation	964	Protein phosphorylation

Chapter 6 - Discussion

1. Biospectroscopy

Infrared (IR) and Raman spectroscopies have capability of providing biochemical information about the structure, functional groups and even the environment of the molecules in the biological samples. Over the past few decades, techniques based on Infrared (IR) and Raman spectroscopies (namely, biospectroscopy) have been extensively used to understand fundamental biology and responses of living systems under diverse physiological and pathological conditions (Diem et al. 1999; Matthäus et al. 2007; Walsh et al. 2007; Wood et al. 2004). Biospectroscopy is not only capable to differentiate cells or tissues based on the spectral properties, but also capable to serve as a potential diagnostic tool for discriminating various diseases or disease progression, as well as detecting biochemical alteration in toxicity assessment. Additionally, biopspectroscopy also provides us a rapid label-free testing method with advantages of non-destructive and time saving, by contrast to the conventional biological assays, which commonly requires high-cost bioreagents and technically labour-intense sample preparation.

The spectra from biological systems contain complex and diverse information of bio-molecules such as proteins, lipids, nucleic acids, carbohydrates *etc.*, which could sometimes even interpret the minor differences between samples with the help of computational data-analysis. The computational analysis mainly consists of two parts: the spectral pre-processing and multivariate data-analysis; the latter including various methods (*e.g.*, PCA, LDA, PLS and PCA-LDA) can efficiently process the huge

dataset derived from the spectra and help with information extraction and biomarker identification.

2. Determining dose-response alterations induced by CNPs

The dose and time are considered as the two key factors in toxicology (Rozman and Doull 2000). However, the toxicological dose response could be complicated and often displayed as a non-linear relationship, especially in the low and high dose. In general, high dose exposure is likely to induce acute toxicity, while the chronic low dose exposure over a life time could potentially increase the incidence of degenerative diseases, which is more predictive of the main public health. In nanotoxicology, it is important to evaluate the toxicity of CNPs at a relevant and realistic environmental level, which can make the conclusions from *in vitro* and *in vivo* experiments more meaningful for public risk assessment; this suggests that it is more urgent to test nanotoxicity on real-world doses rather than high dose.

In the published investigation on the toxicity of CNPs, most of the doses employed were quite high (about ≥1 mg/L), which is unlikely to predict the human pathology from environmental exposure. In our studies, we have validated the application of biospectroscopy in nanotoxicity assessment and significant responses from cells or fish have been detected in parts per billion (ppb) level (Low to 0.001 mg/L) (Chapter 2 and 3).

When MCF-7 cells both in S-phase and G_0/G_1-phase were treated with CNPs (C60, long and short MWCNTs), significant alterations ($P \leq 0.05$) in cells interrogated by ATR-FTIR were observed even at the treatment concentration at 0.0025 mg/L, and most of the dose response appeared to be non-linear (Chapter 2). Especially, low-dose

effects were detected, which is remarkably common in studies of endocrine-disrupting chemicals (EDCs)(Vandenberg et al. 2012). This indicated that biospectroscopy has capability to detect such a response. Similarly, the four types CNPs (C60, long and short MWCNTs, SWCNTs) could induce significant dose-dependent alterations in A549 cell population (Chapter 4), which were interrogated by both ATR-FTIR and surface-enhanced Raman spectroscopy. Moreover, the dose-related effects *in vivo* were more complex. The alterations in tissues, including gill, brain, liver and gonad, of zebrafish induced by the four types CNPs with exposure duration of 21 days were determined by ATR-FTIR, with complement of Raman (Chapter 2). Although no evidence showed the transportation of CNPs into brain and gonad, significant biochemical alterations were observed, which may involve in physiologically-based toxic-kinetics and required further investigations.

In general, biopsectroscopy showed powerful ability of detecting the biochemical alterations induced by CNPs both *in vitro* and *in vivo* at a ppb level, which is real-world or closer to the realistic scenario.

3. Insight into the mechanism underlying the nanotoxicity of CNPs

Multivariate data-analysis approaches, such as PCA, PCA-LDA, possess ability to reduce data dimension and is capable to extract biomarkers corresponding for the biochemical alterations in samples. Loadings plot or cluster vector plot derived from PCA or PCA-LDA can be used in purpose to identify the biomarkers.

In this thesis, studies on MCF-7 cells showed that the spectra profiled the lipid and protein as the main target of CNPs toxicity, as cluster vector plot displayed that the most pronounced wavenumbers were related to lipid (~1750 cm^{-1}), amide I (~1650

cm^{-1}) and amino acid (~1400 cm^{-1}). This suggested CNPs may exert toxicity mainly at the outer site of cells. However, changes in the wavenumbers corresponding to DNA/RNA region were also observed, while cells in S-phase appeared to be more sensitive to genomic injure rather than those in G_0/G_1-phase. Additional evidence of CySS-to-protein ratio indicated that CNPs could elevate the reactive oxygen species (ROS) in cell, which is considered as the predominant mechanism for nanotoxicity, and could possibly exert toxicity onto the cellular internal material, including the DNA/RNA (namely, genotoxicity) (Fu et al. 2014) (Chapter 2).

Loadings plots of Spectral dataset from *in vitro* experiment on A549 cells (Chapter 4) profiled that segregations between the exposed groups and the control one were mostly resulted from lipid and protein region (~1750-1400 cm^{-1}), while DNA/RNA region was slightly affected; it means nanotoxicity of CNPs were mainly activated at the sites of lipid and protein, which was consist with the results in Chapter 3. Additional experiments also determined that CNPs were possibly of capability to elevate global genomic methylation level in A549 cells, which implied the risk of cancer for CNPs exposure. In this experiment SERS also proved to be an ultra-sensitivity technique for biological analysis.

For risk assessment, *in vitro* models are insufficient to alone predict potential hazard for human. Thus zebrafish was employed as an animal model for investigation of nanotoxicity with a chronic exposure (Chapter 3).The gill, as the initial site for CNPs exposure directly contact with CNPs and presented an obvious response to the CNPs treatment, while biochemical alterations were mainly located in protein and lipid. By contrast, alterations in the main metabolic organ of liver were not only limited to lipid and protein, but also involving in the genomic level. Brain and the gonad were the

most concerned sites, since brain acts as a control centre for the whole body, and any biochemical alteration in brain could potentially lead to neuro-dysfunction diseases, while gonad plays a key role in fertility. However, the spectral dataset highlighted that both these two organs were significantly affected by the CNPs exposure, though there were blood-brain barrier (BBB) and blood-gonad barrier (BGB) existing to protect the two organs respectively. Moreover there appeared to be obvious alterations of DNA/RNA in brain and gonad, which gave raise to high risk of genotoxicity in these two sites.

Among the four tested CNPs, long MWCNTs was likely to result in the most pronounced alterations A549 cells, but not in MCF-7, where C60 induced the highest extent of alterations. This is possible because of the different cell lines employed in the experiments. However, all biological models displayed a similar toxic action mode of CNPs.

4. Predicting effects of CNPs interacting with PAHs in cells

When CNPs were released to environment, it will possibly encounter other contamination compounds. The interaction between CNPs and other compounds may affect the biological impact of the CNP itself or the other pre-existing compounds, which is still largely unknown. The dose response relationship is commonly based on the single agent exposure, while cellular response to the co-exposure is difficult to predict. And there is always a debate existing on whether co-exposure of CNPs with other chemical compound will increase the bioavailability of the chemical compounds, or it can reduce the toxicity (Canesi et al.).

Two cell lines, gill cells and MCF-7 cells were employed to investigate the effects pf co-exposure (Chapter 5). Both cell lines showed a dose-response alterations resulted from the exposure of single agents. Infrared spectra highlighted that the B[*a*]P was of high-level genotoxicity, while C60 seems to be more toxic to lipid and protein rather than DNA/RNA. In this study, it was found that low dose of C60 could elevate the toxicity of B[*a*]P, while high concentration of C60 could limit the toxicity of B[*a*]P. In addition, it also interpreted binary test agents at such a low dose could enhance both toxic action mode of the two agents. This suggested the behaviour of such a coexisting mixture is more complex in the realistic environment and it is more unpredictable.

5. General conclusion and future recommendation

In this thesis, biospectroscopy, including both IR and Raman spectroscopy, coupled with computational analysis showed capability to detect biological alteration in subcellular level. Additionally, it was determined to be an excellent tool for naonotoxicity assessment especially at low dose. Moreover, infrared spectroscopy (ATR-FTIR and FTIR microscopy) can provides us global information of the biological samples, as well as Raman spectroscopy. Although SERS is likely to partially collect information from the cells, it turned to be highly sensitive. All methods showed capability of detecting dose–dependent toxicity of CNPs and successfully identified the biomarkers corresponding to the biochemical alterations.

Based on the recent results from this thesis, it would be important to introduce the real environmental condition to the Nanotoxicity assessment both *in vitro* and *in vivo*. It is also important to relate nanotoxicity with diseases, as our studies show that CNPs *in vitro* could cause hypermethylation and *in vivo* it exerted toxicity to brain and gonad regardless of BBB and BGB.

References

Canesi, L., Ciacci, C. and Balbi, T. Interactive effects of nanoparticles with other contaminants in aquatic organisms: Friend or foe? Mar. Environ. Res.

Diem, M., Boydston-White, S. and Chiriboga, L. 1999. Infrared Spectroscopy of Cells and Tissues: Shining Light onto a novel Subject. Appl. Spectrosc. 53, 148A-161A.

Fu, P.P., Xia, Q., Hwang, H.-M., Ray, P.C. and Yu, H. 2014. Mechanisms of nanotoxicity: Generation of reactive oxygen species. J. Food Drug Anal. 22, 64-75.

Matthäus, C., Chernenko, T., Newmark, J.A., Warner, C.M. and Diem, M. 2007. Label-Free Detection of Mitochondrial Distribution in Cells by Nonresonant Raman Microspectroscopy. Biophys. J. 93, 668-673.

Rozman, K.K. and Doull, J. 2000. Dose and time as variables of toxicity. Toxicology 144, 169-178.

Vandenberg, L.N., Colborn, T., Hayes, T.B., Heindel, J.J., David R. Jacobs, J., Lee, D.-H., Shioda, T., Soto, A.M., Saal, F.S.v., Welshons, W.V., Zoeller, R.T. and Myers, J.P. 2012. Hormones and Endocrine-Disrupting Chemicals: Low-Dose Effects and Nonmonotonic Dose Responses. Endocr. Rev. 33, 378-455.

Walsh, M.J., German, M.J., Singh, M., Pollock, H.M., Hammiche, A., Kyrgiou, M., Stringfellow, H.F., Paraskevaidis, E., Martin-Hirsch, P.L. and Martin, F.L. 2007. IR microspectroscopy: potential applications in cervical cancer screening. Cancer Lett. 246, 1-11.

Wood, B.R., Chiriboga, L., Yee, H., Quinn, M.A., McNaughton, D. and Diem, M. 2004. Fourier transform infrared (FTIR) spectral mapping of the cervical transformation zone, and dysplastic squamous epithelium. Gynecol. Oncol. 93, 59-68.

Bibliography

Aiken, G.R., Hsu-Kim, H. and Ryan, J.N. 2011. Influence of Dissolved Organic Matter on the Environmental Fate of Metals, Nanoparticles, and Colloids. Environ. Sci. Technol. 45, 3196-3201.

Albrecht, M.G. and Creighton, J.A. 1977. Anomalously intense Raman spectra of pyridine at a silver electrode. J. Am. Chem. Soc. 99, 5215-5217.

An, H. and Jin, B. 2011. DNA Exposure to Buckminsterfullerene (C60): Toward DNA Stability, Reactivity, and Replication. Environ. Sci. Technol. 45, 6608-6616.

Andrus, P.G. 2006. Cancer monitoring by FTIR spectroscopy. Technol Cancer Res Treat 5, 157-167.

Aschberger, K., Johnston, H.J., Stone, V., Aitken, R.J., Tran, C.L., Hankin, S.M., Peters, S.A.K. and Christensen, F.M. 2010. Review of fullerene toxicity and exposure – Appraisal of a human health risk assessment, based on open literature. Regul. Toxicol. Pharmacol. 58, 455-473.

Aschberger, K., Micheletti, C., Sokull-Klüttgen, B. and Christensen, F.M. 2011. Analysis of currently available data for characterising the risk of engineered nanomaterials to the environment and human health — Lessons learned from four case studies. Environ. Int. 37, 1143-1156.

Azevedo Costa, C.L., Chaves, I.S., Ventura-Lima, J., Ferreira, J.L.R., Ferraz, L., de Carvalho, L.M. and Monserrat, J.M. 2012. In vitro evaluation of co-exposure of arsenium and an organic nanomaterial (fullerene, C60) in zebrafish hepatocytes. Comp. Biochem. Physiol., Part C: Toxicol. Pharmacol. 155, 206-212.

Bagchi, D., Bagchi, M., Hassoun, E.A. and Stohs, S.J. 1995. In vitro and in vivo generation of reactive oxygen species, DNA damage and lactate dehydrogenase leakage by selected pesticides. Toxicology 104, 129-140.

Bai, Y., Zhang, Y., Zhang, J., Mu, Q., Zhang, W., Butch, E.R., Snyder, S.E. and Yan, B. 2010. Repeated administrations of carbon nanotubes in male mice cause reversible testis damage without affecting fertility. Nat Nano 5, 683-689.

Baird, W.M., Hooven, L.A. and Mahadevan, B. 2005. Carcinogenic polycyclic aromatic hydrocarbon-DNA adducts and mechanism of action. Environ. Mol. Mutagen. 45, 106-114.

Baker, M.J., Trevisan, J., Bassan, P., Bhargava, R., Butler, H.J., Dorling, K.M., Fielden, P.R., Fogarty, S.W., Fullwood, N.J., Heys, K.A., Hughes, C., Lasch, P., Martin-Hirsch, P.L., Obinaju, B., Sockalingum, G.D., Sulé-Suso, J., Strong, R.J., Walsh, M.J., Wood, B.R., Gardner, P. and Martin, F.L. 2014. Using Fourier transform IR spectroscopy to analyze biological materials. Nat. Protocols 9, 1771-1791.

Bakry, R., Vallant, R.M., Najam-ul-Haq, M., Rainer, M., Szabo, Z., Huck, C.W. and Bonn, G.K. 2007a. Medicinal applications of fullerenes. Int. J. Nanomed. 2, 639-649.

Bardi, G., Nunes, A., Gherardini, L., Bates, K., Al-Jamal, K.T., Gaillard, C., Prato, M., Bianco, A., Pizzorusso, T. and Kostarelos, K. 2013. Functionalized Carbon Nanotubes in the Brain: Cellular Internalization and Neuroinflammatory Responses. PLoS ONE 8, e80964.

Baughman, R.H., Zakhidov, A.A. and de Heer, W.A. 2002. Carbon Nanotubes--the Route Toward Applications. Science 297, 787-792.

Baun, A., Sørensen, S.N., Rasmussen, R.F., Hartmann, N.B. and Koch, C.B. 2008. Toxicity and bioaccumulation of xenobiotic organic compounds in the presence of aqueous suspensions of aggregates of nano-C60. Aquat. Toxicol. 86, 379-387.

Becheri, A., Dürr, M., Lo Nostro, P. and Baglioni, P. 2008. Synthesis and characterization of zinc oxide nanoparticles: application to textiles as UV-absorbers. J. Nanopart. Res. 10, 679-689.

Bello, D., Wardle, B., Yamamoto, N., Guzman deVilloria, R., Garcia, E., Hart, A., Ahn, K., Ellenbecker, M. and Hallock, M. 2009. Exposure to nanoscale particles and fibers during machining of hybrid advanced composites containing carbon nanotubes. J. Nanopart. Res. 11, 231-249.

Benn, T.M. and Westerhoff, P. 2008. Nanoparticle Silver Released into Water from Commercially Available Sock Fabrics. Environ. Sci. Technol. 42, 4133-4139.

Benton, S., Liang, Z., Hao, L., Liang, Y., Hebbar, G., Jones, D., Coopersmith, C. and Ziegler, T. 2012. Differential regulation of tissue thiol-disulfide redox status in a murine model of peritonitis. J. Inflamm. 9, 1-6.

Bhargava, R. 2012. Infrared Spectroscopic Imaging: The Next Generation. Appl. Spectrosc. 66, 1091-1120.

Bianco, A., Kostarelos, K. and Prato, M. 2005. Applications of carbon nanotubes in drug delivery. Curr. Opin. Chem. Biol. 9, 674-679.

Bihari, P., Vippola, M., Schultes, S., Praetner, M., Khandoga, A.G., Reichel, C.A., Coester, C., Tuomi, T., Rehberg, M. and Krombach, F. 2008. Optimized dispersion of nanoparticles for biological in vitro and in vivo studies. Part. Fibre Toxicol. 5, 14.

Bock, K.W. 1994. Aryl hydrocarbon or dioxin receptor: Biologic and toxic responses. Reviews of Physiology, Biochemistry and Pharmacology, Volume 125, Springer Berlin Heidelberg, pp. 1-42.

Bottini, M., Bruckner, S., Nika, K., Bottini, N., Bellucci, S., Magrini, A., Bergamaschi, A. and Mustelin, T. 2006. Multi-walled carbon nanotubes induce T lymphocyte apoptosis. Toxicol. Lett. 160, 121-126.

Bouwmeester, H., Lynch, I., marvin, H.J.P., Dawson, K.A., Berges, M., Braguer, D., Byrne, H.J., Casey, A., Chambers, G., Clift, M.J.D., Elia, G., Fernandes, T.F., Fjellsbø, L.B., Hatto, P., Juillerat, L., Klein, C., Kreyling, W.G., Nickel, C., Riediker, M. and Stone, V. 2011. Minimal analytical characterization of engineered nanomaterials needed for hazard assessment in biological matrices. Nanotoxicology 5, 1-11.

Brant, J., Lecoanet, H., Hotze, M. and Wiesner, M. 2005. Comparison of Electrokinetic Properties of Colloidal Fullerenes (n-C60) Formed Using Two Procedures†. Environ. Sci. Technol. 39, 6343-6351.

Brittijn, S.A., Duivesteijn, S.J., Belmamoune, M., Bertens, L.F.M., Bitter, W., de Bruijn, J.D., Champagne, D.L., Cuppen, E., Flik, G., Vandenbroucke-Grauls, C.M., Janssen, R.A.J., de Jong, I.M.L., de Kloet, E.R., Kros, A., Meijer, A.H., Metz, J.R., van der Sar, A.M., Schaaf, M.J.M., Schulte-Merker, S., Spaink, H.P., Tak, P.P.,

Verbeek, F.J., Vervoordeldonk, M.J., Vonk, F.J., Witte, F., Yuan, H. and Richardson, M.K. 2009. Zebrafish development and regeneration: new tools for biomedical research. Int. J. Dev. Biol. 53, 835-850.

Buford, M., Hamilton, R., Jr. and Holian, A. 2007. A comparison of dispersing media for various engineered carbon nanoparticles. Part. Fibre Toxicol. 4, 1-9.

Cabiscol, E., Tamarit, J. and Ros, J. 2010. Oxidative stress in bacteria and protein damage by reactive oxygen species. Int. Microbiol. 3, 3-8.

Calabrese, E.J. and Baldwin, L.A. 1998. A general classification of U-shaped dose-response relationships in toxicology and their mechanistic foundations. Hum. Exp. Toxicol. 17, 353-364.

Camden, J.P., Dieringer, J.A., Wang, Y., Masiello, D.J., Marks, L.D., Schatz, G.C. and Van Duyne, R.P. 2008. Probing the Structure of Single-Molecule Surface-Enhanced Raman Scattering Hot Spots. J. Am. Chem. Soc. 130, 12616-12617.

Campion, A. and Kambhampati, P. 1998. Surface-enhanced Raman scattering. Chem. Soc. Rev. 27, 241-250.

Canesi, L., Ciacci, C. and Balbi, T. Interactive effects of nanoparticles with other contaminants in aquatic organisms: Friend or foe? Mar. Environ. Res.

Cao, Y., Jin, R. and Mirkin, C.A. 2001. DNA-modified core-shell Ag/Au nanoparticles. J. Am. Chem. Soc. 123, 7961-7962.

Casey, A., Herzog, E., Davoren, M., Lyng, F., Byrne, H. and Chambers, G. 2007. Spectroscopic analysis confirms the interaction between SWCNT and various dyes commonly used to assess cytotoxicity. Carbon 45, 1425 - 1432.

Castaño, A. and Becerril, C. 2004. In vitro assessment of DNA damage after short- and long-term exposure to benzo(a)pyrene using RAPD and the RTG-2 fish cell line. Mutat. Res., Fundam. Mol. Mech. Mutagen. 552, 141-151.

Chatgilialoglu, C., Ferreri, C., Melchiorre, M., Sansone, A. and Torreggiani, A. 2013. Lipid Geometrical Isomerism: From Chemistry to Biology and Diagnostics. Chem. Rev. 114, 255-284.

Cheng, J., Chan, C.M., Veca, L.M., Poon, W.L., Chan, P.K., Qu, L., Sun, Y.-P. and Cheng, S.H. 2009. Acute and long-term effects after single loading of functionalized multi-walled carbon nanotubes into zebrafish (Danio rerio). Toxicol. Appl. Pharmacol. 235, 216-225.

Chłopek, J., Czajkowska, B., Szaraniec, B., Frackowiak, E., Szostak, K. and Béguin, F. 2006. In vitro studies of carbon nanotubes biocompatibility. Carbon 44, 1106-1111.

Cho, W.J., Kim, Y. and Kim, J.K. 2012. Ultrahigh-Density Array of Silver Nanoclusters for SERS Substrate with High Sensitivity and Excellent Reproducibility. ACS Nano 6, 249-255.

Christian, P., Von der Kammer, F., Baalousha, M. and Hofmann, T. 2008. Nanoparticles: structure, properties, preparation and behaviour in environmental media. Ecotoxicology 17, 326-343.

Circu, M.L. and Aw, T.Y. 2010. Reactive oxygen species, cellular redox systems, and apoptosis. Free Radic. Biol. Med. 48, 749-762.

Clift, M.D., Gehr, P. and Rothen-Rutishauser, B. 2011. Nanotoxicology: a perspective and discussion of whether or not in vitro testing is a valid alternative. Arch. Toxicol. 85, 723-731.

Corte, L., Rellini, P., Roscini, L., Fatichenti, F. and Cardinali, G. 2010. Development of a novel, FTIR (Fourier transform infrared spectroscopy) based, yeast bioassay for toxicity testing and stress response study. Anal. Chim. Acta 659, 258-265.

Crane, M., Handy, R., Garrod, J. and Owen, R. 2008. Ecotoxicity test methods and environmental hazard assessment for engineered nanoparticles. Ecotoxicology 17, 421-437.

Crouzier, D., Follot, S., Gentilhomme, E., Flahaut, E., Arnaud, R., Dabouis, V., Castellarin, C. and Debouzy, J.C. 2010. Carbon nanotubes induce inflammation but decrease the production of reactive oxygen species in lung. Toxicology 272, 39-45.

Cui, L., Chen, P., Chen, S., Yuan, Z., Yu, C., Ren, B. and Zhang, K. 2013. In Situ Study of the Antibacterial Activity and Mechanism of Action of Silver

Nanoparticles by Surface-Enhanced Raman Spectroscopy. Anal. Chem. 85, 5436-5443.

Cui, L., Yao, M., Ren, B. and Zhang, K.-S. 2011. Sensitive and Versatile Detection of the Fouling Process and Fouling Propensity of Proteins on Polyvinylidene Fluoride Membranes via Surface-Enhanced Raman Spectroscopy. Anal. Chem. 83, 1709-1716.

Das, P.M. and Singal, R. 2004. DNA Methylation and Cancer. J. Clin. Oncol. 22, 4632-4642.

Davoren, M., Herzog, E., Casey, A., Cottineau, B., Chambers, G., Byrne, H.J. and Lyng, F.M. 2007. In vitro toxicity evaluation of single walled carbon nanotubes on human A549 lung cells. Toxicol. In Vitro 21, 438-448.

Deguchi, S., Alargova, R.G. and Tsujii, K. 2001. Stable Dispersions of Fullerenes, C60 and C70, in Water. Preparation and Characterization. Langmuir 17, 6013-6017.

Dhawan, A. and Sharma, V. 2010. Toxicity assessment of nanomaterials: methods and challenges. Anal. Bioanal. Chem. 398, 589-605.

Dhawan, A., Taurozzi, J.S., Pandey, A.K., Shan, W., Miller, S.M., Hashsham, S.A. and Tarabara, V.V. 2006. Stable Colloidal Dispersions of C60 Fullerenes in Water: Evidence for Genotoxicity†. Environ. Sci. Technol. 40, 7394-7401.

Diem, M., Boydston-White, S. and Chiriboga, L. 1999. Infrared Spectroscopy of Cells and Tissues: Shining Light onto a novel Subject. Appl. Spectrosc. 53, 148A-161A.

Edgington, A.J., Roberts, A.P., Taylor, L.M., Alloy, M.M., Reppert, J., Rao, A.M., Mao, J. and Klaine, S.J. 2010. The influence of natural organic matter on the toxicity of multiwalled carbon nanotubes. Environ. Toxicol. Chem. 29, 2511-2518.

Ehrlich, M. 2002. DNA methylation in cancer: too much, but also too little. Oncogene 21, 5400-5413.

Ellis, D.I. and Goodacre, R. 2006. Metabolic fingerprinting in disease diagnosis: biomedical applications of infrared and Raman spectroscopy. Analyst 131, 875-885.

Elsaesser, A. and Howard, C.V. 2012. Toxicology of nanoparticles. Adv. Drug Del. Rev. 64, 129-137.

Ema, M., Kobayashi, N., Naya, M., Hanai, S. and Nakanishi, J. 2010. Reproductive and developmental toxicity studies of manufactured nanomaterials. Reprod. Toxicol. 30, 343-352.

Esteller, M. and Herman, J.G. 2002. Cancer as an epigenetic disease: DNA methylation and chromatin alterations in human tumours. J. Pathol. 196, 1-7.

Fan, W., Cui, M., Liu, H., Wang, C., Shi, Z., Tan, C. and Yang, X. 2011. Nano-TiO2 enhances the toxicity of copper in natural water to Daphnia magna. Environ. Pollut. 159, 729-734.

Ferreira, J.L.R., Lonné, M.N., Fran ça, T.A., Maximilla, N.R., Lugokenski, T.H., Costa, P.G., Fillmann, G., Antunes Soares, F.A., de la Torre, F.R. and Monserrat, J.M. 2014. Co-exposure of the organic nanomaterial fullerene C60 with benzo[a]pyrene in Danio rerio (zebrafish) hepatocytes: Evidence of toxicological interactions. Aquat. Toxicol. 147, 76-83.

Folkmann, J.K., Risom, L., Jacobsen, N.R., Wallin, H., Loft, S. and Møller, P. 2009. Oxidatively damaged DNA in rats exposed by oral gavage to C60 fullerenes and single-walled carbon nanotubes. Environ. Health Perspect. 117, 703-708.

Foucaud, L., Wilson, M.R., Brown, D.M. and Stone, V. 2007. Measurement of reactive species production by nanoparticles prepared in biologically relevant media. Toxicol. Lett. 174, 1-9.

Fraser, T.W.K., Reinardy, H.C., Shaw, B.J., Henry, T.B. and Handy, R.D. 2011. Dietary toxicity of single-walled carbon nanotubes and fullerenes (C60) in rainbow trout (Oncorhynchus mykiss). Nanotoxicology 5, 98-108.

Fu, P.P., Xia, Q., Hwang, H.-M., Ray, P.C. and Yu, H. 2014. Mechanisms of nanotoxicity: Generation of reactive oxygen species. J. Food Drug Anal. 22, 64-75.

Ganesh, R., Smeraldi, J., Hosseini, T., Khatib, L., Olson, B.H. and Rosso, D. 2010. Evaluation of Nanocopper Removal and Toxicity in Municipal Wastewaters. Environ. Sci. Technol. 44, 7808-7813.

Gautam, R., Vanga, S., Ariese, F. and Umapathy, S. 2015. Review of multidimensional data processing approaches for Raman and infrared spectroscopy. EPJ Techn Instrum 2, 1-38.

Girault, I., Tozlu, S., Lidereau, R. and Bièche, I. 2003. Expression Analysis of DNA Methyltransferases 1, 3A, and 3B in Sporadic Breast Carcinomas. Clin. Cancer Res. 9, 4415-4422.

Girifalco, L.A. and Hodak, M. 2002. Van der Waals binding energies in graphitic structures. Physical Review B 65, 125404.

Girifalco, L.A., Hodak, M. and Lee, R.S. 2000. Carbon nanotubes, buckyballs, ropes, and a universal graphitic potential. Phys. Rev. B 62, 13104-13110.

Go, Y.-M. and Jones, D.P. 2008. Redox compartmentalization in eukaryotic cells. Biochim. Biophys. Acta, Gen. Subj. 1780, 1273-1290.

Go, Y.-M., Park, H., Koval, M., Orr, M., Reed, M., Liang, Y., Smith, D., Pohl, J. and Jones, D.P. 2010. A key role for mitochondria in endothelial signaling by plasma cysteine/cystine redox potential. Free Radic. Biol. Med. 48, 275-283.

Gonzalez, L., Lison, D. and Kirsch-Volders, M. 2008. Genotoxicity of engineered nanomaterials: A critical review. Nanotoxicology 2, 252-273.

Gooding, J.J. 2005. Nanostructuring electrodes with carbon nanotubes: A review on electrochemistry and applications for sensing. Electrochim. Acta 50, 3049-3060.

Gottschalk, F. and Nowack, B. 2011. The release of engineered nanomaterials to the environment. J. Environ. Monit. 13, 1145-1155.

Gottschalk, F., Sonderer, T., Scholz, R.W. and Nowack, B. 2009. Modeled Environmental Concentrations of Engineered Nanomaterials (TiO2, ZnO, Ag, CNT, Fullerenes) for Different Regions. Environ. Sci. Technol. 43, 9216-9222.

Griveau, J.F., Dumont, E., Renard, P., Callegari, J.P. and Le Lannou, D. 1995. Reactive oxygen species, lipid peroxidation and enzymatic defence systems in human spermatozoa. J. Reprod. Fertil. 103, 17-26.

Halliwell, B. 1991. Reactive oxygen species in living systems: Source, biochemistry, and role in human disease. Am. J. Med. 91, S14-S22.

Hassellöv, M., Readman, J., Ranville, J. and Tiede, K. 2008. Nanoparticle analysis and characterization methodologies in environmental risk assessment of engineered nanoparticles. Ecotoxicology 17, 344-361.

Henry, T.B., Menn, F.-M., Fleming, J.T., Wilgus, J., Compton, R.N. and Sayler, G.S. 2007. Attributing Effects of Aqueous C60 Nano-Aggregates to Tetrahydrofuran Decomposition Products in Larval Zebrafish by Assessment of Gene Expression. Environ. Health Perspect. 115, 1059-1065.

Henry, T.B., Petersen, E.J. and Compton, R.N. 2011. Aqueous fullerene aggregates (nC60) generate minimal reactive oxygen species and are of low toxicity in fish: a revision of previous reports. Curr. Opin. Biotechnol. 22, 533-537.

Henry, T.B., Wileman, S.J., Boran, H. and Sutton, P. 2013. Association of Hg2+ with Aqueous (C60)n Aggregates Facilitates Increased Bioavailability of Hg2+ in Zebrafish (Danio rerio). Environ. Sci. Technol. 47, 9997-10004.

Heraud, P., Wood, B.R., Beardall, J. and McNaughton, D. 2006. Effects of pre-processing of Raman spectra on in vivo classification of nutrient status of microalgal cells. J. Chemom. 20, 193-197.

Hering, K., Cialla, D., Ackermann, K., Dörfer, T., Möller, R., Schneidewind, H., Mattheis, R., Fritzsche, W., Rösch, P. and Popp, J. 2008. SERS: a versatile tool in chemical and biochemical diagnostics. Anal. Bioanal. Chem. 390, 113-124.

Hirano, S., Kanno, S. and Furuyama, A. 2008. Multi-walled carbon nanotubes injure the plasma membrane of macrophages. Toxicol. Appl. Pharmacol. 232, 244-251.

Hirschmugl, C.J. and Gough, K.M. 2012. Fourier Transform Infrared Spectrochemical Imaging: Review of Design and Applications with a Focal Plane Array and Multiple Beam Synchrotron Radiation Source. Appl. Spectrosc. 66, 475-491.

Holder, A.L., Goth-Goldstein, R., Lucas, D. and Koshland, C.P. 2012. Particle-Induced Artifacts in the MTT and LDH Viability Assays. Chem. Res. Toxicol. 25, 1885-1892.

Huang, J., Zhang, L., Chen, B., Ji, N., Chen, F., Zhang, Y. and Zhang, Z. 2010. Nanocomposites of size-controlled gold nanoparticles and graphene oxide: Formation and applications in SERS and catalysis. Nanoscale 2, 2733-2738.

Huang, Q., Zhang, J., Luo, L., Wang, X., Wang, X., Alamdar, A., Peng, S., Liu, L., Tian, M. and Shen, H. 2015. Metabolomics reveals disturbed metabolic pathways in human lung epithelial cells exposed to airborne fine particulate matter. Toxicol. Res. 4, 939-947.

Hughes, G.A. 2005. Nanostructure-mediated drug delivery. Nanomed. Nanotechnol. Biol. Med. 1, 22-30.

Hungerbuehler, H., Guldi, D.M. and Asmus, K.D. 1993. Incorporation of C60 into artificial lipid membranes. J. Am. Chem. Soc. 115, 3386-3387.

Hurt, R.H., Monthioux, M. and Kane, A. 2006. Toxicology of carbon nanomaterials: Status, trends, and perspectives on the special issue. Carbon 44, 1028-1033.

Jeanmaire, D.L. and Van Duyne, R.P. 1977. Surface Raman spectroelectrochemistry: Part I. Heterocyclic, aromatic, and aliphatic amines adsorbed on the anodized silver electrode. J. Electroanal. Chem. Interfacial Electrochem. 84, 1-20.

Jensen, A.W., Wilson, S.R. and Schuster, D.I. 1996. Biological applications of fullerenes. Biorg. Med. Chem. 4, 767-779.

Jia, G., Wang, H., Yan, L., Wang, X., Pei, R., Yan, T., Zhao, Y. and Guo, X. 2005. Cytotoxicity of Carbon Nanomaterials: Single-Wall Nanotube, Multi-Wall Nanotube, and Fullerene. Environ. Sci. Technol. 39, 1378-1383.

Jiang, J., Oberdörster, G. and Biswas, P. 2009. Characterization of size, surface charge, and agglomeration state of nanoparticle dispersions for toxicological studies. J. Nanopart. Res. 11, 77-89.

Jiao, H., Allinson, S.L., Walsh, M.J., Hewitt, R., Cole, K.J., Phillips, D.H. and Martin, F.L. 2007. Growth kinetics in MCF-7 cells modulate benzo[a]pyrene-induced CYP1A1 up-regulation. Mutagenesis 22, 111-116.

Johnston, H., Pojana, G., Zuin, S., Jacobsen, N.R., Møller, P., Loft, S., Semmler-Behnke, M., McGuiness, C., Balharry, D., Marcomini, A., Wallin, H., Kreyling, W., Donaldson, K., Tran, L. and Stone, V. 2013. Engineered nanomaterial risk. Lessons learnt from completed nanotoxicology studies: potential solutions to current and future challenges. Crit. Rev. Toxicol. 43, 1-20.

Kahru, A. and Dubourguier, H.-C. 2010. From ecotoxicology to nanoecotoxicology. Toxicology 269, 105-119.

Katz, E. and Willner, I. 2004. Biomolecule-Functionalized Carbon Nanotubes: Applications in Nanobioelectronics. ChemPhysChem 5, 1084-1104.

Kayat, J., Gajbhiye, V., Tekade, R.K. and Jain, N.K. 2011. Pulmonary toxicity of carbon nanotubes: a systematic report. Nanomed. Nanotechnol. Biol. Med. 7, 40-49.

Kazarian, S.G. and Chan, K.L.A. 2010. Micro- and Macro-Attenuated Total Reflection Fourier Transform Infrared Spectroscopic Imaging. Appl. Spectrosc. 64, 135A-152A.

Kazarian, S.G. and Chan, K.L.A. 2013. ATR-FTIR spectroscopic imaging: recent advances and applications to biological systems. Analyst 138, 1940-1951.

Keller, A.A., Wang, H., Zhou, D., Lenihan, H.S., Cherr, G., Cardinale, B.J., Miller, R. and Ji, Z. 2010. Stability and Aggregation of Metal Oxide Nanoparticles in Natural Aqueous Matrices. Environ. Sci. Technol. 44, 1962-1967.

Kelly, J.G., Trevisan, J.l., Scott, A.D., Carmichael, P.L., Pollock, H.M., Martin-Hirsch, P.L. and Martin, F.L. 2011. Biospectroscopy to metabolically profile biomolecular structure: a multistage approach linking computational analysis with biomarkers. J. Proteome Res. 10, 1437-1448.

Kemsley, E.K. 1996. Discriminant analysis of high-dimensional data: a comparison of principal components analysis and partial least squares data reduction methods. Chemometrics Intellig. Lab. Syst. 33, 47-61.

Kim, J., Song, K., Lee, J. and Yu, I. 2011. Evaluation of biocompatible dispersants for carbon nanotube toxicity tests. Arch. Toxicol. 85, 1499-1508.

Kiser, M.A., Ryu, H., Jang, H., Hristovski, K. and Westerhoff, P. 2010. Biosorption of nanoparticles to heterotrophic wastewater biomass. Water Res. 44, 4105-4114.

Kneipp, K., Kneipp, H., Itzkan, I., Dasari, R.R. and Feld, M.S. 1999. Ultrasensitive Chemical Analysis by Raman Spectroscopy. Chem. Rev. 99, 2957-2976.

Kneipp, K., Wang, Y., Kneipp, H., Perelman, L.T., Itzkan, I., Dasari, R.R. and Feld, M.S. 1997. Single Molecule Detection Using Surface-Enhanced Raman Scattering (SERS). Phys. Rev. Lett. 78, 1667-1670.

Krafft, C., Steiner, G., Beleites, C. and Salzer, R. 2009. Disease recognition by infrared and Raman spectroscopy. J. Biophotonics 2, 13-28.

Kroll, A., Pillukat, M., Hahn, D. and Schnekenburger, J. 2012. Interference of engineered nanoparticles with in vitro toxicity assays. Arch. Toxicol. 86, 1123-1136.

Kroll, A., Pillukat, M.H., Hahn, D. and Schnekenburger, J. 2009. Current in vitro methods in nanoparticle risk assessment: Limitations and challenges. Eur. J. Pharm. Biopharm. 72, 370-377.

Kulakovich, O., Strekal, N., Yaroshevich, A., Maskevich, S., Gaponenko, S., Nabiev, I., Woggon, U. and Artemyev, M. 2002. Enhanced Luminescence of CdSe Quantum Dots on Gold Colloids. Nano Lett. 2, 1449-1452.

Lam, C.-w., James, J.T., McCluskey, R., Arepalli, S. and Hunter, R.L. 2006. A Review of Carbon Nanotube Toxicity and Assessment of Potential Occupational and Environmental Health Risks. Crit. Rev. Toxicol. 36, 189-217.

Lasch, P. 2012. Spectral pre-processing for biomedical vibrational spectroscopy and microspectroscopic imaging. Chemometrics Intellig. Lab. Syst. 117, 100-114.

Lehto, M., Karilainen, T., Róg, T., Cramariuc, O., Vanhala, E., Tornaeus, J., Taberman, H., Jänis, J., Alenius, H., Vattulainen, I. and Laine, O. 2014. Co-Exposure

with Fullerene May Strengthen Health Effects of Organic Industrial Chemicals. PLoS ONE 9, e114490.

Lewinski, N., Colvin, V. and Drezek, R. 2008. Cytotoxicity of nanoparticles. Small 4, 26-49.

Li, J., Strong, R., Trevisan, J., Fogarty, S.W., Fullwood, N.J., Jones, K.C. and Martin, F.L. 2013. Dose-Related Alterations of Carbon Nanoparticles in Mammalian Cells Detected Using Biospectroscopy: Potential for Real-World Effects. Environ. Sci. Technol. 47, 10005-10011.

Li, J., Ying, G.-G., Jones, K.C. and Martin, F.L. 2015a. Real-world carbon nanoparticle exposures induce brain and gonadal alterations in zebrafish (Danio rerio) as determined by biospectroscopy techniques. Analyst 140, 2687-2695.

Li, J.F., Huang, Y.F., Ding, Y., Yang, Z.L., Li, S.B., Zhou, X.S., Fan, F.R., Zhang, W., Zhou, Z.Y., WuDe, Y., Ren, B., Wang, Z.L. and Tian, Z.Q. 2010. Shell-isolated nanoparticle-enhanced Raman spectroscopy. Nature 464, 392-395.

Li, S. and Dai, L. 2011. An Improved Algorithm to Remove Cosmic Spikes in Raman Spectra for Online Monitoring. Appl. Spectrosc. 65, 1300-1306.

Li, X., Gámiz, B., Wang, Y., Pignatello, J.J. and Xing, B. 2015b. Competitive Sorption Used To Probe Strong Hydrogen Bonding Sites for Weak Organic Acids on Carbon Nanotubes. Environ. Sci. Technol.

Limbach, L.K., Wick, P., Manser, P., Grass, R.N., Bruinink, A. and Stark, W.J. 2007. Exposure of Engineered Nanoparticles to Human Lung Epithelial Cells: Influence of Chemical Composition and Catalytic Activity on Oxidative Stress. Environ. Sci. Technol. 41, 4158-4163.

Liu, A., Sun, K., Yang, J. and Zhao, D. 2008. Toxicological effects of multi-wall carbon nanotubes in rats. J. Nanopart. Res. 10, 1303-1307.

Liu, K.-Z., Tsang, K.S., Li, C.K., Shaw, R.A. and Mantsch, H.H. 2003. Infrared Spectroscopic Identification of β-Thalassemia. Clin. Chem. 49, 1125-1132.

Liu, Z., Tabakman, S., Welsher, K. and Dai, H. 2009. Carbon nanotubes in biology and medicine: In vitro and in vivo detection, imaging and drug delivery. Nano Research 2, 85-120.

Llabjani, V., Crosse, J.D., Ahmadzai, A.A., Patel, I.I., Pang, W., Trevisan, J., Jones, K.C., Shore, R.F. and Martin, F.L. 2011a. Differential Effects in Mammalian Cells Induced by Chemical Mixtures in Environmental Biota As Profiled Using Infrared Spectroscopy. Environ. Sci. Technol. 45, 10706-10712.

Llabjani, V., Jones, K.C., Thomas, G.O., Walker, L.A., Shore, R.F. and Martin, F.L. 2009. Polybrominated Diphenyl Ether-Associated Alterations in Cell Biochemistry as Determined by Attenuated Total Reflection Fourier-Transform Infrared Spectroscopy: a Comparison with DNA-Reactive and/or Endocrine-Disrupting Agents. Environ. Sci. Technol. 43, 3356-3364.

Llabjani, V., Trevisan, J., Jones, K.C., Shore, R.F. and Martin, F.L. 2010. Binary Mixture Effects by PBDE Congeners (47, 153, 183, or 209) and PCB Congeners (126 or 153) in MCF-7 Cells: Biochemical Alterations Assessed by IR Spectroscopy and Multivariate Analysis. Environ. Sci. Technol. 44, 3992-3998.

Llabjani, V., Trevisan, J., Jones, K.C., Shore, R.F. and Martin, F.L. 2011b. Derivation by Infrared Spectroscopy with Multivariate Analysis of Bimodal Contaminant-Induced Dose-Response Effects in MCF-7 Cells. Environ. Sci. Technol. 45, 6129-6135.

Lovern, S.B. and Klaper, R. 2006. Daphnia magna mortality when exposed to titanium dioxide and fullerene (C60) nanoparticles. Environ. Toxicol. Chem. 25, 1132-1137.

Lowry, G.V., Gregory, K.B., Apte, S.C. and Lead, J.R. 2012. Transformations of Nanomaterials in the Environment. Environ. Sci. Technol. 46, 6893-6899.

Lu, Y., Yin, Y., Li, Z.-Y. and Xia, Y. 2002. Synthesis and Self-Assembly of Au@SiO2 Core−Shell Colloids. Nano Lett. 2, 785-788.

Ma, H., Zheng, L., Li, Y., Pan, S., Hu, J., Yu, Z., Zhang, G., Sheng, G. and Fu, J. 2013. Triclosan reduces the levels of global DNA methylation in HepG2 cells. Chemosphere 90, 1023-1029.

Ma, K.L., Ruan, X.Z., Powis, S.H., Chen, Y., Moorhead, J.F. and Varghese, Z. 2008. Inflammatory stress exacerbates lipid accumulation in hepatic cells and fatty livers of apolipoprotein E knockout mice. Hepatology 48, 770-781.

Madni, I., Hwang, C.-Y., Park, S.-D., Choa, Y.-H. and Kim, H.-T. 2010. Mixed surfactant system for stable suspension of multiwalled carbon nanotubes. Colloids Surf. Physicochem. Eng. Aspects 358, 101-107.

Manna, S.K., Sarkar, S., Barr, J., Wise, K., Barrera, E.V., Jejelowo, O., Rice-Ficht, A.C. and Ramesh, G.T. 2005. Single-Walled Carbon Nanotube Induces Oxidative Stress and Activates Nuclear Transcription Factor-κB in Human Keratinocytes. Nano Lett. 5, 1676-1684.

Martin, F.L., German, M.J., Wit, E., Fearn, T., Ragavan, N. and Pollock, H.M. 2007. Identifying Variables Responsible for Clustering in Discriminant Analysis of Data from Infrared Microspectroscopy of a Biological Sample. J. Comput. Biol. 14, 1176-1184.

Martin, F.L., Kelly, J.G., Llabjani, V., Martin-Hirsch, P.L., Patel, I.I., Trevisan, J., Fullwood, N.J. and Walsh, M.J. 2010. Distinguishing cell types or populations based on the computational analysis of their infrared spectra. Nat. Protocols 5, 1748-1760.

Matsuda, S., Matsui, S., Shimizu, Y. and Matsuda, T. 2011. Genotoxicity of Colloidal Fullerene C60. Environ. Sci. Technol. 45, 4133-4138.

Matthäus, C., Chernenko, T., Newmark, J.A., Warner, C.M. and Diem, M. 2007. Label-Free Detection of Mitochondrial Distribution in Cells by Nonresonant Raman Microspectroscopy. Biophys. J. 93, 668-673.

Mauter, M.S. and Elimelech, M. 2008. Environmental Applications of Carbon-Based Nanomaterials. Environ. Sci. Technol. 42, 5843-5859.

Maynard, A.D., Baron, P.A., Foley, M., Shvedova, A.A., Kisin, E.R. and Castranova, V. 2004. Exposure to Carbon Nanotube Material: Aerosol Release During the Handling of Unrefined Single-Walled Carbon Nanotube Material. J. Toxicol. Environ. Health, A 67, 87-107.

Mazet, V., Carteret, C., Brie, D., Idier, J. and Humbert, B. 2005. Background removal from spectra by designing and minimising a non-quadratic cost function. Chemometrics Intellig. Lab. Syst. 76, 121-133.

McHedlov-Petrossyan, N.O. 2013. Fullerenes in Liquid Media: An Unsettling Intrusion into the Solution Chemistry. Chem. Rev. 113, 5149-5193.

McNay, G., Eustace, D., Smith, W.E., Faulds, K. and Graham, D. 2011. Surface-Enhanced Raman Scattering (SERS) and Surface-Enhanced Resonance Raman Scattering (SERRS): A Review of Applications. Appl. Spectrosc. 65, 825-837.

Meng, H., Xia, T., George, S. and Nel, A.E. 2009. A Predictive Toxicological Paradigm for the Safety Assessment of Nanomaterials. ACS Nano 3, 1620-1627.

Miller, L.M. and Dumas, P. 2006. Chemical imaging of biological tissue with synchrotron infrared light. Biochim. Biophys. Acta, Biomembr. 1758, 846-857.

Monteiro-Riviere, N.A. and Inman, A.O. 2006. Challenges for assessing carbon nanomaterial toxicity to the skin. Carbon 44, 1070-1078.

Monteiro-Riviere, N.A., Inman, A.O. and Zhang, L.W. 2009. Limitations and relative utility of screening assays to assess engineered nanoparticle toxicity in a human cell line. Toxicol. Appl. Pharmacol. 234, 222-235.

Montellano, A., Da Ros, T., Bianco, A. and Prato, M. 2011. Fullerene C60 as a multifunctional system for drug and gene delivery. Nanoscale 3, 4035-4041.

Moore, M.N. 2006. Do nanoparticles present ecotoxicological risks for the health of the aquatic environment? Environ. Int. 32, 967-976.

Mosier-Boss, P.A., Lieberman, S.H. and Newbery, R. 1995. Fluorescence Rejection in Raman Spectroscopy by Shifted-Spectra, Edge Detection, and FFT Filtering Techniques. Appl. Spectrosc. 49, 630-638.

Moskovits, M. 1985. Surface-enhanced spectroscopy. Rev. Mod. Phys. 57, 783-826.

Mourant, J.R., Yamada, Y.R., Carpenter, S., Dominique, L.R. and Freyer, J.P. 2003. FTIR Spectroscopy Demonstrates Biochemical Differences in Mammalian Cell Cultures at Different Growth Stages. Biophys. J. 85, 1938-1947.

Muller, J., Huaux, F., Moreau, N., Misson, P., Heilier, J.-F., Delos, M., Arras, M., Fonseca, A., Nagy, J.B. and Lison, D. 2005. Respiratory toxicity of multi-wall carbon nanotubes. Toxicol. Appl. Pharmacol. 207, 221-231.

Nasse, M.J., Walsh, M.J., Mattson, E.C., Reininger, R., Kajdacsy-Balla, A., Macias, V., Bhargava, R. and Hirschmugl, C.J. 2011. High-resolution Fourier-transform infrared chemical imaging with multiple synchrotron beams. Nat Meth 8, 413-416.

Naumann, D. 2008. FT-IR spectroscopy of microorganisms at the Robert Koch Institute: experiences gained during a successful project. pp. 68530G-68530G-68512.

Navarro, E., Baun, A., Behra, R., Hartmann, N., Filser, J., Miao, A.-J., Quigg, A., Santschi, P. and Sigg, L. 2008. Environmental behavior and ecotoxicity of engineered nanoparticles to algae, plants, and fungi. Ecotoxicology 17, 372-386.

Nebert, D.W. and Dalton, T.P. 2006. The role of cytochrome P450 enzymes in endogenous signalling pathways and environmental carcinogenesis. Nat. Rev. Cancer 6, 947-960.

Nel, A., Xia, T., Mädler, L. and Li, N. 2006. Toxic Potential of Materials at the Nanolevel. Science 311, 622-627.

Nel, A., Xia, T., Meng, H., Wang, X., Lin, S., Ji, Z. and Zhang, H. 2012. Nanomaterial Toxicity Testing in the 21st Century: Use of a Predictive Toxicological Approach and High-Throughput Screening. Acc. Chem. Res. 46, 607-621.

Nel, A.E., Madler, L., Velegol, D., Xia, T., Hoek, E.M.V., Somasundaran, P., Klaessig, F., Castranova, V. and Thompson, M. 2009. Understanding biophysicochemical interactions at the nano-bio interface. Nat Mater 8, 543-557.

Nowack, B. and Bucheli, T.D. 2007. Occurrence, behavior and effects of nanoparticles in the environment. Environ. Pollut. 150, 5-22.

Oberdörster, E. 2004. Manufactured nanomaterials (fullerenes, C60) induce oxidative stress in the brain of juvenile largemouth bass. Environ. Health Perspect. 112, 1058-1062.

Oberdörster, G., Oberdörster, E. and Oberdörster, J. 2005. Nanotoxicology: an emerging discipline evolving from studies of ultrafine particles. Environ. Health Perspect., 823-839.

Oberley, T.D., Schultz, J.L., Li, N. and Oberley, L.W. 1995. Antioxidant enzyme levels as a function of growth state in cell culture. Free Radic. Biol. Med. 19, 53-65.

Péry, A.R.R., Devillers, J., Brochot, C., Mombelli, E., Palluel, O., Piccini, B., Brion, F. and Beaudouin, R. 2013. A Physiologically Based Toxicokinetic Model for the Zebrafish Danio rerio. Environ. Sci. Technol. 48, 781-790.

Pan, B., Lin, D., Mashayekhi, H. and Xing, B. 2008. Adsorption and Hysteresis of Bisphenol A and 17α-Ethinyl Estradiol on Carbon Nanomaterials. Environ. Sci. Technol. 42, 5480-5485.

Pan, B. and Xing, B. 2008. Adsorption Mechanisms of Organic Chemicals on Carbon Nanotubes. Environ. Sci. Technol. 42, 9005-9013.

Pang, W., Li, J., Ahmadzai, A.A., Heppenstall, L.D., Llabjani, V., Trevisan, J., Qiu, X. and Martin, F.L. 2012. Identification of benzo[a]pyrene-induced cell cycle-associated alterations in MCF-7 cells using infrared spectroscopy with computational analysis. Toxicology 298, 24-29.

Park, J.-W., Henry, T.B., Ard, S., Menn, F.-M., Compton, R.N. and Sayler, G.S. 2011. The association between nC60 and 17α-ethinylestradiol (EE2) decreases EE2 bioavailability in zebrafish and alters nanoaggregate characteristics. Nanotoxicology 5, 406-416.

Park, J.-W., Henry, T.B., Menn, F.-M., Compton, R.N. and Sayler, G. 2010. No bioavailability of 17α-ethinylestradiol when associated with nC60 aggregates during dietary exposure in adult male zebrafish (Danio rerio). Chemosphere 81, 1227-1232.

Patel, I.I., Trevisan, J., Evans, G., Llabjani, V., Martin-Hirsch, P.L., Stringfellow, H.F. and Martin, F.L. 2011. High contrast images of uterine tissue derived using Raman microspectroscopy with the empty modelling approach of multivariate curve resolution-alternating least squares. Analyst 136, 4950-4959.

Peng, S.-Y., Zhang, J., Tian, M.-P., Wang, Z.-L. and Shen, H.-Q. 2012. Determination of Global DNA Methylation in Biological Samples by Liquid Chromatography-Tandem Mass Spectrometry. Chinese J. Anal. Chem. 40, 1201-1206.

Petersen, E.J. and Henry, T.B. 2012. Methodological considerations for testing the ecotoxicity of carbon nanotubes and fullerenes: Review. Environ. Toxicol. Chem. 31, 60-72.

Petersen, E.J., Pinto, R.A., Mai, D.J., Landrum, P.F. and Weber, W.J. 2011a. Influence of Polyethyleneimine Graftings of Multi-Walled Carbon Nanotubes on their Accumulation and Elimination by and Toxicity to Daphnia magna. Environ. Sci. Technol. 45, 1133-1138.

Petersen, E.J., Zhang, L., Mattison, N.T., O'Carroll, D.M., Whelton, A.J., Uddin, N., Nguyen, T., Huang, Q., Henry, T.B., Holbrook, R.D. and Chen, K.L. 2011b. Potential Release Pathways, Environmental Fate, And Ecological Risks of Carbon Nanotubes. Environ. Sci. Technol. 45, 9837-9856.

Pietroiusti, A., Campagnolo, L. and Fadeel, B. 2013. Interactions of Engineered Nanoparticles with Organs Protected by Internal Biological Barriers. Small 9, 1557-1572.

Planeix, J.M., Coustel, N., Coq, B., Brotons, V., Kumbhar, P.S., Dutartre, R., Geneste, P., Bernier, P. and Ajayan, P.M. 1994. Application of Carbon Nanotubes as Supports in Heterogeneous Catalysis. J. Am. Chem. Soc. 116, 7935-7936.

Porter, D., Sriram, K., Wolfarth, M., Jefferson, A., Schwegler-Berry, D., Andrew, M.E. and Castranova, V. 2008. A biocompatible medium for nanoparticle dispersion. Nanotoxicology 2, 144-154.

Powers, K.W., Palazuelos, M., Moudgil, B.M. and Roberts, S.M. 2007. Characterization of the size, shape, and state of dispersion of nanoparticles for toxicological studies. Nanotoxicology 1, 42-51.

Quagliano, L.G. 2004. Observation of Molecules Adsorbed on III-V Semiconductor Quantum Dots by Surface-Enhanced Raman Scattering. J. Am. Chem. Soc. 126, 7393-7398.

Ren, L. and Zhong, W. 2010. Oxidation Reactions Mediated by Single-Walled Carbon Nanotubes in Aqueous Solution. Environ. Sci. Technol. 44, 6954-6958.

Ren, W., Fang, Y. and Wang, E. 2011. A Binary Functional Substrate for Enrichment and Ultrasensitive SERS Spectroscopic Detection of Folic Acid Using Graphene Oxide/Ag Nanoparticle Hybrids. ACS Nano 5, 6425-6433.

Riding, M.J., Martin, F.L., Trevisan, J., Llabjani, V., Patel, I.I., Jones, K.C. and Semple, K.T. 2012a. Concentration-dependent effects of carbon nanoparticles in gram-negative bacteria determined by infrared spectroscopy with multivariate analysis. Environ. Pollut. 163, 226-234.

Riding, M.J., Trevisan, J., Hirschmugl, C.J., Jones, K.C., Semple, K.T. and Martin, F.L. 2012b. Mechanistic insights into nanotoxicity determined by synchrotron radiation-based Fourier-transform infrared imaging and multivariate analysis. Environ. Int. 50, 56-65.

Robertson, K.D. 2005. DNA methylation and human disease. Nat Rev Genet 6, 597-610.

Rozman, K.K. and Doull, J. 2000. Dose and time as variables of toxicity. Toxicology 144, 169-178.

Sager, T.M., Porter, D.W., Robinson, V.A., Lindsley, W.G., Schwegler-Berry, D.E. and Castranova, V. 2007. Improved method to disperse nanoparticles for in vitro and in vivo investigation of toxicity. Nanotoxicology 1, 118-129.

Sahu, R.K., Argov, S., Salman, A., Huleihel, M., Grossman, N., Hammody, Z., Kapelushnik, J. and Mordechai, S. 2004. Characteristic Absorbance of Nucleic Acids in the Mid-IR Region as Possible Common Biomarkers for Diagnosis of Malignancy. Technol Cancer Res Treat 3, 629-638.

Sato, Y., Yokoyama, A., Shibata, K.-i., Akimoto, Y., Ogino, S.-i., Nodasaka, Y., Kohgo, T., Tamura, K., Akasaka, T., Uo, M., Motomiya, K., Jeyadevan, B., Ishiguro, M., Hatakeyama, R., Watari, F. and Tohji, K. 2005. Influence of length on cytotoxicity of multi-walled carbon nanotubes against human acute monocytic leukemia cell line THP-1 in vitro and subcutaneous tissue of rats in vivo. Mol. BioSyst. 1, 176-182.

Savolainen, K., Alenius, H., Norppa, H., Tuomi, T. and Kasper, G. 2010. Risk assessment of engineered nanomaterials and nanotechnologies--a review. Toxicology 269, 92-104.

Sayes, C.M., Reed, K.L. and Warheit, D.B. 2007. Assessing Toxicity of Fine and Nanoparticles: Comparing In Vitro Measurements to In Vivo Pulmonary Toxicity Profiles. Toxicol. Sci. 97, 163-180.

Schirmer, K., Chan, A.G.J., Greenberg, B.M., Dixon, D.G. and Bols, N.C. 1997. Methodology for demonstrating and measuring the photocytotoxicity of fluoranthene to fish cells in culture. Toxicol. In Vitro 11, 107-119.

Schuster, G.B. 2000. Long-Range Charge Transfer in DNA: Transient Structural Distortions Control the Distance Dependence. Acc. Chem. Res. 33, 253-260.

Segner, H. 2009. Zebrafish (Danio rerio) as a model organism for investigating endocrine disruption. Comp. Biochem. Physiol., Part C: Toxicol. Pharmacol. 149, 187-195.

Serpone, N., Dondi, D. and Albini, A. 2007. Inorganic and organic UV filters: Their role and efficacy in sunscreens and suncare products. Inorg. Chim. Acta 360, 794-802.

Sharma, B., Frontiera, R.R., Henry, A.-I., Ringe, E. and Van Duyne, R.P. 2012. SERS: Materials, applications, and the future. Mater. Today 15, 16-25.

Shi, H., Hudson, L.G. and Liu, K.J. 2004. Oxidative stress and apoptosis in metal ion-induced carcinogenesis. Free Radic. Biol. Med. 37, 582-593.

Shin, H. and Markey, M.K. 2006. A machine learning perspective on the development of clinical decision support systems utilizing mass spectra of blood samples. J. Biomed. Inf. 39, 227-248.

Shinohara, N., Matsumoto, K., Endoh, S., Maru, J. and Nakanishi, J. 2009. In vitro and in vivo genotoxicity tests on fullerene C60 nanoparticles. Toxicol. Lett. 191, 289-296.

Shvedova, A.A., Pietroiusti, A., Fadeel, B. and Kagan, V.E. 2012. Mechanisms of carbon nanotube-induced toxicity: Focus on oxidative stress. Toxicol. Appl. Pharmacol. 261, 121-133.

Simon-Deckers, A., Loo, S., Mayne-L'hermite, M., Herlin-Boime, N., Menguy, N., Reynaud, C., Gouget, B. and Carrière, M. 2009. Size-, Composition- and Shape-Dependent Toxicological Impact of Metal Oxide Nanoparticles and Carbon Nanotubes toward Bacteria. Environ. Sci. Technol. 43, 8423-8429.

Simon, A., Maletz, S.X., Hollert, H., Schäffer, A. and Maes, H.M. 2014. Effects of multiwalled carbon nanotubes and triclocarban on several eukaryotic cell lines: elucidating cytotoxicity, endocrine disruption, and reactive oxygen species generation. Nanoscale Res Lett, p. 396.

Simon, H.U., Haj-Yehia, A. and Levi-Schaffer, F. 2000. Role of reactive oxygen species (ROS) in apoptosis induction. Apoptosis 5, 415-418.

Singh, R. and Lillard Jr, J.W. 2009. Nanoparticle-based targeted drug delivery. Exp. Mol. Pathol. 86, 215-223.

Smith, C.J., Shaw, B.J. and Handy, R.D. 2007. Toxicity of single walled carbon nanotubes to rainbow trout, (Oncorhynchus mykiss): Respiratory toxicity, organ pathologies, and other physiological effects. Aquat. Toxicol. 82, 94-109.

Song, M., Wang, F., Zeng, L., Yin, J., Wang, H. and Jiang, G. 2014. Co-exposure of Carboxyl-Functionalized Single-Walled Carbon Nanotubes and 17α-Ethinylestradiol in Cultured Cells: Effects on Bioactivity and Cytotoxicity. Environ. Sci. Technol. 48, 13978-13984.

Spohn, P., Hirsch, C., Hasler, F., Bruinink, A., Krug, H.F. and Wick, P. 2009. C60 fullerene: A powerful antioxidant or a damaging agent? The importance of an in-depth material characterization prior to toxicity assays. Environ. Pollut. 157, 1134-1139.

Srogi, K. 2007. Monitoring of environmental exposure to polycyclic aromatic hydrocarbons: a review. Environ Chem Lett 5, 169-195.

Stiles, P.L., Dieringer, J.A., Shah, N.C. and Van Duyne, R.P. 2008. Surface-Enhanced Raman Spectroscopy. Annu. Rev. Anal. Chem. 1, 601-626.

Su, Y., Yan, X., Pu, Y., Xiao, F., Wang, D. and Yang, M. 2013. Risks of Single-Walled Carbon Nanotubes Acting as Contaminants-Carriers: Potential Release of Phenanthrene in Japanese Medaka (Oryzias latipes). Environ. Sci. Technol. 47, 4704-4710.

Tanneberger, K., Rico-Rico, A., Kramer, N.I., Busser, F.J.M., Hermens, J.L.M. and Schirmer, K. 2010. Effects of Solvents and Dosing Procedure on Chemical Toxicity in Cell-Based in Vitro Assays. Environ. Sci. Technol. 44, 4775-4781.

Tervonen, K., Waissi, G., Petersen, E.J., Akkanen, J. and Kukkonen, J.V.K. 2010. Analysis of fullerene-C60 and kinetic measurements for its accumulation and depuration in Daphnia magna. Environ. Toxicol. Chem. 29, 1072-1078.

Tian, M., Peng, S., Martin, F.L., Zhang, J., Liu, L., Wang, Z., Dong, S. and Shen, H. 2012. Perfluorooctanoic acid induces gene promoter hypermethylation of glutathione-S-transferase Pi in human liver L02 cells. Toxicology 296, 48-55.

Tong, Z., Bischoff, M., Nies, L., Applegate, B. and Turco, R.F. 2007. Impact of Fullerene (C60) on a Soil Microbial Community. Environ. Sci. Technol. 41, 2985-2991.

Trevisan, J., Angelov, P.P., Carmichael, P.L., Scott, A.D. and Martin, F.L. 2012. Extracting biological information with computational analysis of Fourier-transform infrared (FTIR) biospectroscopy datasets: current practices to future perspectives. Analyst 137, 3202-3215.

Trevisan, J., Angelov, P.P., Patel, I.I., Najand, G.M., Cheung, K.T., Llabjani, V., Pollock, H.M., Bruce, S.W., Pant, K., Carmichael, P.L., Scott, A.D. and Martin, F.L. 2010. Syrian hamster embryo (SHE) assay (pH 6.7) coupled with infrared spectroscopy and chemometrics towards toxicological assessment. Analyst 135, 3266-3272.

Trevisan, J., Angelov, P.P., Scott, A.D., Carmichael, P.L. and Martin, F.L. 2013. IRootLab: a free and open-source MATLAB toolbox for vibrational biospectroscopy data analysis. Bioinformatics 29, 1095-1097.

Turrens, J.F. 2003. Mitochondrial formation of reactive oxygen species. J. Physiol. 552, 335-344.

Vandenberg, L.N., Colborn, T., Hayes, T.B., Heindel, J.J., David R. Jacobs, J., Lee, D.-H., Shioda, T., Soto, A.M., Saal, F.S.v., Welshons, W.V., Zoeller, R.T. and Myers, J.P. 2012. Hormones and Endocrine-Disrupting Chemicals: Low-Dose Effects and Nonmonotonic Dose Responses. Endocr. Rev. 33, 378-455.

Vippola, M., Falck, G., Lindberg, H., Suhonen, S., Vanhala, E., Norppa, H., Savolainen, K., Tossavainen, A. and Tuomi, T. 2009. Preparation of nanoparticle dispersions for in-vitro toxicity testing. Hum. Exp. Toxicol. 28, 377-385.

Wörle-Knirsch, J.M., Pulskamp, K. and Krug, H.F. 2006. Oops They Did It Again! Carbon Nanotubes Hoax Scientists in Viability Assays. Nano Lett. 6, 1261-1268.

Walker, P.A., Bury, N.R. and Hogstrand, C. 2007. Influence of Culture Conditions on Metal-Induced Responses in a Cultured Rainbow Trout Gill Epithelium. Environ. Sci. Technol. 41, 6505-6513.

Walsh, M.J., Fellous, T.G., Hammiche, A., Lin, W.-R., Fullwood, N.J., Grude, O., Bahrami, F., Nicholson, J.M., Cotte, M., Susini, J., Pollock, H.M., Brittan, M., Martin-Hirsch, P.L., Alison, M.R. and Martin, F.L. 2008. Fourier Transform Infrared Microspectroscopy Identifies Symmetric PO2− Modifications as a Marker of the Putative Stem Cell Region of Human Intestinal Crypts. Stem Cells 26, 108-118.

Walsh, M.J., German, M.J., Singh, M., Pollock, H.M., Hammiche, A., Kyrgiou, M., Stringfellow, H.F., Paraskevaidis, E., Martin-Hirsch, P.L. and Martin, F.L. 2007. IR microspectroscopy: potential applications in cervical cancer screening. Cancer Lett. 246, 1-11.

Wang, F., Jin, C., Liang, H., Tang, Y., Zhang, H. and Yang, Y. 2014. Effects of fullerene C60 nanoparticles on A549 cells. Environ. Toxicol. Pharmacol. 37, 656-661.

Wang, L., Castranova, V., Mishra, A., Chen, B., Mercer, R.R., Schwegler-Berry, D. and Rojanasakul, Y. 2010. Dispersion of single-walled carbon nanotubes by a natural lung surfactant for pulmonary in vitro and in vivo toxicity studies. Part. Fibre Toxicol. 7, 31.

Wang, L. and Mizaikoff, B. 2008. Application of multivariate data-analysis techniques to biomedical diagnostics based on mid-infrared spectroscopy. Anal. Bioanal. Chem. 391, 1641-1654.

Wang, X., Zhang, J., Huang, Q., Alamdar, A., Tian, M., Liu, L. and Shen, H. 2015. Serum metabolomics analysis reveals impaired lipid metabolism in rats after oral exposure to benzo[*a*]pyrene. Mol. BioSyst. 11, 753-759.

Wang, Y., Becker, M., Wang, L., Liu, J., Scholz, R., Peng, J., Gösele, U., Christiansen, S., Kim, D.H. and Steinhart, M. 2009. Nanostructured Gold Films for SERS by Block Copolymer-Templated Galvanic Displacement Reactions. Nano Lett. 9, 2384-2389.

Warheit, D.B. 2006. What is currently known about the health risks related to carbon nanotube exposures? Carbon 44, 1064-1069.

Warheit, D.B., Laurence, B.R., Reed, K.L., Roach, D.H., Reynolds, G.A.M. and Webb, T.R. 2004. Comparative Pulmonary Toxicity Assessment of Single-wall Carbon Nanotubes in Rats. Toxicol. Sci. 77, 117-125.

Warheit, D.B., Sayes, C.M. and Reed, K.L. 2009. Nanoscale and Fine Zinc Oxide Particles: Can in Vitro Assays Accurately Forecast Lung Hazards following Inhalation Exposures? Environ. Sci. Technol. 43, 7939-7945.

Westerhuis, J.A., Kourti, T. and MacGregor, J.F. 1998. Analysis of multiblock and hierarchical PCA and PLS models. J. Chemom. 12, 301-321.

Win-Shwe, T.-T. and Fujimaki, H. 2011. Nanoparticles and Neurotoxicity. Int. J. Mol. Sci. 12, 6267-6280.

Wohlleben, W., Brill, S., Meier, M.W., Mertler, M., Cox, G., Hirth, S., von Vacano, B., Strauss, V., Treumann, S., Wiench, K., Ma-Hock, L. and Landsiedel, R. 2011. On the Lifecycle of Nanocomposites: Comparing Released Fragments and their In-Vivo Hazards from Three Release Mechanisms and Four Nanocomposites. Small 7, 2384-2395.

Wood, B.R., Chiriboga, L., Yee, H., Quinn, M.A., McNaughton, D. and Diem, M. 2004. Fourier transform infrared (FTIR) spectral mapping of the cervical transformation zone, and dysplastic squamous epithelium. Gynecol. Oncol. 93, 59-68.

Wu, H., Volponi, J.V., Oliver, A.E., Parikh, A.N., Simmons, B.A. and Singh, S. 2011. In vivo lipidomics using single-cell Raman spectroscopy. Proc. Natl. Acad. Sci. U. S. A. 108, 3809-3814.

Xia, Q., Yin, J.J., Cherng, S.-H., Wamer, W.G., Boudreau, M., Howard, P.C. and Fu, P.P. 2006. UVA photoirradiation of retinyl palmitate—Formation of singlet oxygen and superoxide, and their role in induction of lipid peroxidation. Toxicol. Lett. 163, 30-43.

Xia, X.R., Monteiro-Riviere, N.A. and Riviere, J.E. 2010. Intrinsic biological property of colloidal fullerene nanoparticles (nC60): Lack of lethality after high dose exposure to human epidermal and bacterial cells. Toxicol. Lett. 197, 128-134.

Xu, X., Wang, X., Li, Y., Wang, Y. and Yang, L. 2012. A large-scale association study for nanoparticle C60 uncovers mechanisms of nanotoxicity disrupting the native conformations of DNA/RNA. Nucleic Acids Res. 40, 7622-7632.

Xue, W. and Warshawsky, D. 2005. Metabolic activation of polycyclic and heterocyclic aromatic hydrocarbons and DNA damage: A review. Toxicol. Appl. Pharmacol. 206, 73-93.

Yang, K., Zhu, L. and Xing, B. 2006. Adsorption of Polycyclic Aromatic Hydrocarbons by Carbon Nanomaterials. Environ. Sci. Technol. 40, 1855-1861.

Yang, X.Y., Edelmann, R.E. and Oris, J.T. 2010. Suspended C60 nanoparticles protect against short-term UV and fluoranthene photo-induced toxicity, but cause long-term cellular damage in Daphnia magna. Aquat. Toxicol. 100, 202-210.

Zakharian, T.Y., Seryshev, A., Sitharaman, B., Gilbert, B.E., Knight, V. and Wilson, L.J. 2005. A Fullerene−Paclitaxel Chemotherapeutic: Synthesis, Characterization, and Study of Biological Activity in Tissue Culture. J. Am. Chem. Soc. 127, 12508-12509.

Zhang, D. and Ben-Amotz, D. 2002. Removal of Cosmic Spikes from Hyper-spectral Images Using a Hybrid Upper-Bound Spectrum Method. Appl. Spectrosc. 56, 91-98.

Zhang, Y., Chen, Y., Westerhoff, P. and Crittenden, J. 2009. Impact of natural organic matter and divalent cations on the stability of aqueous nanoparticles. Water Res. 43, 4249-4257.

Zhang, Z., Xu, F., Yang, W., Guo, M., Wang, X., Zhang, B. and Tang, J. 2011. A facile one-pot method to high-quality Ag-graphene composite nanosheets for efficient surface-enhanced Raman scattering. Chem. Commun. 47, 6440-6442.

Zhao, J. 2003. Image Curvature Correction and Cosmic Removal for High-Throughput Dispersive Raman Spectroscopy. Appl. Spectrosc. 57, 1368-1375.

Zhao, J., Lui, H., McLean, D.I. and Zeng, H. 2007. Automated Autofluorescence Background Subtraction Algorithm for Biomedical Raman Spectroscopy. Appl. Spectrosc. 61, 1225-1232.

Zhu, S., Oberdörster, E. and Haasch, M.L. 2006. Toxicity of an engineered nanoparticle (fullerene, C60) in two aquatic species, Daphnia and fathead minnow. Mar. Environ. Res. 62, Supplement 1, S5-S9.

Appendix 1

Identification of benzo[*a*]pyrene-induced cell cycle-associated alterations in MCF-7 cells using infrared spectroscopy with computational analysis

Weiyi Pang, **Junyi Li**, Abdullah A. Ahmadzai, Lara D. Heppenstall, Valon Llabjani, Júlio Trevisan, Xiaoqiang Qiu, Francis L. Martin

Toxocology, 2012, *298*, (1–3), 24-29

Contribution:

- I acquired the samples required for the project together with Weiyi;
- I prepared processed and acquired all the data and carried out computational analysis with Weiyi.

…… ……

Junyi Li Prof. Francis L. Martin

Toxicology 298 (2012) 24–29

Contents lists available at SciVerse ScienceDirect

Toxicology

journal homepage: www.elsevier.com/locate/toxicol

Identification of benzo[*a*]pyrene-induced cell cycle-associated alterations in MCF-7 cells using infrared spectroscopy with computational analysis

Weiyi Pang[a,b], Junyi Li[b], Abdullah A. Ahmadzai[b], Lara D. Heppenstall[b], Valon Llabjani[b], Júlio Trevisan[b], Xiaoqiang Qiu[a,c,*], Francis L. Martin[b,**]

[a] *The School of Public Health, Guangxi Medical University, Nanning, Guangxi 530021, PR China*
[b] *Centre for Biophotonics, Lancaster Environment Centre, Lancaster University, Lancaster LA1 4YQ, United Kingdom*
[c] *The School of Public Health, Guilin Medical University, Guilin, Guangxi 541004, PR China*

ARTICLE INFO

Article history:
Received 5 March 2012
Received in revised form 6 April 2012
Accepted 19 April 2012
Available online 26 April 2012

Keywords:
ATR-FTIR spectroscopy
Benzo[*a*]pyrene
Cell cycle
Computational analysis
MCF-7 cells
PCA–LDA

ABSTRACT

Chemical contaminants, such as benzo[*a*]pyrene (B[*a*]P), may modulate transcriptional responses in cells *via* the activation of aryl hydrocarbon receptor (AhR) or through responses to DNA damage following adduct formation. Attenuated total reflection Fourier-transform infrared (ATR-FTIR) spectroscopy can be employed in a non-destructive fashion to interrogate the biochemical signature of cells *via* generation of infrared (IR) spectra. By applying to generated spectral datasets subsequent computational approaches such as principal component analysis plus linear discriminant analysis (PCA–LDA), derived data reduction is achieved to facilitate the visualization of wavenumber-related alterations in target cells. Discriminating spectral variables might be associated with lipid or glycogen content, conformational protein changes and phosphorylation, and structural alterations in DNA/RNA. Using this approach, we investigated the dose-related effects of B[*a*]P in MCF-7 cells concentrated in S- or G_0/G_1-phase. Our findings identified that in PCA–LDA scores plots a clear segregation of IR spectra was evident, with the major spectral alterations associated with DNA/RNA, secondary protein structure and lipid. Dose-related effects were observed and even with exposures as low as 10^{-9} M B[*a*]P, significant ($P \leq 0.001$) separation of B[*a*]P-treated *vs.* vehicle control cells was noted. ATR-FTIR spectroscopy with computational analysis is a novel approach to identify the effects of environmental contaminants in target cells.

1. Introduction

Benzo[*a*]pyrene (B[*a*]P) is an environmental pro-mutagenic and pro-carcinogenic contaminant derived mainly from tobacco smoke, automobile exhaust, industrial wastes and food products (Rubin, 2001; Boström et al., 2002). Although B[*a*]P itself does not exhibit carcinogenic activity, it is a potent ligand for the aryl hydrocarbon receptor (AhR), which may mediate teratogenic and carcinogenic effects of certain environmental pollutants (Birnbaum, 1994; Bock, 1994). B[*a*]P can bind to and activate AhR (Tsuchiya et al., 2003). The activated receptor is a key component of the B[*a*]P-induced target genes' expression response. Several target genes encode xenobiotic metabolizing enzymes involved in the bioactivation of B[*a*]P to its ultimate carcinogenic forms, mainly B[*a*]P-7,8-diol-9,10-epoxide (BPDE), which forms adducts with DNA (Shimizu et al., 2000; Shimada et al., 2003; Shimada, 2006).

Induced responses are associated with modification of genes and proteins involved in the regulation of a plethora of mechanisms including transcription, cell cycle, apoptosis, transport, signal transduction and metabolism (Yoshino et al., 2007; Shen et al., 2008). However, it is difficult to predict biological responses to low-dose exposures based on adverse effects induced by high concentrations (Martin, 2007). Attenuated total reflection Fourier-transform infrared (ATR-FTIR) spectroscopy is a tool that has been employed to examine biochemical effects of chemical contaminants in target cells and to fingerprint specific exposure patterns (Llabjani et al., 2010, 2011). Utilizing infrared (IR) spectroscopy, alterations in spectral variables (*i.e.*, wavenumbers) can reflect DNA adduct formation (Arakawa et al., 2001) or protein structure alterations (Kelly et al., 2009; Llabjani et al., 2009, 2010, 2011). ATR-FTIR

Abbreviations: AhR, aryl hydrocarbon receptor; $\nu_{as}PO_2^-$, asymmetric phosphate; ATR-FTIR, attenuated total reflection Fourier-transform infrared; B[*a*]P, benzo[*a*]pyrene; BPDE, B[*a*]P-7,8-diol-9,10-epoxide; IR, infrared; LD, linear discriminant; LDA, linear discriminant analysis; PC, principal component; PCA, principal component analysis; $\nu_sPO_2^-$, symmetric phosphate.

* Corresponding author at: The School of Public Health, Guangxi Medical University, Nanning, Guangxi 530021, PR China. Tel.: +86 0773 5895812; fax: +86 0773 5895812.
** Corresponding author at: Centre for Biophotonics, Lancaster Environment Centre, Lancaster University, Bailrigg, Lancaster LA1 4YQ, United Kingdom. Tel.: +44 1524 510206.
E-mail addresses: xqqiu9999@sina.com (X. Qiu), f.martin@lancaster.ac.uk (F.L. Martin).

0300-483X/$ – see front matter © 2012 Elsevier Ireland Ltd. All rights reserved.
http://dx.doi.org/10.1016/j.tox.2012.04.009

spectroscopy to address biological questions is based on the concept that biomolecules absorb in the mid-IR region ($\lambda = 2.5–25\ \mu m$) through the vibration of chemical bonds. These detected vibrations give rise to a detailed biomolecular fingerprint of the cells or tissue under investigation in the form of an IR spectrum relating to chemical structures (Petrich, 2001; Kelly et al., 2011).

IR spectroscopy experiments generate complex biochemical datasets containing hundreds or thousands of spectra, and exploratory analysis is best achieved by multivariate approaches such as principal component analysis (PCA) and/or linear discriminant analysis (LDA) (Martin et al., 2007). This allows for data reduction to facilitate the identification of wavenumber-related spectral alterations associated with glycogen content, lipid content, conformational protein changes and phosphorylation characteristics, and structural alterations in DNA/RNA (Martin et al., 2010).

In the current study, we employed ATR-FTIR spectroscopy with subsequent multivariate analysis (PCA–LDA) to investigate alterations in MCF-7 cells induced by various doses of B[*a*]P. Dose-related cell cycle-associated effects, especially high-dose *vs.* low-dose B[*a*]P compared to the corresponding vehicle control, were investigated to determine the magnitude of induced alterations. In addition, a growth-curve experiment was established to determine whether low-dose *vs.* high-dose B[*a*]P exposures differentially alter time-related cell number increases in culture. Traditionally, short-term assessments of genotoxicity have tested high-dose treatments, but how these reflect low-dose contaminant-induced effects consistent with background levels of human exposure (Hattemer-Frey and Travis, 1991) remains obscure. Methods capable of delineating and shedding light into relevant mechanisms of action of real-world exposures in target cells are urgently required.

2. Materials and methods

2.1. Chemicals

B[*a*]P and dimethylsulfoxide (DMSO) were obtained from Sigma Chemical Co. (Poole, Dorset, UK). Cell culture consumables were obtained from Invitrogen Life Technologies (Paisley, UK), unless otherwise stated.

2.2. Cell culture and treatment

Human breast cancer MCF-7 cells were cultured in Dulbecco's modified essential medium (DMEM) supplemented with 10% heat-inactivated foetal bovine serum, penicillin (100 U/mL), and streptomycin (100 μg/mL) in a humidified atmosphere with 5% CO_2 in air at 37 °C. Cells were disaggregated with trypsin (0.05%)/EDTA (0.02%) solution (inactivated with complete medium) before incorporation of cell aliquots for routine culture in T75 flasks. Towards experiments, MCF-7 cells were disaggregated, re-suspended in complete medium and then seeded in T25 flasks, whereupon they were concentrated in either S-phase (grown for 24-h) or G_0/G_1-phase (grown for 96-h) (Jiao et al., 2007) prior to treatment with or without test agent (25 μL stock solution/5 mL culture medium) for a further 24 h. Following treatment, cells were disaggregated into cell suspensions and immediately fixed with 70% ethanol (EtOH).

2.3. ATR-FTIR spectroscopy

Cellular material in 70% EtOH was applied to 1 cm × 1 cm Low-E-reflective glass microscope slides (Kevley Technologies, Chesterland, OH, USA) and allowed to air-dry prior to storage in marked 30-mm Petri dishes kept in a desiccated environment until analysis. IR spectra were obtained using a Bruker Vector 22 FTIR spectrometer with Helios ATR attachment containing a ≈250 μm × 250 μm aperture diamond crystal (Bruker Optics Ltd., Coventry, UK). The ATR crystal was cleaned with sodium dodecyl sulfate (SDS; Sigma Chemical Co.); a new background was taken prior to analysis of a new sample. Each experiment was independently repeated on three separate occasions over three months with duplicate flasks per experimental (*i.e.*, treatment) condition. From each treatment flask (generating one slide), 10 IR spectra (32 co-additions, ≈3.85 cm^{-1} wavenumber spacing, 2.2 kHz mirror speed) were acquired; thus, 60 IR spectra in total were collected per experimental condition.

2.4. Spectral processing and multivariate data analysis

Raw IR spectra obtained from interrogated samples were pre-processed prior to computational analysis. Initially, using OPUS software, IR spectra were individually cut to the biochemical-cell fingerprint region (1800–900 cm^{-1}). Subsequently, spectra were baseline-corrected and normalized to Amide I (1650 cm^{-1}). Following on, multivariate analysis (*i.e.*, PCA–LDA) was applied to the spectral dataset using MATLAB R2009a (The Maths Works, Natick, MA, USA) and a graphical user interface toolkit for spectroscopy (http://bioph.lancs.ac.uk/iroot). PCA allows for the reduction of the number of variables in the spectral dataset, whose small number of PCA factors [*i.e.*, principal components (PCs)] can capture >95% of the variance present in the original dataset (Llabjani et al., 2010). In this study, the first 10 or 20 PCs were used (Fearn, 2002). LDA is a data separation technique to maximize between-category variance over within-category variance of the output variables. PCA can be applied before LDA (thus "PCA–LDA") to reduce computational complexity, increase the recognition accuracy in different categories, and avoid LDA overfitting (Llabjani et al., 2009, 2010). Results were visualized through scores plots and cluster vector plots (Martin et al., 2007).

2.5. Statistical significance tests

To determine whether treatment groups were significantly different from the corresponding vehicle control, repeated-measures one-way analysis of variance (*ANOVA*) with Dunnett's *post hoc* tests were used to examine whether the contaminant-exposed categories observed along linear discriminant (LD)1 were significantly distinct; there was no need to transform data to meet the underlying assumptions of homogeneity of variance between categories and normality of residuals. A small *P*-value (generally below the most commonly used $\alpha = 0.05$) is considered to be statistically significant. In our case, if a significant difference between categories was obtained, it also suggests that one can proceed to the analysis of the corresponding cluster vectors to identify distinguishing regions of the IR spectrum that separate the treated cells from the corresponding vehicle control.

2.6. Determination of cell number

MCF-7 cells were seeded ($\approx 1.0 \times 10^5$) in T25 flasks and were grown for 24 h. This point was taken as time zero (T_0) and duplicate cell counts in triplicate flasks were acquired. These T_0 cell counts ($n = 6$) were averaged and normalized to 100% for the purposes of this experiment. Cells were then exposed to B[*a*]P at concentrations of 10^{-9} M or 10^{-6} M compared to vehicle control (*i.e.*, DMSO) in 5 mL of complete medium in triplicate flasks. Three independent experiments were conducted on separate occasions. Cells were washed, trypsinized, re-suspended and cell number determined at indicated time points employing a haemocytometer. Per flask, two independent cell counts (*i.e.*, one by each of two individuals) were acquired. The acquired values for each experimental condition were then averaged and these contributed to the mean ± SD of the three separate experiments. Results were expressed as relative cell number [%; *i.e.*, ratio of the cell number at indicated time point relative to that determined at T_0 (normalized to 100%) × 100].

3. Results

3.1. Dose–response effects of B[a]P

Throughout the biochemical-cell fingerprint region in the derived IR spectra, no clear differences between the different treatment categories are readily observed (data not shown) (Bi et al., 2007). Given the overlap of data and subtlety of the spectral variations between different treatment categories, exploratory multivariate analysis (*i.e.*, PCA–LDA) was carried out. Using this powerful discriminatory approach, each spectrum is converted into a single point in scores plots in which the best segregation, along with discriminating wavenumbers, can be identified. Two independent sets of experiments were conducted in which MCF-7 cells were cultured in the presence or absence of different concentrations of B[*a*]P. In Experimental set 1, alterations in MCF-7 cells concentrated in S-phase or G_0/G_1-phase of the cell cycle and treated for 24 h with the vehicle (*i.e.*, DMSO), 10^{-9} M, 10^{-8} M, 10^{-7} M, 10^{-6} M or 10^{-5} M B[*a*]P were investigated (Fig. 1).

Over the concentration range of B[*a*]P exposure, spectral points in scores plots representing cells treated with higher concentrations (10^{-6} M or 10^{-5} M) are more segregated from the corresponding vehicle control compared to those treated with lower levels, suggesting that dose-related effects were observed (Fig. 1). *ANOVA* tests indicate that all treatment categories are significantly ($P \leq 0.001$) different from the corresponding vehicle control (Table 1). Along LD1 of the cell-cycle associated scores plots, there is a clear positioning of spectral points from left to right related to

Table 1
P-values (≤) compared to corresponding vehicle control following analysis employing *ANOVA* with Dunnett's *post hoc* tests along LD1 in Fig. 1.

Statistical comparison	B[*a*]P concentration in MCF-7 culture				
	10^{-9} M	10^{-8} M	10^{-7} M	10^{-6} M	10^{-5} M
vs. vehicle control (Fig. 1A)	0.001	0.001	0.001	0.001	0.001
vs. vehicle control (Fig. 1B)	0.001	0.001	0.001	0.001	0.001

increasing B[*a*]P exposure. Interestingly, in these scores plots representing a comparison of six different treatment categories, clearer category segregation is noted with B[*a*]P-treated cells concentrated in G_0/G_1-phase (Fig. 1B) compared to those in S-phase (Fig. 1A). This is primarily because spectral points associated with low-dose treatment categories are more spread out in S-phase concentrated cells (Fig. 1A), possibly reflecting a more varied cell population (Jiao et al., 2007).

3.2. Effects of high-dose vs. low-dose B[a]P

In Experimental set 2, MCF-7 cells concentrated in S-phase or G_0/G_1-phase were treated for 24 h; corresponding vehicle control (DMSO) was compared to low-dose (10^{-9} M) or high-dose (10^{-6} M) B[*a*]P (Figs. 2 and 3). A comparison of Fig. 2 (representing MCF-7 cells concentrated in S-phase) and 3 (in G_0/G_1-phase) clearly shows that low- and high-dose B[*a*]P-induced different dose-related responses. Following 24-h exposure of cells concentrated in S-phase to 10^{-9} M B[*a*]P, a marked shift away from the corresponding vehicle control along LD2 but not LD1 is observed; along LD1 (which will capture the majority of variance), there is a clear segregation with no overlap of the vehicle control and 10^{-6} M B[*a*]P category (Fig. 2A). This suggests that low-dose B[*a*]P induces subtle underlying alterations in these exposed cells compared to the profound effects of high-dose treatment. In contrast, there is a clear dose-related shift of spectral points along LD1 for MCF-7 cells concentrated in G_0/G_1-phase (Fig. 3A). PCA–LDA scores plots exhibit an obvious discrimination following exposure of cells concentrated in G_0/G_1-phase, but the marked segregation of categories amongst S-phase-concentrated cells points to an elevated susceptibility to B[*a*]P-induced alterations in this latter cell population. The effects of low-dose *vs.* high-dose treatment are compared by measuring the distance in LD1 space from the mean of the corresponding vehicle control (Figs. 2B and 3B). Distance in LDA space enables one to determine which treatment induces the most alterations in cellular structures compared to the corresponding control, and cluster vector plots identify the precise biomolecular entities most altered with different treatments (Martin et al., 2010). One-D scores plots of derived IR spectra explored by PCA–LDA confirmed the dose-related increases in B[*a*]P-induced alterations in MCF-7 cells concentrated in G_0/G_1-phase (Fig. 3B), in line with the initial observation in Fig. 1B. Consistent with Fig. 1A, there is overlap of spectral points representing vehicle control *vs.* low-dose treatment categories with a marked segregation compared to the high-dose exposure group (Fig. 2B). No overlap is apparent in the 10^{-6} M B[*a*]P *vs.* vehicle control comparison in which the following wavenumbers (ranked from higher to lower priority) were responsible for segregation: 1215 cm^{-1} [asymmetric phosphate ($\nu_{as}PO_2^-$)], 1701 cm^{-1} (lipid), 1609 cm^{-1} (Amide I), 1304 cm^{-1} (Amide III) and 1381 cm^{-1} (COO— symmetric stretching

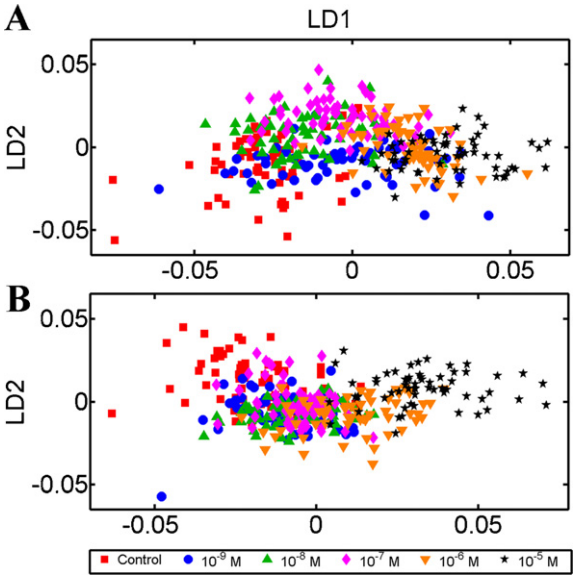

Fig. 1. PCA–LDA scores plots performed on the dataset containing IR spectra derived following indicated B[*a*]P treatments in MCF-7 cells. (A) MCF-7 cell line concentrated in S-phase; and, (B) MCF-7 cell line concentrated in G_0/G_1-phase. The different categories were: DMSO (red), 10^{-9} M (blue), 10^{-8} M (green), 10^{-7} M (magenta), 10^{-6} M (yellow), and 10^{-5} M (black). (For interpretation of the references to colour in this figure legend, the reader is referred to the web version of the article.)

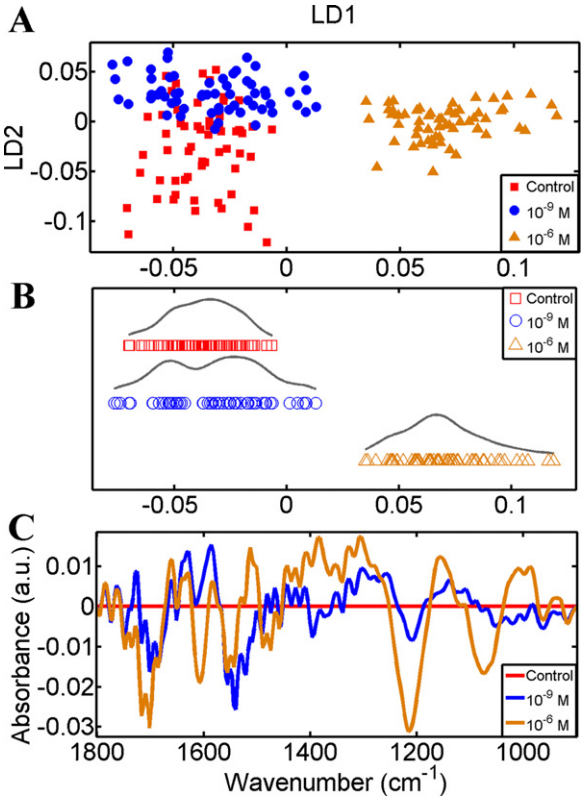

Fig. 2. Effects of 24-h treatment of MCF-7 cells concentrated in S-phase with high dose (10^{-6} M) or low dose (10^{-9} M) B[*a*]P. PCA–LDA scores plots and resultant cluster vectors were derived from triplicate experiments each performed in duplicate ($n = 60$ IR spectra per category derived from 10 measurements per slide). (A) 2-D PCA–LDA scores plot; (B) 1-D PCA–LDA scores plot; and, (C) cluster vectors plot. The different categories were classified as: vehicle control (red), 10^{-9} M B[*a*]P (blue) and 10^{-6} M B[*a*]P (yellow). (For interpretation of the references to colour in this figure legend, the reader is referred to the web version of the article.)

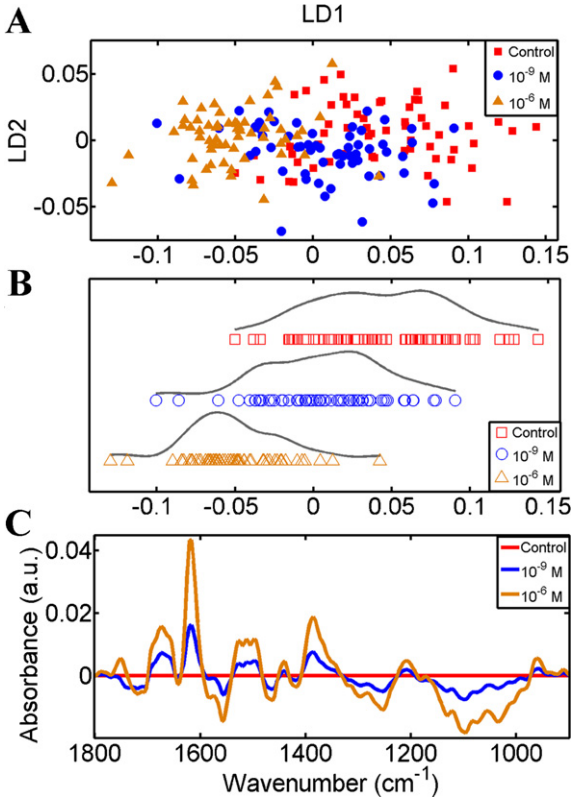

Fig. 3. Effects of 24-h treatment of MCF-7 cells concentrated in G_0/G_1-phase with high dose (10^{-6} M) or low dose (10^{-9} M) of B[*a*]P. PCA–LDA scores plots and resultant cluster vectors were derived from triplicate experiment ($n = 60$ IR spectra per category derived from 10 measurements per slide). (A) 2-D PCA–LDA scores plot; (B) 1-D PCA–LDA scores plot; and, (C) cluster vectors plot. The different categories were classified as: DMSO (red), 10^{-9} M B[*a*]P (blue) and 10^{-6} M (yellow) B[*a*]P. (For interpretation of the references to colour in this figure legend, the reader is referred to the web version of the article.)

vibrations of fatty acids and amino acid). Exposure to 10^{-9} M B[*a*]P resulted in spectral alterations (*vs.* vehicle control) associated with 1539 cm^{-1} (Amide II), 1701 cm^{-1} (lipid), 1586 cm^{-1} (Amide I), 1628 cm^{-1} (Amide I) and 1304 cm^{-1} (Amide III), ranked with a decreasing level of priority (Fig. 2C).

The greatest segregation of spectral points from vehicle control cells concentrated in G_0/G_1-phase is observed in the 10^{-6} M B[*a*]P category, followed by that of the 10^{-9} M treatment. Treatment with 10^{-6} M B[*a*]P induced the most pronounced spectral alterations, with distinguishing wavenumbers (ranked from higher to lower priority) observed at 1616 cm^{-1} (Amide I), 1385 cm^{-1} (COO— symmetric stretching vibrations of fatty acids and amino acid), 1096 cm^{-1} ($\nu_s PO_2^-$), 1674 cm^{-1} (Amide I) and 1034 cm^{-1} (glycogen). The main spectral alterations (ranked with a decreasing level of priority) induced by 10^{-9} M B[*a*]P treatment included 1616 cm^{-1} (Amide I), 1096 cm^{-1} [symmetric phosphate ($\nu_s PO_2^-$)], 1385 cm^{-1} (COO— symmetric stretching vibrations of fatty acids and amino acid), 1674 cm^{-1} (Amide I) and 1555 cm^{-1} (Amide II) (Fig. 3C).

3.3. Cell number with time in culture with exposure to B[a]P

The effects of B[*a*]P on the increases in cell numbers of MCF-7 cells in culture are shown in Fig. 4. Following a 12-h treatment, there are no marked differences between different treatment categories (vehicle control *vs.* 10^{-9} M B[*a*]P *vs.* 10^{-6} M B[*a*]P). After a further 12 h, high-dose B[*a*]P (*i.e.*, 10^{-6} M) gave rise to an elevated cell number, compared to the other two treatment categories.

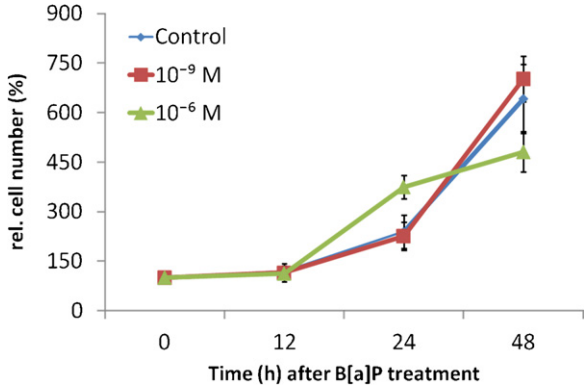

Fig. 4. Effects of B[*a*]P treatment of MCF-7 cells in culture on time-related increases in cell number. Cells were treated with B[*a*]P (10^{-9} M or 10^{-6} M) or DMSO as corresponding vehicle control. Cell numbers were determined at the indicated time points. Results are expressed as relative cell number [%; *i.e.*, ratio of the cell number at indicated time point relative to that determined at T_0 (normalized to 100%) × 100]. Each experiment was conducted on three separate occasions in triplicate with two independent cell counts (*i.e.*, one by each of two individuals) acquired per flask. The acquired values for each experimental condition were then averaged and these contributed to the mean ± SD of the three separate experiments.

However, following 48-h treatment, high-dose B[*a*]P resulted in marked decreases in cell numbers; in contrast, low-dose B[*a*]P (*i.e.*, 10^{-9} M) exposure resulted in a similar if not slightly higher level of cell numbers compared to the corresponding vehicle control.

4. Discussion

ATR-FTIR spectroscopy with multivariate analysis was applied to characterize B[*a*]P-induced alterations of MCF-7 cells concentrated in different phases of the cell cycle. The multivariate approach of PCA–LDA was employed to extract subtle differences in the complex dataset of derived IR spectra (Trevisan et al., 2010). Between-category (*i.e.*, different treatment categories) segregation was best demonstrated in scores plots. This approach appears capable of identifying dose-related effects of B[*a*]P over a large concentration range, down to levels lower than that required to induce cytotoxicity (Hockley et al., 2006; Hamouchene et al., 2011). Traditionally, high-dose concentrations (primarily ≥μM) have been investigated in short-term genotoxicity assays; how the observed effects under these experimental conditions extrapolate to real-world low-dose environmental exposures over some decades is uncertain (Weisz et al., 2012).

Nearness in multivariate distance implies similarity, whilst segregation of category clusters in the PCA–LDA scores plots signifies dissimilar groups of cellular structures (Martin et al., 2007, 2010). Both 1-D and 2-D scores plots demonstrated that the 10^{-6} M category exhibited a greater degree of segregation from the corresponding vehicle control than the 10^{-9} M group, irrespective of whether exposed cells were concentrated in S-phase or in G_0/G_1-phase. Extracted distinguishing features (or variables) induced by 10^{-6} M B[*a*]P treatment compared to the corresponding control in S-phase-concentrated cells were associated with alterations in DNA/RNA (*e.g.*, $\nu_{as} PO_2^-$), lipid, secondary structures of proteins (Amide I and Amide III) and, COO— symmetric stretching vibrations of fatty acids and amino acid (Figs. 2C and 3C). In contrast, low-dose (10^{-9} M) B[*a*]P resulted in marked alterations associated with secondary structures of proteins (Amide I, Amide II and Amide III) and lipid (Figs. 2C and 3C).

These dissimilar alteration profiles induced by different concentrations of B[*a*]P exposure even within cells concentrated in the same phase of the cell cycle point to different mechanisms of action; however, most definitive is the observations that high-dose B[*a*]P

is most effective in producing DNA/RNA alterations. In addition, B[*a*]P-induced spectral alterations following low-dose or high-dose exposure in cell populations concentrated in G_0/G_1-phase were associated with secondary structures of proteins, DNA/RNA and, COO— symmetric stretching vibrations of fatty acids and amino acids. This combination of alterations in DNA/RNA and proteins is suggestive of a genotoxic insult; alterations in protein may also be a consequence of AhR-stimulated influences on gene expression (Hockley et al., 2007; Hooven and Baird, 2008; Takemura et al., 2010).

MCF-7 cell lines differ in their response to B[*a*]P exposure in a time- and concentration-specific manner. B[*a*]P appears capable of inducing MCF-7 cell proliferation in comparison to corresponding control (Fig. 4); high-dose exposure induces short-term proliferation but long-term inhibition of cell growth (Kalantzi et al., 2004) and cytotoxicity (Myllynen et al., 2007), whereas exposure to low-dose exposure appears to generate no short-term effect. B[*a*]P-induced proliferation in the oestrogen-responsive human cell line human MCF-7 cell could be mediated by the oestrogenic properties of B[*a*]P (Tsai et al., 2004). It is intriguing that humans are rarely exposed to acute high-dose levels of environmental contaminants akin to those tested in short-term genotoxicity assays, but do have chronic lifetime exposures to low-dose levels. The aetiology of many age-related diseases may involve subtle alterations accumulated over a number of decades; this study demonstrates that low-dose exposures are capable of inducing alterations in exposed cell populations. Critically, these alterations occur in surviving cells. Biospectroscopy techniques could be an adjunct to other emerging technologies such as epigenetic profiling in order to better understand mechanisms of contaminant-induced effects (Tian et al., 2012).

The application of IR spectroscopy with computational analysis offers the possibility to investigate the mechanistic effects of low-dose levels of environmental contaminants. The potential to produce an integrated response profile to environmental effects (Malins et al., 1997) that may exhibit a nonlinear dose-response or linear dose–response (Llabjani et al., 2011) relationship is novel and exciting. Employing multivariate analysis techniques such as PCA–LDA could allow for an objective classification approach for alterations induced by test agents in target cells.

Conflict of interest statement

The authors declare that there are no conflicts to interest.

Funding

Francis L. Martin: China Scholarship Council; Rosemere Cancer Foundation; NERC; Unilever plc.

Acknowledgement

WP was funded by the China Scholarship Council.

References

Arakawa, H., Neault, J.F., Tajmir-Riahi, H.A., 2001. Silver(I) complexes with DNA and RNA studied by Fourier transform infrared spectroscopy and capillary electrophoresis. Biophys. J. 81, 1580–1587.

Bi, X., Walsh, M.J., Wei, X., Sheng, G., Fu, J., Martin-Hirsch, P.L., Thomas, G.O., Jones, K.C., Martin, F.L., 2007. Infrared spectral analysis of MCF-7 cells treated with serum-lipid extracts segregates predominantly brominated flame retardant-exposed subjects from those with mainly organochlorine exposures. Environ. Sci. Technol. 41, 5915–5922.

Birnbaum, L.S., 1994. The mechanism of dioxin toxicity: relationship to risk assessment. Environ. Health Perspect. 102 (Suppl. 9), 157–167.

Bock, K.W., 1994. Aryl hydrocarbon or dioxin receptor: biologic and toxic responses. Rev. Physiol. Biochem. Pharmacol. 125, 1–42.

Boström, C.E., Gerde, P., Hanberg, A., Jernström, B., Johansson, C., Kyrklund, T., Rannug, A., Törnqvist, M., Victorin, K., Westerholm, R., 2002. Cancer risk assessment, indicators, and guidelines for polycyclic aromatic hydrocarbons in the ambient air. Environ. Health Perspect. 110 (Suppl. 3), 451–488.

Fearn, T., 2002. Discriminant analysis. In: Chalmers, J., Griffiths, P.R. (Eds.), Handbook of Vibrational Spectroscopy. John Wiley & Sons, New York, pp. 2086–2093.

Hamouchene, H., Arlt1, V.M., Giddings, I., Phillips, D.H., 2011. Influence of cell cycle on responses of MCF-7 cells to benzo[*a*]pyrene. BMC Genomics 12, 333–349.

Hattemer-Frey, H.A., Travis, C.C., 1991. Benzo-a-pyrene: environmental partitioning and human exposure. Toxicol. Ind. Health 7, 141–157.

Hockley, S.L., Arlt, V.M., Brewer, D., Giddings, I., Phillips, D.H., 2006. Time- and concentration-dependent changes in gene expression induced by benzo(a)prene in two human cell lines, MCF-7 and HepG2. BMC Genomics 7, 260–283.

Hockley, S.L., Arlt, V.M., Brewer, D., Te Poele, R., Workman, P., Giddings, I., Phillips, D.H., 2007. AHR- and DNA-damage-mediated gene expression responses induced by benzo(a)pyrene in human cell lines. Chem. Res. Toxicol. 20, 1797–1810.

Hooven, L.A., Baird, W.M., 2008. Proteomic analysis of MCF-7 cells treated with benzo[*a*]pyrene, dibenzo[*a,l*]pyrene, coal tar extract, and diesel exhaust extract. Toxicology 249, 1–10.

Jiao, H., Allinson, S.L., Walsh, M.J., Hewitt, R., Cole, K.J., Phillips, D.H., Martin, F.L., 2007. Growth kinetics in MCF-7 cells modulate benzo[*a*]pyrene-induced *CYP1A1* up-regulation. Mutagenesis 22, 111–116.

Kalantzi, O.I., Hewitt, R., Ford, K.J., Cooper, L., Alcock, R.E., Thomas, G.O., Morris, J.A., McMillan, T.J., Jones, K.C., Martin, F.L., 2004. Low dose induction of micronuclei by lindane. Carcinogenesis 25, 613–622.

Kelly, J.G., Martin-Hirsch, P.L., Martin, F.L., 2009. Discrimination of base differences in oligonucleotides using mid-infrared spectroscopy and multivariate analysis. Anal. Chem. 81, 5314–5319.

Kelly, J.G., Ahmadzai, A.A., Hermansen, P., Pitt, M.A., Saidan, Z., Martin-Hirsch, P.L., Martin, F.L., 2011. A biospectroscopic interrogation of fine needle aspirates points towards segregation between graded categories: an initial study towards diagnostic screening. Anal. Bioanal. Chem. 401, 957–967.

Llabjani, V., Jones, K.C., Thomas, G.O., Walker, L.A., Shore, R.F., Martin, F.L., 2009. Polybrominated diphenyl ether-associated alterations in cell biochemistry as determined by attenuated total reflection Fourier-transform infrared spectroscopy: a comparison with DNA-reactive and/or endocrine-disrupting agents. Environ. Sci. Technol. 43, 3356–3364.

Llabjani, V., Trevisan, J., Jones, K.C., Shore, R.F., Martin, F.L., 2010. Binary mixture effects by PBDE congeners (47, 153, 183, or 209) and PCB congeners (126 or 153) in MCF-7 cells: biochemical alterations assessed by IR spectroscopy and multivariate analysis. Environ. Sci. Technol. 44, 3992–3998.

Llabjani, V., Trevisan, J., Jones, K.C., Shore, R.F., Martin, F.L., 2011. Derivation by infrared spectroscopy with multivariate analysis of bimodal contaminant-induced dose–response effects in MCF-7 cells. Environ. Sci. Technol. 45, 6129–6135.

Malins, D.C., Polissar, N.L., Gunselman, S.J., 1997. Infrared spectral models demonstrate that exposure to environmental chemicals leads to new forms of DNA. Proc. Natl. Acad. Sci. U.S.A. 94, 3611–3615.

Martin, F.L., 2007. Complex mixtures that may contain mutagenic and/or genotoxic components: a need to assess *in vivo* target-site effect(s) associated with *in vitro*-positive(s). Chemosphere 69, 841–848.

Martin, F.L., German, M.J., Wit, E., Fearn, T., Ragavan, N., Pollock, H.M., 2007. Identifying variables responsible for clustering in discriminant analysis of data from infrared microspectroscopy of a biological sample. J. Comput. Biol. 14, 1176–1184.

Martin, F.L., Kelly, J.G., Llabjani, V., Martin-Hirsch, P.L., Patel, I.I., Trevisan, J., Fullwood, N.J., Walsh, M.J., 2010. Distinguishing cell types or populations based on the computational analysis of their infrared spectra. Nat. Protoc. 5, 1748–1760.

Myllynen, P., Kurttila, T., Vaskivuo, L., Vähäkangas, K., 2007. DNA damage caused by benzo(a)pyrene in MCF-7 cells is increased by verapamil, probenecid and PSC833. Toxicol. Lett. 169, 3–12.

Petrich, W., 2001. Mid-infrared and Raman spectroscopy for medical diagnostics. Appl. Spectrosc. Rev. 36, 181–237.

Rubin, H., 2001. Synergistic mechanisms in carcinogenesis by polycyclic aromatic hydrocarbons and by tobacco smoke: a bio-historical perspective with updates. Carcinogenesis 22, 1903–1930.

Shen, W., Liu, H., Yu, Y., 2008. Translation initiation proteins, ubiquitin–proteasome system related proteins, and 14-3-3 proteins as response proteins in FL cells exposed to anti-benzo[*a*]pyrene-7,8-dihydrodiol-9,10-epoxide. Proteomics 8, 3450–3468.

Shimada, T., Sugie, A., Yamada, T., Kawazoe, H., Hashimoto, M., Azuma, E., Nakajima, T., Inoue, K., Oda, Y., 2003. Dose–response studies on the induction of liver cytochromes P450 1A1 and 1B1 by polycyclic aromatic hydrocarbons in arylhydrocarbonresponsive C57BL/6J mice. Xenobiotica 33, 957–971.

Shimada, T., 2006. Xenobiotic-metabolizing enzymes involved in activation and detoxification of carcinogenic polycyclic aromatic hydrocarbons. Drug Metab. Pharmacokinet. 21, 257–276.

Shimizu, Y., Nakatsuru, Y., Ichinose, M., Takahashi, Y., Kume, H., Mimura, J., Fujii-Kuriyama, Y., Ishikawa, T., 2000. Benzo[*a*]pyrene carcinogenicity is lost in mice lacking the aryl hydrocarbon receptor. Proc. Natl. Acad. Sci. U.S.A. 97, 779–782.

Takemura, H., Nagayoshi, H., Matsuda, T., Sakakibara, H., Morita, M., Matsui, A., Ohura, T., Shimoi, K., 2010. Inhibitory effects of chrysoeriol on DNA adduct formation with benzo[*a*]pyrene in MCF-7 breast cancer cells. Toxicology 274, 42–48.

Tian, M., Peng, S., Martin, F.L., Zhang, J., Liu, L., Wang, Z., Dong, S., Shen, H., 2012. Perfluorooctanoic acid induces gene promoter hypermethylation of glutathione-S-transferase Pi in human liver L02 cells. Toxicology, http://dx.doi.org/10.1016/j.tox.2012.03.003.

Tsai, K.S., Yang, R.S., Liu, S.H., 2004. Benzo[*a*]pyrene regulates osteoblast proliferation through an estrogen receptor-related cyclooxygenase-2 pathway. Chem. Res. Toxicol. 17, 679–684.

Tsuchiya, Y., Nakajima, M., Itoh, S., Iwanari, M., Yokoi, T., 2003. Expression of aryl hydrocarbon receptor repressor in normal human tissues and inducibility by polycyclic aromatic hydrocarbons in human tumor-derived cell lines. Toxicol. Sci. 72, 253–259.

Trevisan, J., Angelov, P.P., Patel, I.I., Najand, G.M., Cheung, K.T., Llabjani, V., Pollock, H.M., Bruce, S.W., Pant, K., Carmichael, P.L., Scott, A.D., Martin, F.L., 2010. Syrian hamster embryo (SHE) assay (pH 6.7) coupled with infrared spectroscopy and chemometrics towards toxicological assessment. Analyst 135, 3266–3272.

Weisz, J., Shearer, D.A., Murata, E., Patrick, S.D., Han, B., Berg, A., Clawson, G.A., 2012. Identification of mammary epithelial cells subject to chronic oxidative stress in mammary epithelium of young women and teenagers living in USA: implication for breast carcinogenesis. Cancer Biol. Ther. 13, 101–113.

Yoshino, I., Kometani, T., Shoji, F., Osoegawa, A., Ohba, T., Kouso, H., Takenaka, T., Yohena, T., Maehara, Y., 2007. Induction of epithelial–mesenchymal transition-related genes by benzo[*a*]pyrene in lung cancer cells. Cancer 110, 369–374.

Appendix 2

I collected and presented the data at the 35th Annual Meeting of the United Kingdom Environmental Mutagen Society.

Mechanistic insights into nanotoxicology in target cell populations employing biospectroscopy techniques

Junyi Li, Francis L. Martin

Centre for Biophotonics, Lancaster Environment Centre, Lancaster University, Bailrigg, Lancaster LA1 4YQ, UK

Nanotechnology has introduced a wide variety of man-made materials designed to nanoscale, especially nanoparticles, into our environment. Because of their unique physico-chemical properties, nanoparticles may pose a potential risk to human health and the environment. Most recent investigations assessing the risk of nanotoxicology have mainly focused on high-dose effects. However, classic toxicokinetic or toxicodynamic considerations applied for chemical risk assessment may not apply to nanoparticle exposures. There is also a significant lack of understanding of their mechanism(s) of action. Biospectroscopy techniques have been employed as a novel approach to identify low-dose effects induced by test agents in target cell populations [1]. In this study, MCF-7 cells concentrated in S-phase or G_0/G_1-phase were treated for 24 h with short multi-walled carbon nanotubes at the following concentration range: 0.0025 mg/L, 0.005 mg/L, 0.01 mg/L, 0.025 mg/L, 0.05 mg/L and 0.1 mg/L. Cells were then examined using attenuated total reflection-Fourier-transform infrared (ATR-FTIR) spectroscopy coupled with multivariate analysis; this approach allows the derived data [*i.e.*, infrared (IR) spectra] to be visualized as spectral points within respective categories, *e.g.*, treatments. Even at the lowest concentrations employed, significant ($P \leq 0.05$) separation of IR spectra representing treatment categories *versus* vehicle control was observed. Dose-related effects were also noted. To identify the discriminating biomolecular entities segregating various spectral categories, cluster vector plots were employed. These showed that the major alterations induced by short multi-walled carbon nanotubes were associated with the DNA/RNA spectral region [primarily 1080 cm^{-1} ($\nu_s PO_2^-$) and 1225 cm^{-1} ($\nu_{as} PO_2^-$)]. These results suggest that short multi-walled carbon nanotubes may cross the cell membrane in order to generate a genotoxic mechanism of action.

References

1. Llabjani, V., Trevisan, J., Jones, K. C., Shore, R. F. and Martin, F. L. (2011) Derivation by infrared spectroscopy with multivariate analysis of bimodal contaminant-induced dose-response effects in MCF-7 cells. *Environ. Sci. Technol.*, **45,** 6129-6135.